A Study on Building Process and Microstructure Formation of Biomedical CoCrMo Alloy in Electron Beam Powder-bed Additive Manufacturing

TOHOKU UNIVERSITY

By

Yufan Zhao

Department of Materials Processing,

Graduate School of Engineering, Tohoku University

A thesis submitted to Tohoku University for the degree of Doctor of philosophy

July 2019

A Study on Building Process and Microstructure Formation of Biomedical CoCrMo Alloy in Electron Beam Powder-bed Additive Manufacturing

By

Yufan ZHAO

Department of Materials Processing,

Graduate School of Engineering, Tohoku University

Approved by:

Professor **Akihiko CHIBA** (Supervisor)

Department of Materials Processing, Tohoku University

Professor **Koichi ANZAI**

Department of Metallurgy, Tohoku University

Professor **Yutaka SATO**

Department of Materials Processing, Tohoku University

Professor **Naoyuki NOMURA**

Department of Materials Processing, Tohoku University

Associate Professor **Kenta YAMANAKA**

Department of Materials Processing, Tohoku University

Content

Abstract

Additive manufacturing (AM) plays a notable role in producing components with complex structural geometries that are hard or even impossible to produce via conventional techniques. AM for metallic components has gained acceptance for applications in aerospace, automotive, and biomedical industries. AM of metal systems can be classified into powder bed, powder feed, and wire feed system. The most famous powder bed systems are electron beam melting from ARCAM and laser melting from EOS.

In this study, we will focus on powder bed fusion with electron beam (PBF-EB) in which an electron beam is used as a heat source to melt metal powders selectively and produce parts in a layer-by-layer fashion. Compared with other powder bed systems, electron beam gun can generate high beam power and high scan speed, therefore high building rate. Since powder bed is preheated at high temperature, less support is needed, and residual stress is low. The vacuum atmosphere (pressure: 0.01–0.1 Pa) in PBF-EB provides a controlled environment that prevents the oxidation or other reactions for materials containing active elements, such as Co–Cr alloys and Ti alloys. In addition, free-form shaping can be achieved without a mold or the limitations of cutting tools. PBF-EB allows components to be fabricated with complex geometries or topological structures. Although PBF-EB has shown great potential for producing full-density functional metallic parts, a few critical issues related to processing stability, part defects, quality variations, and microstructure evolution need to be addressed before this process can be employed for broad applications and large-scale production.

Co-Cr-Mo (CCM) alloys, an alloy commonly used for surgical implants, present high strength, superior corrosion resistance, non-magnetic behavior, and excellent biocompatibility. PBF-EB plays a significant role in the development of medical implants via computer-aided design and provides extensive customization based on the individual patient data that can be captured by computed tomography and magnetic resonance imaging technology.

PBF-EB process includes four steps, raking powder layer, preheating powder layer, selectively melting and stage down. These steps will be repeated again and again until the 3D component building process is finished. In the powder raking step, the (i) powder layer properties are essential for process stability and determine resulting materials properties. How the raking process affect the uniformity of the powder bed is currently not examined very well. Then, the electron beam scans the powder layer; the powder particles melt and form an agitated molten pool for some milliseconds. (ii) Molten pool behavior is related to the formation of a variety of defects, and because the moving liquid transports heat, it often dominates heat transport and has a profound effect on solidification conditions. The continuous building process leads to characteristic microstructures due to rapid and directional solidification. Solidification is mainly directed in building direction and predominantly epitaxial. (iii) Microstructure control is significant for extensive application of PBF-EB-built components. The current knowledge involves in these aspects is helpful but still does not address many of the critical features of PBF-EB. These issues are corresponding to the contents of my Ph.D. study.

Single-track melting and block building experiments were performed using an Arcam®A2X machine. The means of observation include an optical microscope, scanning electron microscopy based on the backscattered electron (BSE) signals and electron backscattering diffraction (EBSD) measurements. For elucidating underlying mechanisms for powder layer formation, molten pool behavior, and microstructure evolution, numerical simulations were utilized. The dynamic behavior of the powder raking process was simulated using the discrete element method (DEM) modeling. We applied computational thermal-fluid dynamics (CtFD) simulations to analyze the temperature field and melt dynamics. Multi-phase field (MPF) simulations were performed to clarify the solidification microstructure evolution.

The main conclusions derived from this study can be summarized as follows:

■ Effects of the different physical parameters on powder bed pattern, focusing on packing density, powder flowability, particle size distribution, and their interplays:

1) Powder packing density increased with increasing layer thickness.

2) The better flowability of powder was preferable for homogeneity of powder layer with higher packing density.

3) The mixture of powder with large and small size could increase packing density, but it might be detrimental to the flowability and homogeneity.

■ Fundamentals of molten pool behavior in PBF-EB, focusing on the forming quality-correlated fluid dynamics and the differences compared with PBF-L(laser):

1) CtFD simulation showed greater agreement with experiment than the FEM (pure-thermal) model because fluid flow shows essential effects on temperature distribution and molten pool geometry.

2) Simulation results revealed the decisive influence of the Marangoni effect on fluid behavior and heat convection. The Marangoni effect primarily determined the molten pool geometry and significantly affects molten pool instability and forming quality.

3) Owing to the weak vapor reoil pressure and being without multiple beam reflection, PBF-EB possessed a wider process window, ensuring process stability compared with PBF-L.

4) Fluid flow played a vital role in determining the solidification rate, R. The increasing R values could be attributed to changes in the spatial relation to the scan direction under the effect of active fluid convection.

■ Characteristics of the powder bed with consideration of physical properties and their influences on PBF-EB fusion process:

1) Powder layer, with its stochastic nature, provided more fluid disturbance caused by non-uniform capillary actions, efficiently producing the irregularity or disconnection of melt-track with increasing scan speed.

2) Concerning particle size, for the powder bed with small-size powder, the increased emissivity of powder bed caused the absorbed beam energy to become insufficient to melt the surrounding particles.

3) Amount of heat radiation was different for different powder types. PREP powder with high circularity and small surface area was appropriate for PBF-

EB, which was favorable for melt stability and enlarging the process window.

- Mechanisms governing the grain morphology and texture formation and proposing method for improving CET in PBF-EB-built Co-28Cr-6Mo alloy:

  1) Typical growth behavior of columnar grains and the resulting near-cubic texture were determined by competitive epitaxial grain growth governed by the heat flow characteristics with xy-scanning.

  2) The crystallographic texture was closely related to the transient geometry of the molten pool boundary, where the heat flow direction determines the crystallographic orientation during solidification.

  3) By manipulating molten pool geometry and remelting fraction of adjacent melt track, forming of new grains instead of complete epitaxial growth could be possible depending on process conditions.

  4) Nucleation and growth of new grains occurred ahead of inclined cell/dendrite with respect to the temperature gradient of the solidification front.

  5) Enlarged undercooling and probable dendrite fragmentation owing to fast fluid flow would promote the nucleation probability and new grains formation, which suggested that fluid convection is an essential factor promoting CET during the PBF-EB process.

- Mechanisms for microstructural inhomogeneity regarding matrix phase constitution of PBF-EB-built Co-28Cr-6Mo alloy, addressing the role of thermal history:

  1) The isothermal and athermal $\gamma \rightarrow \varepsilon$ phase transformations took place in CCM alloy during PBF-EB. Isothermal $\gamma \rightarrow \varepsilon$ transformation occurred through both manners: diffusionless-martensitic and diffusion-massive transformation.

  2) Depending on PBF-EB process conditions, thermal history determined the mechanism by which the $\gamma \rightarrow \varepsilon$ phase transformation was taking place.

  3) In the sample with a lower energy input ($E_{area} = 2.6$ J/mm^2), $\gamma \rightarrow \varepsilon$ martensitic transformation with S-N OR was dominant. In the sample with a higher energy input ($E_{area} = 4.4$ J/mm^2), the ε phase with near-random orientation formed via diffusional-massive transformation.

Chapter 1
Introduction

1.1. Additive manufacturing for metallic components

Additive Manufacturing is a new paradigm for industrial manufacturing in which components are built by melting thin layers of powder. Material is being added instead of removing that is the case in conventional machining. AM that is known as 3D printing is an innovative approach for industrial manufacture and is capable of fabricating stronger and lighter components with complex geometry. Metal AM favors for the fabrication of components that often cannot be produced using other conventional processes [1]. A lot of metals and alloys can be fabricated by AM techniques, from noble metals like gold and silver to strategic metals like stainless steel, titanium, and some other high-performance alloy such as nickel-based alloys and cobalt chrome alloys [2]. AM uses data obtain by computer-aided-design or 3D object scanners for the material forming process in a layer-by-layer fashion with precise geometry [3][4][5].

AM is adept in producing components with weight-saving and design of complex geometry. Therefore, AM is an ideal method for producing aerospace parts with a high strength-to-weight ratio. Northwestern Polytechnical University fabricated a 3-meter-long titanium alloy parts of China's COMAC C919 aircraft in 2013 [6]. In 2015, the Federal Aviation Administration (FAA) cleared the first AM-built part for commercial jet engine [7]. In 2017, Boeing 787 was equipped with the FAA-certified, titanium structural parts fabricated by AM [8]. AM also satisfies the needs of the automotive industry, favoring advances in components design. For example, AM-built aluminum alloys are used to produce air intake and exhaust system. Recently, BMW reported that they had produced one-millionth AM-built component in batch production since 2010 [9]; Volkswagen had established a new and highly AM center in Wolfsburg, soon being able to go into 3D series production [10]. In the medical industry, AM has already fabricated FDA-approved spinal and hip implants. Employing AM, implants

manufacturing time has been dramatically reduced compared with conventional processes [11]. Implants are produced according to a patient's anatomy, thus ensuring a better fit with greater customization.

During the AM process, 3D metallic component grows layer-by-layer. Each successive layer is bonded with each other through the melting or partial melting of metallic powder bed or feeding wire/powder [12]. AM techniques for metals use metal powder or wire feedstock, depending on the exact approach used [13]. Although all AM processes for metals involve the layer-by-layer building of 3D components, there is a variety of different AM approaches for metals: directed energy deposition (DED), material/binder jetting, sheet lamination, and powder bed fusion (PBF) [14]. These AM approaches include notable variations on the material forming methods and technical features. Material state (powder, liquid, wire), heat sources (laser, electron beam, plasma arc), material-supply systems, and building chamber characteristics vary depending on processes.

Among these approaches, DED (Fig. 1.1) and PBF (Fig. 1.2) gain much attention from manufacturers and researchers. DED utilizes laser, electron beam or plasma arc to melt feeding metal powder or wire filament. Laser engineered net shape (LENS) technology [15] fabricates solid components through the melting of the dispensed powder from nozzles by a laser heat source. In electron beam additive melting (EBAM) [16], metal melting and fusing occur via an electron beam firing in a vacuum chamber. In rapid plasma deposition (RPD) [17], a wire filament is melted by a plasma arc in the building chamber filled with argon gas to produce components that require less post-processing. PBF is a process including a variety of popular AM technologies – powder bed fusion with electron beam (PBF-EB) [18], selective laser melting (SLM) [19], selective laser sintering (SLS) [20] and selective heat sintering (SHS) [21]. PBF melts the powder to a sufficient degree and fuses the powder. Powders are sintered (partially melted) or melted in various PBF technologies. Concerning applications, DED is appropriate for parts repairing or integrated manufacturing combined with other techniques. While PBF is ideal for flexible design and fabricating of complex geometries. PBF-built components typically possess high strength and stiffness.

1.2. Powder bed fusion with electron beam

Powder bed fusion with electron beam (PBF-EB) is an AM system that utilizes a high-energy electron beam to melt metal powders and fabricates full-dense metallic parts in a layer-building fashion [22]. Schematic of PBF-EB system is shown in Fig. 1.3. The heat source and chamber atmosphere (vacuum: 0.01 to 0.1 Pa) are different from those of SLM process, which is in favor of PBF-EB to be beneficial for materials that contain active elements such as cobalt–chrome and titanium alloys. Electromagnetic coils manage the electron beam, providing high-speed and accurate beam control, which allows several molten pools to be formed simultaneously [23]. Owing to the high melting capacity and productivity of the electron beam, PBF-EB produces components quickly and efficiently. PBF-EB process performs in a vacuum chamber and keeps at high temperature; thus, residual stress of components is low, and components properties are better than cast and comparable to wrought ones. The comparison between PBF-EB and SLM is shown in Table 1-1.

Benefiting from the vacuum system, a chamber pressure of $1 \times 10\text{-}5$ mbar or better is obtained throughout the entire building cycle. During the PBF-EB melting process, the partial pressure of Helium is introduced to $2 \times 10\text{-}3$ mbar. This clean and controlled build environment is essential to maintain the chemical specification of the building material. In each layer during building, the powder bed is entirely heated for keeping an appropriate ambient temperature that is specific for the powder used. As a result, the parts produced with the EBM process are almost free from residual stresses [24].

Being similar to SLM, the PBF-EB system generates a layer of metal powder by rake onto the building platform, and the powder layer is selectively melted by a heat source. The specific process stages (Fig. 1.4) consists of (i) preheating process in which the base plate is heated to the pre-set temperature by using a de-focused beam at a considerably high scan speed of 14600 mm/s; (ii) heating & building process in which preheating repeats following the building of each layer to slightly sinter the newly raked powder and keep the temperature of the base plate to be almost constant; and (iii) cooling after completion of the total build objects. The preheating is conducted to avoid

powder smoke in which if repulsive electrostatic forces are higher than the forces holding particles, particles may be ejected from the layer. Once a component has been fabricated, the building envelope is removed, and the building platform and attached component are removed from the loose powder. Powder clinging to the component or trapped in internal cavities can be blown or blasted away.

In common with some other manufacturing technologies, there are advantages and disadvantages while fabricating components using PBF-EB. Concerning advantages, building rates are almost 3-5 times those of other AM technologies. PBF-EB components usually need fewer support structures than SLM -built ones do. The PBF-EB process has approximately 95-percent energy efficiency, which is 5 to 10 times better than AM processes using a laser. It is possible to reduce residual stress during the preparation of CAD data, during building and in post-processing. During building, preheating of powder bed and heating of the material before the electron beam striking reduces residual stress. PBF-EB technology eliminates sintering, enabling users to gain precise control over porosity. PBF-EB manufacturers further minimize porosity issues through the adjustment of electron beam parameters [25]. About the limitations, the surface of a PBF-EB-built component typically possesses low accuracy and needs post-processing, while the smooth surfaces of SLM-built components do not typically require much post-processing. The choice of materials that can be applied in the PBF-EB process is somewhat limited; this is partly since the process requires high-quality and expensive metallic powders, which must also undergo thorough testing beforehand. The cost of materials, along with the cost of PBF-EB systems, make this technology an expensive solution, suitable only for industrial applications [26][27].

In the cases of right applications, PBF-EB could also be a cost-efficient way to produce prototypes and low-run production components. The most common applications of PBF-EB process lies in the medical (Fig. 1.5) and aerospace (Fig. 1.6) industrial production. In the medical industry, PBF-EB has been widely used to produce trabecular implants and other medical implants, depending on the customized data of patients. In 2012, the U.S. Food and Drug Administration first cleared orthopedic implants fabricated by PBF-EB technology [28]. Several years later, the FDA approved

craniofacial implants printed by PBF-EB systems [29]. In the aerospace industry, PBF-EB is mainly applied for producing aerospace components with a substantial weight reduction. For example, the GE company has already been using PBF-EB technology to build turbine blades for jet engines [30].

To sum up, although PBF-EB is most suited to demanding industrial applications, the technology demonstrates the considerable potential of AM for metal. As with the ability to produce complex metallic components that is comparable to traditional manufacturing technologies, PBF-EB offers an innovative solution to manufacturing small series, prototypes and even support structures using AM technique.

1.3. Key scientific issues involved in PBF-EB

In the powder raking step, the powder layer properties are essential for process stability and determine resulting materials properties. Then, the electron beam selectively scans the powder layer, the powder particles melt and form an agitated molten pool for some milliseconds. After melting, solidification mainly occurs directionally along the building direction and predominantly epitaxial. Thus, microstructure control is also significant for the broad application of PBF-EB-built components.

1.3.1. Powder bed generation

In addition to determining the input energy required and the fabrication conditions (i.e., the power (P), scan speed (V), and scan path to be used), comprehensive understanding of the generation of a powder bed and its properties is essential for improving the quality of the fabricated parts. The powder packing characteristics are among the most critical issues for powder-bed-based AM because there is only a limited number of particles can be directly subjected to the irradiation of electron beam at a given time. These characteristics bring critical complexity to the PBF-EB process because the wetting of the melt, as well as the thermal conductivity and emissivity of the packed powder layer, may affect the amount of energy absorbed and the heat and mass transfer processes along with the geometrical accuracy of the solidified part.

However, it is not easy to experimentally quantify the characteristics of the powder bed. Modeling efforts are currently underway to better understand how fluctuations in local effective densities or size distributions in the powder beds and their effects on melting behavior. Numerical simulations of particulate systems have become useful tools for investigating powder bed generation and are a convenient way of performing data analyses of the powder packing properties [31][32] and understanding the underlying consolidation process.

With regards to the modeling of the phenomenon of powder packing, a simple arrangement consisting of ideally spherical powder particles arranged in a predefined packing sequence (Fig. 1.7) has been used previously for simulating the PBF process [33][34]. However, significant differences exist between this model and actual powder packing because uniform particle size and regular arrangement are assumed in the case of the model, while in reality, the powder would consist of nonuniformly sized particles arranged irregularly. A later model for the generation of a powder bed depends on a sequential addition algorithm in which a container is successively filled with powder particles (Fig. 1.8), which are added one by one under the gravitational force [35]. This model depends on the particle size distribution (PSD). However, it does not account for the forces between the particles, such as the frictional force or viscoelastic force. Markl et al. [36] and Xiang et al. [37] conducted dynamic simulations by discrete element method (DEM) while taking into account the interparticle interactions but used a simple free-fall process within a box instead of actual powder-bed-generating processes such as squeezing, rolling, recoating, or raking (Fig. 1.9). The configuration of the powder particles and their resultant density of packing in the powder bed generated under the effect of gravity alone would be different from those for an actual powder bed. The motion of the powder particles caused by the horizontal motion of the rake would be multidirectional and complex. Lee et al. [38] and Mindt et al. [39] performed DEM simulations of powder bed generation by rolling and recoating (Fig. 1.10), respectively; these are processes that are performed during laser-beam PBF.

In currently used PBF-EB processes, the powder bed is generated by raking. The raking process is complicated, as it involves (i) the falling powder, (ii) the translatory

motion of the rake, and (iii) the various contact interactions. These interactions include the (i) powder-to-powder, (ii) powder-to-rake, and (iii) powder-to-building-plane (i.e., the top of the part being built) interactions, which depend on the mechanical properties of the materials being used as well as those of the rake. In powder bed generation, how the raking process affects the uniformity of the powder bed is currently not examined very well. The effects of the physical parameters on powder bed pattern, focusing on packing density, flowability, particle size distribution, and their interplays needs to be clarified.

1.3.2. Fluid flow and heat transfer within the molten pool

As shown in Fig. 1.11, the molten pool behavior involves Marangoni convection, metal evaporation, and capillary and wetting action; heat transfer occurs through absorption, conduction, and radiation. The principal objective of the melting step is to melt the entire powder bed and to reduce or eliminate the formation of voids and defects in the final parts. Fluid flow is related to the creation of a variety of defects, and because the moving liquid transports heat, it often dominates heat transport. More importantly, the fluid flow has a profound effect on solidification conditions [40]. The thermal field is intrinsically altered by fluid flow, such that the temperature gradient and solidification rate at the solidification front can be significantly influenced, which subsequently affects the solidification microstructural properties, including grain morphology, size, and growth direction. However, molten pool behavior under specific process conditions of PBF-EB has not been clarified.

The dynamics of the melt pool are highly transient and localized. Therefore, in-situ monitoring or direct measurements of the flow of the molten metal and its temperature distribution are difficult to perform. Researchers in this field have usually employed simulations based on computational thermal-fluid dynamics (CtFD) to model the AM consolidation process. Using accurate calculations of the temperature and velocity fields, it is possible to determine the solidification conditions that produce improved solidified microstructure. Bauereiß et al. [41] modeled a two-dimensional (2D) powder

bed using the lattice Boltzmann method to investigate the melting process and fundamental consolidation mechanisms of the individual powder particles. Their model considered capillary and wetting of the melt. Jamshidinia et al. [42] used a coupled thermal-fluid flow model (Fig. 1.12) that considered the influence of fluid convection to investigate molten pool geometry. The authors found that the outward flow from the front of the molten pool was induced by surface tension (Marangoni flow). To simulate the PBF-EB process with greater precision and reliability, Körner's group [41][43] modeled the powder using the 2-D lattice Boltzmann method (LBM) to study the fundamental consolidation mechanisms of individual powder particles (Fig. 1.13). Their studies indicated that hydrodynamics, such as capillary action and wetting, combined with the stochastic powder layer, are the origins of the defects. Liu's group [44][45] developed an integrated modeling framework that consists of a discrete element model of powder spreading and a computational fluid dynamics model of powder melting to investigate defect formation during PBF-EB of multiple tracks and layers (Fig. 1.14). These studies showed that numerical simulations could aid in understanding the underlying physical phenomenon of a system, which can be used to optimize the quality of PBF-EB-fabricated parts. However, given the exclusive process conditions during PBF-EB, the molten pool behavior under specific process conditions of PBF-EB and their effect on forming quality have not been clearly clarified. In particular, because of the differences in heat source, building environment, and heat transfer manner between PBF-EB and PBF-L(laser), the comparison between the two types of powder-bed fusion AM is desired to be elucidated.

The stochastic powder layer, along with the hydrodynamics-related phenomena that occur, including capillarity and wetting, influence the formation of different types of defects and, consequently, the forming quality. With powder layer, previous studies endeavored to figure out the relationship between process parameters and forming quality. However, a thorough discussion of thermal properties (i.e., emissivity and thermal conductivity) of the powder layer depending on the characteristics (i.e., its spatial arrangement and PSD) of the powder layer and their influences on fusion behavior and process stability are still demanded.

1.3.3. Solidification and microstructure formation

As shown in Fig. 1.15, the solidification process in powder bed AM tends to be dominated by epitaxial grain growth [46]. In AM, for alloys with cubic crystal, alloys tend to solidify epitaxially, efficiently producing columnar grains with {001} texture oriented along the building direction due to the overall heat flow [47]. The anisotropy of the parts composed of columnar grains is detrimental for practical applications involving multiaxial stress [48]. Misoriented fine grains are sometimes necessary to meet specific performance requirements; for example, tailor-made artificial hip joints must possess stem parts with low Young's moduli and neck parts with substantial strength. These two features correspond to epitaxially columnar and misoriented polycrystalline structures, respectively. Thus, the primary challenge in the wide application of PBF-EB-built components, especially Co-Cr-Mo medical implants, is flexible control of the grain morphology and texture development associated with anisotropic mechanical properties.

Different methods are tailoring the microstructure. Also, specific melting strategies may cause columnar to equiaxed transition. For site-specific microstructure control, many researchers have attempted to clarify the correlations between the solidification microstructure and process parameters in AM. For instance, Helmer et al. [49] investigated the microstructure of and established a processing window for the nickel-based alloy IN718 by PBF-EB. They found that a more focused beam induced the formation of new grains that hindered the development of a columnar grain structure, due to the stronger melt motion and steeper flanks of the molten pool (Fig. 1.16). Dehoff et al. [50] generated solid/liquid (S/L) interface instability and constitutional undercooling during epitaxial solidification, demonstrating the feasibility of producing both epitaxial and near-equiaxed grains by adjusting the scan strategy and PBF-EB parameters for IN718. Körner et al. [51] studied the effects of the scan strategy on the solidification conditions and showed that the direction of the thermal gradient during solidification could be altered by adjusting the scan strategy to produce either epitaxial growth or stray grains in PBF-EB of IN718. Raghavan et al. [52] proposed a new melt-

scan strategy (point heat source fill) to control the grain size and primary dendrite arm spacing by altering the transient curvature of the molten pool and the solidification parameters in PBF-EB (Fig. 1.17). These researchers demonstrated the possibility of tailoring grain structures by modifying the molten pool geometry, the motion of the molten metal, and spatial-temporal variation of the thermal gradient and solidification rate during AM. Generally, researchers try to control microstructure by plotting process map (Fig. 1.18) that figuring out the relationship between process parameters and solidification microstructure. However, this method is time- and cost-consuming and is not suitable for all parameters. Meanwhile, the mechanisms of grain morphology evolution and texture formation have not been sufficiently clarified for PBF-EB-built alloy depending on the process conditions. The choice of optimum strategies to produce a required microstructure with the targeted PBF-EB-built alloy performance still requires exploration without extensive trial-and-error experimentation.

1.4. Co-Cr-Mo alloy fabricated by PBF-EB

CoCr-based alloys are the proper choice of medical biomaterials. Especially the Co-Cr-Mo (CCM) alloy, which does not contain the element nickel that can induce allergy or even cancer, can be applied to the bone implants owing to the excellent mechanical properties and corrosion resistance [58].

There is a habit of epitaxial solidification in PBF-EB process of CCM alloys. As a result of the overall heat flow direction, along the building direction, directional columnar grains with {001} texture are efficiently produced [47]. The as-built sample possesses higher ultimate tensile strength than wrought or as-cast ASTM F75 CCM alloys [59]. In terms of the matrix phase constitution, however, the microstructural inhomogeneity may present along the building direction. In CCM alloys, there are two equilibrium phases — one is γ-face-centered cubic (fcc) phase, which is stable at high temperature, typically exceeding 900 °C; the other is ε-hexagonal closed packed (hcp) phase which is stable at a lower temperature. In PBF-EB of CCM alloys, after the far-from-equilibrium solidification immediately, the γ-fcc phase can exist as a metastable

phase even at a low temperature where the ε-hcp phase is stable. However, the repeated heating at a temperature of 850 °C and subsequent thermal cycling facilitate the phase constitution to vary spatially. According to the studies conducted by Sun et al. [47] and Wei et al. [60], along the building direction of the as-built sample, constituent phase varied from single ε-hcp phase in the bottom to single γ-fcc phase in the top (Fig. 1.19). The repeated heating process that acts as an aging process promotes the phase transformation from the metastable γ-fcc phase to the stable ε-hcp phase in the early-built parts. Microstructural inhomogeneity (i.e., the distributions and fractions of γ-fcc and ε-hcp phases) significantly affects the mechanical properties of PBF-EB-built CCM alloy, since the phase transformation from γ-fcc to ε-hcp enhances the wear-resistance but deteriorates the ductility of the component. Depending on temperature conditions, the γ → ε phase transformation in CCM alloy can take place via diffusionless-martensitic transformation or diffusional-massive transformation. Previous studies revealed the variability of microstructure of PBF-EB-built CCM alloy. However, the more in-depth understanding of the mechanisms governing phase transformation depending on thermal history still deserve exploration. And manipulating the phase constitution depending on the thermal history during PBF-EB fabricating is essential to obtain the appropriate performance of PBF-EB-built CCM alloy.

1.5. Objective and research contents of this study

The objective of the present study is to study the process mechanisms and aim at guiding for improving forming quality and microstructure of materials fabricated by PBF-EB.

According to the above description, current research still needs further (1) interpretation of how the powder properties affects the powder bed quality during the raking process; (2) investigation into the molten pool dynamics and their influences on the forming quality under the specific process conditions of PBF-EB; (3) discussion of powder bed characteristics with consideration of thermal properties and their influences on fusion behavior; (4) clarification of the mechanisms governing as-built

microstructure evolution and proposing efficient method for CET in as-built microstructure. These aspects are corresponding to the research contents of the present study.

The present study was conducted by taking the CCM alloy as the primary object of study. Also, to clarify the effects of material characteristics on the building process, some comparisons were made between CCM and IN718. The chemical compositions of CCM and IN718 alloys are shown in Table 1-2 and Table 1-3.

Because of the specific features of PBF-EB process, experimental quantifications of the transient and localized process in PBF-EB are difficult, thus, numerical simulations considering the unique processing conditions of PBF-EB, in conjunction with experiments, were used to analyze the building process.

Table 1-3. Comparison between electron beam melting and selective laser melting.

	PBF-EB	SLM
Typical equipment	Arcam A2X	EOS M 290
Build dimension	200×200×350 mm	250×250×325 mm
Largest power	50 - 3000 W	~ 400 W
Beam size	0.2 ~ 1.0 mm	0.1 mm
Highest scanning speed	~ 8000 mm/s	~ 7 m/s
Building speed	15 ~22 mm^3/s	2 ~8 mm^3/s
Preheating temperature	(0.5-0.8) T_m / ~ 1100 $^\circ$C	

Table 1-2. Chemical composition of typical CCM alloy.

	Cr	Mo	Ni	Fe	Si	Mn	C	N	Co
mass%	27.7	6.1	0.02	0.05	0.57	0.6	0.05	0.1	Bal.

Table 1-3. Chemical composition of typical IN718 alloy.

	Ni	Cr	Mo	Nb	Ti	Al	Co	Mn	Fe
mass%	52.5	19	3	5	0.9	0.5	1	0.35	Bal.
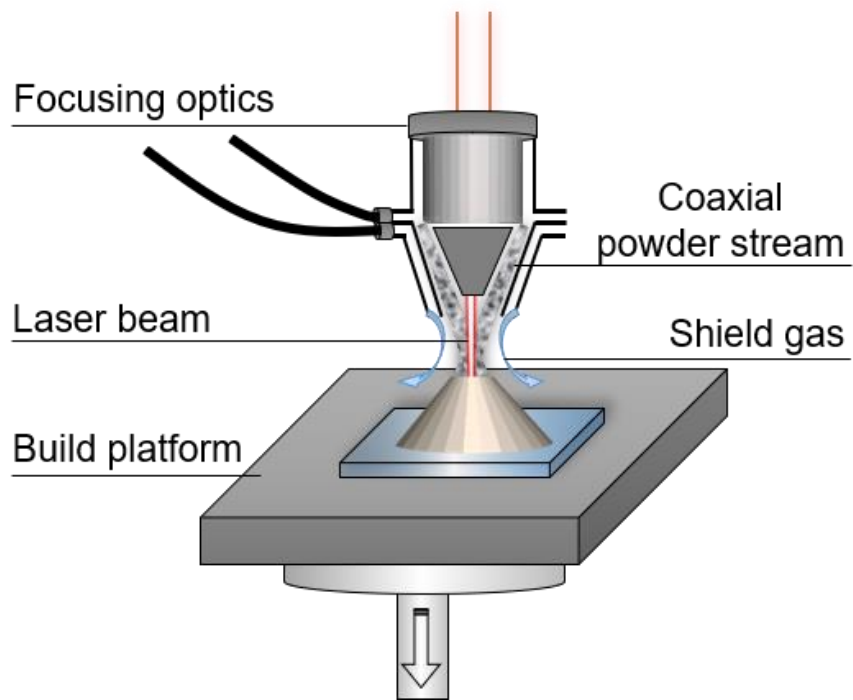
Fig. 1.1. Schematic illustration of the laser DED process.
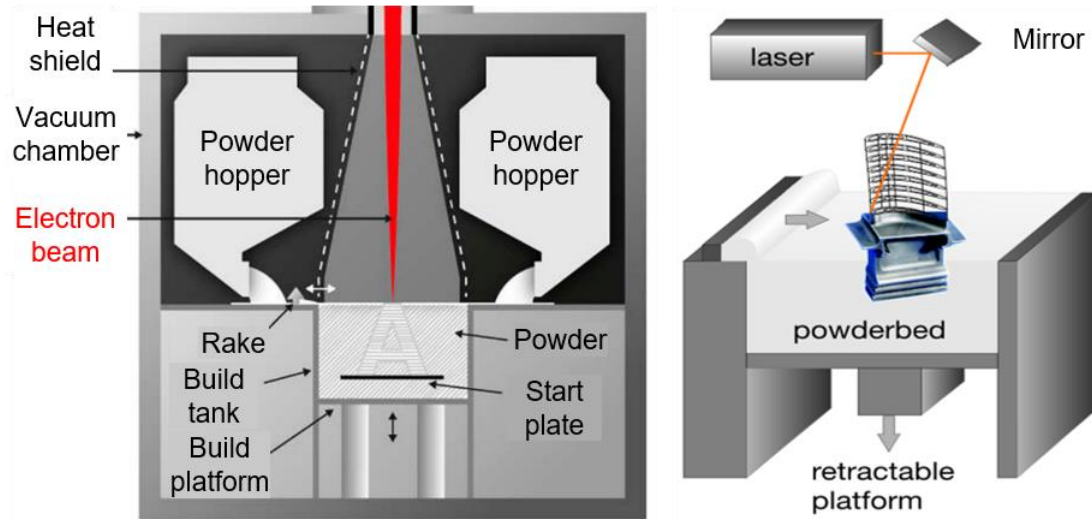
Fig. 1.2. Schematic illustration of the PBF process using an electron beam (left) [53] or a laser (right) [54] as the heat source.
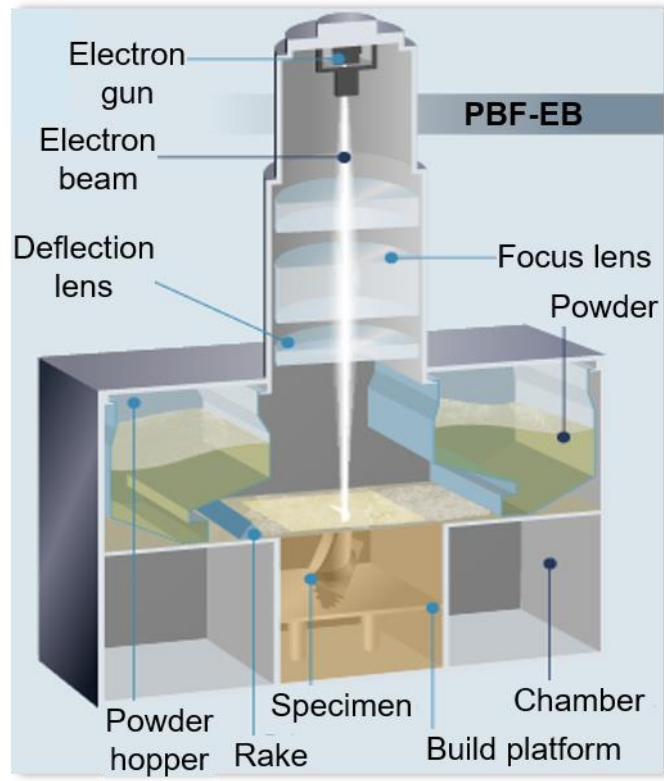
Fig. 1.3. Schematic illustration of the PBF-EB system.
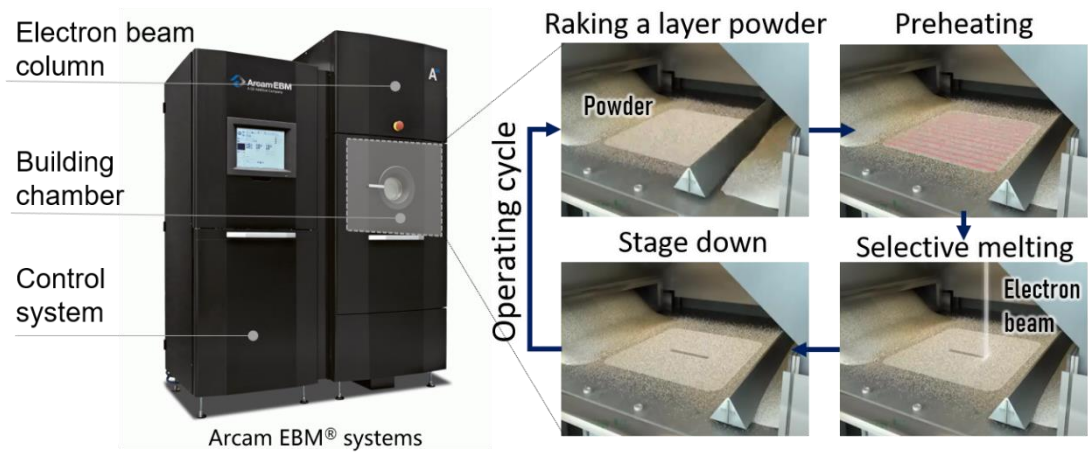
Fig. 1.4. Schematic illustration of the PBF-EB process stages.
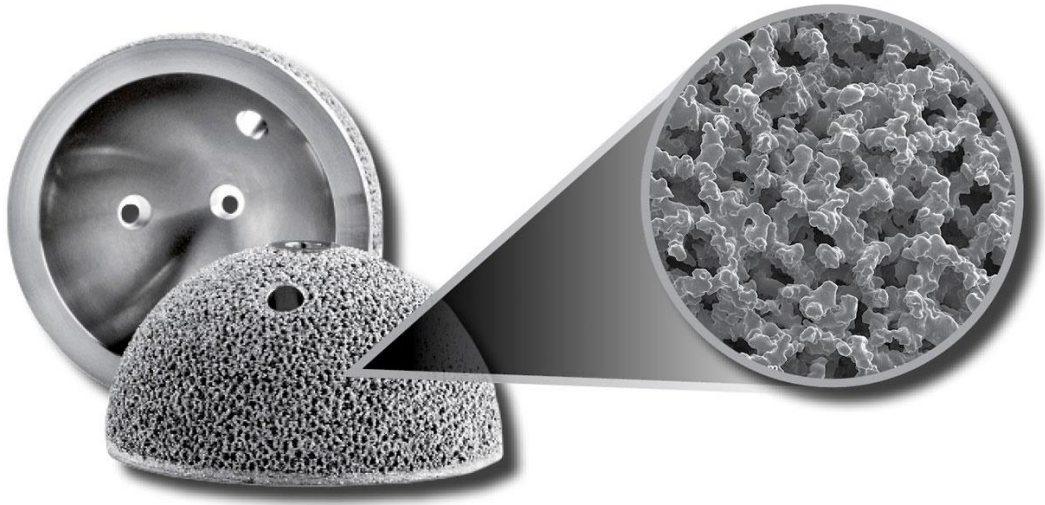
Fig. 1.5. PBF-EB-built acetabular cups with integrated Trabecular Structures for improved osseointegration [55].

Fig. 1.6. PBF-EB-built Low-Pressure Turbine blade in γ-titanium aluminide [56].
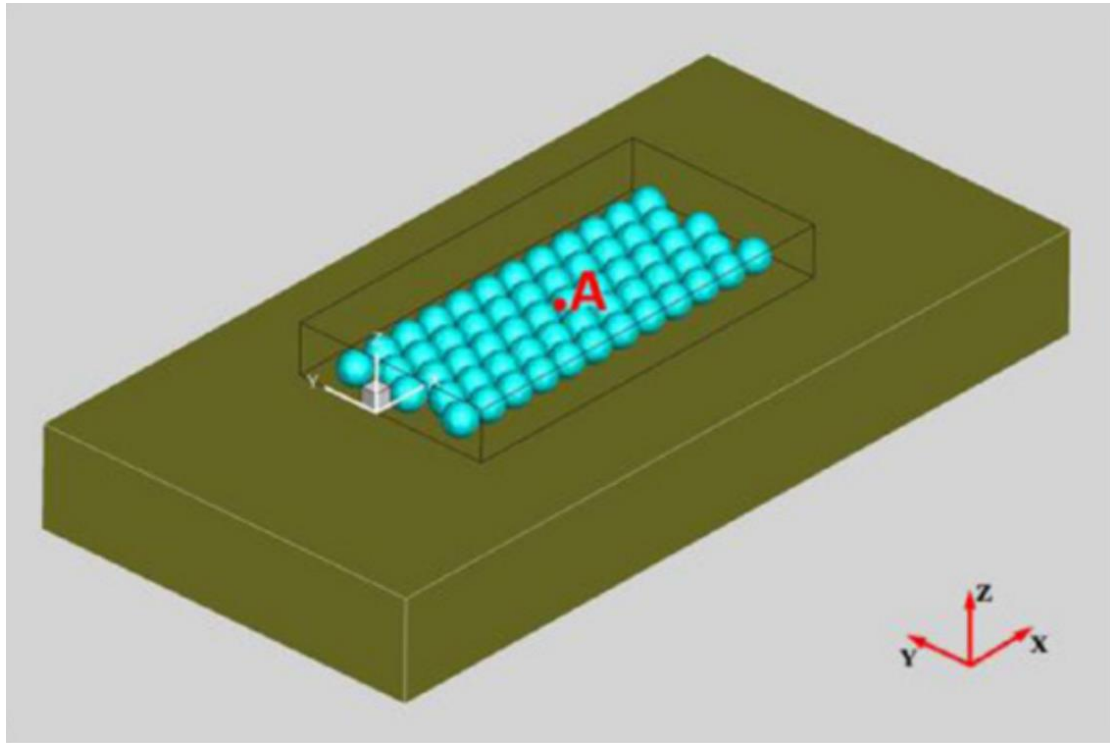
Fig. 1.7. Predefined packing sequence model where the green balls represent the powder layer, and the brown rectangle represents the substrate [34].
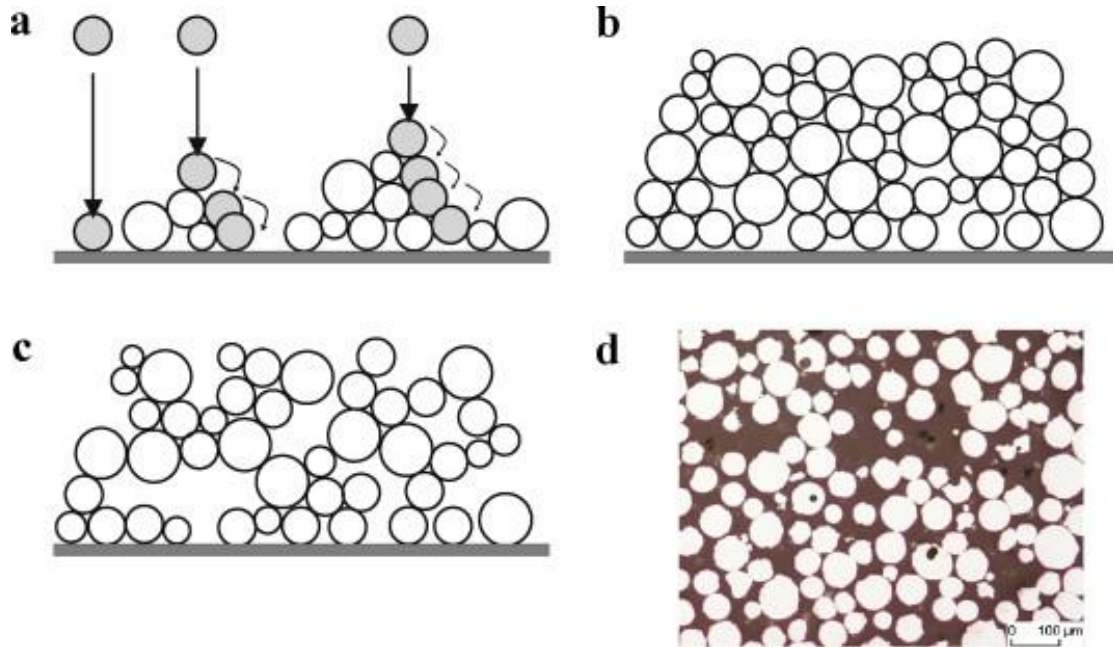
Fig. 1.8. Random powder bed model depending on a sequential addition algorithm. (a) Schematic of the rain model for random packing with rotations. (b) Powder bed produced by the rain model. (c) Adjusting the relative density by removing some of the particles. (d) Cross section of a real powder bed (titanium alloy) [35].
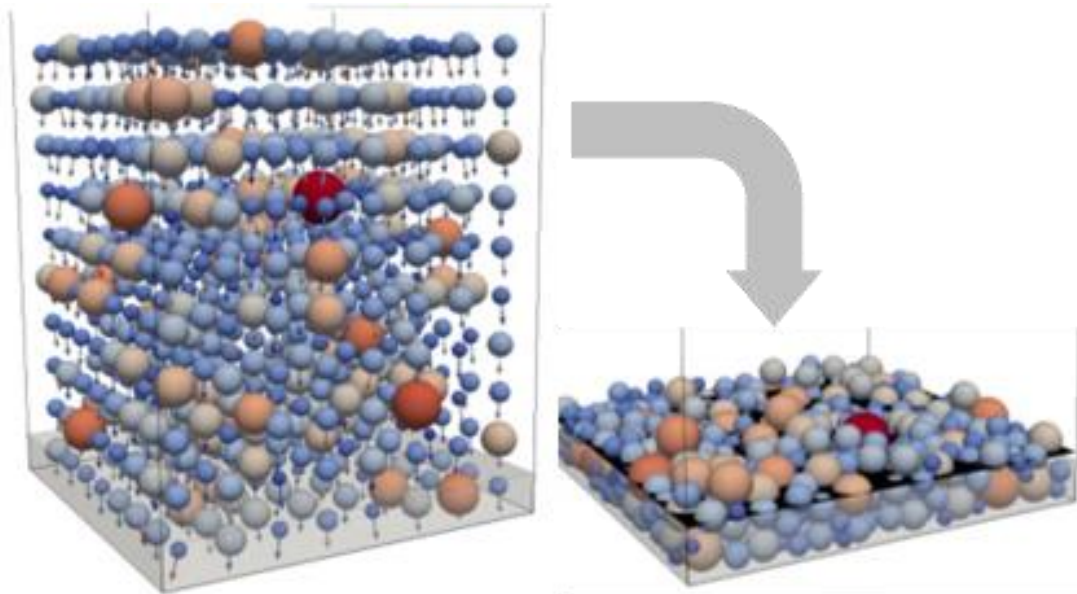
Fig. 1.9. Dynamic simulations by discrete element method (DEM) while taking into account the interparticle interactions but used a simple free-fall process [36].
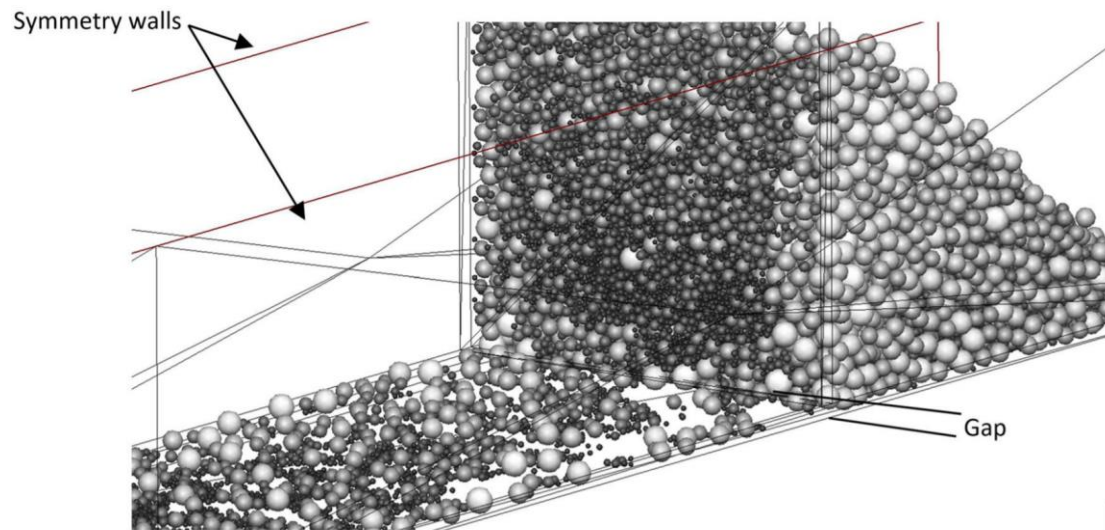
Fig. 1.10. DEM simulations of powder bed generation by recoating [39].
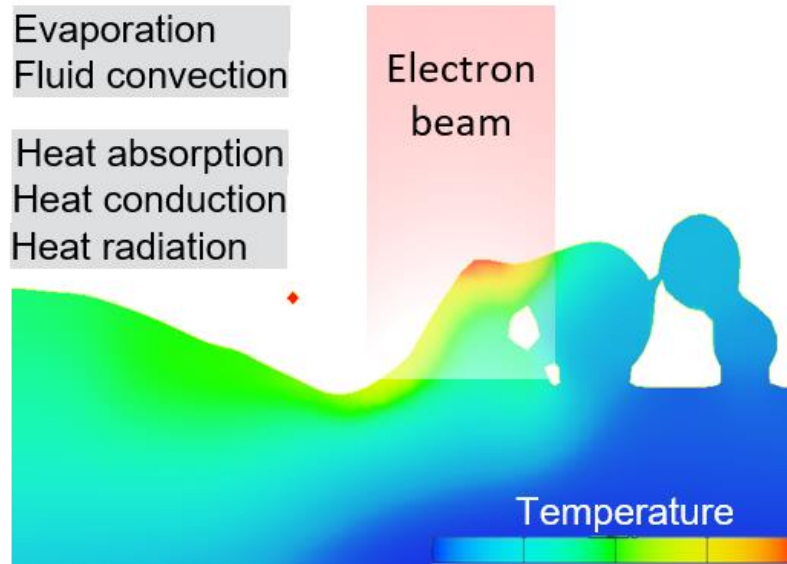
Fig. 1.11. Heat transfer and molten metal dynamics during PBF-EB.
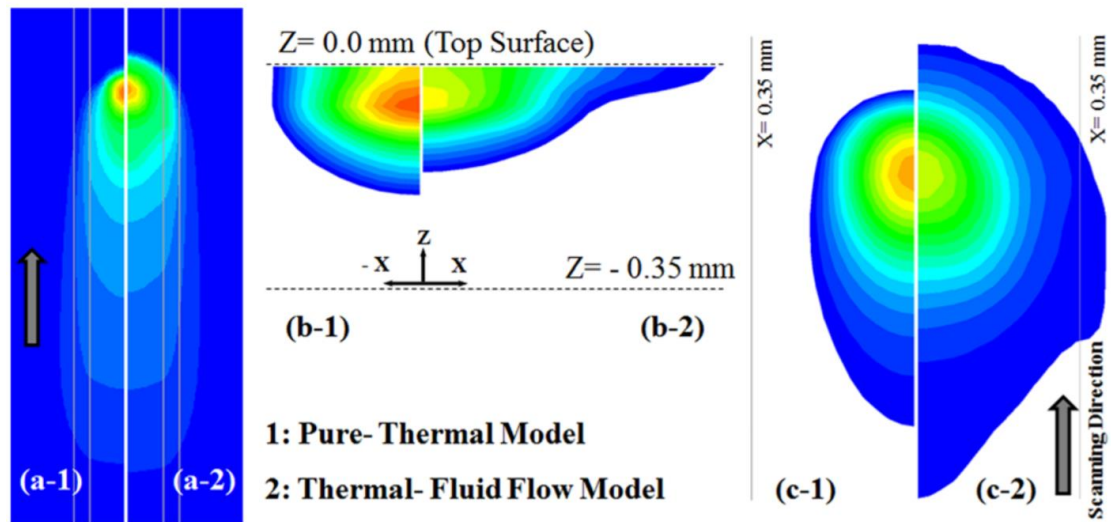
Fig. 1.12. Effect of fluid convection on temperature distribution and molten pool geometry, (a) temperature distribution on the powder bed top surface, (b) molten pool geometry at Y 5 6 mm along the electron beam scanning direction, and (c) molten pool geometry on the powder bed top surface, (1) pure-thermal model, (2) thermal-fluid flow mode [42].
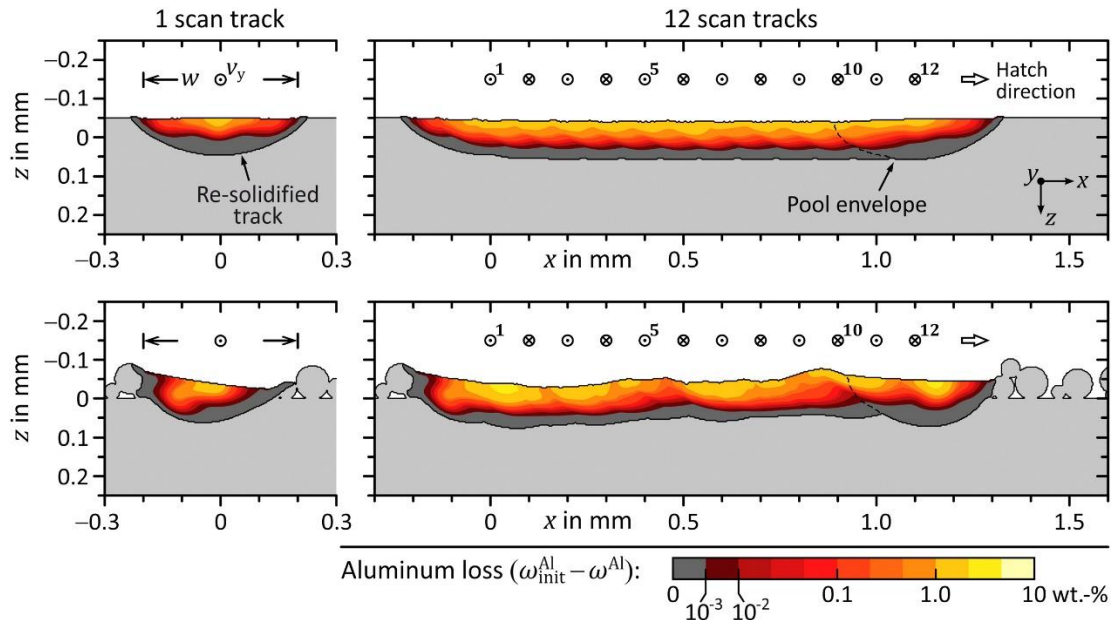
Fig. 1.13. Melting of a compact sample (top) is compared with the melting of a powder bed, using a two-dimensional multi-distribution function model based on the lattice Boltzmann method (LBM) with two D2Q9 lattices, one for simulating hydrodynamics and one for thermodynamics [43].
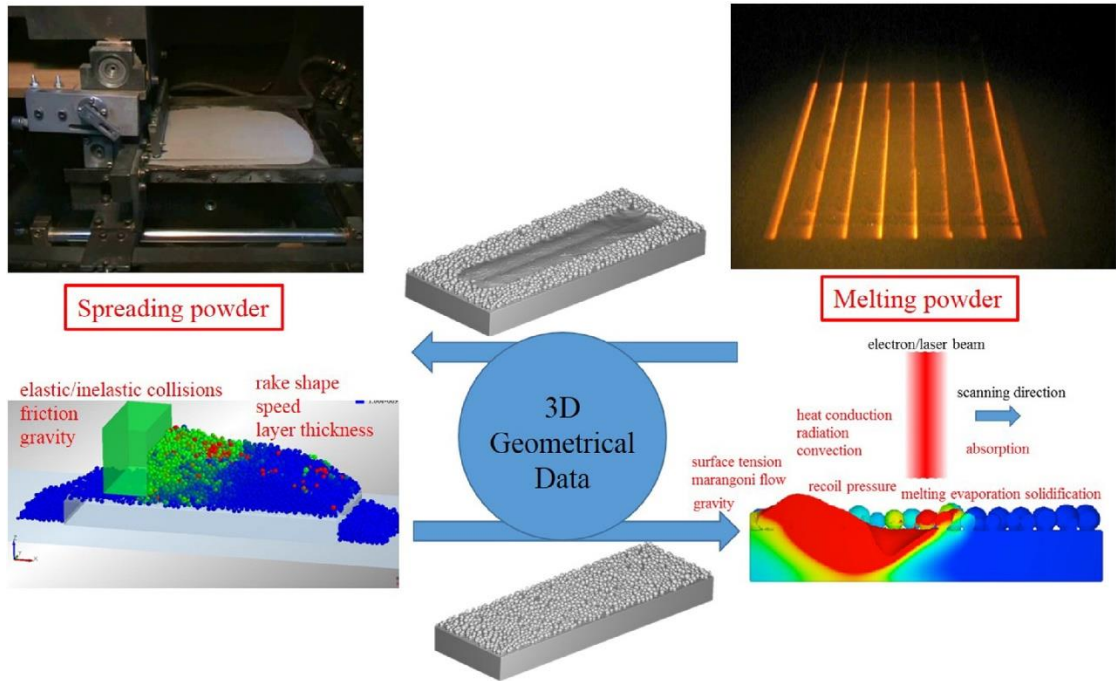
Fig. 1.14. Integrated modeling framework to reproduce the major procedures of PBF-EB developed by Liu's group [45].
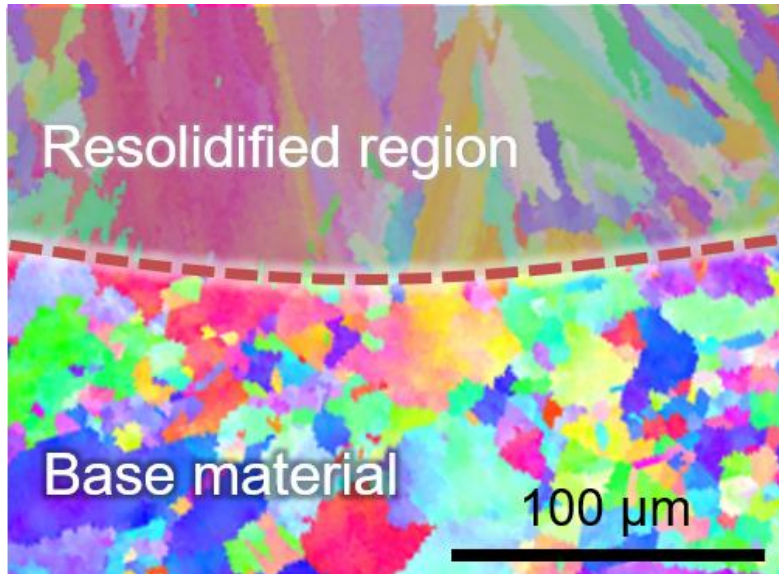
Fig. 1.15. PBF-EB melting of Co-Cr-Mo alloy on a base material with the epitaxial grain growth.
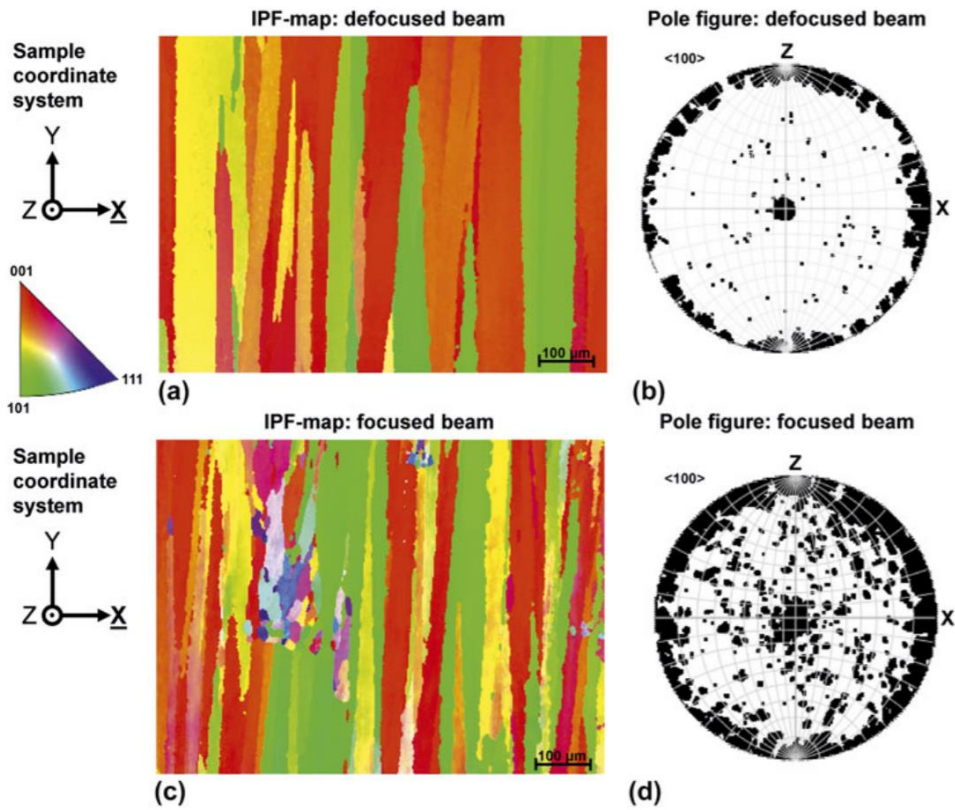
Fig. 1.16. In (a) and (c), IPF-maps of PFB-EB-built Inconel 718 are shown with colored crystallographic orientations relative to the sample axis X. Stray grains can be observed for the focused beam in (c) indicating nucleation ahead of the solidification front, which results in texture with less strongly aligned grains [49].
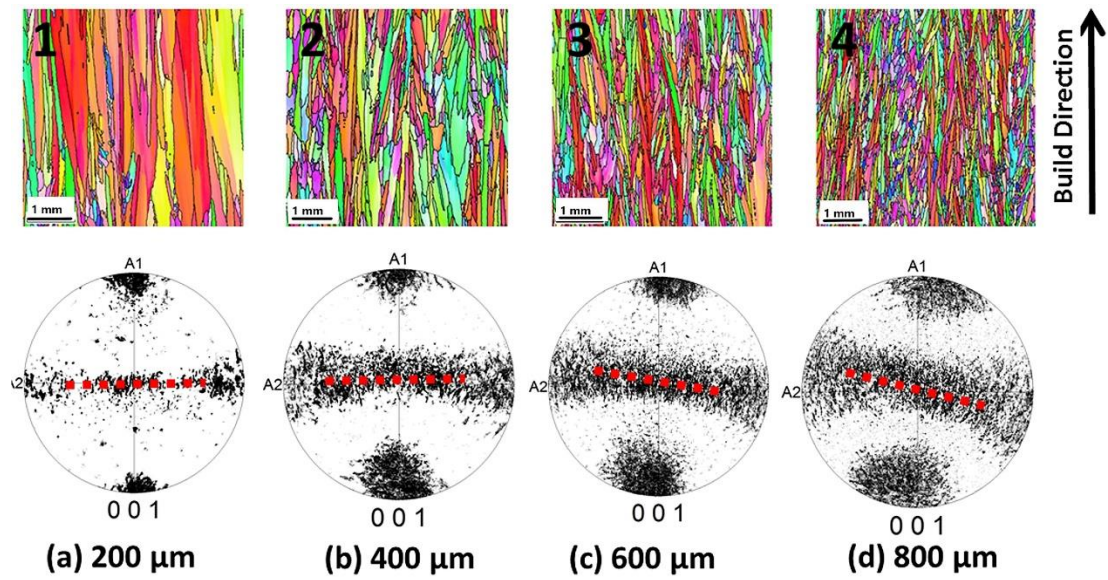
Fig. 1.17. Localized melt-scan strategy for site-specific control using a new melt-scan strategy (point heat source fill). Comparison of grain size and corresponding qualitative texture plot as a function of internal point offset (a) 200 μm (b) 400 μm (c) 600 μm (d) 800 μm [52].
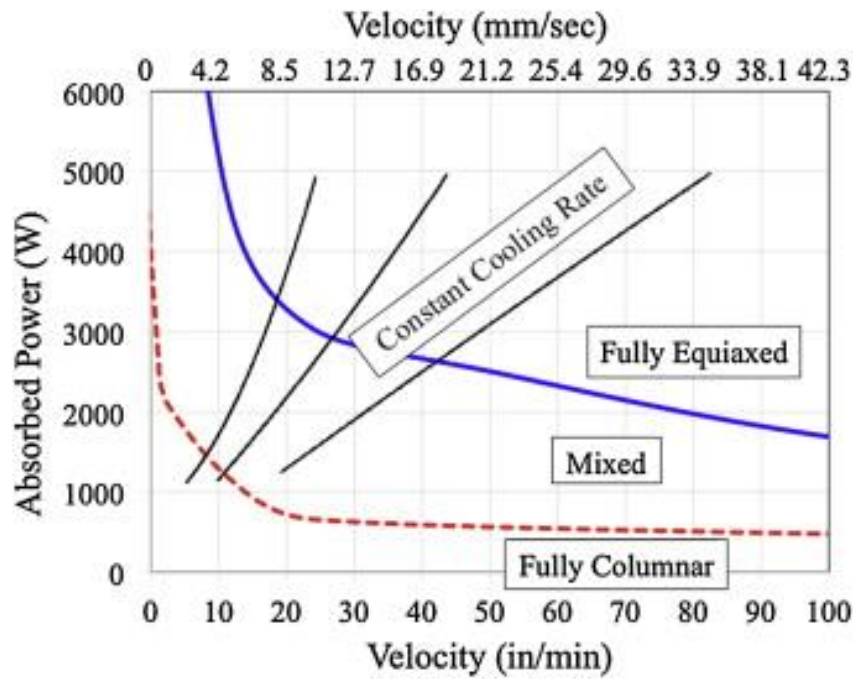
Fig. 1.18. Process map for controlling solidification microstructure of single bead deposits of Ti64 in electron beam wire feed AM [57].
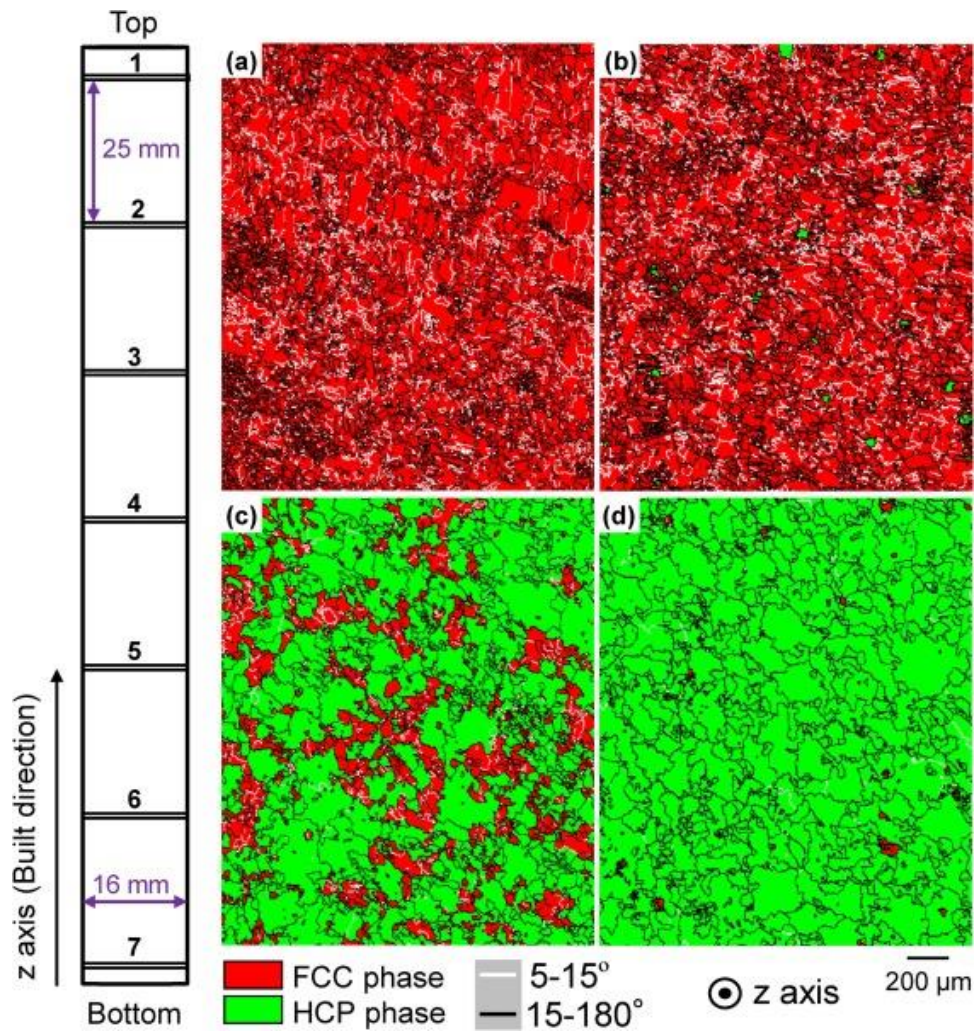
Fig. 1.19. Phase maps of (a) Samples 1, (b) Sample 3, (c) Sample 4, and (d) Sample 7, illustrating the phase variation along the building direction of PBF-EB-built CCM alloy [60].

References

[1]   B. Vayre, F. Vignat, and F. Villeneuve, "Metallic additive manufacturing: state-of-the-art review and prospects," *Mechanics & Industry*, vol. 13, no. 2, pp. 89–96, 2012.

[2]   GE Additive, "Materials Used in Additive Manufacturing." [Online]. Available: https://www.ge.com/additive/additive-manufacturing/information/additive-manufacturing-materials. [Accessed: 08-May-2019].

[3]   M. Javaid and A. Haleem, "Additive manufacturing applications in medical cases: A literature based review," *Alexandria Journal of Medicine*, Oct. 2017.

[4]   T. DebRoy, H. L. Wei, J. S. Zuback, T. Mukherjee, J. W. Elmer, J. O. Milewski, A. M. Beese, A. Wilson-Heid, A. De, and W. Zhang, "Additive manufacturing of metallic components – Process, structure and properties," *Progress in Materials Science*, vol. 92, pp. 112–224, Mar. 2018.

[5]   D. Herzog, V. Seyda, E. Wycisk, and C. Emmelmann, "Additive manufacturing of metals," *Acta Materialia*, vol. 117, pp. 371–392, Sep. 2016.

[6]   Y. Jin and J. Yu, "Research on 3D Printing in China: A Review," 2016.

[7]   T. Khaled, "Rev. A ADDITIVE MANUFACTURING (AM)," 2015.

[8]   Norsk Titanium, "Norsk Titanium to Deliver the World's First FAA-Approved, 3D-Printed, Structural Titanium Components to Boeing." [Online]. Available: https://www.norsktitanium.com/media/press/norsk-titanium-to-deliver-the-worlds-first-faa-approved-3d-printed-structural-titanium-components-to-boeing. [Accessed: 08-May-2019].

[9]   Forbes, "Additive Manufacturing Is Driving The Future Of The Automotive Industry." [Online]. Available: https://www.forbes.com/sites/sarahgoehrke/2018/12/05/additive-manufacturing-is-driving-the-future-of-the-automotive-industry/#56c630a375cc. [Accessed: 08-May-2019].

[10]   Volkswagen, "How Volkswagen is using 3D printing." [Online]. Available:

https://www.volkswagenag.com/en/news/stories/2018/12/brake-calipers-and-wheels-now-from-a-3d-printer.html. [Accessed: 08-May-2019].

[11] M. H. Elahinia, M. Hashemi, M. Tabesh, and S. B. Bhaduri, "Manufacturing and processing of NiTi implants: A review," *Progress in Materials Science*, vol. 57, no. 5, pp. 911–946, Jun. 2012.

[12] W. J. Sames, F. A. List, S. Pannala, R. R. Dehoff, and S. S. Babu, "The metallurgy and processing science of metal additive manufacturing," *International Materials Reviews*, vol. 61, no. 5, pp. 315–360, Jul. 2016.

[13] B. AlMangour, Ed., *Additive Manufacturing of Emerging Materials*. Cham: Springer International Publishing, 2019.

[14] J.-C. Wang, H. Dommati, and S.-J. Hsieh, "Review of additive manufacturing methods for high-performance ceramic materials," *The International Journal of Advanced Manufacturing Technology*, pp. 1–21, Apr. 2019.

[15] W. E. Frazier, "Metal Additive Manufacturing: A Review," *Journal of Materials Engineering and Performance*, vol. 23, no. 6, pp. 1917–1928, Jun. 2014.

[16] J. Fuchs, C. Schneider, and N. Enzinger, "Wire-based additive manufacturing using an electron beam as heat source," *Welding in the World*, vol. 62, no. 2, pp. 267–275, Mar. 2018.

[17] F. Martina, J. Mehnen, S. W. Williams, P. Colegrove, and F. Wang, "Investigation of the benefits of plasma deposition for the additive layer manufacture of Ti–6Al–4V," *Journal of Materials Processing Technology*, vol. 212, no. 6, pp. 1377–1386, Jun. 2012.

[18] Y. Zhao, Y. Koizumi, K. Aoyagi, D. Wei, K. Yamanaka, and A. Chiba, "Molten pool behavior and effect of fluid flow on solidification conditions in selective electron beam melting (SEBM) of a biomedical Co-Cr-Mo alloy," *Additive Manufacturing*, vol. 26, pp. 202–214, Mar. 2019.

[19] E. O. Olakanmi, R. F. Cochrane, and K. W. Dalgarno, "A review on selective laser sintering/melting (SLS/SLM) of aluminium alloy powders: Processing, microstructure, and properties," *Progress in Materials Science*, vol. 74, pp.

401–477, Oct. 2015.

[20] J. Kruth, P. Mercelis, J. Van Vaerenbergh, L. Froyen, and M. Rombouts, "Binding mechanisms in selective laser sintering and selective laser melting," *Rapid Prototyping Journal*, vol. 11, no. 1, pp. 26–36, Feb. 2005.

[21] M. Baumers, C. Tuck, and R. Hague, "SELECTIVE HEAT SINTERING VERSUS LASER SINTERING: COMPARISON OF DEPOSITION RATE, PROCESS ENERGY CONSUMPTION AND COST PERFORMANCE."

[22] L. E. Murr, S. M. Gaytan, D. A. Ramirez, E. Martinez, J. Hernandez, K. N. Amato, P. W. Shindo, F. R. Medina, and R. B. Wicker, "Metal Fabrication by Additive Manufacturing Using Laser and Electron Beam Melting Technologies," *Journal of Materials Science & Technology*, vol. 28, no. 1, pp. 1–14, Jan. 2012.

[23] Arcam AB, "Electron Beam Melting - EBM Process, Additive Manufacturing." [Online]. Available: http://www.arcam.com/technology/electron-beam-melting/. [Accessed: 10-May-2019].

[24] Arcam, "Arcam EBM® Technology Creating new opportunities in design and production."

[25] S. L. Sing, J. An, W. Y. Yeong, and F. E. Wiria, "Laser and electron-beam powder-bed additive manufacturing of metallic implants: A review on processes, materials and designs," *Journal of Orthopaedic Research*, vol. 34, no. 3, pp. 369–385, Mar. 2016.

[26] M. Dhanesh, A. Dhanawade, and S. G. A. Bhatwadekar, "A Review on Types of Powder Bed Fusion Process in Additive Manufacturing Technology," 2017.

[27] AMFG, "An Introduction to Electron Beam MeltingAMFG." [Online]. Available: https://amfg.ai/2018/05/16/electron-beam-melting-introduction/. [Accessed: 11-May-2019].

[28] Arcam AB, "Arcam announces FDA clearance of implants produced with Additive Manufacturing." [Online]. Available: http://www.arcam.com/arcam-announces-fda-clearance-of-implants-produced-with-additive-manufacturing/. [Accessed: 11-May-2019].

[29] 3D Printing Industry, "FDA Approves 3D Printed Titanium Craniofacial Implants." [Online]. Available: https://3dprintingindustry.com/news/fda-approves-3d-printed-titanium-craniofacial-implants-66136/. [Accessed: 11-May-2019].

[30] GE Reports, "This Electron Gun Builds Jet Engines." [Online]. Available: https://www.ge.com/reports/post/94658699280/this-electron-gun-builds-jet-engines/. [Accessed: 11-May-2019].

[31] J. Zhou, Y. Zhang, and J. K. Chen, "Numerical Simulation of Random Packing of Spherical Particles for Powder-Based Additive Manufacturing," *Journal of Manufacturing Science and Engineering*, vol. 131, no. 3, p. 031004, Jun. 2009.

[32] T. Jia, Y. Zhang, and J. K. Chen, "Simulation of granular packing of particles with different size distributions," *Computational Materials Science*, vol. 51, no. 1, pp. 172–180, Jan. 2012.

[33] F. J. Gürtler, M. Karg, K. H. Leitz, and M. Schmidt, "Simulation of laser beam melting of steel powders using the three-dimensional volume of fluid method," in *Physics Procedia*, 2013, vol. 41, pp. 881–886.

[34] G. Yu, D. Gu, D. Dai, M. Xia, C. Ma, and Q. Shi, "On the role of processing parameters in thermal behavior, surface morphology and accuracy during laser 3D printing of aluminum alloy," *Journal of Physics D: Applied Physics*, vol. 49, no. 13, p. 135501, Apr. 2016.

[35] C. Körner, E. Attar, and P. Heinl, "Mesoscopic simulation of selective beam melting processes," *Journal of Materials Processing Technology*, vol. 211, no. 6, pp. 978–987, Jun. 2011.

[36] M. Markl, "Numerical Modeling and Simulation of Selective Electron Beam Melting Using a Coupled Lattice Boltzmann and Discrete Element Method Doktor-Ingenieur," 2015.

[37] Z. Xiang, M. Yin, Z. Deng, X. Mei, and G. Yin, "Simulation of Forming Process of Powder Bed for Additive Manufacturing," *Journal of Manufacturing Science and Engineering*, vol. 138, no. 8, p. 081002, Mar. 2016.

[38] Y. S. Lee and W. Zhang, "Modeling of heat transfer, fluid flow and

solidification microstructure of nickel-base superalloy fabricated by laser powder bed fusion," *Additive Manufacturing*, vol. 12, pp. 178–188, 2016.

[39] H. W. Mindt, M. Megahed, N. P. Lavery, M. A. Holmes, and S. G. R. Brown, "Powder Bed Layer Characteristics: The Overseen First-Order Process Input," *Metallurgical and Materials Transactions A: Physical Metallurgy and Materials Science*, vol. 47, no. 8, pp. 3811–3822, Aug. 2016.

[40] W. J. Boettinger, S. R. Coriell, A. L. Greer, A. Karma, W. Kurz, M. Rappaz, and R. Trivedi, "Solidification microstructures: recent developments, future directions," *Acta Materialia*, vol. 48, no. 1, pp. 43–70, Jan. 2000.

[41] A. Bauereiß, T. Scharowsky, and C. Körner, "Defect generation and propagation mechanism during additive manufacturing by selective beam melting," *Journal of Materials Processing Technology*, vol. 214, no. 11, pp. 2522–2528, Nov. 2014.

[42] M. Jamshidinia, F. Kong, and R. Kovacevic, "Temperature Distribution and Fluid Flow Modeling of Electron Beam Melting® (EBM)," in *Volume 7: Fluids and Heat Transfer, Parts A, B, C, and D*, 2012, p. 3089.

[43] A. Klassen, V. E. Forster, V. Juechter, and C. Körner, "Numerical simulation of multi-component evaporation during selective electron beam melting of TiAl," *Journal of Materials Processing Technology*, vol. 247, pp. 280–288, Sep. 2017.

[44] W. Yan, W. Ge, J. Smith, S. Lin, O. L. Kafka, F. Lin, and W. K. Liu, "Multi-scale modeling of electron beam melting of functionally graded materials," *Acta Materialia*, vol. 115, pp. 403–412, Aug. 2016.

[45] W. Yan, Y. Qian, W. Ge, S. Lin, W. K. Liu, F. Lin, and G. J. Wagner, "Meso-scale modeling of multiple-layer fabrication process in Selective Electron Beam Melting: Inter-layer/track voids formation," *Materials & Design*, vol. 141, pp. 210–219, Mar. 2018.

[46] A. Rai, H. Helmer, and C. Körner, "Simulation of grain structure evolution during powder bed based additive manufacturing," *Additive Manufacturing*, vol. 13, pp. 124–134, Jan. 2017.

[47] S.-H. Sun, Y. Koizumi, S. Kurosu, Y.-P. Li, and A. Chiba, "Phase and grain size inhomogeneity and their influences on creep behavior of Co–Cr–Mo alloy additive manufactured by electron beam melting," *Acta Materialia*, vol. 86, pp. 305–318, Mar. 2015.

[48] N. Raghavan, R. Dehoff, S. Pannala, S. Simunovic, M. Kirka, J. Turner, N. Carlson, and S. S. Babu, "Numerical modeling of heat-transfer and the influence of process parameters on tailoring the grain morphology of IN718 in electron beam additive manufacturing," *Acta Materialia*, vol. 112, pp. 303–314, Jun. 2016.

[49] H. E. Helmer, C. Körner, and R. F. Singer, "Additive manufacturing of nickel-based superalloy Inconel 718 by selective electron beam melting: Processing window and microstructure," *Journal of Materials Research*, vol. 29, no. 17, pp. 1987–1996, Sep. 2014.

[50] R. R. Dehoff, M. M. Kirka, F. A. List, K. A. Unocic, and W. J. Sames, "Crystallographic texture engineering through novel melt strategies via electron beam melting: Inconel 718," *Materials Science and Technology*, vol. 31, no. 8, pp. 939–944, 2015.

[51] C. Körner, H. Helmer, A. Bauereiß, and R. F. Singer, "Tailoring the grain structure of IN718 during selective electron beam melting," *MATEC Web of Conferences*, vol. 14, p. 08001, Aug. 2014.

[52] N. Raghavan, S. Simunovic, R. Dehoff, A. Plotkowski, J. Turner, M. Kirka, and S. Babu, "Localized melt-scan strategy for site specific control of grain size and primary dendrite arm spacing in electron beam additive manufacturing," *Acta Materialia*, vol. 140, pp. 375–387, Nov. 2017.

[53] Arcam AB, "EBM Hardware." [Online]. Available: http://www.arcam.com/technology/electron-beam-melting/hardware/. [Accessed: 11-May-2019].

[54] J. Kruth, P. Mercelis, J. Van Vaerenbergh, L. Froyen, and M. Rombouts, "Binding mechanisms in selective laser sintering and selective laser melting," *Rapid Prototyping Journal*, vol. 11, no. 1, pp. 26–36, Feb. 2005.

[55]   Arcam AB, "EBM for Orthopedic Implants - Additive Manufacturing."
       [Online]. Available: http://www.arcam.com/solutions/orthopedic-implants/.
       [Accessed: 11-May-2019].

[56]   Arcam AB, "EBM in Aerospace - Additive Manufacturing." [Online].
       Available: http://www.arcam.com/solutions/aerospace-ebm/. [Accessed: 11-
       May-2019].

[57]   J. Gockel, J. Beuth, and K. Taminger, "Integrated control of solidification
       microstructure and melt pool dimensions in electron beam wire feed additive
       manufacturing of Ti-6Al-4V," *Additive Manufacturing*, vol. 1–4, pp. 119–126,
       Oct. 2014.

[58]   B. AlMangour, ed., *Additive Manufacturing of Emerging Materials*, Springer
       International Publishing, Cham, 2019.

[59]   S.M. Gaytan, L.E. Murr, E. Martinez, J.L. Martinez, B.I. Machado, D.A.
       Ramirez, F. Medina, S. Collins, R.B. Wicker, "Comparison of Microstructures
       and Mechanical Properties for Solid and Mesh Cobalt-Base Alloy Prototypes
       Fabricated by Electron Beam Melting," *Metallurgical and Materials
       Transactions A*, vol. 41, pp. 3216–3227, 2010.

[60]   D. Wei, Y. Koizumi, A. Chiba, K. Ueki, K. Ueda, T. Narushima, Y. Tsutsumi, T.
       Hanawa, "Heterogeneous microstructures and corrosion resistance of
       biomedical Co-Cr-Mo alloy fabricated by electron beam melting (EBM),"
       Additive Manufacturing, vol. 24, pp. 103–114, 2018.

Chapter 2
Fundamentals of powder bed generation in PBF-EB

2.1. Introduction

Powder packing information is one of the dominant factors for powder-bed systems because only a limited number of powder are directly subject to the beam irradiation at a given time. The characteristics of powder bed add significant complexity to PBF-EB process and show an impact on final part properties. In particular, understanding the dynamic behavior of the powder particles during the layer-by-layer building process is essential for developing optimized strategies towards controlled component quality and shorter production lead time. It is hard to obtain and quantify the powder bed information via the experimental method, while numerical simulation has become a useful method to investigate powder bed generation and is convenient to conduct data analysis of powder packing properties. In this study, the dynamic behavior of a collection of powder during the raking process was simulated by utilizing discrete element method (DEM), aiming at investigating the effects of the different physical parameters on resultant powder rearrangement, focusing on packing density, powder flowability, particle size distribution (PSD), and their interplays. They are all useful information for optimizing PBF-EB process with less experimental effort in trial-and-error.

2.2. Methodology

2.2.1. DEM modeling setup

Experimental investigation of powder is usually limited to measuring bulk properties (e.g., mean size, particle size distribution, and packing density) and is not able to resolve the local configuration of individual particles on the powder bed.

The DEM is a well-known numerical technique that allows for the modeling of discrete granular objects as a collection of particles that interact at the contact points while following a governing force-displacement relationship [1]. A finite number of spherical particles, which are assigned predefined radii and mechanical properties, are generated to simulate different materials. The motion of the particles is dependent on the particle-to-particle contact and friction as well as on gravity. Based on the soft-contact mode, which permits local overlapping, the exact relationship between particle deformation and the contact force can be determined. In brief, the underlying principle of DEM modeling is based on two laws: contact law and motion law (Fig. 2.1). Further, depending on the time-stepping algorithm used, the contact force is evaluated during each timestep and consists of the normal and tangential components taking place at the contact points. Newton's second law is used to control the translational and rotational motions of each granular objects:

$$m_i \frac{dv_i}{dt} = F_i + m_i g, \tag{2-1}$$

$$I_i \frac{d\omega_i}{dt} = T_i, \tag{2-2}$$

where m_i is the mass of particle i, v_i its translational velocity, F_i the total force, I_i the particle's momentum of inertia, ω_i its angular velocity, and T_i the total torque. The movement of the particles is determined at each timestep on the basis of the previous movement data and the contact forces experienced during the current timestep [2]. In brief, the underlying principle of DEM modeling is on the basis of two laws: the contact law (i.e., the force–displacement relationship) and motion law (i.e., Newton's second law). The force–displacement relationship defines how the particles interact with each other and determines the changes in the force. Given that the particles of metal powder are never perfectly rigid but react to the loads to which they are normally subjected by undergoing contact deformations, the elastic deformability of the particles should be considered when modeling their interactions. The nonlinear elastic Hertz–Mindlin no-slip contact model [3] was adopted in this study. The relationship between the elastic normal contact force, F_n^E, and the overlap, U_n, between the particles of two materials [4] can be expressed as follows:

$$F_{\mathrm{n}}^{\mathrm{E}} = K_{\mathrm{n}}U_{\mathrm{n}} = \frac{4}{3}E^{*}\sqrt{R^{*}}U_{\mathrm{n}}^{\frac{3}{2}}, \tag{2-3}$$

where K_{n} is the stiffness in the normal direction, E^{*} is the equivalent Young's modulus expressed as $((1 - \nu_{i}^{2})/E_{i} + (1 - \nu_{j}^{2})/E_{j})^{-1}$, and R^{*} is the equivalent radius when two particles come in contact $(1/R_{i} + 1/R_{j})^{-1}$. U_{n} is calculated by the difference between the sum of the radii and the distance between the centroids of the two bodies which is $R_{i} + R_{j} - D_{ij}$ for particle to particle or $R_{i} - D_{ip}$ for particle to plane. According to Mindlin's "no microslip" solution [5], the force in the tangential direction can be given as follows:

$$F_{\mathrm{t}}^{\mathrm{E}} = K_{\mathrm{t}}U_{\mathrm{t}} = 8G^{*}\sqrt{R^{*}U_{\mathrm{n}}}U_{\mathrm{t}}, \tag{2-4}$$

where U_{t} is composed of a rotational component with a rotational angle θ and a translational component D and is thus equal to $D + R_{i}\theta$. Further, G^{*} is the equivalent shear modulus when two objects come in contact and is $((2 - \nu_{i})/G_{i} + (2 - \nu_{j})/G_{j})^{-1}$. Moreover, the tangential contact force is also limited, otherwise Coulomb's law of micro-sliding friction will be introduced. Finally, we can see that the normal and tangential contact stiffness is equal to:

$$K_{\mathrm{n}} = 2E^{*}\sqrt{R^{*}U_{\mathrm{n}}}, \tag{2-5}$$

$$K_{\mathrm{t}} = 8G^{*}\sqrt{R^{*}U_{\mathrm{n}}}. \tag{2-6}$$

Contact stiffness is dependent on the overlap between two bodies, rather than a constant determined by the given material, displaying the nonlinearity of this contact model.

In actual particle flow, energy is dissipated by inelastic collisions and can also be converted into heat or sound energy until the system become stationary eventually [6]. However, in general DEM simulations, the energy inputted into the system can be dissipated only through frictional sliding in an elastic contact model. This model does not explain the changes in the kinetic energy for the case investigated in the present study, in which the rolling behavior between particles is dominant even in the absence of an external force. Thus, damping must be considered in DEM models when accounting for the consumption of energy. In simulations related to physics and

engineering, viscous damping is modeled mathematically as a force that is synchronous with the object's velocity but has a direction opposite to that of the velocity. The force of viscous damping has a relation with the relative velocity:

$$F_i^D = -\eta v_i. \tag{2-7}$$

The damping coefficients, η, in the normal direction and tangential direction are respectively expressed by

$$\eta_n = 2\sqrt{m^* 2E^* \sqrt{R^*} U_n^{\frac{1}{2}}} \zeta_n, \tag{2-8}$$

$$\eta_t = 4\sqrt{m^* 2G^* \sqrt{R^*} U_n^{\frac{1}{2}}} \zeta_s, \tag{2-9}$$

where m^* is the effective mass of the objects expressed as $(m_i \cdot m_j)/(m_i + m_j)$. The damping ratio ζ is determined by the collisional properties of the system and can be expressed by the coefficient of restitution, e, between the two bodies in contact:

$$\zeta = \frac{-ln\ e}{\sqrt{\pi^2 + (lne)^2}}. \tag{2-10}$$

Viscous damping force bases on the damping coefficient η, in particular on the coefficient of restitution $e = v_1/v_0$ (v_0 and v_1 are the relative velocity at the contact point before and after the collision), which is a valuation of the kinetic energy exchange between the impaction particle and the target material during the impact process. Strictly speaking, coefficient of restitution is not a material property, nor yet a constant for any given material but depends on the details of the interaction force and the impact velocity [7]. However, the correlation between e and impact velocity has been shown to be significant only at high impact velocities (>10m/s), and for practical purpose e is often taken to be a constant not irrespective of impact velocity in DEM simulation [6].

In summary, the model used is based on a nonlinear elastic model for contact law and a viscous damping effect for energy dissipation. The motivation of a particles collection during the raking process in PBF-EB was simulated using the open-source software Yade. A detailed introduction of Yade-DEM implementations is available in the code's documentation [8]. If one uses the appropriate initial conditions and parameters for the contacting models, soft particles can be used in simulations to

elucidate the mechanical behaviors of different materials reasonably. As the input parameters, the continuum mechanical properties, including Young's modulus, E; Poisson's ratio, ν; and shear modulus, G $(= E/2(1 + \nu))$, were used to calculate the nonlinear elastic contact force, while the friction angle of the alloy powder particles can be used to determine the interparticle frictional characteristics.

2.2.2. Simulation implementation and validation

The repose angle of a granular material (Fig. 2.2) is the steepest angle of descent of dip relative to the horizontal plane to which a material can be piled without slumping. Repose angle is related to the density, surface area and shapes of the particles, and the friction coefficient of the granular material. The smaller the repose angle, the frictional force is smaller, and the flowability is better. Thus, the properties and the interaction behavior of large numbers of powder can be reflected by the degree of this angle. In order to verify whether the contact model is approximated for the powder we used in this study, the DEM simulations that mimic the scenarios of measurement process of repose angle, were conducted, then compare to the practical powder accumulation form for validation (Fig. 2.3). By calibrating the coefficients related to the damping and friction, the simulated repose angle of CCM and IN718 alloy powders were matched those observed by experiments. The delivery of the metallic powder depends on the specific process condition. In this study, a series of powder raking simulations were performed. The powder bed generation process was simulated using a mobilizable rake, a fixed ground plane with a building box, and a collection of the alloy powder particles. Figure 2.4 shows a snapshot of the DEM simulation of the powder bed generation process. A cloud of particles with a predefined PSD was dropped and allowed to settle to the floor under gravity. The powder was then moved to the building box by the side-to-side motion of the rake. The height of the building box was equal to the nominal thickness of the powder layer. All of the materials involved in the DEM simulations were assigned their respective mechanical properties. For validating the DEM model, the raking of the gas atomized CCM alloy powder was performed on the building

platform of an Arcam$^{\circledR}$ EBM A2X machine, and the obtained results were compared with those of the simulations.

Figure 2.5 shows the simulated and experimental results for single-layer raking. The images of the particles distributed on the baseplate correspond to two different layer thicknesses. A larger layer thickness makes the particle distribution dense and uniform. More importantly, all of the simulated distribution patterns for the different powder layer thicknesses match those observed experimentally.

The input parameters of the simulations and the properties of the CCM and IN718 alloy powders [6][9][10] are listed in Table 2-1.

2.3. Factors influencing powder bed packing density

For PBF-EB process, the powder packing structure is a critical parameter. The powder bed packing density and the distribution of particles are expected to be a primary parameter affecting the material behavior and the process evolution. The energy absorption by the powder layer on powder-bed largely depends on the packing density of the powder bed. Thus, more attention should also be paid to the powder raking process and the characteristics of the powder bed.

From Fig. 2.6 that shows the powder delivery in the PBF-EB process, and we must understand a point that the practical layer thickness will change with the proceeding instead of a constant. In the first process step, a thin powder layer is applied with a stainless-steel rake on the building area. The gap distance between rake and platform is equal to the nominal layer thickness L_0. After preheating and melting, the height of the melted part become smaller than the original layer thickness because of solidification shrinkage. Then lower the platform with the descent height equaling to nominal layer thickness. The downward height of building platform will remain the same in the complete process. Therefore, the thickness of new delivered powders is larger than the nominal thickness. With considering that the proportion of solidification shrinkage is approximately equals to the powder packing density by raking ρ_p, then the variation rule of real-powder layer thickness L_n can be deduced:

$$L_n = L_0 \cdot \sum_{k=0}^{n-1} \left(1 - \rho_p\right)^k,$$ (2-11)

where n and $n-1$ denote the new and previous layer, respectively.

By plotting this equation, it can be seen that the final steady thickness is reached after a few iterations and final steady thickness is inversely proportional to the packing density. Generally, we assume a uniform powder packing density of 50% [11]. Given a nominal layer thickness, the real-layer thickness evolves from one layer to another, as shown in Fig. 2.7 (a). After approximately ten processed layers, the real-layer thickness reaches a steady value that is almost twice the original nominal layer thickness. On the other hand, packing density can affects the real-layer thickness when the nominal layer thickness is given. Fig. 2.7 (b) shows that the final steady real-layer thickness is inversely proportional to the packing density. Hence, if the powder packing density is high, the variation in the real layer thickness over time will be indistinctive. Moreover, a lower packing density tends to postpone the advent of uniform layer thickness.

However, during the actual PBF-EB process, the powder packing density depends on the material and raking process. With considering the significant difference in real powder layer thickness, as shown above, an estimation of practical powder packing density is necessary for predicting the final quality and porosity of PBF-EB-built material. Actually, the powder packing density is not constant during the whole building process. The simulation results in Fig. 2.8 revealed that relative packing density increased with increasing powder layer thickness. The results are attributed to the following two factors. One is the filtering effect of the gap between the baseplate and rake, which rejects particles larger than the layer thickness. The other is the better compaction caused by a larger number of powder particles. An increase in the powder layer thickness results in higher relative packing density, but the dimensional accuracy of built parts might be sacrificed to some degree. Moreover, as shown in Fig. 2.9, with an increase in L_0, final steady L_n increases and high powder packing density can be obtained. In other words, for a higher product accuracy after PBF-EB — smaller layer thickness, the powder packing density may be sacrificed in some degree, which has a stronger effect on the amount of porosity that has to be released during the melting process. Thus, selecting the nominal layer thickness, not only the production speed,

dimensional accuracy, but also the resulting porosity of product, must be considered appropriately.

2.4. Effect of powder flowability on powder bed pattern

Powder layers themselves include many different properties such as the particle size distribution and related powder packing density, especially as well as flowability, which directly affect the features of powder bed pattern. The density and homogeneity of the final component rely on the layer-by-layer melting being performed on thin and uniform powder layers that are accurately generated by the powder raking device.

To investigate the effect of powder flowability, two other kinds of virtual powder, with different flowability, were artificially created by adjustment of friction and damping effect of powder but with the same particle number and size distribution. The different flowability in simulation can be reflected by the different magnitude of repose angle of powder heap, as shown in the upper left of Fig. 2.10(a)(b)(c). The simulation results of layer patterns indicated that powder layer for greater flowability was more uniform and with a higher fraction of fine powder, as shown in Fig. 2.10(a)(d). The homogeneity of powder bed is an important prerequisite for high forming quality of PBF-EB-built component. Note that the high fraction of fine powder should contribute to the high powder bed homogeneity in the case of great flowability. The snapshot of powder heaping up by rake in Fig. 2.11 shows that better flowability is good for not only the fluent powder delivery but also the greater tendency for segregation of fine particles during powder flowing. In other words, the homogeneity of the powder layer can be improved by using powder with better flowability, and a sufficient flowability of a powder is essential for a successful PBF-EB process.

Shape and surface quality of the particles essentially determine the powder flow behavior and powder bed quality. The qualities of the metallic powder depend on their producing process. Concerning the powder produced by the plasma rotating electrode process (PREP), the particles show near-perfect spherical shape, which is favorable for

powder flow during powder raking process. By contrast, the powder produced by gas atomization (GA) method that has a problem with the formation of satellites usually possesses non-spherical shape because of the adhesion with fine particles nearby. GA powder is usually irregular in shape with coarse surface texture resulting in deteriorate flowability. Moreover, PREP powder has finer overall size and much lower porosity than that of GA powder. Accordingly, PREP powder is more appropriate to be applied in PBF-EB process than GA powder that has an inherent weakness of flowability. Powder bed generation depending on the flow behavior of powder that is determined by particle size and particle shape is an essential prerequisite of successful fabrication by PBF-EB.

2.5. Effect of particle size distribution on powder bed pattern

Another factor that can influence the powder packing density is particle size distribution (PSD). The PSD of a metallic powder has a significant influence on the forming density of a component fabricated by powder-bed AM. Although it is possible to get high-density values by using different powder types, the process conditions also have to be adjusted accordingly, in order to promote the process productivity. Moreover, the PSD does affect not only the density but also the powder layer homogeneity because the flowability would also be affected by PSD [12]. Therefore, PSD is thought to be one of the critical metal powder characteristics for additive manufacturing, and it seems commonly accepted that if the quantity of small spheres is high enough to fill up the gap between the large spheres, the higher overall relative packing density can be obtained [13]. With this in mind, the artificially created powder with a smaller overall size, as shown in Fig. 2.12(b), were mixed with original powder to make a half-and-half in the number of particles powder mixture in simulation, aiming at increasing the proportion of fine powder. The comparison of simulation results between the cases of using original powder (Fig. 2.12(c)) and blended powder (Fig. 2.12(d)) illustrated that even though the relative packing density was higher in partial regions, the powder layer

homogeneity was decreased owing to the decreased flowability. Because an excessive fraction of fine powder increased the contact area between particles, friction became a primary factor that limiting powder flowability. Thus, powder packing density and powder bed homogeneity, both factors cannot be attended to one thing without neglecting the other. To produce PBF-EB-built components to be sufficiently dense and have excellent mechanical properties, the PSD should be designed to facilitate good packing behavior and powder bed homogeneity, and the appropriate fractions of powder with different size should be continued to explore.

In addition, during the interaction between the electron beam and powder bed, heat transfer in terms of energy absorption and heat radiation relies on PSD and resulting spatial distribution of particles on powder bed to a great extent, which will be investigated and discussed in later chapters.

Conclusions

The dynamic behaviors of the powder raking process were simulated using DEM modeling to examine how the powder properties affects the quality of the powder bed during the raking process. The effects of the physical parameters on powder bed pattern, focusing on packing density, flowability, particle size distribution, and their interplays:

1) The practical powder packing density was influenced by corresponding layer thickness, and with an increase in nominal thickness, final steady layer thickness increases, and high powder packing density was obtained.

2) The better flowability of powder was preferable for homogeneity of powder layer with higher packing density because the higher flowability favored the greater tendency for a fine particle moving downward during powder raking.

3) The mixture of powder with large and small size could increase packing density, but it might be detrimental to the flowability and homogeneity. The excessive fraction of fine powder made the friction to be the main factor that limited the powder flowability. PSD should be designed to facilitate good packing behavior and powder bed homogeneity.

Table 2-1. Simulation input parameters of the simulations and the properties of the CCM alloy powders.

Parameters	CCM
Particle density, ρ_a	8287 kg/m^3
Young's modulus, E	210 GPa
Poisson's ratio, ν	0.30
Repose angle, Φ	29°
Restitution coefficient, e	0.15
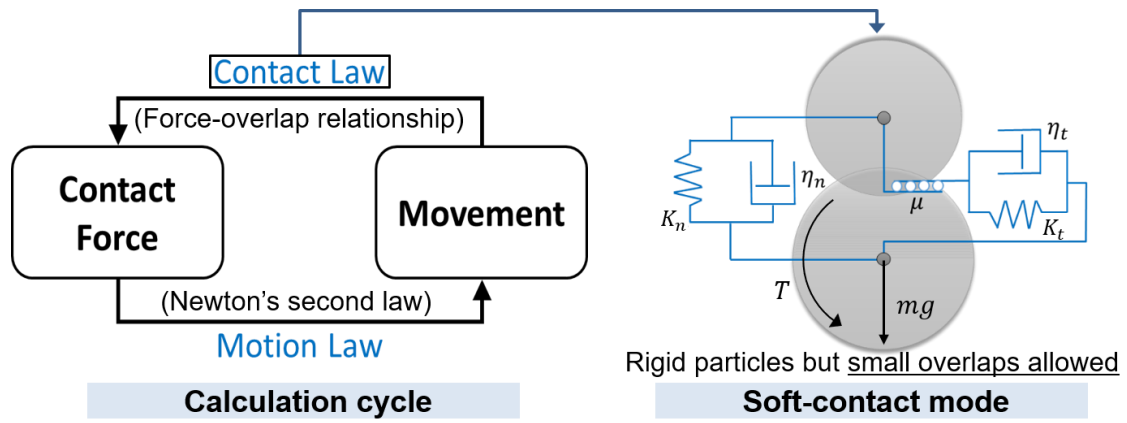
Fig. 2.1. Schematic illustration of the underlying principles of DEM modeling.
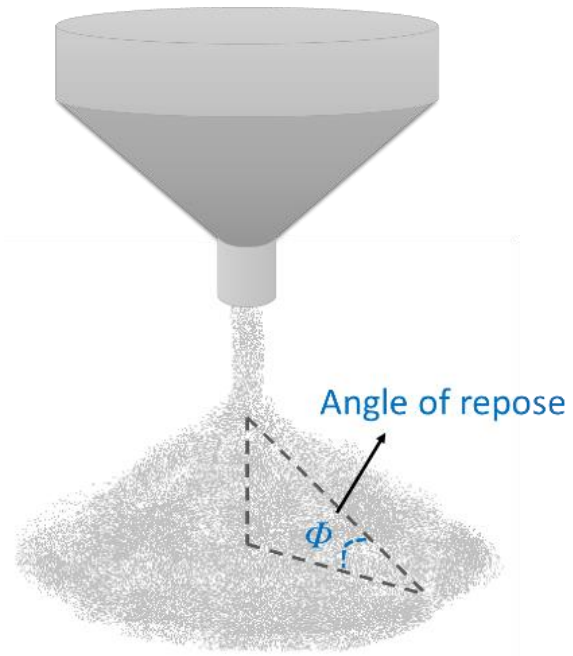
Fig. 2.2. Schematic of repose angle that is and indicator for powder density, friction and flowability.
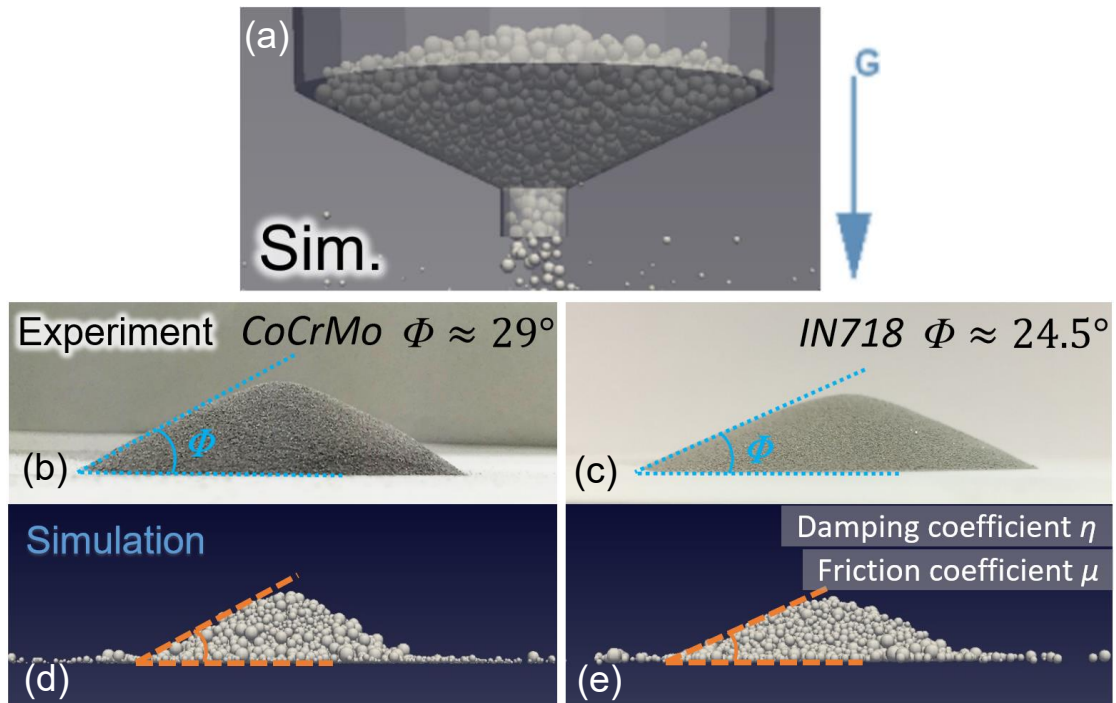
Fig. 2.3. Calibrating the coefficients related to the damping and friction of the powder used in this study. (a) DEM simulations that mimic the scenarios of measurement process of repose angle. The simulated repose angle of (d) CCM and (e) IN718 alloy powders were matched those observed by (b)(c) experiments.
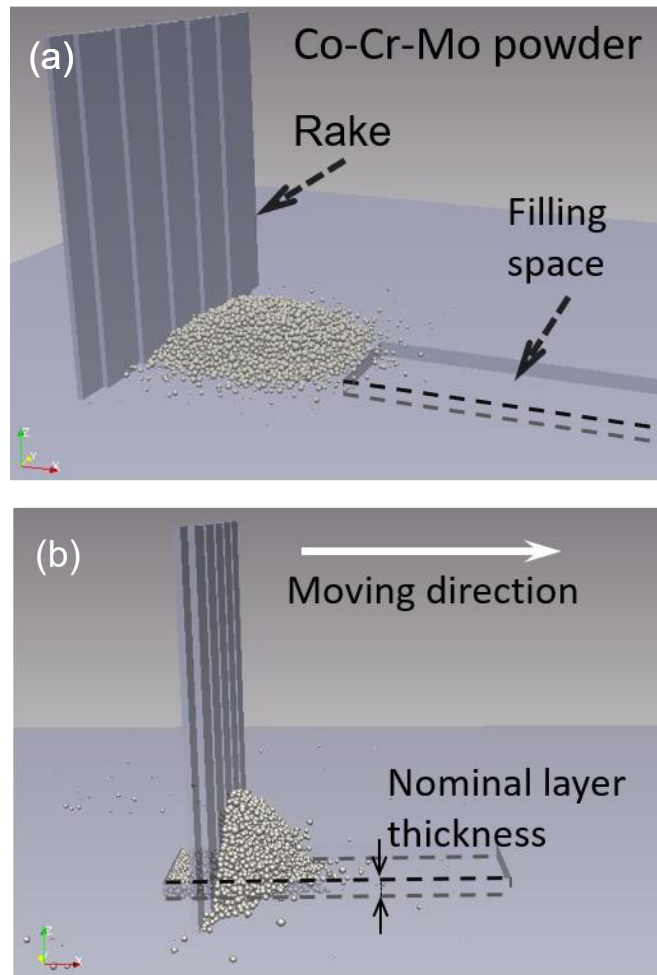
Fig. 2.4. Snapshots of the DEM simulation of powder bed generation process: (a) before raking, (b) during raking.
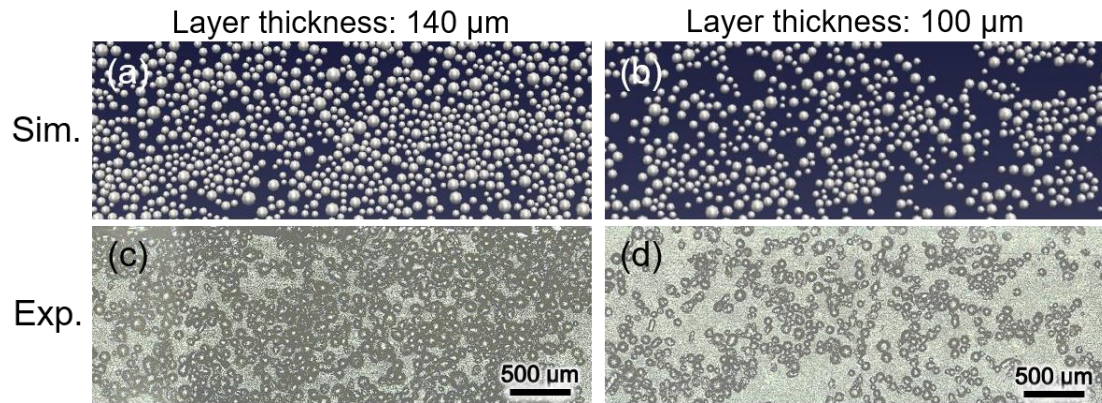
Fig. 2.5. (a)(b) Simulated and (c)(d) experimental results for single layer raking with CCM alloy powder corresponding to the layer thickness of (a)(c) 140 μm and (b)(d) 100 μm.
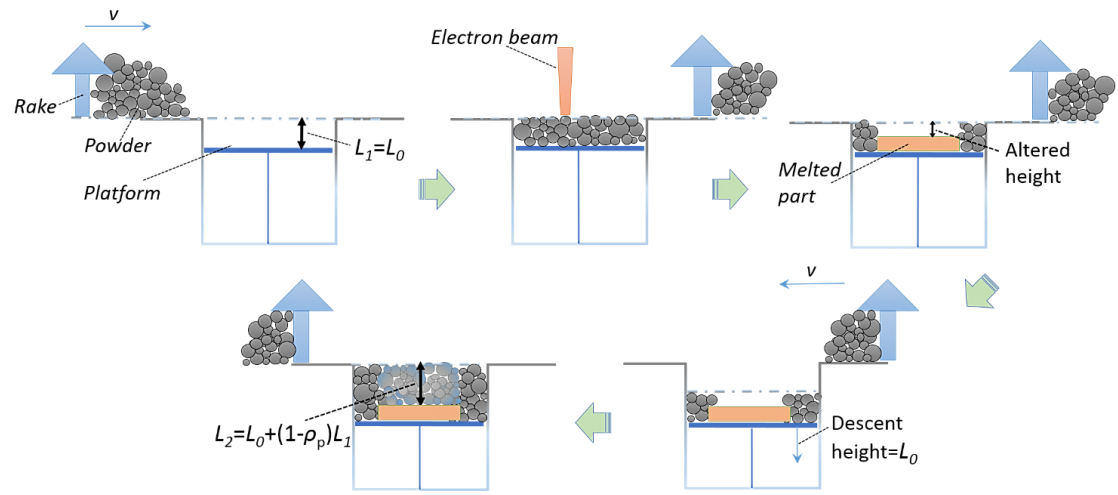
Fig. 2.6. Schematic illustration of the evolution of practical powder layer thickness.
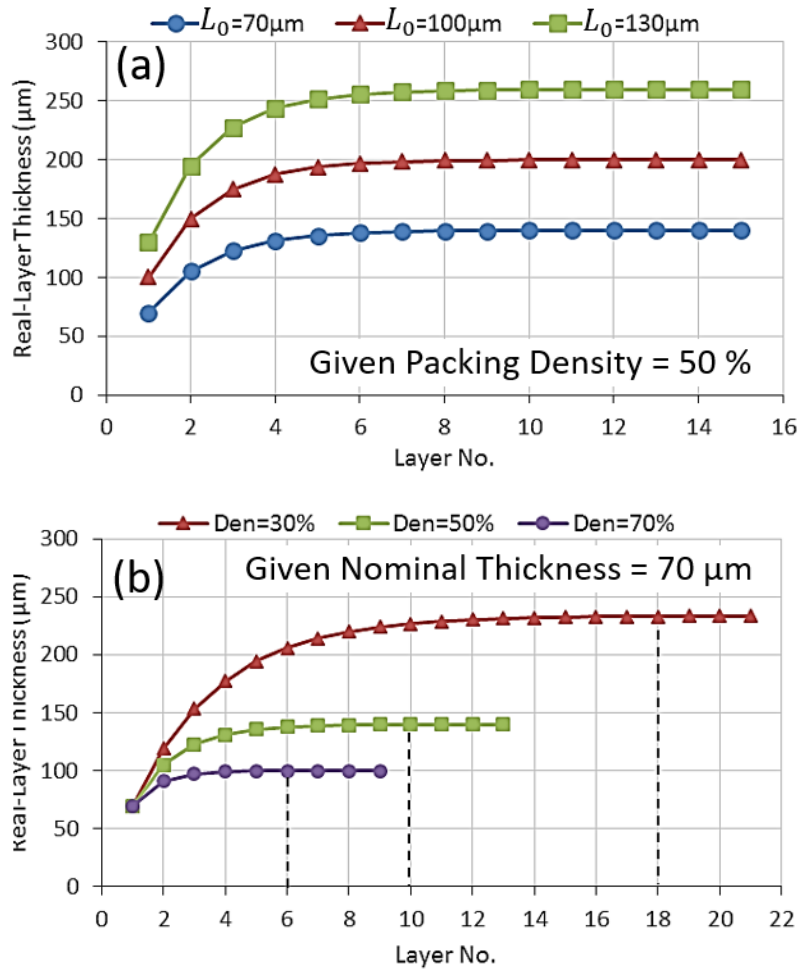
Fig. 2.7. Evolution of practical layer thickness for different (a) nominal layer thickness L_0 and (b) different packing density ρ_p.
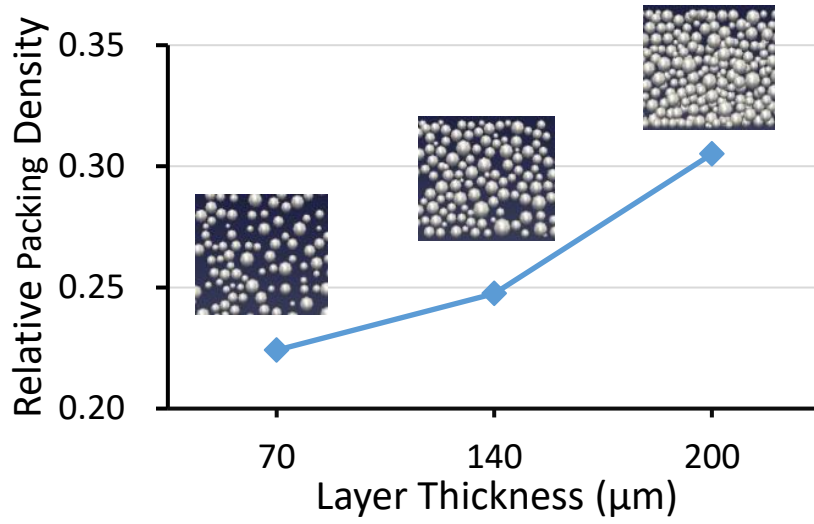
Fig. 2.8. Simulated powder bed with different packing density under different layer thickness.
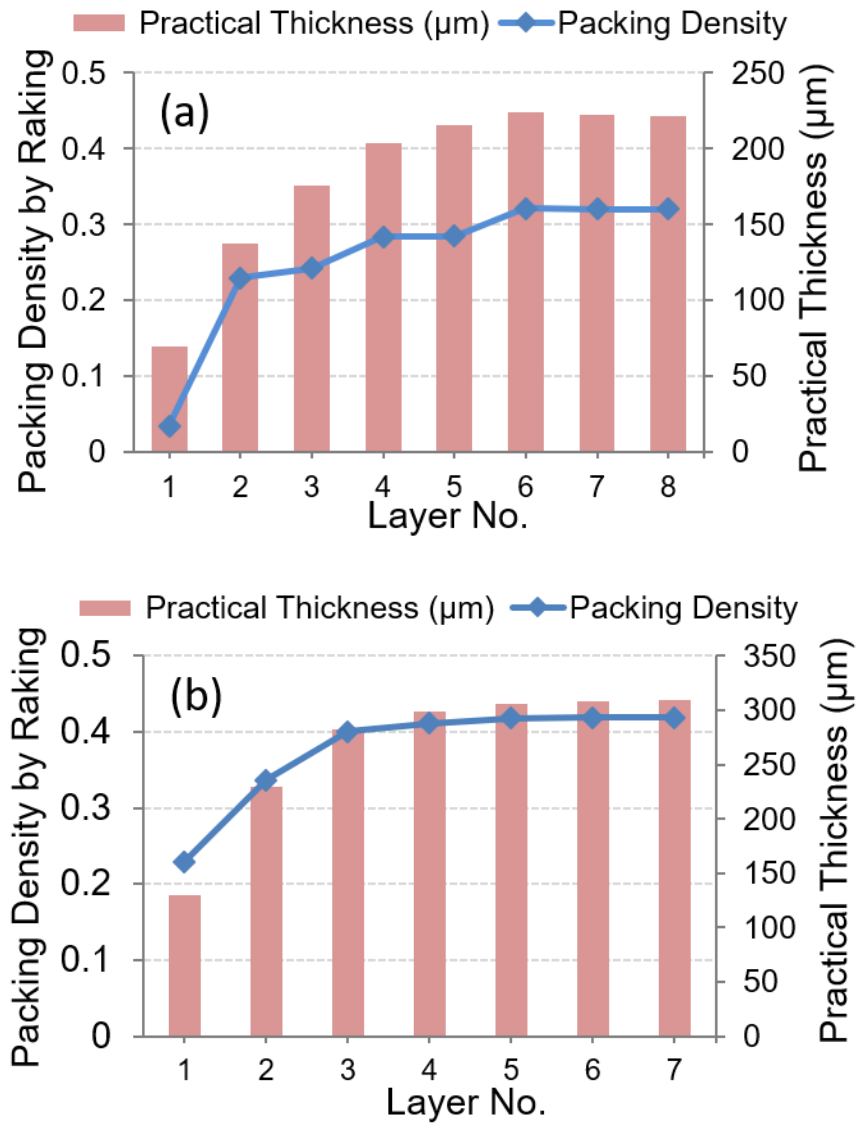
Fig. 2.9. Simulation results of the evolution of packing density and practical layer thickness under different nominal layer thickness L_0 of (a) 70 μm and (b) 140 μm.
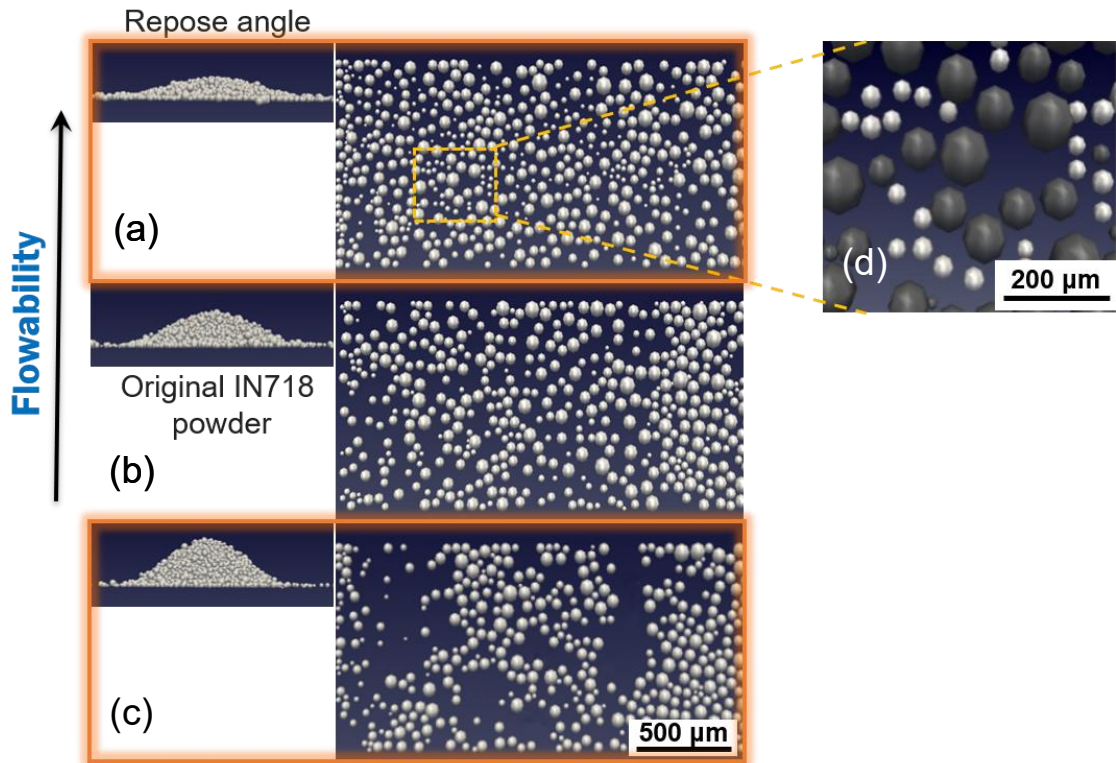
Fig. 2.10. Powder layer patterns with different flowability and corresponding powder repose angle: (a) powder with better flowability; (b) original powder; (c) powder with worse flowability; (d) high magnified image of layer pattern with better flowability.
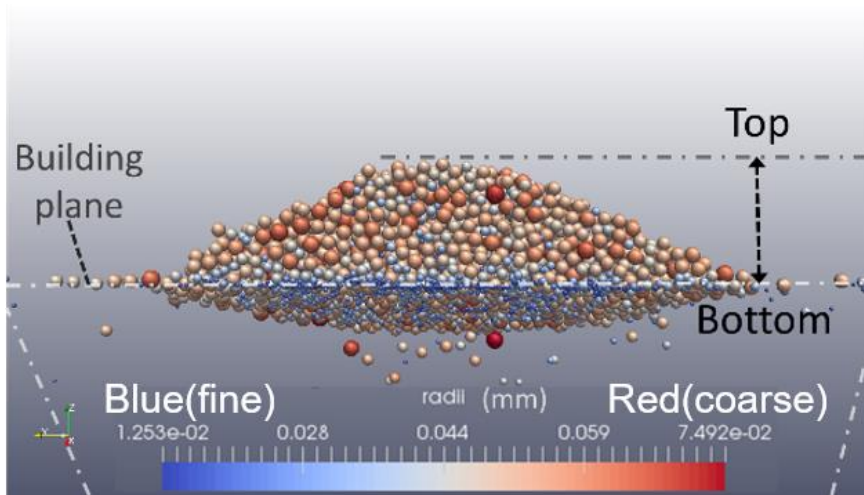
Fig. 2.11. Simulation snapshot of powder heaping up by rake during powder bed generation.
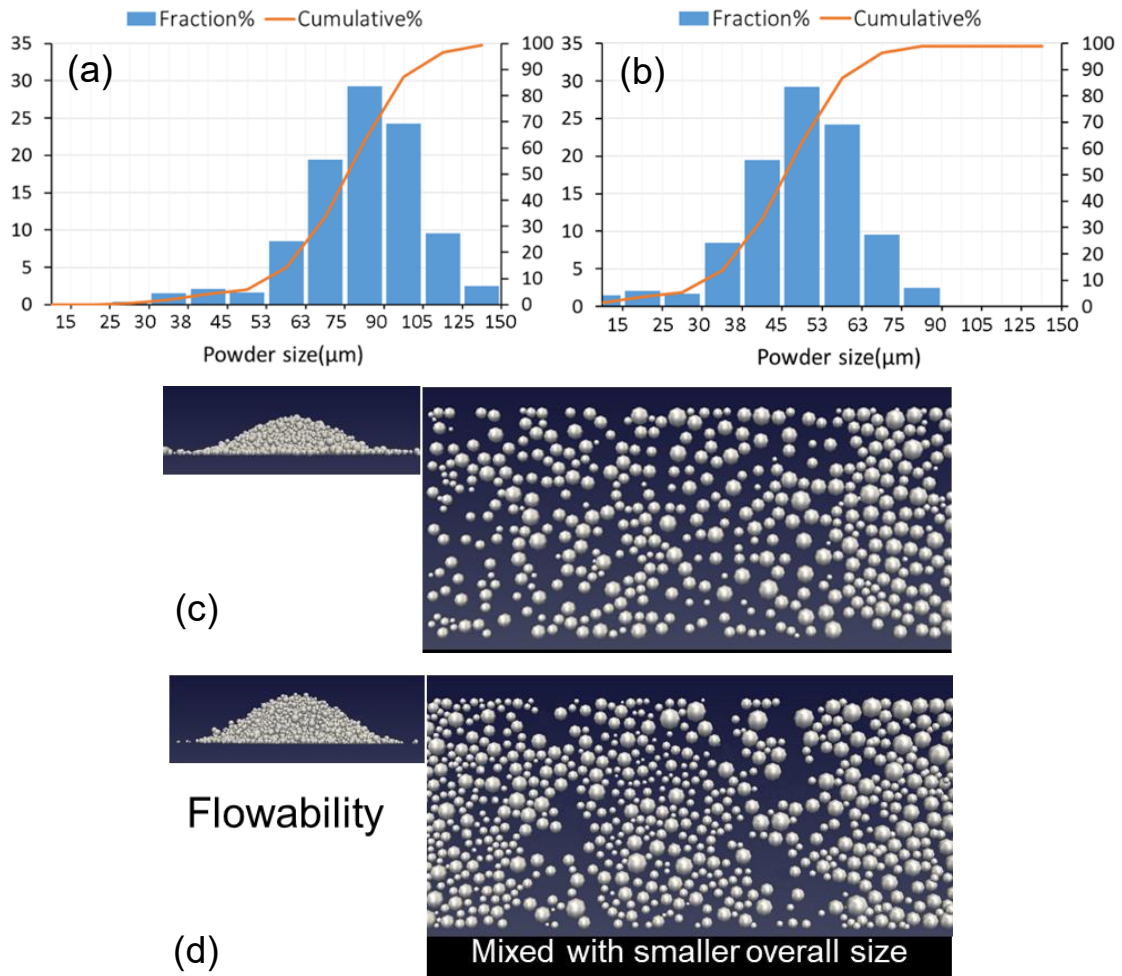
Fig. 2.12. (a) PSD of original alloy; (b) PSD of artificially created powder mixture with smaller overall size. Powder layer patterns and with corresponding powder repose angle of (c) original powder and (d) powder mixture.

References

[1]   C. Modenese, "Numerical study of the mechanical properties of lunar soil by the discrete element method," University of Oxford, 2013.

[2]   B. Peng, "Discrete Element Method (DEM) Contact Models Applied to Pavement Simulation," Virginia Polytechnic Institute and State University, 2014.

[3]   F. P. Di Maio and A. Di Renzo, "Modelling particle contacts in distinct element simulations: Linear and non-linear approach," *Chemical Engineering Research and Design*, vol. 83, no. 11 A, pp. 1287–1297, 2005.

[4]   V. A. Yastrebov, G. Anciaux, and J. F. Molinari, "The contact of elastic regular wavy surfaces revisited," *Tribology Letters*, vol. 56, no. 1, pp. 171–183, 2014.

[5]   R. D. Mindlin, "Compliance of Elastic Bodies in Contact," in *The Collected Papers of Raymond D. Mindlin Volume I*, vol. 16, 1989, pp. 197–206.

[6]   K. F. Malone and B. H. Xu, "Determination of contact parameters for discrete element method simulations of granular systems," *Particuology*, vol. 6, no. 6, pp. 521–528, Dec. 2008.

[7]   Müller, Patric, and Thorsten Pöschel. "Collision of viscoelastic spheres: Compact expressions for the coefficient of normal restitution." *Physical Review E* vol. 84, no. 2, 021302, 2011.

[8]   V. Šmilauer and B. Chareyre, "Yade DEM Formulation," 2011.

[9]   Carpenter, "CarTech® BioDur® CCM® Alloy." [Online]. Available: http://cartech.ides.com/datasheet.aspx?i=101&E=8. [Accessed: 17-Jan-2018].

[10]   NASA, "Inconel Alloy 718," in *Materials Data Handbook*, 1972.

[11]   H. W. Mindt, M. Megahed, N. P. Lavery, M. A. Holmes, and S. G. R. Brown, "Powder Bed Layer Characteristics: The Overseen First-Order Process Input," *Metallurgical and Materials Transactions A*, vol. 47, no. 8, pp. 3811–3822, Aug. 2016.

[12]   Strondl, A., Lyckfeldt, O., Brodin, H., & Ackelid, U, "Characterization and control of powder properties for additive manufacturing," *Jom*, 67(3), 549-554.

2015.

[13]   K. Rietema, *The Dynamics of Fine Powders*. Springer Netherlands, 1991.

Chapter 3

Fundamentals of molten pool behaviors in PBF-EB

3.1. Introduction

PBF-EB is a type of AM that involves multiple physical processes. Because of its unique process conditions compared to other AM processes, a detailed investigation into the molten pool behavior and dominant physics of PBF-EB is required. Fluid convection involves mass and heat transfer; therefore, fluid flow can have a profound effect on solidification conditions. This study focused on the fluid behavior, associated thermal status, and resultant solidification conditions during PFB-EB melting process. Because of the specific nature of the PBF-EB process, experimental characterization of temperatures is only possible on easily accessible surfaces of the sample but not at the interior sites. In this study, computational thermal-fluid dynamics (CtFD) simulations considering the unique processing conditions of PFB-EB, in conjunction with single-bead scan experiments, were used to analyze the molten pool behavior and other solidification-related factors. The simulations and experiments in this study were performed without a powder layer, to investigate molten pool behavior without interference specifically. Using numerical methods, we clarified the dominant physics determining the fluid behavior in PBF-EB and elucidated the differences in molten pool behaviors between PBF-EB and PBF-L(laser). By comparing simulations of actual viscosity and artificially high viscosity (limited fluidity), the specific influence of fluid flow in PFB-EB was demonstrated. Understanding the fundamental processes of melting and gaining insight into processing mechanisms and factors influencing solidification is necessary to achieve microstructural control of PFB-EB-fabricated materials.

3.2. Methodology

3.2.1. CtFD modeling setup

CtFD is a computational solution of the equations governing thermo-fluid dynamics, including the conservation of mass/momentum/energy: $\frac{\partial \rho}{\partial t} + \nabla \cdot (\rho \vec{V}) = 0$, $\frac{\partial \vec{V}}{\partial t} + (\vec{V} \cdot \nabla)\vec{V} = -\frac{1}{\rho}\nabla p + [1 - \beta(T - T_\mathrm{m})]\vec{g} + \vartheta\nabla^2\vec{V}$, $\frac{\partial(\rho H)}{\partial t} + \nabla(\rho H\vec{V}) = \nabla \cdot (\kappa\nabla T) + \nabla(\rho\Delta H\vec{V})$, respectively. Further details are provided in the literature [1] [2].

The 3D transient molten pool model was developed using FLOW-3D, a commercial CtFD software program [3]. The fluid free surfaces were modeled through Volume of Fluid (VOF) method in which a volume fraction of a fluid occupying each element in the computational domain is defined by an index F: $\frac{\partial F}{\partial t} + \nabla \cdot (F\vec{V}) = 0$, where $0 \leqslant F \leqslant 1$. For a reasonably accurate description of the PBF-EB process, the physical model should be customized using specific conditions. The salient features pertinent to the specific problems addressed in this study are described below.

Buoyant flow (i.e., thermal convection) can occur because of fluid density variations caused by thermal expansion: $\rho(T) = \rho_\mathrm{ref}[1 - \beta(T - T_\mathrm{ref})]$, where β is the volumetric thermal expansion coefficient. The buoyancy effect is inherently included in the calculation by using a temperature-dependent density. The density of solid alloys as a function of temperature can be calculated from thermal expansion data, while the temperature-dependent density of pure liquid metals can be reasonably estimated from the empirical equation provided in a study [4]. Surface force terms contain three factors: capillary force, Marangoni force, and vapor recoil pressure, and must be incorporated into the model. The surface tension creates a capillary force, $\gamma c\vec{n}$, that acts along the normal direction, $\vec{n}$, to the molten pool surface to reduce the surface and shape, limiting the volume of the liquid to minimize the surface tension potential. Here, γ is the surface tension and c is the local curvature of the molten pool surface. The temperature-dependent surface tension produces the Marangoni effect:

$$\gamma(T) = \gamma_\mathrm{L} + \frac{d\gamma}{dT}(T - T_\mathrm{L}), \tag{3-1}$$

where γ_L is the surface tension (J/m^2) at the liquidus and $d\gamma/dT$ represents the

temperature coefficient of surface tension (J/m^2·K). Subsequently, the Marangoni force, acting along the tangent of the surface, can be written as:

$$\frac{d\gamma}{dx} = \frac{d\gamma}{dT}\nabla T, \tag{3-2}$$

where ∇T is the temperature gradient (K/m) at the liquid/gas interface. Another driving force of the melt pool flow is the vapor recoil pressure, a normal counterforce caused by the interaction between the metal vapor and atmosphere:

$$p_{\text{recoil}}(T) = Ap_0\exp\left[\frac{\Delta H_{\text{LV}}(T - T_{\text{V}})}{RTT_{\text{V}}}\right], \tag{3-3}$$

where p_0, ΔH_{LV}, T_{V}, and R are the atmospheric pressure (Pa), latent heat of vaporization (J/kg), vapor saturation temperature (boiling temperature), and universal gas constant (J/K·mol), respectively. A is a ratio coefficient that is generally assumed to be 0.54, indicating that the recoil pressure due to evaporation is 54% of the vapor pressure at equilibrium on the liquid surface. This is a common assumption, whereby vapor flow velocity reaches its maximum possible (sonic) value [5]. The Clausius-Clapeyron equation expresses the saturation vapor pressure at the corresponding temperature:

$$p_{\text{sat}}(T) = p_{V1}\exp\left[\frac{k\Delta H_{\text{LV}}}{(k - 1)C_{\text{P}}}\left(\frac{1}{T_{V1}} - \frac{1}{T_{\text{V}}}\right)\right], \tag{3-4}$$

where p_{V1} and T_{V1} are the standard atmospheric pressure and the boiling point at p_{V1}; k is the adiabatic index (the ratio of the heat capacity at a constant pressure C_{P} to heat capacity at constant volume C_{V}); and T_{V} in Eq. (3-3) is a function of atmospheric pressure. Moreover, especially for PBF-EB, a high-speed stream of electrons bombards the material to be melted. Therefore, impact pressure on the molten pool surface may be introduced by the incident electron beam:

$$p_{\text{eb}} = \frac{I}{q_{\text{e}}}\frac{4}{\pi D^2}\alpha p^*, \tag{3-5}$$

where I, q_{e}, p^*, and α are the current (A), electronic charge (C), electron momentum (kg·m/s), and the corresponding fractional change in momentum, respectively.

For the thermal conditions of PBF-EB, the heat source must be described as the energy input by the electron beam, which can be approximated as a Gaussian surface heat source:

$$q(r) = \frac{2\eta Q}{\pi r_0^2} \exp\left(-\frac{2r^2}{r_0^2}\right), \tag{3-6}$$

where, r_0 is the effective beam radius (m) at which the energy density decays to $1/e^2$ at the center of the beam spot, Q is the beam power (W), r is the actual spot radius, and η is the energy efficiency, which was assumed to be 90% [6]. Though the practical electron beam is a volumetric heat source, simulation results by applying a simplified surface heat source matched the experiments well according to our previous studies.

For thermal balance, apart from the heat loss due to conduction, the radiation is governed by the Stefan-Boltzmann law:

$$j^* = \epsilon\sigma(T^4 - T_0^4), \tag{3-7}$$

where σ is the Stefan-Boltzmann constant (W/m^2·K^4), ϵ is the material emissivity, and T_0 is the ambient temperature (K). In addition, evaporative cooling is a naturally occurring process and it is commonly assumed that vapors evolve at a sonic velocity from the Knudsen layer adjacent to the molten surface. Applying the laws of conservation and kinetics across this vapor flow discontinuity allows the relevant thermal and pressure boundary conditions to be calculated for the molten pool surface. If the temperature of the liquid, T, at a free surface is greater than the saturation temperature, T_V, evaporative cooling can be described as follows [7]

$$q_{\text{vap}} = \frac{0.82\Delta H^*}{\sqrt{2\pi MRT}} p_0 \exp\left[\frac{\Delta H^*(T - T_V)}{RTT_V}\right], \tag{3-8}$$

where M is the molar mass of the vapor and ΔH^* is the effective enthalpy (J/kg), which can be defined as

$$\Delta H^* = \Delta H_{\text{LV}} + \frac{k(k+1)RT}{2(k-1)}. \tag{3-9}$$

It should be noted that cooling by air convection is neglected given the high vacuum (0.1 Pa) in the PBF-EB chamber, which also improves the calculation efficiency. The physical properties of the material and coefficients used in the developed model are listed in Table 3-1. These properties were obtained from values produced or deduced in the literature [4][8][9][10][11][12]. The computational domain established by Flow 3D$^\circledR$ has dimensions of 13 mm (length), 1.5 mm (width), and 1.25 mm (height). A biased

mesh for the finer mesh (20 μm) around the molten region and a coarser mesh (40 μm) in the surrounding base material was used for a total of 2.1 million cells. Regarding the computational cycle, the automatic time-step selection configuration was used as part of the input data. The program automatically adjusted the time-step size without violating the stability conditions. These conditions satisfy the criteria that no quantity should diffuse more than approximately one mesh cell in a single time-step [13]. A single-track melting simulation with a scan length of 10 mm took approximately 48 h to complete using an Intel® Xeon® CPU E5-1620 (3.70 GHz) with 32 GB of RAM.

3.2.2. Experiments

The CtFD model was validated using a series of experimental melting trials. To clearly understand the interaction between the electron beam and material, the process conditions were simplified to concentrate on the molten pool behavior. Based on this starting point for both the simulations and experiments, single-track melting trials were performed on CCM alloy substrates without powder using an Arcam® A2X machine. In the experiments, the utilized power (P) was calculated as the product of the acceleration voltage (constant: 60 kV) and beam current. In this study, the single-track melting was implemented at P = 200, 400, 600, 800, and 1000 W and scan speeds (V) = 100, 300, 1000 mm/s. The trials were conducted without preheating, and the initial temperature of the substrate was 296 K. The composition of the substrate is listed in Table 3-2. To illustrate the differences in molten pool behavior depending on material properties, simulations and experiments were performed using IN718 for comparison. The melt track morphology was measured using laser confocal scanning microscopy (LCSM). Standard metallographic techniques were used to prepare the cross-sections of the PBF-EB single-track samples. Electron backscatter diffraction mapping was used for solidification structure analysis. Grain morphology measurements (aspect ratio) were performed using the ImageJ software package (National Institutes of Health, USA).

3.3. Feasibility of CtFD simulation

3D transient and localized temperature field is an essential prerequisite in order to understand the critical process parameters that affect the consolidation quality of the components. CtFD is the accurate calculation method of 3D temperature fields requiring a fully coupled solution of both heat transfer and fluid flow equations.

At first, we conducted a feasibility test of CtFD simulation by comparing with a finite element method (FEM) model that is a pure thermal model without considering fluid flow. The effects of fluid flow in temperature field and molten pool geometry were investigated by the comparison between CtFD and FEM models. As shown in Fig. 3.1(a), a single-track melt region of IN718 was taken as the object of study. The chemical composition of IN718 base plate is shown in Table 3-3. As described, fluid convection often dominates the heat transfer when molten pool formation. Seen from the simulation result of molten pool geometry based on FEM model (Fig. 3.1(b)) and CtFD model (Fig. 3.1(c)) under the same PBF-EB process condition of $P = 400$ W and $V = 300$ mm/s, the pure-thermal FEM model showed a molten pool with narrower width and shorter length. CtFD simulation shows greater agreement with the experiment on molten pool geometry, compared with FEM simulation. The negative temperature coefficient of surface tension is responsible for an outward fluid flow on the molten pool top surface, which results in a shallow penetration with a large molten pool width and a long molten pool length.

Considering that the fluid flowability has a significant effect on molten pool geometry [14], a comparison between the simulation case of actual fluid viscosity and the simulation case of artificially high fluid viscosity that is 50 times of actual one, was performed. As shown in Fig. 3.2, the transverse cross-sections of the simulated molten pool based CtFD model and FEM model revealed that by increasing the viscosity, molten pool geometry based on the CtFD model becomes close to that based on the FEM model. Moreover, the molten pool surface temperature shown in Fig. 3.3 clearly showed that the temperature profile along longitudinal molten pool surface of CtFD simulation case of artificially high viscosity significantly increased and became close to that of FEM simulation because the heat transfer by fluid convection is restrained. Eliminating the fluid convection in the FEM model allows the total energy of the

electron beam to be absorbed to increase the molten pool temperature. Therefore, considering the molten metal convection is associated with a decrease in the maximum temperature of the molten pool surface. In conclusion, fluid flow shows essential effects on temperature distribution and resultant molten pool geometry.

3.4. Dominant factors affecting fluid behavior

Fluid flow is related to the formation of a variety of defects, and because the moving liquid transports heat, it often dominates heat transport. Figure. 3.4(a) and (c) show an optical micrograph and corresponding 3D laser microscopy surface profile, respectively, of a 10 mm experimental melt track on a CCM substrate. The depression is shown at the front and the trailing end uplifts. The morphology of the solidified melt track generated by numerical simulation exhibits a similar overall melt track geometry compared to the experimentally observed geometry, as shown in Fig. 3.4(b) and (d). Good matching between the simulation and experimental measurements were obtained with respect to the dimensions and shape of the melt region, as shown in Fig. 3.4(e). Fig. 3.5 shows the simulated molten pool with temperature distribution and fluid flow. A flow cycle was generated from the front to the rear, then back through the bottom of the molten pool. The strong backward flow on the surface formed behind the hot molten pool front, contributing to the accumulation of molten metal at the trailing end during translation.

Three major surface effects determine the fluid flow and profile of the molten pool (Fig. 3.6). The convective flow of molten metal inside the molten pool is primarily driven by the Marangoni effect arising from the temperature-dependent surface tension. The non-uniform temperature distribution results in a surface tension gradient on the molten pool surface that drives the flow of molten metal. The second is the normal counterforce caused by interactions between the metal vapor and atmosphere. The molten pool would experience the recoil pressure due to vaporization of alloying elements. Finally, high-velocity incident electrons with momentum may induce an electron counter pressure, the magnitude of which depends on the input power.

In the simulation, Case A (reference case) includes all these effects. Comparisons of the reference with the cases using the same process parameters but excluding one of the factors to examine the individual influence and significance were performed. Fig. 3.7 shows the simulated melt track and its associated temperature distribution under the process parameters: P=600 W; V=300 mm/s.

In Case A (Fig. 3.7(a)), the molten metal flows backward from the depressed molten pool front. In Case B (Fig. 3.7(b)), the electron counter pressure was omitted from the simulation, but it did not affect the profile or thermal status of the molten pool. The impact of the electron beam carrying high-speed electrons negligibly influenced the molten pool surface. In Case C (Fig. 3.7(c)), no recoil pressure due to evaporation was stipulated. The depressed deformation of the molten pool front remained almost unchanged. It should be noted that the effect of metal evaporation plays a vital role in other processes (laser welding or selective laser melting) under nearly atmospheric pressure [15][16]. Just as in Eq. (3-3), vapor recoil pressure is highly dependent on the atmospheric pressure, p_0. Low chamber pressure produces a feeble metal vapor counterforce and the recoil effect of evaporation on the liquid surface is also weaker. The PBF-EB process operates under high vacuum (10^{-1} Pa) and such a low ambient pressure insufficient to induce a noticeable change in the molten pool. The vapor recoil pressure would have a more significant effect if the process were performed with considerably higher energy input because of the massive evaporation that would be induced. From Eq. (3-3), p_{recoil} is also a function of temperature (T), so a higher peak power density resulted in a higher peak temperature of the molten metal and recoil pressure. For example, the vapor recoil pressure contributes to keyhole formation in high-energy-density electron beam welding [4], where the energy density can be several tens of times higher than that in PBF-EB. The authors used a similar power (1000 W), but their welding speed (17 mm/s) was much lower than that used in this study. This suggests that the effect of the vapor recoil pressure is relatively insignificant under typical PBF-EB processing conditions. In Case D (Fig. 3.7(d)), Marangoni convection was eliminated by specifying a constant surface tension, resulting in a noticeable change in the molten pool profile and temperature distribution. Neither a visible

depression nor backward flow was observed in the molten pool. Moreover, without heat transfer by Marangoni convection, and with restricted surface cooling due to a smaller superficial area, the maximum temperature significantly increased. These results illustrate the significant influence of the Marangoni effect on fluid flow and heat convection in the PBF-EB process.

The formation quality is closely associated with fluid behavior. In welding or AM, balling occurs if the length-to-width ratio of the molten pool is greater than π (the Raleigh instability) [17]. If a disturbance occurs in the liquid stream, the molten metal may collapse into droplets under the surface tension. According to the above results, the molten pool is dynamic under thermocapillary convection caused by the Marangoni effect. The surface tension of molten metal depends on temperature and composition. A comparison of CCM and IN718 alloys was performed using the same process parameters. Compared to CCM (Fig. 3.8(a) and (b)), IN718 (Fig. 3.8(d) and (e)) shows a regular and smooth melt track, and the simulated molten pool with fluid velocity vectors (Fig. 3.8(f)) suggest a gentler fluid flow and steadier surface. The Marangoni force $d\gamma/dx = (d\gamma/dT)\nabla T$ depends on the temperature coefficient of the surface tension, $d\gamma/dT$, and temperature gradient on the molten pool surface, ∇T. Considering the melt hydrodynamic-related properties of the two alloys [18][19][20][21] listed in Table 3-4, CCM exhibits a larger magnitude of $d\gamma/dT$, approximately four times that of IN718. From the temperature distribution in Fig. 3.8(e) and (f), ∇T is not significantly different in the two alloys. In other words, the Marangoni force of the CCM melt is larger than that of the IN718 melt, indicating that stronger Marangoni convection occurs in the molten pool of the CCM alloy. Regarding the other melt hydrodynamic properties, such as viscosity and density, the values of the alloys are similar (Table 3-4). Thus, the irregularity and disconnection of the melt track in the CCM alloy are mainly induced by perturbations arising from the stronger Marangoni flow. The large magnitude of $d\gamma/dT$ indicates that the molten pool formed by the liquid CCM alloy is more easily disturbed by Marangoni flow. Thus, it can be concluded that the Marangoni effect primarily determines the fluid behavior and significantly affects the molten pool instability and forming quality in PBF-EB

processes, especially for the CCM alloy, which has a high temperature coefficient of surface tension.

3.5. Differences in molten pool behavior between PBF-EB and PBF-L

For the powder-bed fusion AM, PBF-EB and PBF-L(laser) are the most popular and commercially available processes. The major differences in the two types of systems are the heat source and building environment.

Concerning the heat source, the electron beam is focused using a magnetic lens in PBF-EB, while optical lenses manage the laser beam in PBF-L. In PBF-EB, incident electrons with high-velocity strike on material, and then the kinetic energy of electron converts into heat energy. In PBF-L, the laser photon is released by excited atom, and then the focused beam of photons provides the concentrated heat energy, but part of the energy is absorbed, and the rest is reflected. Compared with laser, the electron beam can penetrate deeply into the material, and no reflection occurs. Therefore, PBF-EB possesses high energy efficiency. Concerning the building environment, a vacuum setup in the building chamber is necessary because of the nature of the electron beam. By contrast, argon is infilled into the building chamber with a pressure near atmosphere to prevent oxidation.

As discussed previously, vapor recoil pressure is highly dependent on the building atmosphere pressure, p_0. Low chamber pressure in PBF-EB produces a feeble metal vapor counterforce and the recoil effect of evaporation on the liquid surface is also weaker. The comparison between the simulation cases under vacuum (0.1 Pascal) and 1 atm are shown in Fig. 3.10. The results clearly revealed that the molten pool became instable and convex-concave fluid surface presented under atmospheric pressure. Accordingly, vapor recoil pressure exerts a significant influence on the molten pool behavior in PBF-L. In addition, the multiple reflection effect of laser plays an important role during molten pool formation in PBF-L. Especially, in the case of high energy input, keyhole-mode melting that possesses a narrow and concave melt surface can be

activated because of a high vapor recoil pressure. Owing to the multiple reflections of laser, the keyhole allows the laser beam to propagate and reach the molten pool bottom. As a result, the total heat transfer rate is increased and the concave melt surface becomes deeper.

For elucidating the differences in molten pool behavior between PBF-EB and PBF-L, the CtFD simulation of PBF-L was performed for comparison. In the modeling of PBF-L, the vapor recoil pressure under atmospheric pressure and laser multiple reflections were introduced (Fig. 3.11). The effect of multiple laser reflections was implemented and coupled with the Fresnel energy absorption model that governs the energy portion absorbed from the reflected ray [22]. The simulation results of single-track melting in PBF-EB and PBF-L under high line energy of 10 J/mm are shown in Fig.3.12. The input energy efficiency η was set as 90 % and 40 % for electron beam and laser respectively. The initial temperature of the computational domain was 1323 K (preheating) in PBF-EB and 298 K (room temperature) in PBF-L. We can see, because of the deep concave molten pool induced by vapor recoil pressure and laser multiple reflections, numbers of pore defects formed after solidification in PBF-L. By contrast, without beam reflection and vapor recoil pressure being weak, the molten pool was stable, and no visible defect could be observed under the process condition of PBF-EB. Thus, PBF-EB possesses a wider process window than PBF-L, ensuring process stability and forming quality.

3.6. Effect of fluid flow on solidification parameters

Fluid flow plays an essential role in the solidification process because the convective transport of heat at the solidification front determines the growth conditions of the solid phase. Using accurate calculations of the temperature and velocity fields, it is possible to determine the solidification conditions that produce improved solidified microstructure. The solidification mode of a metal alloy can be determined by the constitutional undercooling occurring in the liquid immediately in front of solid/liquid (S/L) interfaces. The degree of constitutional undercooling can be expressed by the

temperature gradient (G) and solidification rate (R) ahead of the advancing solidification front.

The G of a cell in the computational domain can be expressed as:

$$G = \sqrt{G_\mathrm{x}^2 + G_\mathrm{y}^2 + G_\mathrm{z}^2},$$ (3-10)

where G_x, G_y, and G_z are the spatial components of the temperature gradient. The R can be subsequently calculated using the correlation with the cooling rate, and is equivalent to the velocity of the isotherms:

$$R = \frac{1}{G} \times \frac{\partial T}{\partial t}.$$ (3-11)

As shown in Fig. 3.13(a), G and R at the solidification front were calculated at each time step and extracted from each cell within the solidification front over time on a fixed and monitored cross-section of the computational domain as solidification proceeds. The mid-section of the melt track along the scan direction was chosen as the ideal cross-section to monitor. In Fig. 3.13(b), the solidification front in the simulation is represented by the collection of cells whose solid fraction is $0 < x < 1$. The boundaries are equivalent to the liquidus and solidus isotherm. The corresponding fluid velocity (U) of each cell within the solidification front was collected for further analysis. The time, t_0, is defined as the time when the maximum cross-sectional area of the molten pool occurs, indicating the start of solidification. Subsequently, G, R, and U values of the cells at the evolutive solidification front as the molten pool solidifies were collected step-by step over computational time until the entire pool passed through the plane (i.e., the monitored cross-section), as shown in Fig. 3.13(c). The $G - R$ plot obtained from the CtFD simulation was compared with that obtained from the 3D Rosenthal solution, which is a commonly used analytical method. The G - R distributions determined using the two methods agreed, indicating the reliability of the data obtained from the CtFD simulation (Fig. 3.14). Further details regarding these methods are given in the Appendix.

To illustrate the specific effect of fluid flow on solidification, a simulation with artificially high viscosity (50 times greater than the actual value) was performed for comparison. Viscosity is a quantity that describes a fluid's resistance to flow. Fig. 3.15

shows the variation of G and R with artificially high and actual viscosity values as solidification proceeds where each point represents the G or R value of each cell within the solidification front at a specific time step. As solidification proceeds, G decreases and R increases significantly at artificially high viscosity, as expected. Using actual viscosity, G also clearly decreased, but before solidification proceeds for 0.0055 s, R exhibits a relatively ambiguous trend with higher values than those obtained with artificially high viscosity. Thus, it can be assumed that higher fluid activity increases the uncertainty of the solidification conditions.

The results presented in the above section indicate that fluid flow plays a vital role in determining the solidification rate (solid-liquid interface velocity). The solidification rate, R, is related to the beam scan speed as follows:

$$R = V \cos \theta, \qquad (3\text{-}12)$$

where θ is the angle of deviation of the normal to the S/L interface with respect to the scan direction (Y direction) and is calculated by:

$$\theta = \cos^{-1} \left(\frac{G_y}{G} \right). \qquad (3\text{-}13)$$

Thus, R increases as θ decreases. The evolution of θ as solidification proceeds in the two simulations is shown in Fig. 3.15. The box plot shows the data at each time step. Before the solidification proceeds for 0.0055 s, the θ in the simulation with actual viscosity shows a lower general distribution level compared to that with artificially high viscosity. The effect of convective heat transfer on the solidification rate should be correlated with the fluid flow characteristics at the solidification front. The components of fluid velocity along the X, Y, and Z directions at the solidification front under actual viscosity conditions are shown in Fig. 3.16(a). The fluid flow along the +Y direction, corresponding to the scan direction, dominates the flow pattern during solidification. Similarly, the fluid flows in all directions dramatically decrease after 0.0055 s because coexistence with the pure liquid phase significantly enhances fluid activity at the solidification front. The simulated results of the flow pattern shown in Section 3.4 demonstrated that the active fluid flow could push the cooler liquid from the trailing end through the bottom to the hot front of the molten pool. In other words, the fluid

flow along the +Y direction involves the cooled molten metal. The R direction (i.e., normal to the S/L interface) is opposite to the heat dissipation direction. Thus, for a cell within the solidification front, the flow of the cooler fluid along the +Y direction decreases θ because of the change in heat dissipation direction, as depicted in the schematic in Fig. 3.16(b).

The description above explains the ambiguous trend of the high values of R before solidification proceeds for 0.0055 s. In other words, the increase in R can be attributed to the change in spatial relation concerning the scan direction under active fluid convection. It should be noted that the discussion regarding the solidification rate does not consider the influence of crystal orientation or solute profile around the dendrite tip, which can also affect crystal growth under fluid flow [23]. Nevertheless, the mechanism influencing heat transfer by fluid flow was clarified by our modeling.

Conclusions

The molten pool behavior with associated the thermal status and solidification conditions of PBF-EB of the CCM alloy were investigated via CtFD simulations and experimental analysis under specific process conditions of PBF-EB. The specific effect of fluid flow was examined by comparison between simulation cases with actual and artificially high viscosities. The following conclusions can be drawn:

1) In comparison with the pure-thermal FEM model, CtFD simulation showed greater agreement with experiment than the pure-thermal model, because fluid flow showed essential effects on temperature distribution and molten pool geometry.

2) The CtFD simulation results revealed the decisive influence of the Marangoni effect on fluid behavior and heat convection of the molten pool. The Marangoni effect of molten metal primarily determined the molten pool geometry and significantly affected molten pool instability and resultant formation quality in PBF-EB of the CCM alloy.

3) Without beam reflection and vapor recoil pressure being weak, the molten pool was stable, and no visible defect could be observed under the process condition of PBF-

EB. Thus, PBF-EB possessed a wider process window than PBF-L, ensuring process stability and forming quality.

4) Fluid flow played a vital role in determining the solidification rate, R (solid-liquid interface velocity). The increasing R values was attributed to changes in the spatial relation to the scan direction under the effect of active fluid convection.

Appendix

The 3D Rosenthal modeling method is an analytical tool that provides a quasi-steady-state solution to the 3D heat conduction equation for bulk 3D geometries. The attractiveness of this method lies in its simplicity, as the computing expense for a massive number of points is negligible compared to entirely numerical techniques. However, this technique inherently cannot consider complex boundary conditions or non-uniform material properties [24].

The Rosenthal point source solution for the 3D flow of heat in an infinite half-space [25] can be expressed in a dimensionless form as follows:

$$\bar{T} = \frac{e^{-\left(\bar{z_0}+\sqrt{\bar{x_0}^2+\bar{y_0}^2+\bar{z_0}^2}\right)}}{2\sqrt{\bar{x_0}^2+\bar{y_0}^2+\bar{z_0}^2}}, \tag{3-A1}$$

where

$$\bar{T} = \frac{T-T_0}{(\eta P/\pi\kappa)(\rho C_{\mathrm{P}}V/2\kappa)}, \qquad \bar{x_0} = \frac{x_0}{2\kappa/\rho C_{\mathrm{P}}V}, \qquad \bar{y_0} = \frac{y_0}{2\kappa/\rho C_{\mathrm{P}}V},$$

$$\text{and } \bar{z_0} = \frac{z_0}{2\kappa/\rho C_{\mathrm{P}}V}. \tag{3-A2}$$

In the above normalizations, T is the temperature at a certain location (x_0, y_0, z_0) relative to the moving point heat source and T_0 is the initial temperature of the solid. The thermophysical properties ρ, C_{P}, and κ are assumed to be temperature-independent and their values are listed in Table 3-A1. The cooling rate and thermal gradient can be obtained via differentiation of Eq. (3-A1).

Table 3-1. Thermophysical properties of alloys and coefficients and constants applied to the simulation.

	Symbol and unit	Value for CCM	Value for IN718
Density	ρ (g/cm^3)	8.28~7.13	8.19~7.16
Viscosity	μ (mPa·s)	5.6~7.9	5.3~7.2
Thermal conductivity	κ (W/m·K)	14.5~37.6	8.9~29.6
Specific heat	C_P (J/kg·K)	465~760	435~720
Emissivity	ε	0.23	0.32
Liquidus temperature	T_L (K)	1703	1608
Solidus Temperature	T_S (K)	1623	1523
Boiling point at standard atmospheric pressure	T_{V1} (K)	3225	3111
Latent heat of fusion	ΔH_{SL} (J/kg)	3.14e+05	2.10e+05
Latent heat of vaporization	ΔH_{LV} (J/kg)	6.34e+06	3.62e+06
Surface tension at T_L	γ_L (J/m^2)	1.85	1.88
Temperature coefficient of surface tension	$\frac{d\gamma}{dT}$(J/m^2·K)	-0. 00043	-0.00011
Adiabatic index	k	1.4	
Stefan-Boltzmann constant	σ (W/m^2·K^4)	5.67e-08	
Universal gas constant	R (J/K·mol)	8.314	
Environment pressure	P_0 (Pa)	0.1	
Environment temperature	T_0 (K)	298	
Energy efficiency	η (%)	90	

Table 3-2. Chemical composition of Co-Cr-Mo alloy substrate.

Composition	Cr	Mo	Ni	Fe	Si	Mn	C	N	Co
Value (mass.%)	28	6	0.02	0.05	0.57	0.6	0.05	0.1	Bal.

Table 3-3. Chemical composition of Inconel 718 alloy substrate.

Composition	Ni	Cr	Mo	Nb	Ti	Al	Co	Mn	Fe
Value (mass.%)	52.5	19	3	5	0.9	0.5	1	0.35	Bal.

Table 3-4. Melt hydrodynamics-related alloy properties.

	Surface tension (γ) at T_m (J/m^2)	$d\gamma/dT$ ($J/m^2 \cdot K$)	Viscosity ($mPa \cdot s$)	Density (g/cm^3)
CCM	1.85	-0.00043	5.6~7.9	8.28~7.13
IN718	1.88	-0.00011	5.3~7.2	8.19~7.16

Table 3-A1 Thermophysical properties of CCM alloy used for Rosenthal solution.

Density (g/cm^3)	Thermal conductivity ($W/m \cdot K$)	Specific heat ($J/kg \cdot K$)	Melting temp. (K)	Energy efficiency (%)
8.01	28.1	635	1663	90
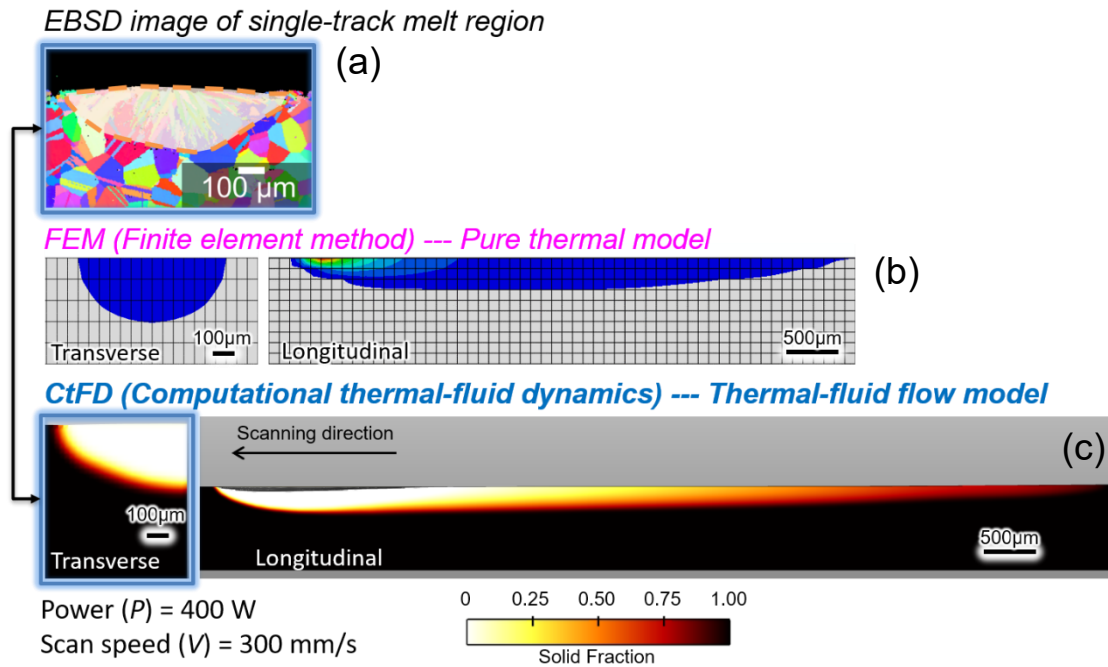
Fig. 3.1. (a) EBSD IPF map of single-track melting of IN718 under the process condition of P = 400 W and V = 300 mm/s. The corresponding simulation results of molten pool geometries based on (b) FEM model and (c) CtFD model.
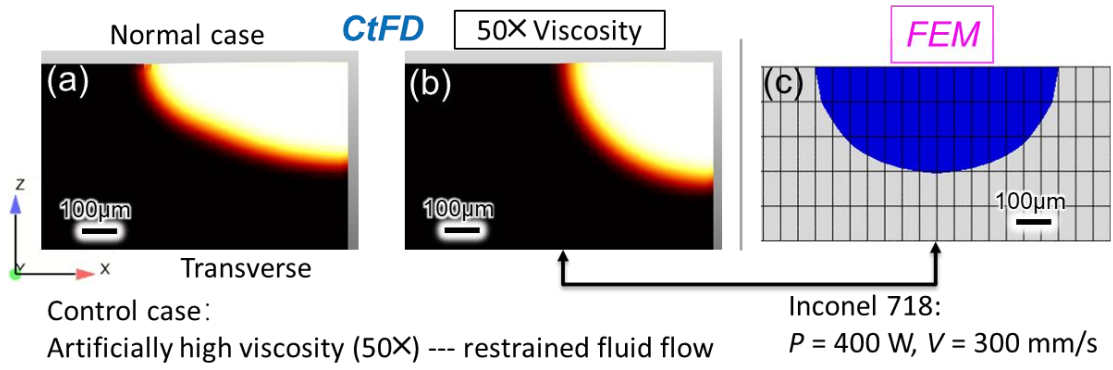
Fig. 3.2. Transverse cross-sections of the simulated molten pool obtained by single-track melting of IN718 under the process condition of P = 400 W and V = 300 mm/s and based on CtFD model in the case of (a) actual viscosity and (b) artificially high viscosity, and (c) FEM model.
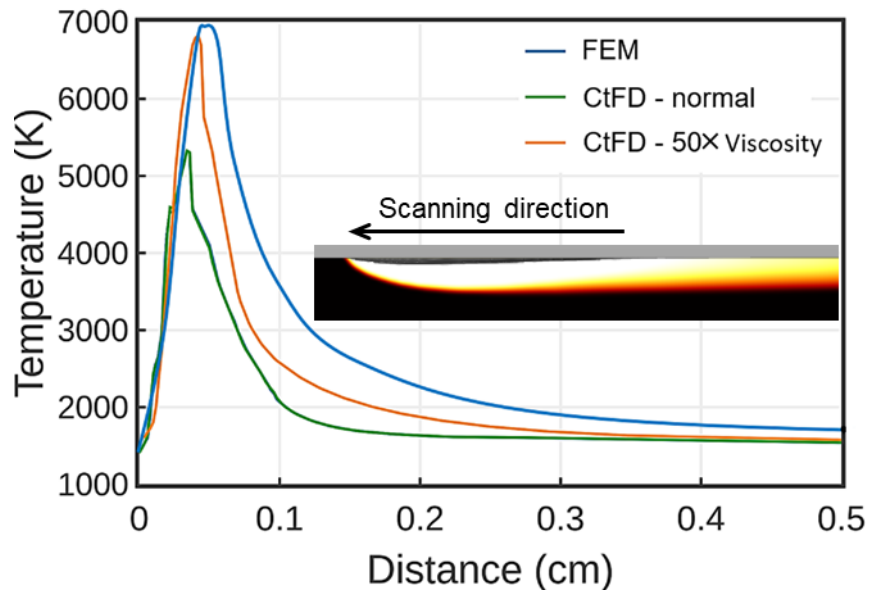
Fig. 3.3. Temperature profiles along longitudinal molten pool surface obtained by single-track melting of IN718 under the process condition of $P = 400$ W and $V = 300$ mm/s and based on CtFD model in the case of actual viscosity and artificially high viscosity, and FEM model.
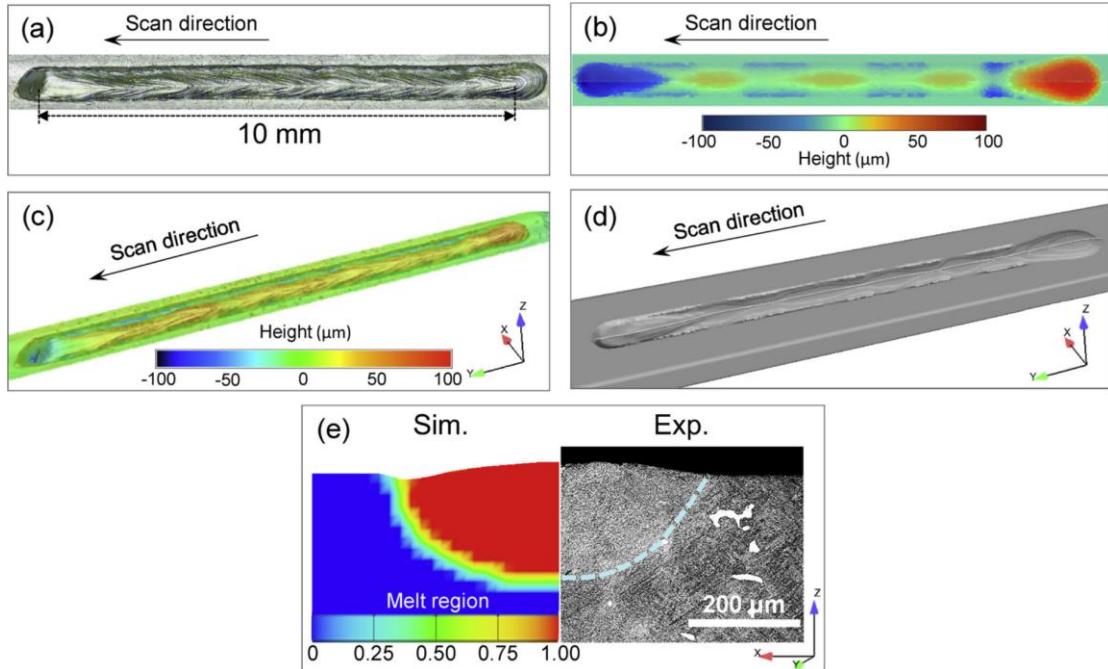
Fig. 3.4. Morphology of solidified melt performed by (a, c) experimental measurements and (b, d) simulation. (a) is optical micrograph and (b) is 3D LSCM image of the surface profile. Surface height and profile obtained from the simulation are shown in (c) and (d), respectively. (e) shows a good match of the dimension and shape of the melt region (cross-section) between the simulation and experiment. Process parameters: $P = 600$ W, $V = 300$ mm/s.
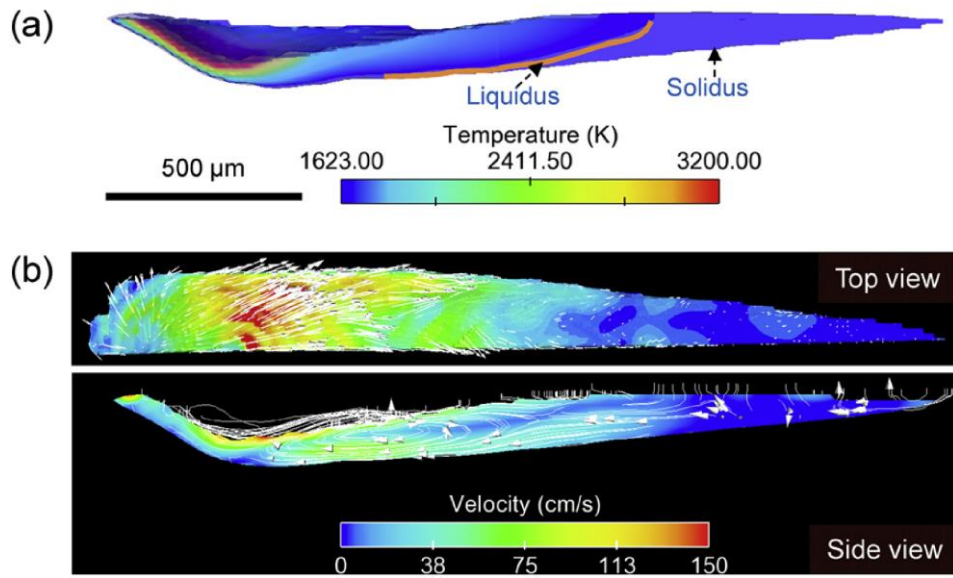
Fig. 3.5. Simulated molten pool with (a) temperature distribution and (b) fluid flow. Streamlines indicate fluid flow.
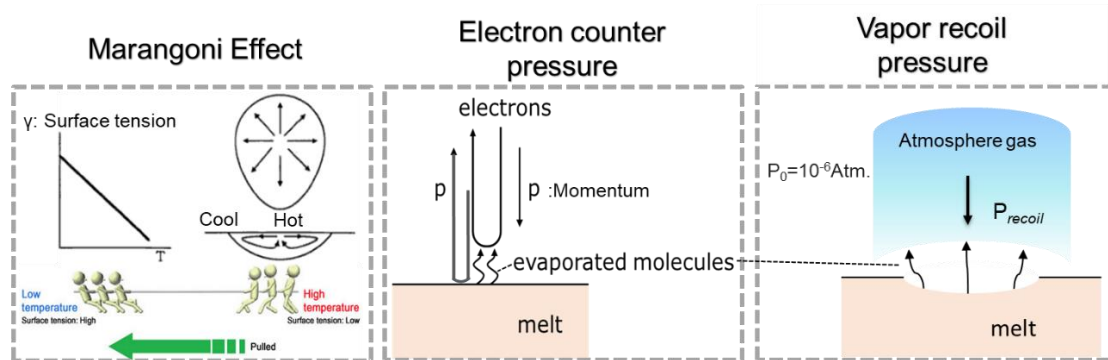
Fig. 3.6. Schematic illustration of three major surface effects determining the fluid flow and profile of the molten pool.
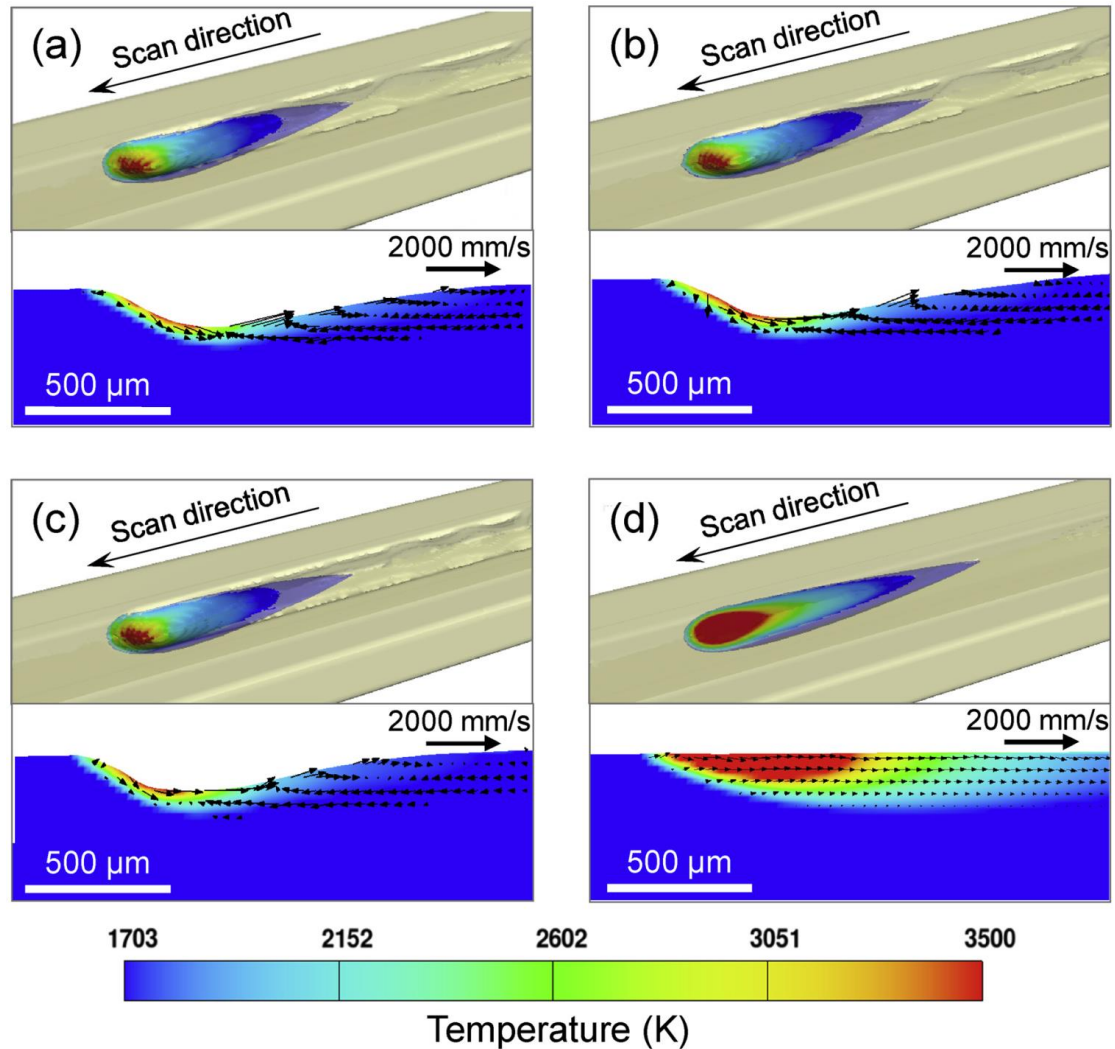
Fig. 3.7. Simulated molten pool with multiple physics: (a) Case A (reference case) with Marangoni effect, electron counter pressure, and vapor recoil pressure, (b) Case B without electron counter pressure, (c) case C without vapor recoil pressure, (d) Case D without Marangoni convection. In each figure, the upper part shows a 3D view of the melt track, and the lower part shows a 2D centrally longitudinal cross-section. The arrow with the value of velocity is the scale of the fluid velocity vector. Process parameters: $P = 600$ W, $V = 300$ mm/s.
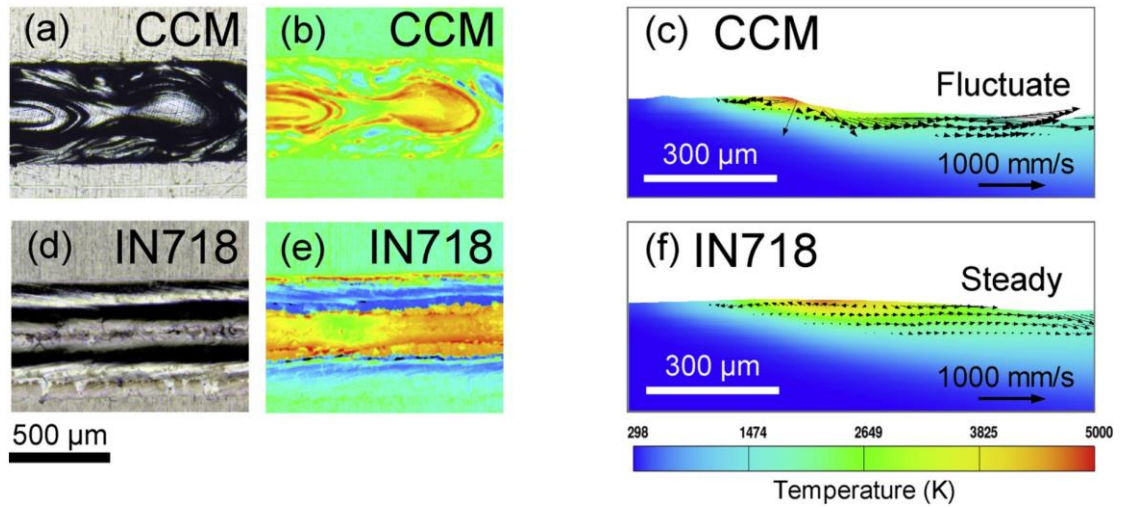
Fig. 3.8. Comparison of melt tracks between (a, b, c) CCM and (d, e, f) IN718 under the same process parameter: P = 600 W, V = 1000 mm/s. The solidified melt tracks were characterized by (a, d) optical microscopy and (b, e) laser confocal scanning microscopy. Simulated molten pool with fluid velocity vectors shows different dynamic features between (c) CCM and (f) IN718.
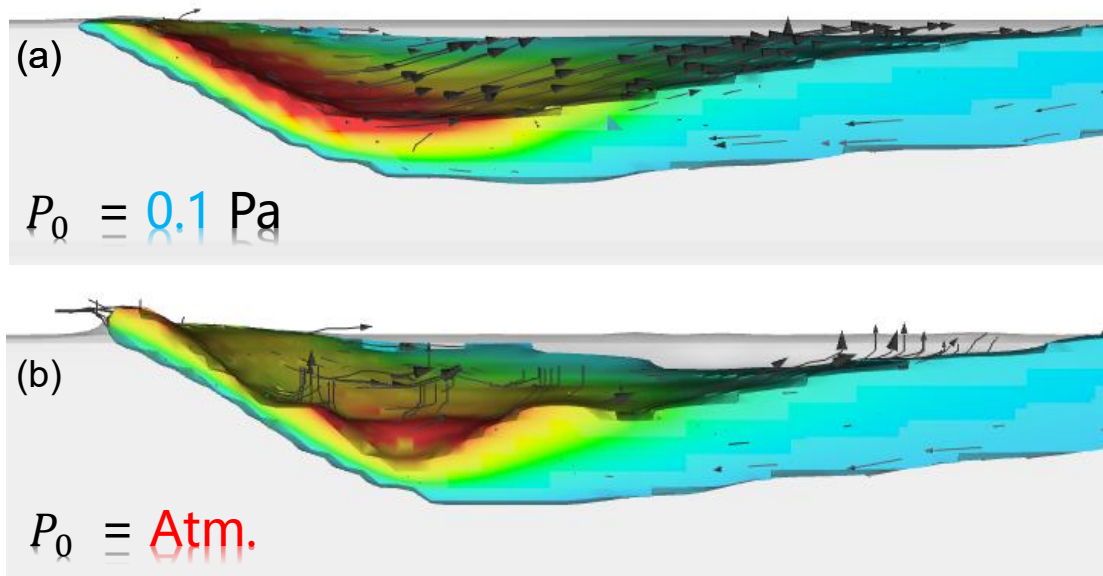
Fig. 3.9. Comparison of simulated molten pool under (a) vacuum and (b) 1 atm, which illustrated that the vapor recoil pressure was highly dependent on the ambient pressure. Process parameter: P = 600 W, V = 300 mm/s.
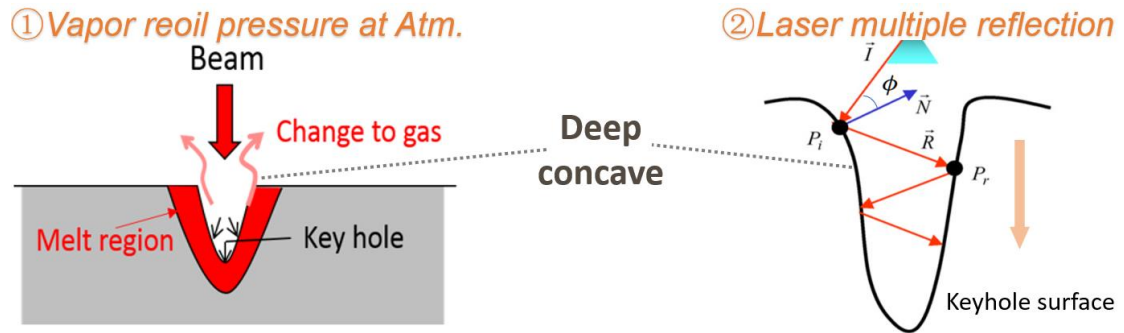
Fig. 3.10. Schematics illustrating the effects of vapor recoil pressure and laser multiple reflection in PBF-L. Both effects give rise to the deep concave molten pool and strong pore forming tendency in PBF-L.

Time = 0.0462
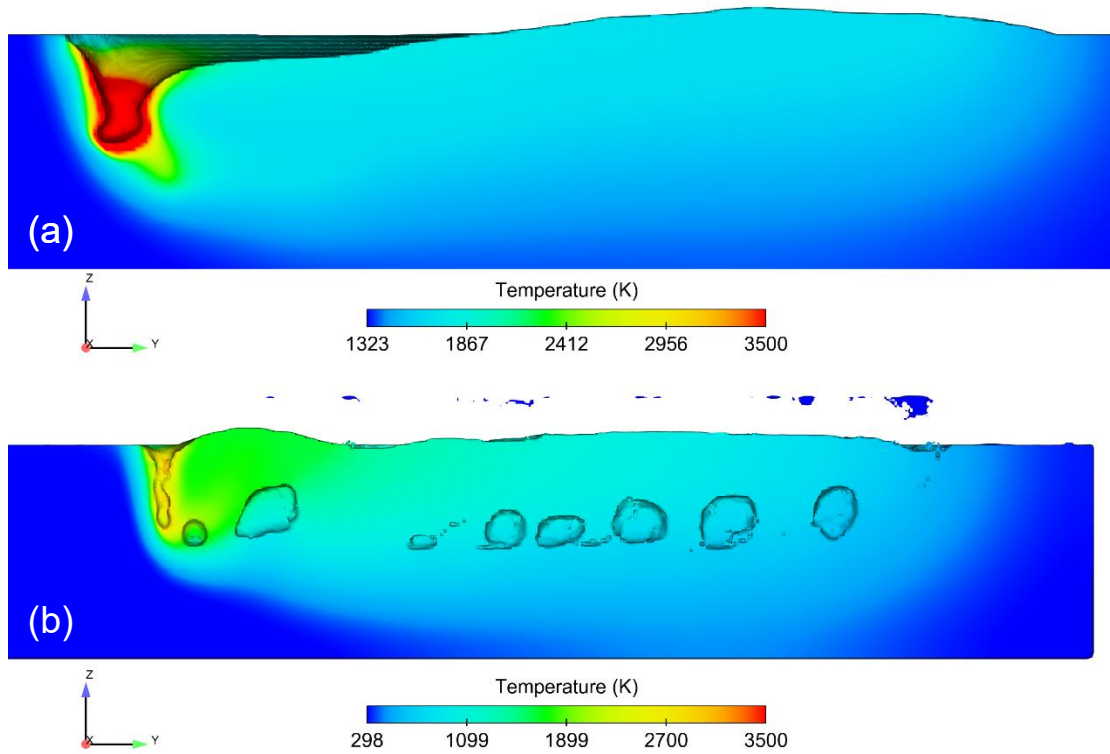
Fig. 3.11. Simulation results of single-track melting in (a) PBF-EB and (b) PBF-L under high line energy of 10 J/mm. Process parameter: P = 1000 W, V = 100 mm/s. The input energy efficiency η was set as (a) 90 % and (b) 40 %. The initial temperature of the computational domain was (a) 1323 K and (b) 298 K.
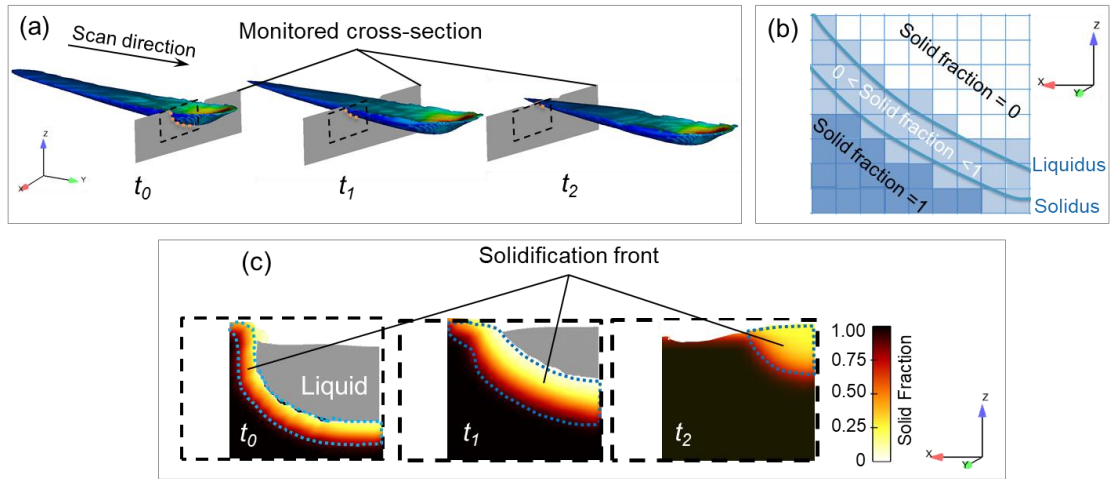
Fig. 3.12. Schematic of data extraction and representation form: (a) data is extracted from the cells of the solidification front located in a monitored cross-section of the computational domain over time. (b) Solidification front is represented by the collection of the cells whose solid fraction is less than 1 and higher than 0, and boundaries are equivalent to liquidus and solidus isotherm. G, R, and U of the cells only at (c) the evolutive solidification front which is encompassed by the dashed line and depicted in the color range between blue and red were collected step by step in computational time as the molten pool passes through this monitored cross-section.
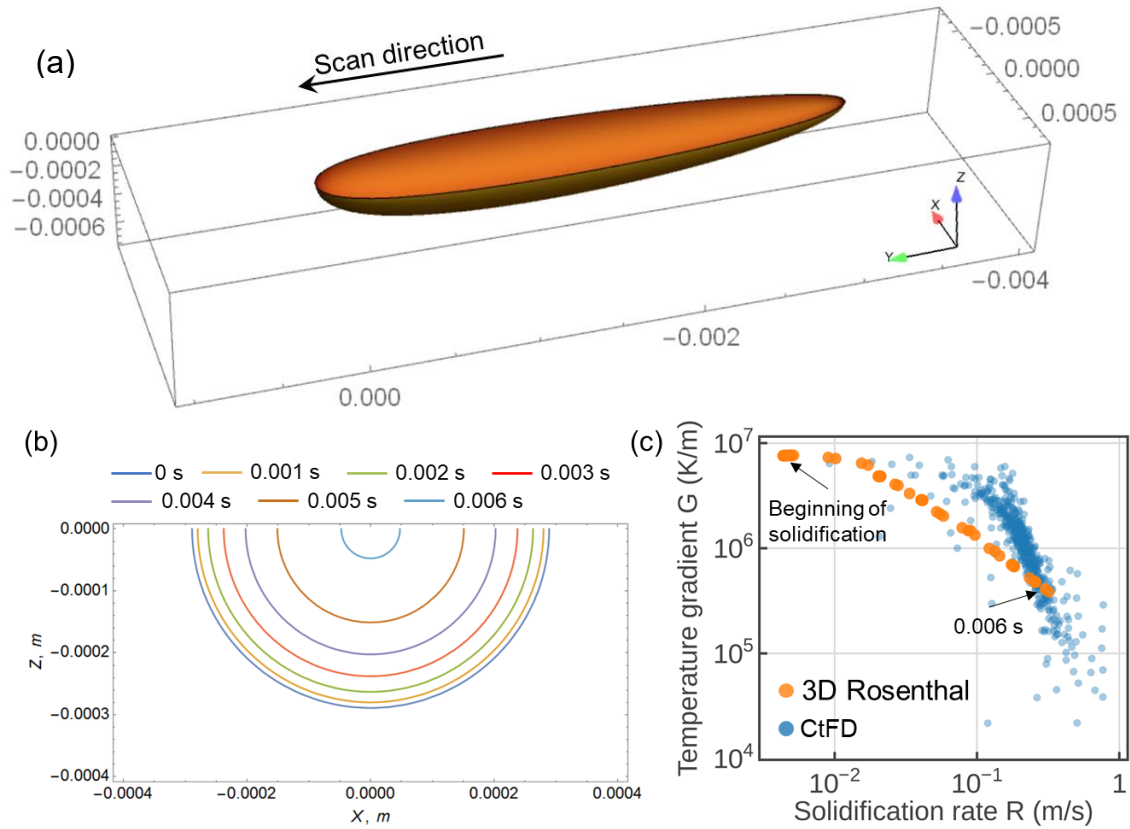
Fig. 3.13. (a) 3D Rosenthal solution for a molten pool. The S/L interface is depicted as isothermal. (b) Transient S/L interface on the monitored cross-section by 3D Rosenthal solution, tracking from the beginning of solidification to 0.006 s. *G-R* value at S/L interface in (b) is plotted in (c), compared with the data extracted from CtFD simulation (Case: artificially high viscosity). Process parameter: $P = 800$ W, $V = 300$ mm/s.
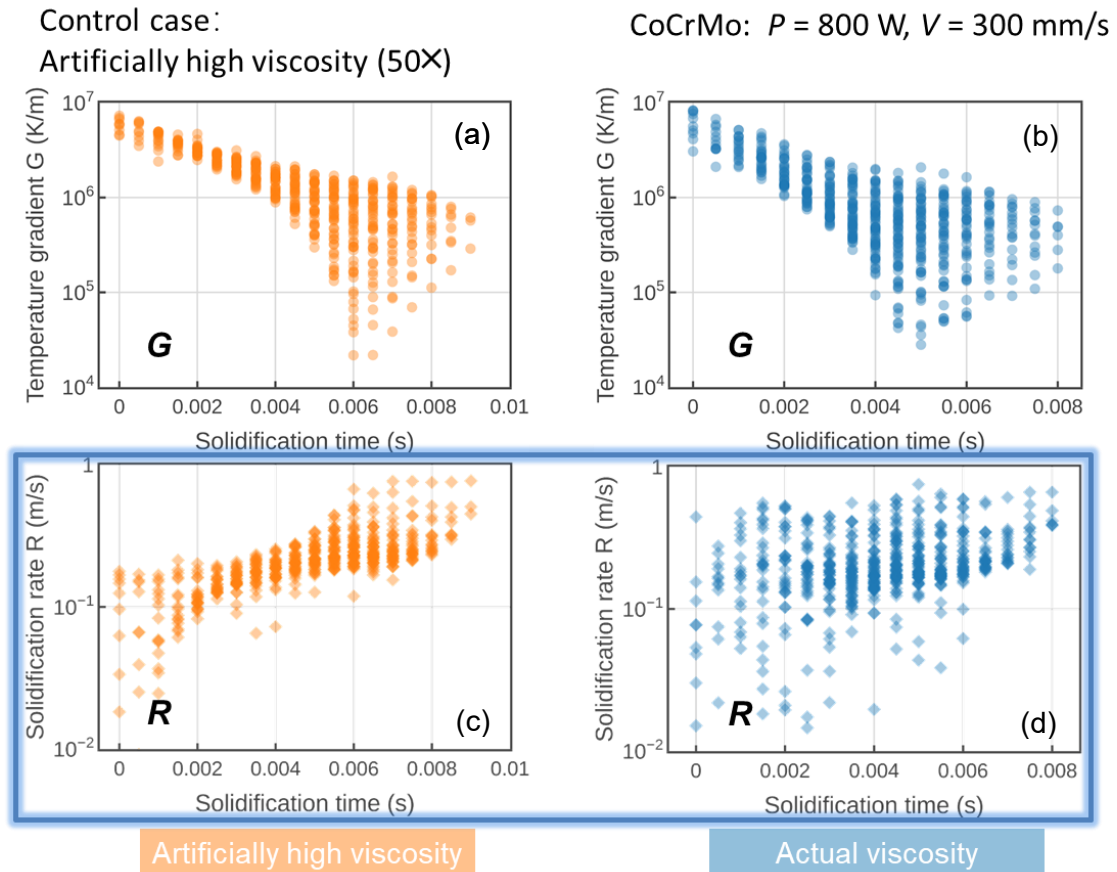
Fig. 3.14. Variation of temperature gradient G and solidification rate R of the cases with (a, c) artificially high viscosity and (b, d) actual viscosity as solidification proceeds. Each point represents the G or R value of each cell within the solidification front at a specific time step. Process parameters: $P = 800$ W, $V = 300$ mm/s.
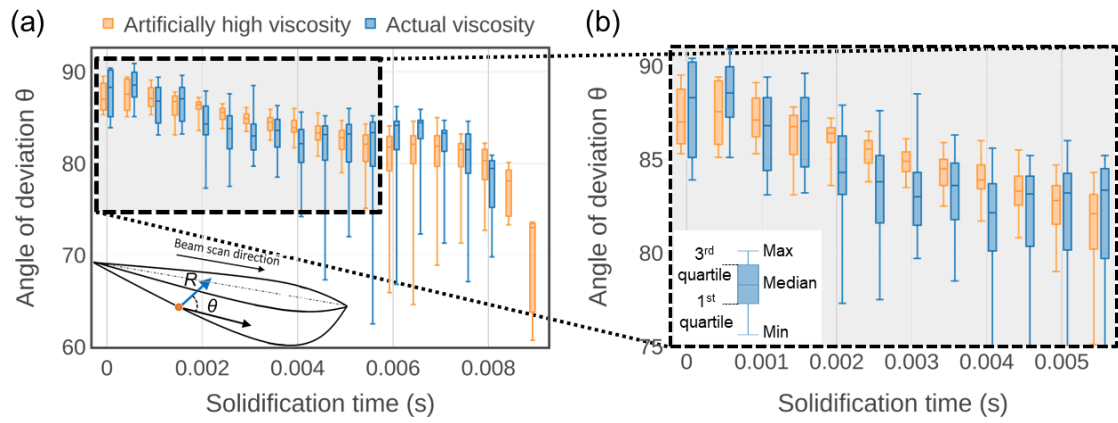
Fig. 3.15. Evolution of the deviation angle of the normal to the S/L interface with respect to the scan direction. Box plot depicts data at each time step. Process parameters: $P = 800$ W, $V = 300$ mm/s.
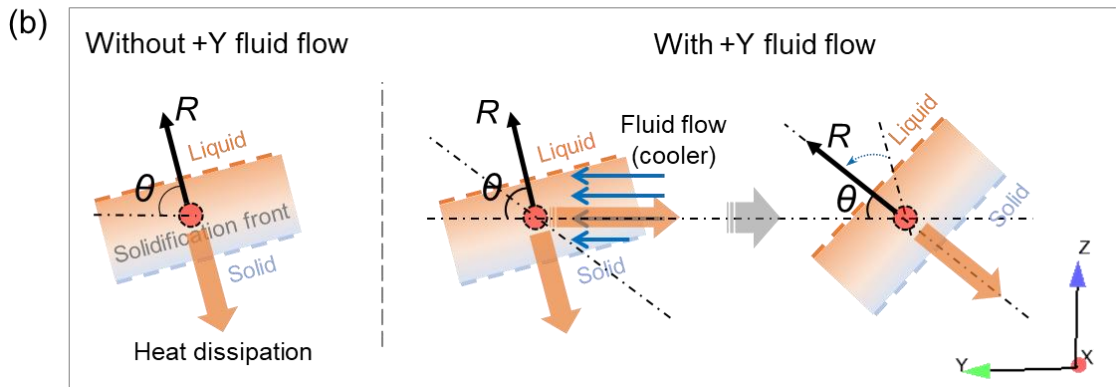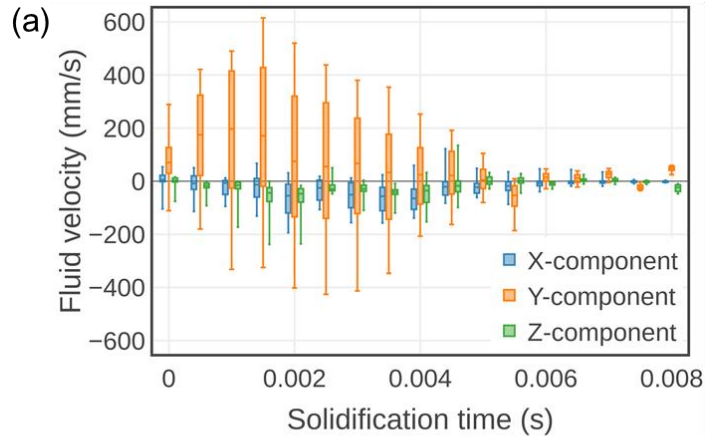
Fig. 3.16. Box plot in (a) depicts the components of fluid velocity along the X, Y, and Z directions at solidification front in the case with actual viscosity. Schematic shown in (b) showing the cooling fluid flow along +Y direction can decrease θ for a cell within the solidification front because of the change in the direction of heat dissipation. Process parameters: $P = 800$ W, $V = 300$ mm/s.

References

[1]   John D Anderson, "Governing equations of fluid dynamics," *Computational Fluid Dynamics*, pp. 15–51, 2009.

[2]   C. . Hirt and B. . Nichols, "Volume of fluid (VOF) method for the dynamics of free boundaries," *Journal of Computational Physics*, vol. 39, no. 1, pp. 201–225, Jan. 1981.

[3]   FlowScience, "FLOW-3D | Highly-Accurate CFD Software | Free Surface Transient Flows," 2015. [Online]. Available: https://www.flow3d.com/products/flow-3d/. [Accessed: 17-Feb-2018].

[4]   J. J. Valencia, "Thermophysical Properties Sources and Availability of Reliable Data," 2008.

[5]   J. Schou and Risø, "Laser-beam interactions with materials: Physical principles and applications," *Nuclear Instruments and Methods in Physics Research Section B: Beam Interactions with Materials and Atoms*, vol. 124, no. 4, pp. 647–648, May 1997.

[6]   R. W. Messler, *Principles of welding: processes, physics, chemistry, and metallurgy*, vol. 138, no. 10. 1999.

[7]   J.-H. Cho, D. F. Farson, J. O. Milewski, and K. J. Hollis, "Weld pool flows during initial stages of keyhole formation in laser welding," *Journal of Physics D: Applied Physics*, vol. 42, no. 17, p. 175502, Sep. 2009.

[8]   Matweb, "Carpenter BioDur^{TM} CCM® Medical Implant Alloy, Annealed," 2017. [Online]. Available: http://www.matweb.com/search/DataSheet.aspx?MatGUID=36aaab3c917a4c4 da752798bcd39fb88&ckck=1. [Accessed: 17-Jan-2018].

[9]   J. J. Valencia and Quested P.N, "Thermophysical properties," *ASM Handbook: Casting*, vol. 15, no. Ref 24, pp. 468–481, 2008.

[10]   Carpenter, "CarTech® BioDur® CCM® Alloy." [Online]. Available: http://cartech.ides.com/datasheet.aspx?i=101&E=8. [Accessed: 17-Jan-2018].

[11]   C. Costa, S. Delsante, G. Borzone, D. Zivkovic, and R. Novakovic,

"Thermodynamic and surface properties of liquid Co-Cr-Ni alloys," *Journal of Chemical Thermodynamics*, vol. 69, pp. 73–84, 2014.

[12] S. W. Strauss, "The Temperature Dependence of the Viscosity of Liquid Metals," *Nuclear Science and Engineering*, vol. 12, no. 3, pp. 436–439, 1962.

[13] FlowScience, *Flow3D: Version 11.1: User Manual*. Santa Fe, NM, USA, 2015.

[14] X. Ding and L. Wang, "Heat transfer and fluid flow of molten pool during selective laser melting of AlSi10Mg powder: Simulation and experiment," *Journal of Manufacturing Processes*, vol. 26, pp. 280–289, Apr. 2017.

[15] S. A. Khairallah, A. T. Anderson, A. Rubenchik, and W. E. King, "Laser powder-bed fusion additive manufacturing: Physics of complex melt flow and formation mechanisms of pores, spatter, and denudation zones," *Acta Materialia*, vol. 108, pp. 36–45, 2016.

[16] Y. Liu, Y. Yang, S. Mai, D. Wang, and C. Song, "Investigation into spatter behavior during selective laser melting of AISI 316L stainless steel powder," *Materials and Design*, vol. 87, pp. 797–806, 2015.

[17] J. P. Kruth, G. Levy, F. Klocke, and T. H. C. Childs, "Consolidation phenomena in laser and powder-bed based layered manufacturing," *CIRP Annals - Manufacturing Technology*, vol. 56, no. 2, pp. 730–759, 2007.

[18] K. C. Mills, *Recommended values of thermophysical properties for selected commercial alloys*. Woodhead, 2002.

[19] Y. S. Lee and W. Zhang, "Modeling of heat transfer, fluid flow and solidification microstructure of nickel-base superalloy fabricated by laser powder bed fusion," *Additive Manufacturing*, vol. 12, pp. 178–188, 2016.

[20] S. W. Strauss, "The Temperature Dependence of the Viscosity of Liquid Metals," *Nuclear Science and Engineering*, vol. 12, no. 3, pp. 436–439, Mar. 1962.

[21] C. Costa, S. Delsante, G. Borzone, D. Zivkovic, and R. Novakovic, "Thermodynamic and surface properties of liquid Co–Cr–Ni alloys," *The Journal of Chemical Thermodynamics*, vol. 69, pp. 73–84, Feb. 2014.

[22] Cho, Jung-Ho, and Suck-Joo Na. "Implementation of real-time multiple

reflection and Fresnel absorption of laser beam in keyhole." *Journal of Physics D: Applied Physics* vol. 39, no. 24, pp. 5372, 2006.

[23] H. Takatani, C.-A. Gandin, and M. Rappaz, "EBSD characterisation and modelling of columnar dendritic grains growing in the presence of fluid flow," *Acta Materialia*, vol. 48, no. 3, pp. 675–688, Feb. 2000.

[24] A. Plotkowski, M. M. Kirka, and S. S. Babu, "Verification and validation of a rapid heat transfer calculation methodology for transient melt pool solidification conditions in powder bed metal additive manufacturing," *Additive Manufacturing*, vol. 18, pp. 256–268, Dec. 2017.

[25] S. Bontha, N. W. Klingbeil, P. A. Kobryn, and H. L. Fraser, "Effects of process variables and size-scale on solidification microstructure in beam-based fabrication of bulky 3D structures," *Materials Science and Engineering: A*, vol. 513–514, pp. 311–318, Jul. 2009.

Chapter 4
Effects of physical properties of powder layer on the fusion process

4.1. Introduction

The generation of a powder bed and the physical properties of the powder layer are the primary factors affecting the melting behavior during powder bed fusion (PBF)-based additive manufacturing. A thorough discussion of thermophysical properties of the powder layer depending on the characteristics of the powder bed (i.e., its spatial arrangement and particle size distribution) and their influences on fluid behavior, is still demanded to be clarified.

In this study, we investigated the characteristics of the powder bed (i.e., its spatial arrangement and PSD) with consideration of physical properties (i.e., emissivity and thermal conductivity) and their influences on the PBF-EB process using a numerical framework. A particle-based DEM model proposed by Cundall and Strack [1] was utilized to simulate the generation of the powder bed. To our knowledge, the effects of the powder characteristics such as the PSD and packing density on the processability for PBF-EB have not been investigated in depth before. The information obtained from the DEM simulation regarding the packing structure of the powder bed was the initial geometrical data for the CtFD simulations of the heat transfer and fluid behavior. The properties of the simulated powder bed and, in particular, the particle distribution pattern and morphology after melting were then compared to those observed experimentally for validation. The effects of the powder layer on the process stability and the melting behavior of the powder for different PSDs were also investigated. Moreover, the effect of powder shape on the melting behavior was revealed. The obtained results should serve as guidelines for PBF-EB-based AM in the future.

4.2. Simulations and experimental tests

In this work, DEM simulation was utilized to simulate the generation of the powder bed. The different characteristics of powder such as the particle size distribution and packing density determine the thermophysical properties of the powder bed, consequently the process stability and quality variation. Taking CCM alloy powder as an example (Fig. 4.1), there are two types of powder, namely, one fabricated by gas atomization (GA) and one fabricated by the plasma rotating electrode process (PREP). GA powder has a larger overall size than that of PREP powder. Thus, in this study, the powders with the ①**large size** (GA) and ②**small size** (PREP) were taken as the objects of study.

The information obtained from the DEM simulation regarding the packing structure of the powder bed was the initial geometrical data for the CtFD simulations of the heat transfer and fluid behavior. After the powder bed generation simulation, the single-track melting behavior of the simulated powder bed in response to a high-energy electron beam as a moving heat source was simulated by CtFD. Concerning the energy absorption in the powder bed, PBF-EB is free form the influence of surface morphology. As shown in Fig. 4.2, compared with PBF-L in which reflected heat flux depends on the deviation angle between the incident ray and surface normal, electron beam penetrates material without reflection so that the absorbed heat flux is the same for a plated and a curved surface of the particle. On the other hand, the heat transfer in the powder bed was realized by heat conduction through solid and heat radiation from particle surface (Fig. 4.3). The shape factor $S_{1\rightarrow2}$ that is the proportion of the radiation which leaves surface 1 and strikes surface 2 was automatically calculated according to the equation $S_{1\rightarrow2} = \frac{1}{A_1}\int_{A_1}\int_{A_2}\frac{\cos\theta_1\cos\theta_2}{\pi s^2}dA_2 dA_1$. An example of the single-track melting simulation is shown in Fig. 4.4, in which the colors are indicative of the temperature. There is a depression at the front, and the trailing end is lifted, implying that a backward fluid flow caused by the Marangoni effect resulted in the accumulation of the molten metal at the trailing end. For verification of simulation results, the PBF-EB melting experiments were performed on the building platform of an Arcam$^{®}$ EBM A2X AM machine, and the obtained results from the experiments were compared with

those of the simulations.

4.3. On the role of powder layer in stability of the molten pool

With powder layer, previous studies endeavored to figure out the relationship between process parameters and forming quality. However, the role of physical properties of powder layer on fusion behavior and process stability have not been clarified. For investigating the effect of the powder layer on the melt pool behavior and the resultant melt track profile, a series of single-track melting simulations were performed for two cases: with and without the powder (substrate only). Figure 4.5 shows the simulated melt tracks with and without the powder layer for three sets of process parameters. In these simulations, the powder was assigned the PSD of a small size powder. The colors of the melt tracks are indicative of the surface height. Depression is present in the front, and the trailing end is lifted owing to the Marangoni effect, which drives the fluid flow from the hot front of the molten pool towards the cold rear because of the temperature-dependent surface tension. Without the powder layer, the profile of the melt tracks was stable, with the surface being smooth for all three sets of process parameters (Fig. 4.5). On the other hand, with the powder layer present, the molten metal became unstable at relatively higher beam scan speeds. The melt track tended to break into segments under the following process parameters: $P = 600$ W and $V = 1500$ mm/s. Thus, the simulation results suggest that the degree of influence of the powder layer on the solidified profile of the melt tracks depends on the process parameters used.

The forming quality is closely related to the fluid behavior, and we expected to be able to avoid balling or separation of the melt track. The mechanism responsible for the formation of irregularities or disconnections in molten metal is the capillary effect resulting from the interplay between the surface tension and the wetting conditions, which depends on the local stochastic configuration of the powder [2]. The capillary action of the molten pool is a combination of the surface tension caused by cohesion

within the fluid and adhesion between the fluid and the surrounding solid phase. The wetting property of a fluid is its ability to maintain contact with a solid surface. For a smooth and horizontal surface, the wetting conditions remain constant, and consequently, the molten pool should be highly stable. Regarding melting on a powder layer, unlike melting on a solid base without a powder, nonuniform capillary action occurs longitudinally along the melt track because the wetting properties of the adjacent powder particles, which have an irregular distribution, determine the lateral spreading of the molten pool. Thus, given the stochastic nature of the powder layer, these irregularities can be correlated to the arrangement of the particles.

With an increase in the scan speed, the Plateau-Rayleigh instability [3] tends to become significant when the length-to-width ratio of the molten pool increases. Under these circumstances, if a disturbance were to occur in a fluid stream, the molten metal probably collapses into droplets under the action of the surface tension. Thus, when the powder layer was present, given its stochastic nature, the nonuniform capillary action caused disturbances along the melt track, leading to its separation or the formation of disconnections, with balling occurring at relatively higher scan speeds.

4.4. Thermophysical properties of powder bed

The stochastic nature of the powder bed mainly causes the thermal behavior to be different from that in the case of melting on the solid base without the powder. Figure 4.6 shows cross sections of the simulated molten pool of the single track shown in Fig. 4.5. The volume of the molten pool without the powder layer is larger than that with the powder layer; this is the case for all three sets of process parameters.

Above results indicate that the existence of the powder layer alters the conditions for energy transfer. The emissivity and thermal conductivity of the powder layer are critical parameters during the PBF-EB process. The emissivity of a material determines the amount of energy it emits through thermal radiation; this affects the effective energy absorbed by the material. The surface state of the powder bed is different from that of the solid base in the absence of the powder. Thus, evaluating the emissivity becomes

necessary for predicting melting efficiency. The effective heat absorbed by the powder bed surface, Q_{bed} (W/m²), which depends on the beam power, P, can be expressed by the following equation, which is on the basis of the Stefan–Boltzmann law:

$$Q_{bed} = \frac{\eta P}{\pi r^2} - \varepsilon_{bed} \sigma S (T_s^4 - T_a^4), \tag{4-1}$$

where η is the absorption efficiency, r is the radius of the electron beam (m), and ε_{bed} is the emissivity of the powder bed. Note that a powder bed with a single layer is not a complete powder packing box. Since the nominal powder layer thickness is close to the mean diameter of the powder particles, the particles do not fully cover the solid base with the horizontal movement of the powder rake. As shown in Fig. 4.7, energy from the electron beam is absorbed not only by the powder but also directly by the solid base of the substrate. Thus, ε_{bed} can be expressed as follows:

$$\varepsilon_{bed} = F_{powder} \varepsilon_{powder} + (1 - F_{powder}) \varepsilon_{plate}, \tag{4-2}$$

where F_{powder} is the area fraction of the projected plane of the powder in the direction of the electron beam. Further, ε_{powder} and ε_{plate} are the emissivities of the packed powder and bare plate (= ε_{solid}), respectively. The emission from the packed powder is assumed to be induced by the heated particles and the space between the particles [4]:

$$\varepsilon_{powder} = A_h \varepsilon_h + (1 - A_h) \varepsilon_{solid}, \tag{4-3}$$

where A_h is the area fraction of the surface that is occupied by the radiation-emitting holes. The emissivity of the holes, ε_h, is a function of the solid emissivity and the packing porosity, φ. They can be expressed as follows [5]:

$$A_h = \frac{0.908 \varphi^2}{1.908 \varphi^2 - 2\varphi + 1}, \qquad \varepsilon_h = \frac{\varepsilon_{solid} \left[2 + 3.082 \left(\frac{1-\varphi}{\varphi} \right)^2 \right]}{\varepsilon_{solid} \left[1 + 3.082 \left(\frac{1-\varphi}{\varphi} \right)^2 \right] + 1}. \tag{4-4}$$

As per the above expressions, ε_h should be larger than ε_{solid}. Hence, ε_{bed} would be larger than ε_{solid}. The variables involved and the simulation results for the surface temperature, T_s, are summarized in Tables 4-1 and 4-2, respectively. ε_{bed} was almost twice as large as ε_{solid}. Moreover, the mean value of T_s with a powder layer was larger than that without the powder; this may be a result of the low thermal conductivity

of the powder layer. For the same ambient temperature, T_a, the heat absorbed by the powder bed, Q_{bed}, was lower than the heat Q, absorbed by the solid base without the powder. In conclusion, the presence of the powder layer increased the emissivity of the material, resulting in a decrease in the absorbed heat flux and thus the volume of the molten pool.

4.5. Effect of powder size distribution (PSD) on the fusion process

PSD is another essential characteristic of the metal powder during AM. In this work, powder beds were generated during the DEM simulations using different PSDs under the same layer thickness (140 μm). The PSDs of ① **large-size** powder and ②**small-size** powder, and a half-and-half powder mixture of these two powders were used in the simulations (Fig. 4.1). The left side of Fig. 4.8 shows snapshots of the simulated powder beds with the three different PSDs. The corresponding porosity, φ, values are shown below the figures. The greater the fraction of small-size powder, the lower the φ value was. Since large-size powder has a larger overall particle size, the packing density in a constant volume should increase with an increase in the proportion of small-size powder. It is commonly accepted that when a sufficient number of particles are present to fill the gaps between the larger ones, the packing density will be high [6]. Simulating single-track melting with the same process parameters using CtFD resulted in different surface profiles for the different PSDs, as shown in the right side of Fig. 4.8. An irregular profile and concave–convex surface reliefs were observed for a high fraction of small-size powder.

As described previously, the forming quality is closely associated with the capillary action of the molten pool. The interactions between the rapidly formed molten pool and the surrounding particles/solid base determine the progression of the melt track. If the molten metal wets the substrate, the molten pool will spread horizontally and solidify with a relatively smoother surface. Conversely, when the molten metal encounters a particle, the melting of adjacent particles and the limited thermal conduction in the

horizontal direction suppress the horizontal spreading of the molten pool to a great extent. The surface tension then pulls the molten particles into the molten pool, thus increasing the probability of melt humping. In the case of a powder bed composed of a significant fraction of small-size powder with a high packing density, the horizontal wetting of the melt on the substrate would be significantly restricted.

As discussed in Section 4.4, the presence of the powder layer affects the thermal behavior during the melting process. The equation for the thermal conductivity of powder beds has been given in the literature [4][7]; this equation contains a term related to thermal conduction by radiative heat transfer, κ_r. In the case of the high vacuum in the building chamber of the PBF-EB system, the thermal conductivity of the continuous gas phase is assumed to approach zero. Thus, κ_{bed} should also consist of components related to the solid base and packed powder (Fig. 4.7). Hence, the equation for thermal conductivity used in this study was the following:

$$\kappa_{bed} = F_{powder}\left\{\left(1 - \sqrt{1 - \varphi}\right)\varphi\kappa_r + \sqrt{1 - \varphi}\left[(1 - \Lambda)\kappa_r + \phi\kappa_s\right]\right\}$$
$$+ \left(1 - F_{powder}\right)\kappa_s, \tag{4-5}$$

where Λ is the fractional contact area of solid-solid contact, κ_s is the thermal conductivity of the solid material, and ϕ is the Juttner modulus for the first-order irreversible chemical reaction. Further, κ_r is the thermal conductivity component of the powder bed caused by the radiation and is given by the Wakao–Kato expression [7]:

$$\kappa_r = \frac{4\varepsilon_{powder}\sigma T_s^3 X_r}{1 - 0.132\varepsilon_{powder}}, \tag{4-6}$$

where X_r is the effective length for radiation between the particles or the diameter of the powder particles. From Eqs. (4-3) and (4-5), it can be concluded that different PSDs with variable packing densities (1- φ) result in different emissivity (ε_{bed}) and thermal conductivity (κ_{bed}) values. As can be seen from the calculated results in Table 4-3, ε_{bed} increased, and κ_{bed} decreased with an increase in the fraction of small-size powder. Thus, owing to the increased emissivity of the powder bed, ε_{bed}, the energy absorbed from the electron beam became insufficient to melt the surrounding particles completely. Further, the decreased thermal conductivity of the powder bed, κ_{bed},

hampered the lateral heat transfer in the molten pool. Both effects limited the horizontal spreading of the molten pool and increased the instability of the melt track when a large fraction of small-size powder was used. Thus, it can be concluded that a relatively greater amount of input energy is needed to melt the small-size powder layer. The experimentally determined surface profiles for large-size and small-size powders after single-track melting shown in Fig. 4.9 were similar to those obtained from the simulations. It can be also seen clearly in that, under high-power conditions, the surface quality of the melting track of small-size powder improves, as expected.

C. Körner et al. [2] investigated the consolidation mechanisms of powder particles during the PBF-EB process using simulations. They claimed that a lower powder packing density results in a less stable molten pool and higher porosity. This conclusion seems to be based on their numerical model, in which the emissivity of the packed powder was not considered, and the melting process was simulated for a 2D layer of the packed powder without considering the surrounding substrate, especially in the horizontal direction. However, it needs to be emphasized that, during PBF-EB processes, the powder bed consists of not only the powder particles but also the part of the solid base of the substrate that is not covered by the powder. The effect of the substrate below the powder bed on the melting behavior should be considered when determining the effects of the powder bed properties such as the layer thickness and PSD, among others, on the forming quality.

In summary, for powders with different PSDs and packing densities, the differences in the capillary-driven motion and thermal transfer characteristics on the powder bed lead to variations in the melting behavior and the resultant profile of the melt tracks. In addition, the use of powders with different PSDs and packing densities may be necessary for tuning the process parameters in order to ensure exceptional forming quality.

4.6. Effect of powder shape on the fusion process

Above results indicated the essential influence of heat radiation on the fusion process

of the powder bed. To investigate the role that emissivity of powder layer plays in the interaction between the electron beam and powder bed. The simulation cases with and without heat radiation were created and compared with each other. As shown in Fig. 4.10, it clearly shows that if heat radiation is eliminated, a relatively smooth melt-track can be obtained, which illustrates the importance of heat radiation.

Different powder types with different surface conditions would possess variation in heat radiation. So next, the effect of powder shape on the fusion process in PBF-EB should be investigated. The IN718 alloy powder was selected for performing simulations and single-track melting experiments. There are two types of IN718 alloy powders, namely, one fabricated by gas atomization (GA) and one fabricated by the plasma-rotating electrode process (PREP). Gas atomization during which the molten steel is atomized thanks to inert gas jets into fine metal droplets which cool down during their fall in the atomizing tower, is the most significant and the most common approach of powder production. Plasma-rotating electrode process is a centrifugal atomization process developed by Starmet in which plasma arc is utilized, and this approach is currently a leading candidate for powder production applying to AM [8]. In PREP production, the metallic powder is produced by melting of the end of a metal bar using an electric arc or plasma. Owing to the metal bar rotating about its longitudinal axis, molten metal is centrifugally ejected, which results in fine droplets that are then collected as solidified powders. The geometrical characteristics of the two powders are significantly different. As shown in Fig. 4.11, concerning GA powder, there are a significant fraction of powder particles featured satellites, irregularly shaped particle. By contrast, concerning PREP powder, almost all the particles are spherical, and the circularity of the particles is significantly higher than that of GA powder. Being different from the CCM alloy powder, the two types of IN718 powders possess almost consistent PSD. Thus, in this study, the two types of IN718 alloy powders without interference from PSD were applied to investigate the effect of powder shape on the fusion process.

In DEM numerical simulation, to model the dynamics of non-spherical powder with satellite particles attaching, particle clumping method [9] by which rigid aggregate of

individual particles can be created was applied. Particles within the rigid aggregation can overlap if interforce was released before the simulation starts [10]. Additionally, DEM simulation supports to satisfy the roundness of a clump or roundness coefficient of a packing. In this study, the circularity of powder in 2D SEM images was taken to approximate the roundness (Fig. 4.12). As shown in Fig. 4.13, by using the four types of predefined particle clumping and adjustment of their fraction for circularity matching with the experimental circularity of GA powder of IN718 in DEM simulation, GA powder can be created and possesses the same PSD with that of PREP powder.

The spherical and non-spherical powders should possess different surface area even with the same volume; thus, the amount of heat radiation would be different. Seen from the simulation results of the single-track melting of PREP and GA powders in Fig. 4.14, a more uneven surface profile of melt track can be observed for GA power, compared with that for PREP powder under the same process condition. The relative packing density and surface area of powder layers with different types of powder are shown in Table 4-4. We can see, as with the large fraction of fine satellite particles, GA powder layer possesses higher packing density than PREP powder layer, meanwhile, the surface area is large in the GA powder layer. As a result, a high emissivity of GA powder layer due to a large total surface area decreased the energy absorption from the incident electron beam. The insufficient melting and wetting of molten metal and base plate promoted the molten pool instability and made the surface profile to be uneven.

The experimentally determined surface profiles for PREP and GA powders of IN718 after single-track melting is shown in Fig. 4.15 were similar to those obtained from the simulations. It can be concluded that the powder shape can influence the energy absorption because heat radiation is significantly determined by the surface area of the powder layer.

Conclusions

In this work, the dynamic behaviors of a powder collection during the powder raking process was simulated using DEM modeling. In addition, CtFD simulations of the heat

transfer and fluid flow processes were also performed to elucidate the fusion of the powder bed during the PBF-EB process. The main conclusions derived from this study can be summarized as follows:

1) Powder layer, with its stochastic nature, provided more fluid disturbance caused by non-uniform capillary actions, efficiently producing the irregularity or disconnection of melt-track with increasing scan speed.

2) Concerning the particle size, for the powder bed with small-size powder, the increased emissivity and decreased thermal conductivity of the powder bed induced the instability of the melt track.

3) The spherical and non-spherical powders possessed different surface features; thus, the amount of heat radiation was different. PREP powder with high circularity and small surface area was appropriate for PBF-EB, which was favorable for molten pool stability and could enlarge the process window.

Table 4-1 Calculated ε_{bed} and involved variables of the powder bed.

Variables	ε_{bed}	$\varepsilon_{\text{bare plate}}$	$\varepsilon_{\text{powder}}$	ε_{h}	F_{powder}	A_{h}	φ
Value	0.42 W/m²	0.25 W/m²	0.43 W/m²	0.48 W/m²	0.93	0.78	0.664

Table 4-2 Simulated results of surface temperature T_{s}.

Process condition	w/o powder layer	w/ powder layer
P=600 W, V=300 mm/s	1191 K	1272 K
P=600 W, V=1000 mm/s	1148 K	1159 K
P=600 W, V=1500 mm/s	1139 K	1144 K

Table 4-3 Calculated κ_{bed}, ε_{bed} of powder bed with different powders.

	κ_{bed}	ε_{bed}
Large-size powder	14.83 W/m·K	0.33 W/m²
Half-and-half mixture	10.24 W/m·K	0.37 W/m²
Small-size powder	2.30 W/m·K	0.42 W/m²

Table 4-4 Relative packing density and surface area of powder layers with different types of IN718 alloy powder.

	Packing density	Surface area (cm²)
PREP	0.3084	38.3285
GA	0.3507	46.8526

① Large size   ② Small size

(a) GA-powder   (b) PREP-powder

300 μm   300 μm

Fig. 4.1. SEM images of two types of CCM alloy powder samples: one produced by (a) gas atomization (GA) and one produced by (b) plasma rotating electrode process (PREP), possessing large and small overall size respectively. (c) Particle size distributions (PSDs) of the two samples measured by the laser diffraction method.

Fig. 4.2. Schematics showing the energy absorption in (a) PBF-EB and (b) PBF-L. Compared with (b) PBF-L in which reflected heat flux depends on the deviation angle between the incident ray and surface normal, electron beam penetrates material without reflection so that energy absorption in (a) PBF-EB is free from the influence of surface morphology.
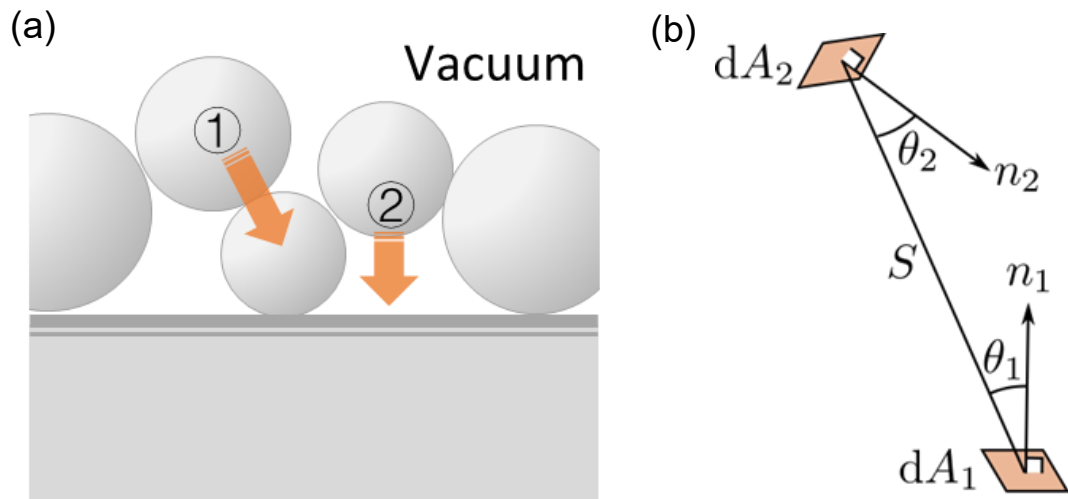
Fig. 4.3. (a) Schematic showing the heat transfer in the powder bed through ① heat conduction and ② heat radiation which takes account of the (b) shape factor of two differential areas..
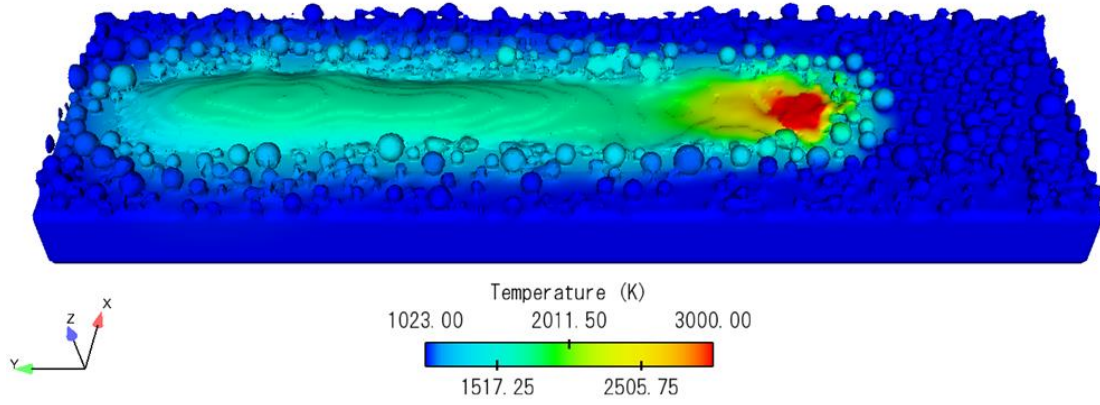
Fig. 4.4. Snapshot of an example of CtFD simulation of single-track melting in the case of power $P = 600$ W, scanning velocity $V = 300$ mm/s.
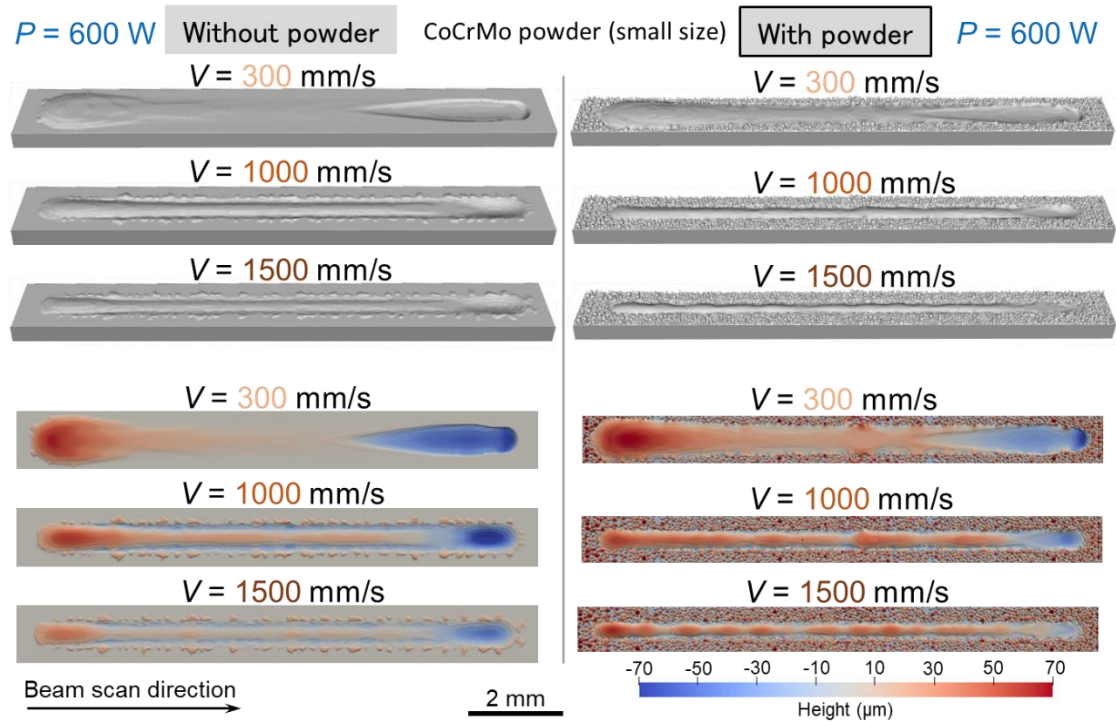
Fig. 4.5. Simulated melt tracks without and with powder layer for three sets of process parameters. In the lower side, the colors of the melt tracks are indicative of the surface height.
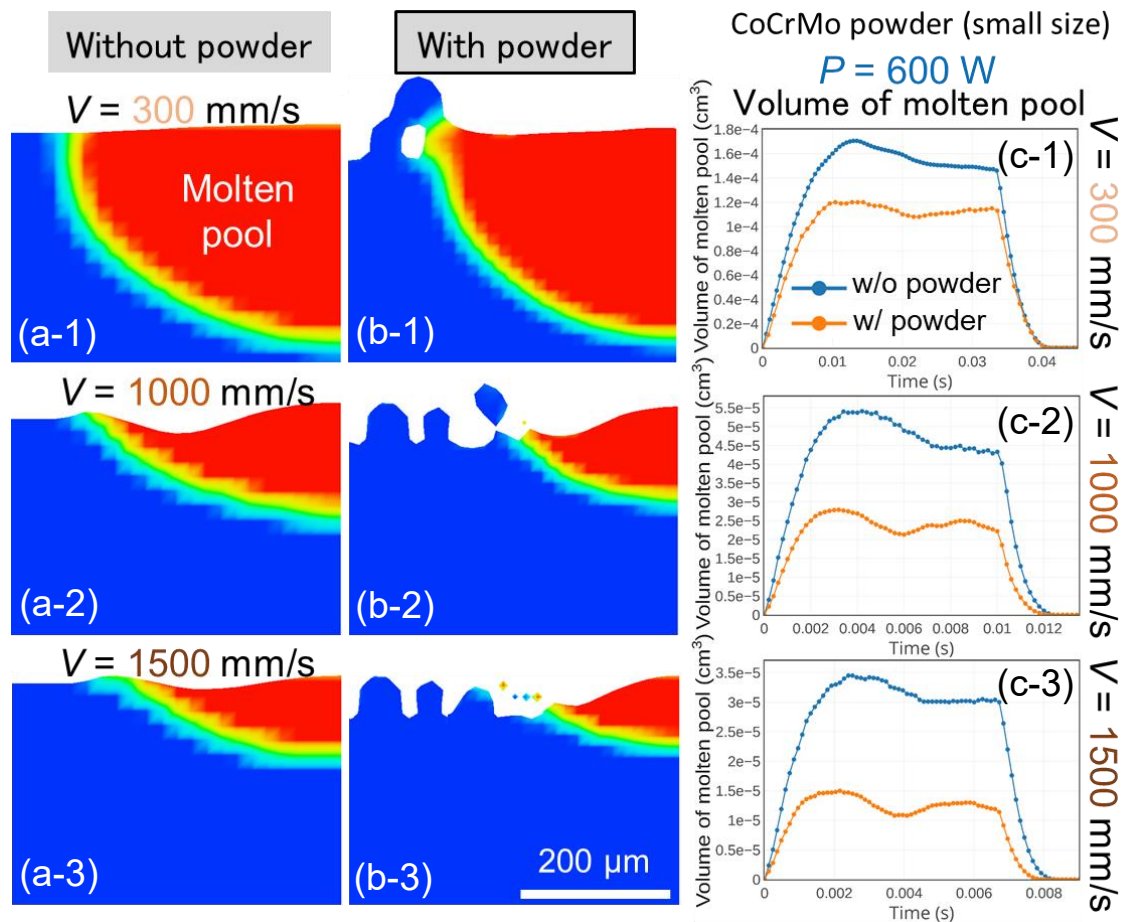
Fig. 4.6. Cross sections of the simulated molten pool of the single track (a) without and (b) with powder layer. (c) Evolution of molten pool volume during the melting process. Process parameters from top to bottom: $P = 600$ W and (a-1)(b-1)(c-1) $V = 300$ mm/s, (a-2)(b-2)(c-2) $V = 1000$ mm/s, (a-3)(b-3)(c-3) $V = 1500$ mm/s.
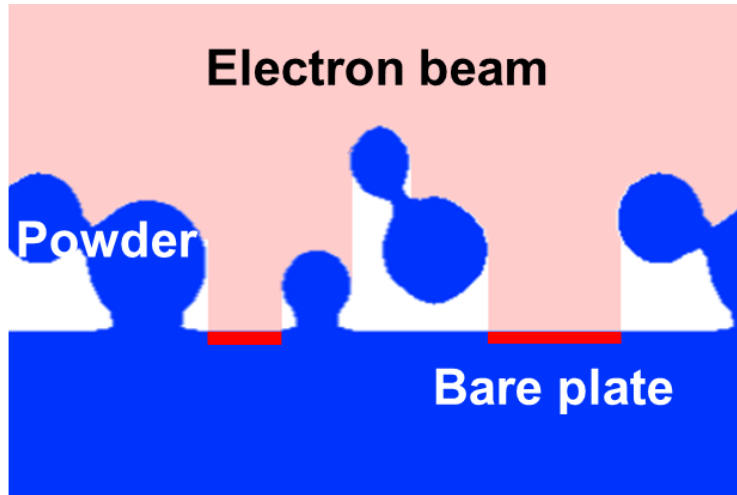
Fig. 4.7. The schematic show that energy from the electron beam is absorbed not only by the powder but also directly by the bare plate without powder (depicted as the red line).
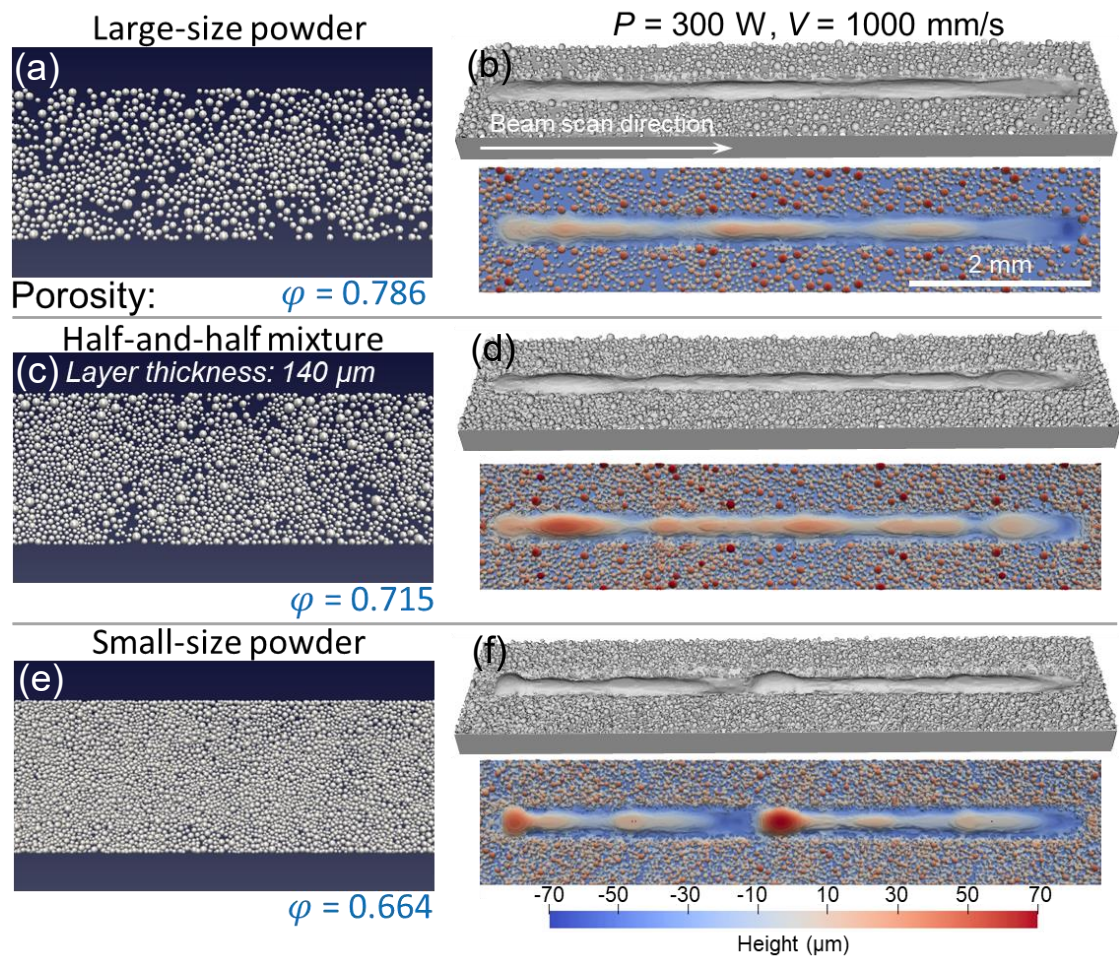
Fig. 4.8. Snapshots of the simulated powder beds with the three different PSDs: (a) large-size powder; (c) a half-and-half powder mixture; (e) small-size powder. The corresponding porosity, φ, values are shown below the figures. Simulating single-track melting under the process parameters: $P = 300$ W, $V = 1000$ mm/s, resulted in different surface profiles for the different PSDs. The melt tracks are colored as the surface height. Powder types from top to bottom: (b) large-size powder; (d) a half-and-half powder mixture; (f) small-size powder.
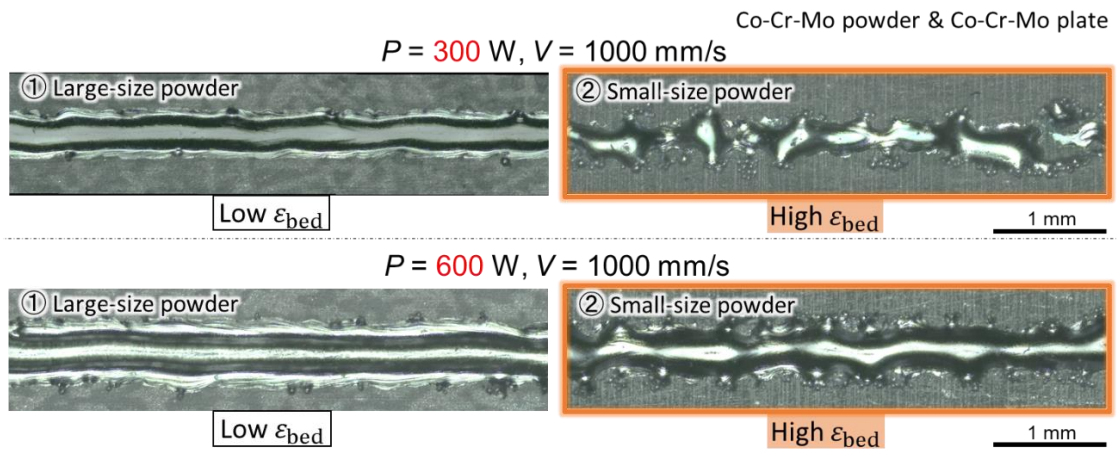
Fig. 4.9. Experimentally determined surface profiles for large-size powder and small-size powders after single-track melting under the process parameters: P = 300 W, V = 1000 mm/s and P = 600 W, V = 1000 mm/s.

CoCrMo powder (small size): *P* = 300 W, *V* = 1000 mm/s

Height (μm)
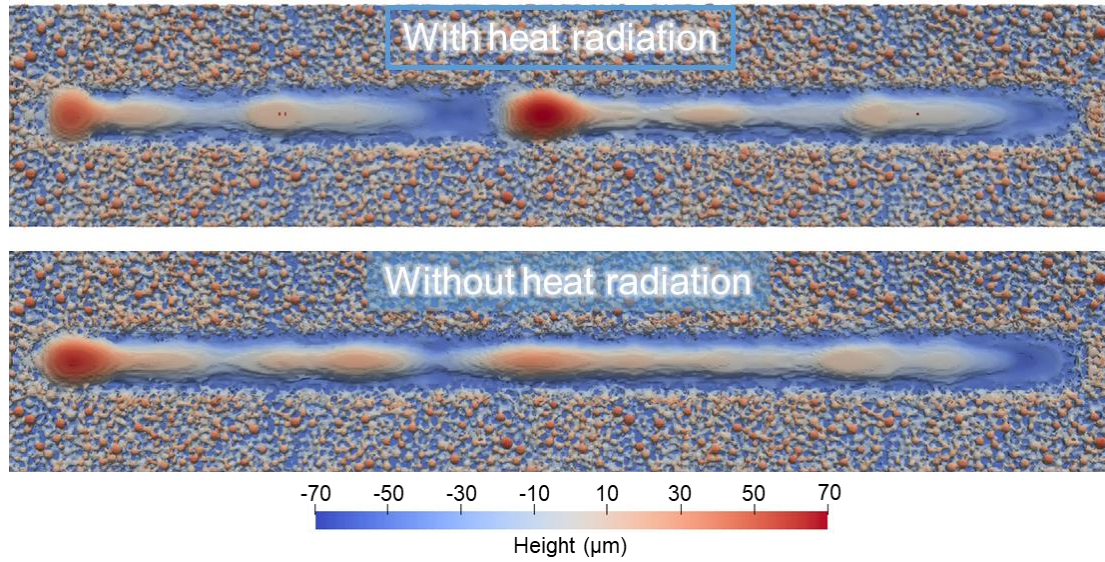
Fig. 4.10. Simulated surface profile on single-track melting of CCM powder in the cases of with and without heat radiation. Process parameter: $P = 300$ W, $V = 1000$ mm/s.

(a) GA-powder

(b) PREP-powder

(c)
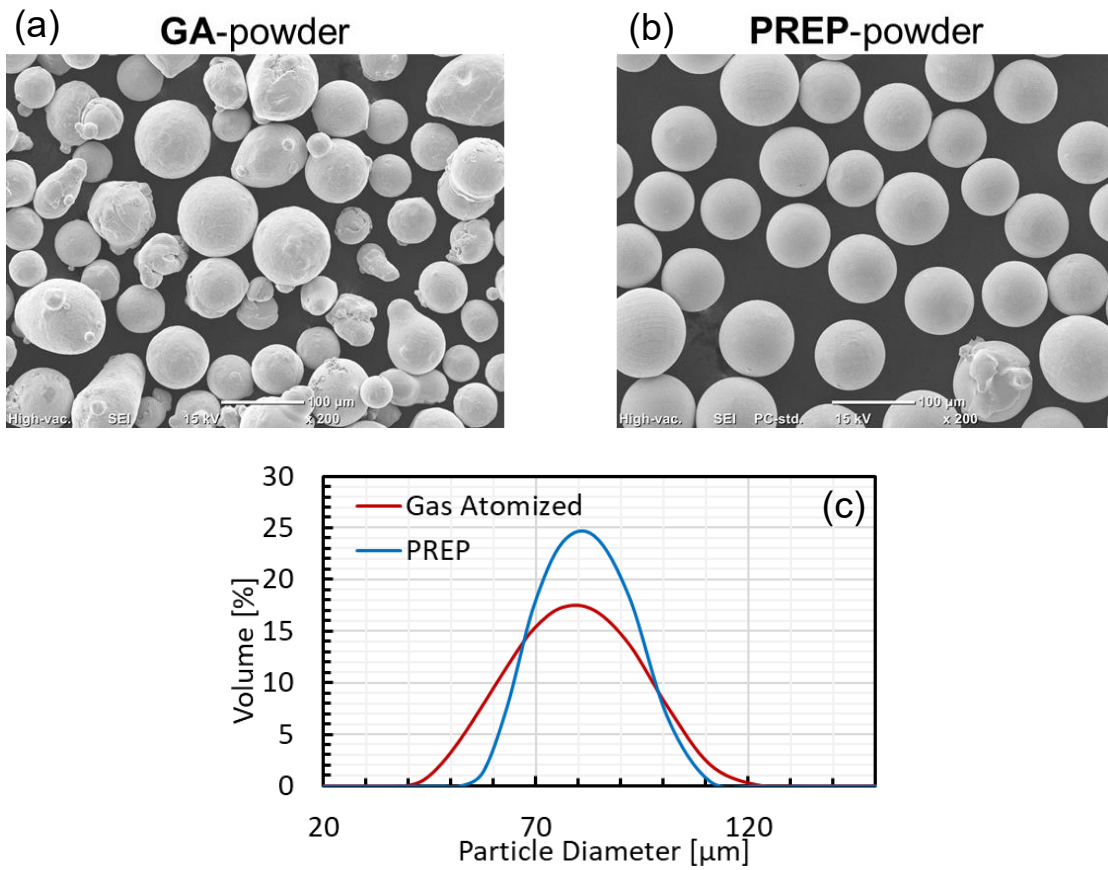
Fig. 4.11. SEM images of two types of IN718 alloy powder samples: one produced by (a) gas atomization (GA) and one produced by (b) plasma rotating electrode process (PREP), possessing almost consistent PSD. (c) PSD of the two samples measured by the laser diffraction method.

$$Circularity =$$

$$\frac{Circle\ circumference}{Perimeter\ of\ projected\ particle\ image} = \frac{2\sqrt{\pi A_\text{p}}}{P_\text{p}}$$

■ Area of the particle A_p

↔ Diameter of circle with the same area

— Perimeter of the particle P_p

○ Circle with the same area as particle
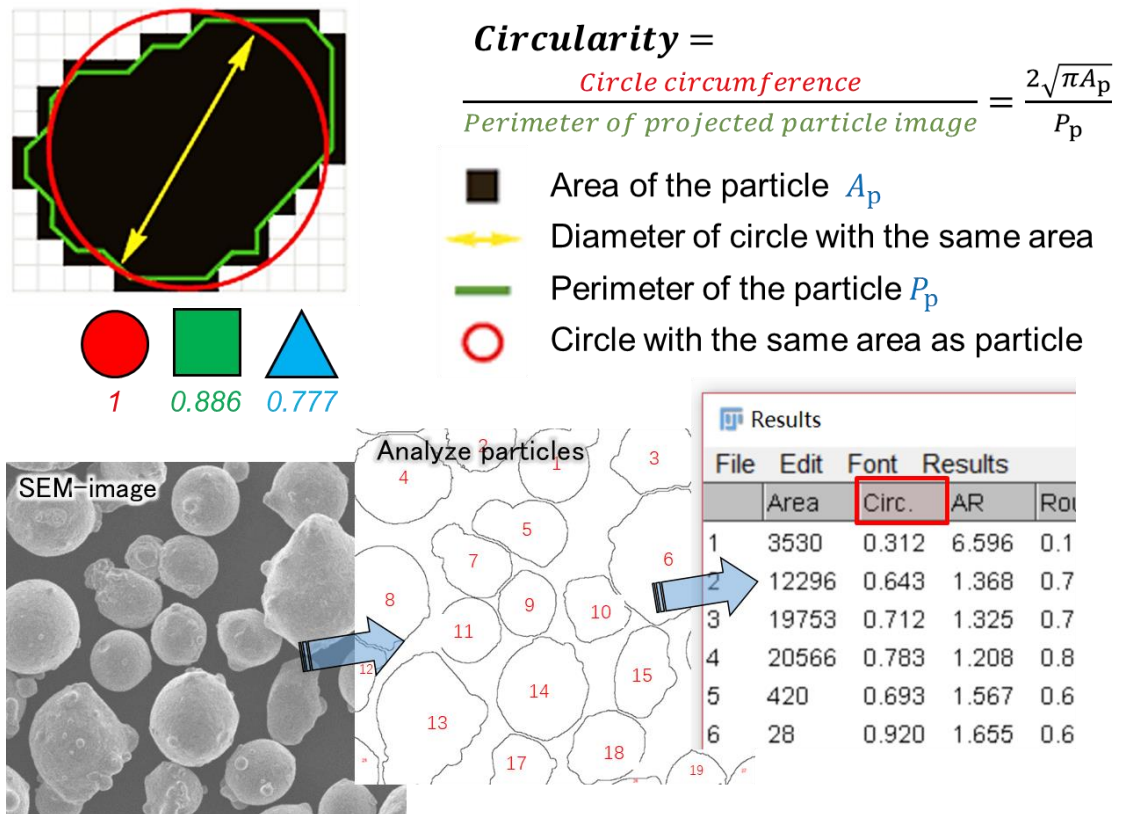
Fig. 4.12. Schematic illustration of powder circularity measurement by Image J depending on SEM images of powder.

Four types of predefined powder clumping in DEM

A
5%

B
15%

C
25%

D
20%

(b) PREP-powder
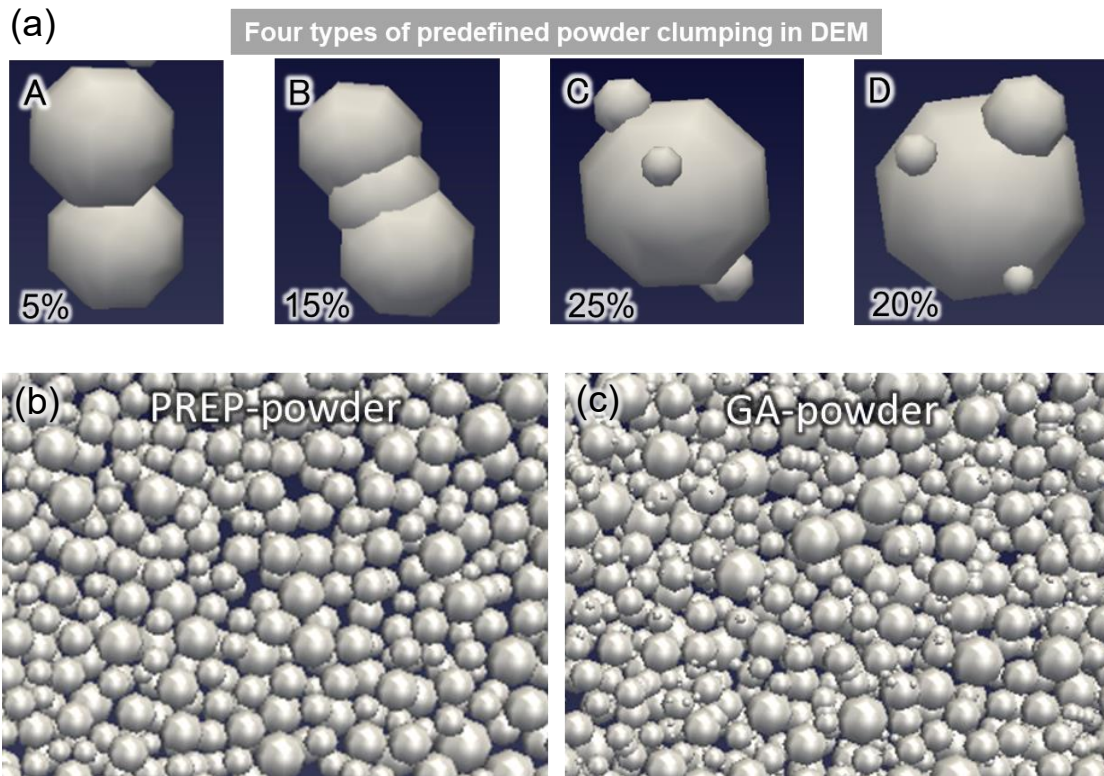
(c) GA-powder

Fig. 4.13. By using the (a) four types of predefined particle clumping and adjustment of their fraction for circularity matching with experimental one in DEM simulation,(c) GA powder can be created and possesses the same PSD with that of (b) PREP powder.

Inconel 718: P = 300 W, V = 1000 mm/s

PREP-powder

GA-powder

1 mm

-175 -125 -75 -25 25 75 125 175
Height (μm)
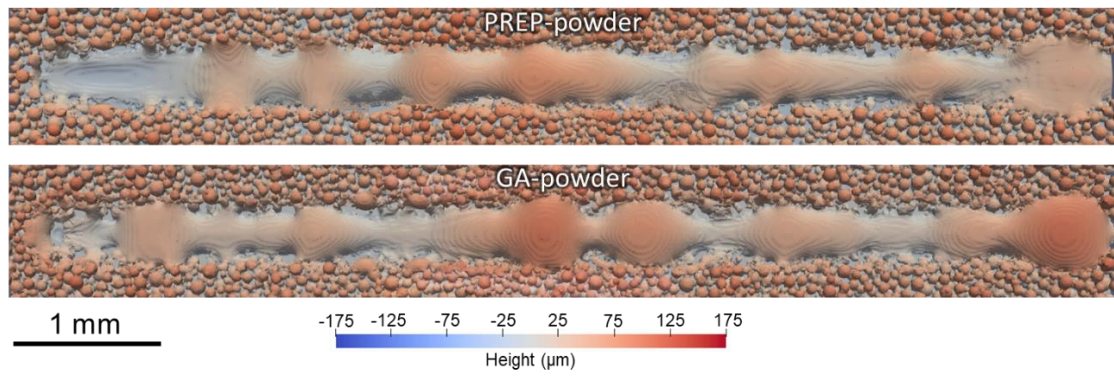
Fig. 4.14. Simulation results of single-track melting of PREP and GA IN718 alloy powder. Process parameter: P = 300 W, V = 1000 mm/s.
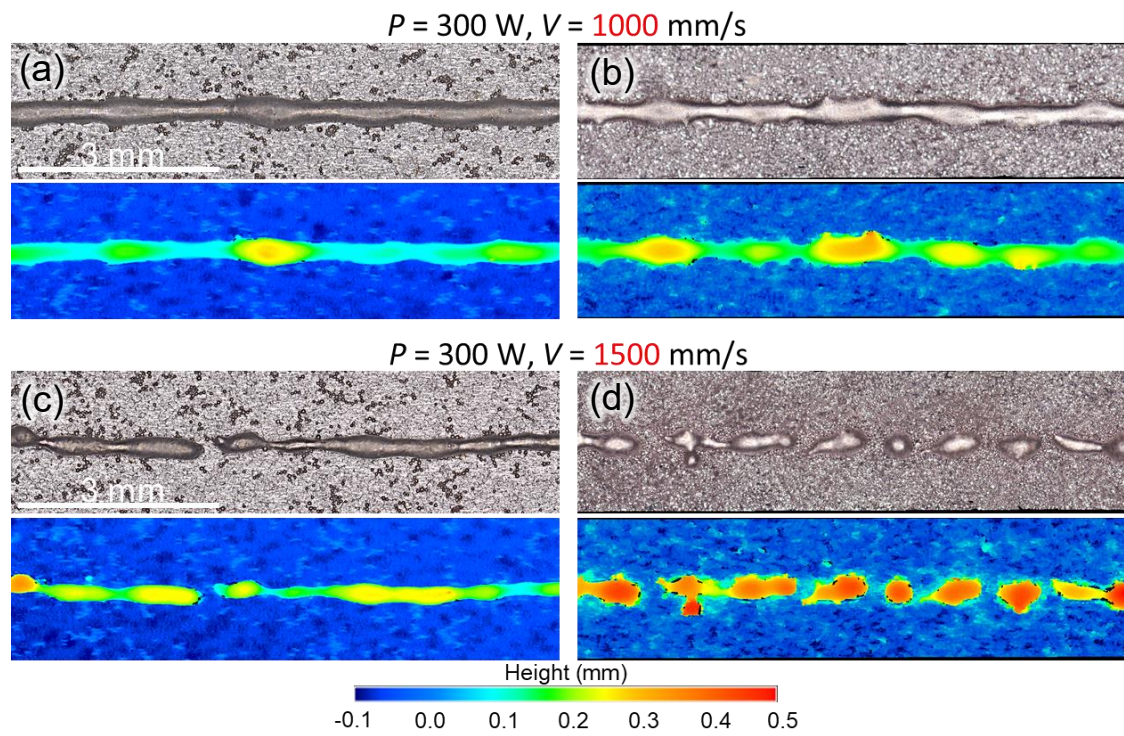
Fig. 4.15. Experimentally determined surface profiles for (a)(c) PREP and (b)(d) GA powders of IN718 after single-track melting under two sets of process conditions.

References

[1] P. Cundall, O. S.- geotechnique, and undefined 1979, "A discrete numerical model for granular assemblies," *websrv.cs.umt.edu*.

[2] C. Körner, A. Bauereiß, and E. Attar, "Fundamental consolidation mechanisms during selective beam melting of powders," *Modelling and Simulation in Materials Science and Engineering*, vol. 21, no. 8, p. 085011, Dec. 2013.

[3] J. P. Kruth, G. Levy, F. Klocke, and T. H. C. Childs, "Consolidation phenomena in laser and powder-bed based layered manufacturing," *CIRP Annals - Manufacturing Technology*, vol. 56, no. 2, pp. 730–759, 2007.

[4] S. S. Sih and J. W. Barlow, "The Prediction of the Thermal Conductivity of Powders," *Proceedings of the Solid Freeform Fabrication Symposium*, vol. 22, no. 2, pp. 397–401, Jul. 1994.

[5] S. S. Sih and J. W. Barlow, "EMISSIVITY OF POWDER BEDS."

[6] K. Rietema, *The Dynamics of Fine Powders*. Dordrecht: Springer Netherlands, 1991.

[7] N. Wakao and S. Kagei, *Heat and mass transfer in packed beds*, 1st ed. New York: Gordon and Breach Science Publishers, 1982.

[8] C. Zhong, J. Chen, S. Linnenbrink, A. Gasser, S. Sui, and R. Poprawe, "A comparative study of Inconel 718 formed by High Deposition Rate Laser Metal Deposition with GA powder and PREP powder," *Materials & Design*, vol. 107, pp. 386–392, Oct. 2016.

[9] E. J. R. Parteli, "DEM simulation of particles of complex shapes using the multisphere method: Application for additive manufacturing," in *AIP Conference Proceedings*, 2013, vol. 1542, no. 1, pp. 185–188.

[10] V. Šmilauer, E. Catalano, B. Chareyre, S. Dorofeenko, J. Duriez, N. Dyck, J. Eliáš, B. Er, A. Eulitz, A. Gladky, N. Guo, C. Jakob, F. Kneib, J. Kozicki, D. Marzougui, R. Maurin, C. Modenese, L. Scholtès, L. Sibille, J. Stránský, T. Sweijen, K. Thoeni, and C. Yuan, "Yade Documentation." .

Chapter 5

Mechanisms for grain morphology evolution and texture development of PBF-EB-built Co-Cr-Mo alloy

5.1. Introduction

Grain morphology, size, and growth direction are crucial in determining the performances of PBF-EB-built components. The solidification process in powder bed AM tends to be dominated by epitaxial grain growth [1][2]. In PBF-EB, alloys with cubic crystal tend to solidify epitaxially, efficiently producing columnar grains with {001} texture oriented along the building direction due to the overall heat flow [3][4]. The anisotropy of the parts composed of columnar grains is detrimental for practical applications involving multiaxial stress [5][6]. Misoriented fine grains are sometimes necessary to meet specific performance requirements; for example, tailor-made artificial hip joints must possess stem parts with low Young's moduli and strong neck parts. These two features correspond to epitaxially columnar and misoriented polycrystalline structures, respectively. Thus, understanding the effects of the manufacturing characteristics PBF-EB, an additive manufacturing process, on microstructure formation and anisotropy development during solidification is essential to achieve flexible microstructure control. As discussed in Chapter 1, researchers have demonstrated the possibility of tailoring grain structures by modifying the molten pool geometry, the motion of the molten metal, and spatial-temporal variation of the thermal gradient and solidification rate during AM. However, the mechanisms of grain morphology evolution and texture formation have not been sufficiently clarified for PBF-EB-built alloy with different process parameters. The choice of optimum strategies to produce a required microstructure with the targeted alloy performance still requires exploration without extensive trial-and-error experimentation.

In this study, the grain morphology and crystallographic texture development with

systematically varied PBF-EB parameters were analyzed by experimental characterization with the aid of computational thermal–fluid dynamics (CtFD) simulations. The CtFD simulations accounted for the transient heat transfer and fluid flow, as well as the temperature gradient (G) and solidification rate (R) at the solidification front [7][8][9]. As in-situ monitoring and direct measurement of molten pool geometry and thermal fields are difficult, systematic and quantitative simulations are useful for studying the fundamental mechanisms responsible for different solidification structures. Through experimental characterization of the microstructure and analysis of the simulation results, the solidification and grain growth mechanisms were preliminarily studied. Especially, the limitations of microstructure control depending on *G-R* were elucidated and the effect of fluid flow on grain morphology was revealed. In addition, a method for promoting CET in solidification microstructure was proposed.

5.2. Methodology

5.2.1. PBF-EB processing

Cube-shaped samples with dimensions of 10 mm ×10 mm ×10 mm were fabricated using an Arcam®A2X. Gas-atomized Co-28Cr-6Mo alloy powder (size ranging from 45 to 150 μm with mean diameter: 65 μm) was applied with a layer thickness of 70 μm. The alloy powder was supplied by Sanyo Special Steel Co., Ltd. In Arcam systems, electrons are emitted from a hot tungsten filament or a lanthanum hexaboride LaB_6 cathode and then are accelerated to 60 keV. The beam is focused and deflected by the electromagnetic lenses. The power is exerted by beam current that varies between 1 and 50 mA, generating a maximum beam power of about 3 kW [10]. The electron beam power (P) and scan speed (V) were varied in relatively extensive ranges of 100–1000 W and 100–10000 mm/s, respectively, which is determined from our prior experience of processability for CCM. The line offset (l_{off}) was determined based on pre-implemented single-track melting experiments, depending on the dimensions of the cross-section of the melt region. For dense formations, the line offsets were adjusted so

that the overlap between adjacent melt tracks would be more than 1.5 times the layer thickness. The resulting line energy ($E_{\text{line}} = P/V$) ranged from 0.1 J/mm to 10 J/mm, and the area energy ($E_{\text{area}} = P/(V \cdot l_{\text{off}})$) ranged from 2.2 J/mm^2 to 11 J/mm^2. The preheating temperature was set at 850 °C to avoid powder smoke in which if repulsive electrostatic forces are greater than the forces holding particles, particles may be ejected from the layer. As depicted in Fig. 5.1, an xy-scanning strategy in which the bidirectional scanning direction was rotated by 90° in each layer was applied for the building process. The building direction was defined as being along the z-axis, and the beam scan directions were defined as being along the x- and y-axes.

5.2.2. Experimental microstructure characterization

The grain morphology and crystallographic texture were observed with various P, V, and l_{off}. The samples were cut along the building direction (z-axis), and the cross-sections were ground and polished by standard metallographic techniques. The microstructural observations were made at the same height at which the samples were built, i.e., 500 μm below the top surface and near the center of the width. The grain structure was analyzed by scanning electron microscopy based on the backscattered electron (BSE) signals at the polished sample surface. Scanning Electron Microscopy-Electron Backscattering Diffraction (SEM-EBSD) measurements were performed to analyze the grain orientation and texture. The grain size was characterized by the average intercept length (L_{avg}) calculated using the linear intercept method. The horizontal intercept lines were perpendicular to the building direction. The number of horizontal lines was the number of rows in the EBSD scan divided by 3. The grain shape was described by the aspect ratio determined by fitting an ellipse to the points making up a grain, and the aspect ratio was defined as the length of the minor axis divided by that of the major axis and thus ranged from 0 to 1. The grain morphology of each individual sample was represented by the average aspect ratio $\left(A_{\text{avg}}\right): \sum_{i=1}^{i=n} A_i \times F_i$, where A_i is the aspect ratio of grain i and F_i is the area fraction of grain i in the observation field.

5.2.3. Numerical simulation

CtFD is a means of computationally solving the equations governing thermal–fluid dynamics, including the conservations of mass, momentum and energy equations. Further details are available in the literature [11]. In addition to the molten pool geometry and fluid motion, the simulated temperature field was used to calculate the spatiotemporal values of G and R from each mesh at the solidification front in the computation domain. The 3-dimension modeling was developed using Flow 3D®, a commercial CtFD program [12]. In the model, the buoyancy effect was inherently considered by introducing a temperature-dependent density. Moreover, the surface force terms contained three factors (capillary force, Marangoni force, and vapor recoil pressure), and they were incorporated into the model. The energy from the electron beam was approximated as a Gaussian surface heat source, and the energy efficiency was assumed to be 90% [13]. Besides the heat loss through conduction, radiation and evaporative cooling were also introduced. Cooling through air convection was neglected because of the high vacuum (0.1 Pa) in the PBF-EB chamber. Detailed descriptions of the physics of the model, physical properties of the material, parameters/coefficients applied in the simulation, and modeling validation are available in [14].

5.3. Mechanism for crystal growth during the layer-by-layer process

In a molten pool, the direction of the temperature gradient is consistent with the direction normal to the solidification front [15]. Considering that the S/L interface moves in the opposite direction compared to the heat flux, the cells/dendrites would be expected to solidify and grow in the radial direction of a molten pool. However, the ideal arrangement of grains in the radial direction has seldom been observed in practice, which suggests that the crystal growth is governed by not only the thermal gradient but also some other factors. According to the above results, the samples with columnar grains had firm textures in the building direction, due to the epitaxial crystal growth

and overall heat flow parallel to the building direction [16]. The crystal growth during the layer-by-layer process with the *xy*-scanning strategy can be seen clearly in Fig. 5.2. The IPF map and pole figures of one-layer melting (Figs. 5.2(d) and (e)) were obtained to refer to the grain structure of the first layer built by PBF-EB. In the first layer, grains with arbitrary orientations grow almost perpendicularly to the molten pool boundary, since the original grains in the polycrystalline base plate are oriented randomly. After grains grow over the layers, the grains become coarse and align mainly with the building direction in the top part of the building block (Figs. 5.2(b) and (c)). Moreover, in addition to the primary orientation along the building direction, an intense concentration of <001> was found in the *x*- and *y*-scanning directions. This feature is similar to that reported for AM-built materials with cubic structures [21][17].

Along with the building process, the grain selection in the specific scan strategy affects the microstructure development. In the schematic diagram shown in Fig. 5.3(a), the single-track melt region is assumed to be a semi-circular cylinder. The directions of the temperature gradient and cell growth are indicated by the red and gray arrows, respectively. The direction of the temperature gradient varies layer by layer: it is parallel to the *yz*-plane in the layer with *x*-scanning and the *xz*-plane in the layer with *y*-scanning. It is worth noting that grain growth is inherently competitive. Competitive growth among different structures, including phases, dendrites, and grains, is common in microstructure evolution [18]. The growth of grains with the <001> orientation, which is mostly consistent with the direction of maximum heat extraction (the reverse of the temperature gradient), is significantly favored in this case. Some other grains must stop growing after encountering grains that are growing in more favorable heat extraction directions, depending on the angle between the directions of the grain growth and temperature gradient. Thus, with the competitive growth in the layer-by-layer process, the preferred <001> orientation tends to be limited in the *yz*- and *xz*-planes because of the *x*- and *y*-scans, respectively, due to the conditional temperature gradient, as shown in Fig. 5.3(b). Fewer grains with constrained crystallographic orientations can survive for further growth, and the <001> alignment develops not only along the *z*-axis but also along the *x*- and *y*-axes, indicating that the bidirectional scan with 90° rotation between

successive layers could enhance the texture substantially. Consequently, *xy*-scanning leads to relatively coarse columnar grains typically with near-cubic texture within the CCM sample. These results indicate that the growth behavior of the columnar cells is determined by the competitive epitaxial grain growth governed by the heat flow characteristics when *xy*-scanning is employed.

5.4. Crystallographic texture evolution in samples with columnar grains

Generally, strong <001> alignments along the *x*-, *y*-, and *z*-axes develop when *xy*-scanning is employed. The near-cubic texture is common in AM [19]and is generally favored under bidirectional *xy*-scanning strategy [20][21]. However, in some particular samples that also contained columnar grains, the crystallographic texture was not single-crystal-like.

Figure. 5.4 presents crystallographic orientation maps that were acquired with two different sets of process parameters. The crystallographic orientation is indicated along the normal direction (scan direction) and building direction for each sample with corresponding pole figures. Although the grain aspect ratio and average intercept length are similar for the two cases, their texture features are different. Typical single-crystal-like texture (Fig. 5.4(a), (b), (e), and (f)) was obtained with $P = 200$ W and $V = 300$ mm/s, while a <001> fiber texture (Fig. 5.4(c), (d), (g), and (h))—a ring-like distribution of <001> around the *z*-axis in the *xy*-plane in addition to the concentration peak along the *z*-axis—developed with $P = 400$ W and $V = 300$ mm/s.

Under ideal conditions, *xy*-scanning with two mutually perpendicular sample directions produces strong <001> alignment along the *x*-, *y*-, and *z*-axes, as demonstrated by the above results and discussion. However, the results in Section 3.3 indicate that, in some samples consisting of columnar grains, the crystallographic texture is not always single-crystal-like.

A crystal prefers to grow in the direction of the maximum temperature gradient. As can be inferred from the fiber texture results (Fig. 5.5(c), (d), (g), and (h)), the temperature

gradient should be oriented randomly in the *xy*-plane. Figure. 5.5 presents the results of CtFD simulations of multi-track melting with the process parameters of the samples shown in Fig. 5.4, which were conducted to verify this speculation. The base metal, melt region, and molten pool are depicted in the top view of the simulated melting process in both cases. The projections of the thermal gradients on the *xy*-plane at the solidification front are marked with black arrows, and the track-by-track melting sequences are displayed from top to bottom. With $P = 200$ W and $V = 300$ mm/s (Fig. 5.5(a)), the molten pool maintains a normal teardrop shape and solidifies independently between adjacent melt tracks. The resulting temperature gradients at the solidification front are almost perpendicular to the scanning direction, promoting uniformity of the <001> orientation in the *xy*-plane. On the other hand, with $P = 400$ W and $V = 300$ mm/s (Fig. 5.5(b)), the molten pool gradually becomes larger with increasing energy input and does not solidify completely within a single beam-scan track. Consequently, the molten pool connection between adjacent melt tracks increases the remelting times of the local region and irregular fusion boundary. The near-random temperature gradient direction resulted in random <001> orientation around the *z*-axis in the *xy*-plane. Since the development of the <001> orientation relative to the building direction is not likely to be influenced by the overall heat flow direction (except in the case of strong turbulence of the molten metal), the near-random directions of the temperature gradients in the *xy*-plane resulted in rotationally symmetric <001> orientations. Such crystal growth induces the development of a one-dimensional fiber-like texture. Therefore, the crystallographic texture is closely related to the transient geometry of the molten pool boundary, where the heat flow direction determines the crystal orientation during solidification.

Researchers generally control the texture by changing scanning strategies because changing the scanning directions can substantially alter the main heat flow directions within building components [20][21][22]. The analysis shown above suggests that without changing the scanning strategy, only by varying the process parameters (power, scan speed, line offset), the texture features can be adjusted depending on the modified molten pool status.

5.5. Columnar grain size evolution

Grain size is regarded as one of the most critical factors affecting the performances of materials, such as their mechanical properties and corrosion resistance. Since epitaxial grain growth tends to be dominant in solidification during AM, the grain size of the base plate partly determines the final grain size of the as-built material [23]. However, the effect of the substrate grain size is negligible when the built part is large since epitaxial growth is competitive and grains oriented in the preferred growth direction (i.e., mostly <001>) grow over other grains that are not preferably oriented.

Figure. 5.6 clearly shows that the grain sizes of the samples consisting of columnar grains increase with increasing E_{line}, and the average intercept lengths (L_{avg}) of the columnar grains, as determined based on Fig. 5.6, are summarized in Table 5-1. The grains in the sample built with a low E_{area} of 2.67 J/mm^2 (Fig. 5.6(a)) are finer than those in the sample built with a high E_{area} of 8.00 J/mm^2 (Fig. 5.6(b) and (c)). Interestingly, the comparison of Fig. 5.6(b) and (c) reveals that different columnar grain sizes can be obtained even with the same area energy (E_{area}= 8 J/mm^2) by applying different parameter combinations. L_{avg} of the coarse-grained sample (Fig. 5.6(c), P = 600 W, V = 100 mm/s), 72.9 μm, is approximately twice that of the fine-grained sample (Fig. 5.6(b), P = 400 W, V = 100 mm/s), 41.0 μm. Figure. 5.7 shows the average intercept lengths of the columnar grains as functions of E_{line} and E_{area} and demonstrates that L_{avg} is more closely correlated with E_{line} than with E_{area}.

Theoretically, the cooling rate (in the form of $G \times R$) during solidification primarily determines the scale of the solidification structure by reducing the undercooling for further nucleation. The higher the cooling rate, the finer the microstructure. Based on the multi-track melting simulation results obtained under the conditions corresponding to Figs. 5.6(b) and (c), the cooling rate (dT/dt) at the solidification front was calculated by differentiating the spatial–temporal thermal field of the molten pool. The solidification front in the simulation is represented by the collection of cells whose solid fractions are greater than 0 and less than 1. Fig. 5.8 shows box plots of the cooling rate at the solidification fronts of the first melt tracks in

both cases and the fourth and third tracks in the fine-grained case (Fig. 5.6(b)) and coarse-grained case (Fig. 5.6(c)), respectively. At the first track, the cooling rate is higher in the fine-grained case with higher power than in the coarse-grained case. However, the components fabricated via PBF-EB were the consolidations of individual melt tracks; therefore, the heat effects of the previous tracks could no longer be ignored. As shown in Fig. 5.8, the cooling rates at the solidification fronts of the fourth and third tracks in the individual cases become similar to each other and are directly controlled by the energy input during the process [24]. Thus, with the same E_{area} in both cases, the cooling rate that corresponds to melting and solidification of multiple tracks tends to be consistent.

Figure. 5.9(a) shows the cross-section of single-track melting on the CCM base plate with single-layer powder. With $P = 600$ W and $V = 100$ mm/s, the molten pool is deeper and larger than that with $P = 400$ W and $V = 100$ mm/s. The transient volume of the molten pool increases with increasing line energy, providing a massive space for grain growth. As grains grow competitively, some grains stop growing after encountering grains growing in a more favorable heat dissipation direction. The decrease in grain number and an increase in grain size are the results of the competition. A schematic illustration of competitive epitaxial grain growth in the molten pool during solidification is shown in Fig. 5.9(b), which demonstrates that the average columnar grain intercept length at location ①, which has limited space for grain growth, is less than that at location ②, where competitive growth is highly developed. Thus, with high E_{line}, the large molten pool is conducive to the extensive development of competitive grain growth and promotes the formation of coarse-columnar grains.

Similarly to the features of repeated heating in PBF-EB, the effects of the process conditions on the grain size are reflected not only in the cooling rate during solidification but also in the crystal growth kinetics in the heat-affected zone (HAZ) [25]. The kinetic grain growth model assumes that nucleation is complete, and grain growth within the HAZ is controlled by diffusion. Furthermore, the grain size (g) can be expressed as a function of E_{line} [26][27]:

$$g = \sqrt{k_1 \alpha \tau \, exp\left(-\frac{Q}{RT_p}\right) + g_0^2}, \qquad (5\text{-}1)$$

where

$$\alpha = \sqrt{\frac{2\pi RT_p}{Q}}, \qquad (5\text{-}2)$$

$$\tau = \frac{E_{line}}{2\pi\lambda e} \frac{1}{(T_p - T_0)}, \qquad (5\text{-}3)$$

where g_0 is the initial grain size, T_p is the peak temperature (solidus), Q is the activation energy for grain growth, T_0 is the preheating temperature, λ is the thermal conductivity, and k_1 is a kinetic constant. At the same starting T_0, τ (a characteristic time constant for the thermal cycle) at elevated temperature increases with E_{line}, also resulting in the growth of larger grains.

In conclusion, the columnar grain size is primarily controlled by E_{line}. The large molten pool is conducive to the development of competitive growth, and the kinetics of crystal growth in the HAZ can be induced by increasing E_{line}, promoting the formation of coarse columnar grains.

5.6. Mechanism for grain morphology evolution

5.6.1. Evaluation of *G-R* depending on *P* and *V*

A solidification map showing the solidification structures as a function of fundamental solidification parameters can illuminate the underlying correlation between solidification morphology and G and R values. This is based on the theory of constitutional undercooling, which describes the evolution of the solidified structure morphology as a function of solidification conditions.

Hunt [27] first established a widely accepted criterion for the columnar-to-equiaxed transition (CET) during alloy solidification. The lower bound on G required for fully columnar growth is given by:

$$G \geq 0.617(100N_0)^{1/3}\left(1 - \frac{\Delta T_n^{\,3}}{\Delta T_c^{\,3}}\right)\Delta T_c, \qquad (5\text{-}1)$$

and the upper bound on G for fully equiaxed growth is:

$$G \leq 0.617 N_0^{1/3} \left(1 - \frac{\Delta T_n^{\ 3}}{\Delta T_c^{\ 3}}\right) \Delta T_c. \tag{5-2}$$

where N_0 is the heterogeneous nuclei density (m^{-3}), ΔT_n is the undercooling necessary for nucleation (K), and ΔT_c is the constitutional undercooling on the dendrite tip (K). Dendrite growth velocity, R, as a function of ΔT_c can be fit with a third-order polynomial [28]:

$$R = a_2 \Delta T_c^{\ 2} + a_3 \Delta T_c^{\ 3}. \tag{5-3}$$

The fitting coefficients, a_2 and a_3, are associated with the liquidus slope and solute partitioning, respectively. The values of N_0 and ΔT_n used in this study were 1×10^{11} m^{-3} and 8 K, respectively. The thermodynamic simulations performed using ProCAST$^{®}$ estimate both a_2 and a_3. The qualitative solidification map of CCM alloy obtained using the above described analytical model is shown in Fig. 5.10.

As G/R ratio decreases, the solidification morphology tends to change from planar to cellular and then to columnar dendritic. With further undercooling, the liquid can be supercooled to the point at which nucleation may occur within the liquid, leading to the formation of new grains. Researchers usually regulate the solidification parameters (G & R) depending on beam power (P) and scan speed (V) manipulation to control the solidification mode. In the present study, to evaluate G and R depending on power and scan speed. The centroid of G-R points extracted from CtFD simulation was taken as the representation under each process condition and seen from the simulation results of CCM alloy shown in Fig. 5.11, G is determined by input energy density while R is determined by beam scan speed, which indicated that under high power and fast scan speed, a small G/R ratio could be obtained.

As shown in Fig. 5.12, there is a common perception that the G value is highest at the fusion boundary (start of solidification) in contact with the cooler and unmelted base solid, such that heat flow into the surrounding base metal is most efficient. The value of G decreases approaching the trailing end of the molten pool (end of solidification) because the molten metal is in contact with the hotter resolidified metal. The value of R changes depending on its spatial relation to the scan velocity [29]. As the trailing end of the molten pool is approached, R increases because the angle between

145

the scan and growth directions (normal direction of the solidification front) decreases. Changes in both values are also functions of energy input and molten pool translation speed. However, regulating the P and V shows limited impact on solidification parameters. First, flexible control of the solidification rate by manipulating scan speed is difficult. Theoretically, V can be controlled in a wide range (~8000 mm/s) for Arcam A2X machine we used, which is possible to regulate R extensively as well. In CtFD simulation, for evaluating the effect of V on R, V values in simulation cases were set as 500, 1000, and 2000 mm/s, while P values were also regulated for keeping line energy as a constant of 1 J/mm. The simulation results of G-R plots of CCM alloy under three sets of process parameters shown in Fig. 5.13 revealed that even though the V increased in twice times, the resultant R did not increase proportionally with the increase of V as expected. Seen from the simulation results of longitudinal cross-sections of the molten pool under the three sets of process parameters shown in Fig. 5.14(a), the molten pool geometry was elongated, and solid/liquid interface tended to be horizontal as V increased, by which the angle between V and R increased (Fig. 5.14(b)). As a result, a further increase in R would be hindered. Depending on the condition of steady molten pool:

$$R \cdot \rho \Delta H_{SL} + \kappa_L \left(\frac{dT}{dx}\right)_L \leq \kappa_S \left(\frac{dT}{dx}\right)_S, \qquad (5\text{-}4)$$

where ΔH_{SL} is latent heat of solidification (J/kg) and κ_L, κ_S are thermal conductivity of liquid and solid respectively (J/s·m·K), if R increases beyond a critical value, the sum of latent heat and heat transferred from liquid would exceed the heat dissipation capacity of solidified material.

In addition, there is a drawback in control of G by manipulating beam power. Seen from the experimental results shown in Fig. 5.15, as P continued to increase, surface roughness deteriorated, and pore defect tended to appear in samples. This can be attributed to the overheating by further increased power. The overheating would generate an oversized molten pool that exists for an extended period, which raises the instability of the melt and result in uneven surface morphology, hence to a deteriorated forming quality. In conclusion, grain morphology control depending on solidification

map through the regulation of P and V is difficult and not feasible. Based on the above analysis, microstructure control only by P and V has limitations. Therefore, the other mechanisms for grain morphology evolution need to be investigated.

5.6.2. Method for grain morphology control

Similar to the solidification in welding on a base material with the epitaxial growth that occurs, the initial stage of solidification in AM also usually eliminates nucleation [30]. Generally, columnar grains become elongated over many layers, and grain nucleation ahead of the solidification front is suppressed due to the steep temperature gradient [31]. The development of a feasible method of grain morphology control that restricts the extensive epitaxial growth of columnar grains and reduces the crystallographic texture remains a challenging issue in PBF-EB. This approach, which is expected to convert columnar grains with large aspect ratios into near-equiaxed/equiaxed grains with small aspect ratios, promotes the probability of nucleation and new grain growth. The solidification mode of the alloy can be determined based on the constitutional undercooling that exists in the liquids immediately in front of S/L interfaces [32]. As $\frac{G}{R}$ decreases, the solidification morphology tends to change from planar to cellular and then to columnar dendritic. With further undercooling, the liquid ahead of the solidification front can be supercooled to the point at which nucleation may occur within the liquid, leading to the formation of new grains. In addition, varying the direction of the temperature gradient (the normal direction of the solidification front), which deviates from the building direction (fast growth <001>), affects the competitive grain growth as well as the tendency of new grain formation. Greater undercooling can be achieved ahead of the cell/dendrite tip oriented towards the temperature gradient [33]. Consequently, a region with an increased driving force for heterogeneous nucleation can be generated [34].

Figure. 5.16 presents the results for samples fabricated with different P but the same V and E_{area}. The formation of new/stray grains is facilitated under high P, and the associated texture is weakened due to the random orientation of these new/stray

grains. To investigate the reason for the grain morphology evolution, the solidification parameters G and R at the solidification front under the two sets of processing conditions were derived by performing a numerical simulation. Figure. 5.17(a) shows that with the same V and E_{area}, G vs. R tends to be consistent after several scans under the two sets of conditions, suggesting that these quantities do not determine the grain morphology. The molten pool geometries obtained in the experiments and simulations under the two sets of processing conditions are shown in Figs. 5.17(b)–(e). Increasing P with constant V increases the depth of the molten pool more obviously than the width [35] or length [29]. As the power increases, the slope of the solidification front increases, yielding a significant deviation of the temperature gradient with respect to the building direction.

The significant mismatch between the resulting temperature gradient and fast growth <001> direction (building direction) can provoke nucleation ahead of the solidification front. The mechanism causing the high nucleation rate appearing ahead of the inclined cell/dendrite with respect to the temperature gradient is illustrated in Fig. 5.18. The cell/dendrite from the previous layer with the preferred <001> direction aligned with the building direction tilts relative to the direction of the temperature gradient of the sloping S/L interface. If both grains continued epitaxial growth, the velocity of the inclined columnar dendrite tip V_φ in the temperature gradient direction $V_\varphi \cos \varphi$ would be equal to the velocity of the liquidus isotherm:

$$V_\varphi \cos \varphi = V_T = V_0. \tag{5-5}$$

Since the dendrite tip undercooling increases monotonically with velocity,

$$|V_\varphi| \ \& \ |V_0| \ \propto \ |undercooling|^2, \tag{5-6}$$

$$A\{\Delta T_{\text{col}}(\varphi)\}^2 \cos \varphi = A\{\Delta T_{\text{col}}(0)\}^2, \tag{5-7}$$

where A is a coefficient relating the growth rate to undercooling and $\Delta T_{\text{col}}(\varphi)$ and $\Delta T_{\text{col}}(0)$ are the undercooling at the inclined and parallel columnar dendrite tips, respectively. Then,

$$\Delta T_{col}(\varphi) = \frac{\Delta T_{col}(0)}{(\cos \varphi)^{0.5}}. \tag{5-8}$$

Thus, considerable undercooling ahead of the inclined dendrites/cells is necessary, and nucleation may occur when it is larger than undercooling required for grain nucleation ΔT_n:

$$\Delta T_{col}(\varphi) > \Delta T_n > \Delta T_{col}(0). \tag{5-9}$$

Consequently, an increased nucleation probability promotes the formation of new grains.

Figure. 5.19 shows evidence of new grain formation under relatively high power. On the single-crystal substrate, single-track melting was conducted with increased P but the same V. New grains are observable under high power. Thus, as the power increases, the slope of the S/L interface of the molten pool increases, causing a considerable mismatch between the resulting temperature gradient and the fast growth <001> direction of grains solidified in the preceding layer. Consequently, the nucleation probability ahead of the solidification front increases.

The PBF-EB-built part is a result of the combination of adjacent melt tracks. The remelting phenomenon is also essential to obtain the final grain structure. In Fig. 5.20, the columnar ($P = 200$ W, $V = 300$ mm/s) and near-equiaxed ($P = 100$ W, $V = 100$ mm/s) grain structures are shown with the same E_{area} of 2.6 J/mm^2. The corresponding texture becomes weak due to the lack of extensive epitaxial growth in the sample with near-equiaxed grains, in which the bimodal grain structure is composed of a few elongated columnar grains and more irregular grains with random orientation. Based on our previous analysis, with the same E_{area}, the G vs. R distribution tends to be consistent at the solidification front. However, as can be seen from the simulated melt region with the thermal gradient direction (depicted as black arrows) in Fig. 5.21(a), the resulting temperature gradients are distributed radially and oriented inconsistently with a small remelting fraction of adjacent melt tracks for the sample with near-equiaxed grains. In Fig. 5.21(b), the BSE images show the grain structures near the tops of the two samples. The molten pool trace of the top layer is more easily recognizable in the sample with a small remelting fraction than in the other sample, because the grains almost strictly follow the radial growth direction perpendicular to

the molten pool boundary and intersect each other between adjacent melt tracks. Thus, with a small remelting fraction, the grain growth is fragmented within a single molten pool under the induced complicated thermal field. Since the remelting fraction of the adjacent melt tracks is very small, the subsequent melt tracks do not share a preferred growth direction. Consequently, the epitaxial growth is hampered, and new grains can form in the subsequent track and layer.

By increasing the beam power with a constant scanning speed, the temperature gradient direction at the S/L interface of the molten pool can be made to deviate sharply from the fast growth <001> direction (building direction). Alternatively, an appropriately large line offset could be applied to decrease the remelting fraction and allow the thermal gradient to be oriented diversely at the resulting solidification front. These strategies may be universal, applying not only to the CCM alloy but also to other alloy systems.

5.6.3. Role of fluid flow in grain morphology evolution

According to the above results and discussions, through the modification of the molten pool geometry or remelting fraction between adjacent melt-tracks, the direction would be locally diverse and deviate from building direction (Z-direction). The significant mismatch between the resulting temperature gradient and fast-growth <001> direction (Z-direction) can provoke nucleation ahead of the solidification front.

However, interestingly, in Fig. 5.22(a)(b), even though both the PBF-EB-built CCM alloy samples were fabricated under modified remelting fraction, the average aspect ratios of grains were different, or to say, the tendencies for new/stray grains formation are different in the two samples. First, in Fig. 5.22(c)(d), the *G-R* plots corresponding to the two samples were extracted from CtFD simulation. However, we can see, the *G-R* plots show opposite tendencies to the experimental results. Thus, we need to investigate some other controlling factor in solidification, especially the fluid convection.

The fluid velocity at the solidification front represented by box plot under the

process conditions of the above two samples during solidification was extracted from CtFD simulation are shown in Fig. 5.23. We can see, the fluid velocity was different depending on process conditions. Under the process parameter of P= 100 W, V= 100 mm/s, fluid velocity was almost two times that under the process parameter of P= 200 W, V= 100 mm/s. For clarifying the effect of fluid flow on grain morphology and microstructure, the subgrain structures of the two samples were characterized. In Fig. 5.24, subgrain structures showed different geometrical features under the above process conditions and fluid velocity. In the case of slow fluid flow, cellular subgrain structure grows directional along building direction. By contrast, dendritic subgrain structure was observed in the case of fast fluid flow, which indicated that the undercooling around the dendrite/cell trunk was greater than that in the case of slow fluid flow. According to the above study results in Chapter 3, the flow stream within the molten pool should be vertical to the grow direction of dendrite/cell during solidification (Fig. 5.25(a)). The researchers performed phase-field simulation [36] and experimental X-ray observation [37] to reveal that the fluid convection dramatically influences the formation of the solidification microstructure because they enhance dendritic growth along the direction of the fluid flow. As shown in Fig. 5.26, fluid flow can change the local gradient of solute concentration near the solid/liquid interface. For alloys with $k_0 < 1$ (CCM alloy in this study), as solute concentration decreases, liquidus increases. Thus, under fast fluid flow, the local gradient of solute concentration near the solid/liquid interface increases, as a result, the undercooling ahead of the solidification front can be enlarged. In a word, the effect of fluid flow facilitating the dendrite arm growth lies in the large undercooling ahead of the solid/liquid interface. Importantly, the enlarged undercooling owing to fast fluid flow would promote the nucleation probability, and new grains may form.

Another method for determining the relationship between grain morphology and fluid flow is collecting G–R–morphology data under a series simulations and single-track melting experiments of CCM alloy under different process parameters ($P = 200$, 400, 600, 800, and 1000 W; $V = 300$ mm/s). As shown in Fig. 5.27, the spatiotemporal values of G, R, and fluid velocity (U) were obtained from each mesh at the solidification

front of the computing domain. They corresponded to the grain morphology determined experimentally. The *G–R*–grain morphology overlapping was performed on two cross-sections of the melt track. The matchup and results derived from the simulation and experiments were implemented using a customized R code. The grain morphology can be described by the aspect ratio, i.e., the ratio of the length to width of the grains. The aspect ratio changes from large to small indicates that the grain morphology changed from columnar to equiaxed. In Fig. 5.28, the obtained data were organized into segments depending on fluid velocity. Importantly, it is difficult to draw dividing lines to distinguish the distribution region between the points for columnar and equiaxed grains in solidification maps, which suggests that the grain morphology of single-track melting cannot be well predicted only by solidification parameters (*G&R*). However, as the fluid velocity increases, points with the smaller aspect ratios (blue-colored) become more common, indicating that the grain growth under PBF-EB is affected by the fluid flow of the molten metal.

Regarding the other possible effects of fluid flow on solidification microstructure, nuclei formation can be promoted by dendrite fragmentation [33]. Dendrite fragmentation owing to melt convection can occur during casting in which the fluid flow is governed by natural convection [33][38]. According to the simulation results in this study, the maximum fluid velocity at the solidification front can exceed 700 mm/s, which is higher than that of conventional casting. However, the dendrite fragmentation process in AM remains unclear due to the lack of direct evidence. Nevertheless, as discussed previously, convective transport of the rejected solute from the solid may change the solute concentration gradient. Moreover, fluid convection can modify the local thermal field and affect the speed of the isotherms. Undercooling near the dendrite arms may also be enlarged, leading to an increase in nucleation probability near the solidifying interfaces.

Conclusions

The experimental results obtained in this study revealed the various microstructural

features of PBF-EB-built CCM alloy. Epitaxial growth with resulting columnar grains and near-cubic texture dominated the crystal growth. However, nucleation and new grain growth rather than extensive epitaxial growth could be achieved by manipulating the molten pool behaviors. Through the experimental characterization of the microstructure and analysis of the simulation results, the microstructure evolution mechanisms can be summarized as follows:

1) The typical growth behavior of columnar grains and the resulting near-cubic texture were determined by competitive epitaxial grain growth governed by the heat flow characteristics with xy-scanning.

2) The molten pool connection between adjacent melt tracks produced a random orientation of <001> around the z-axis in the xy-plane, resulting in the development of a fiber-like texture. Therefore, the crystallographic texture was closely related to the transient geometry of the molten pool boundary, where the heat flow direction determined the crystallographic orientation during solidification.

3) E_{line} primarily controlled the columnar grain size. The large molten pool was conducive to the development of competitive growth, and the kinetic grain growth in the HAZ was induced by increasing E_{line}, promoting the formation of coarse columnar grains.

4) As the power increased, the slope of the S/L interface of the molten pool increased, producing in a considerable mismatch between the resulting temperature gradient and the fast growth <001> orientation of the grains solidified in the preceding layer. Consequently, nucleation ahead of the solidification front was facilitated.

5) Investigation of the sub-grain structure and the G–R–grain morphology considering the fluid flow showed that the enlarged undercooling and probable dendrite fragmentation owing to fast fluid flow would promote the nucleation probability and new grains may form, which suggested that fluid convection was an important mechanism promoting CET during the PBF-EB process.

Table 5-1. Process parameters and L_{avg} of samples in Fig. 5.6.

	P (W)	V (mm/s)	l_{off} (µm)	E_{line} (J/mm)	E_{area} (J/mm^2)	L_{avg} (µm)
Fig. 5.6(a)	100	300	125	0.33	2.67	30.0
Fig. 5.6(b)	400	100	500	4.00	8.00	41.0
Fig. 5.6(c)	600	100	750	6.00	8.00	72.9
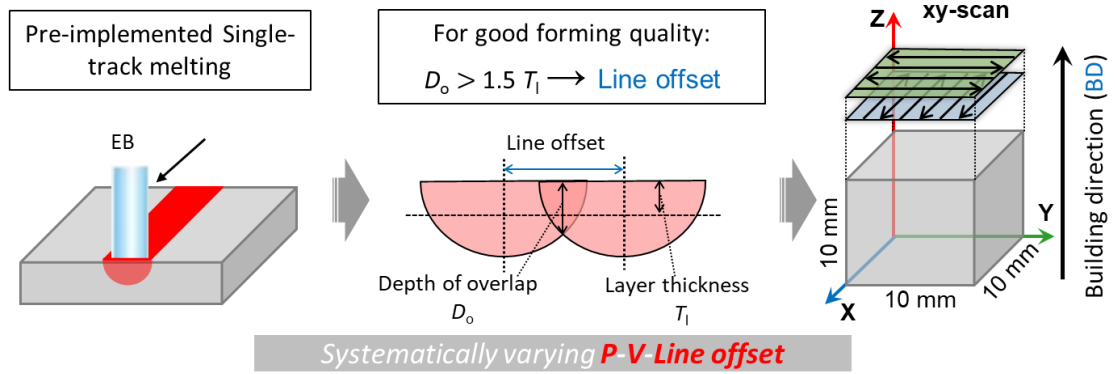
Fig. 5.1. Schematic illustration of PBF-EB experiments procedures and scanning strategy applied.
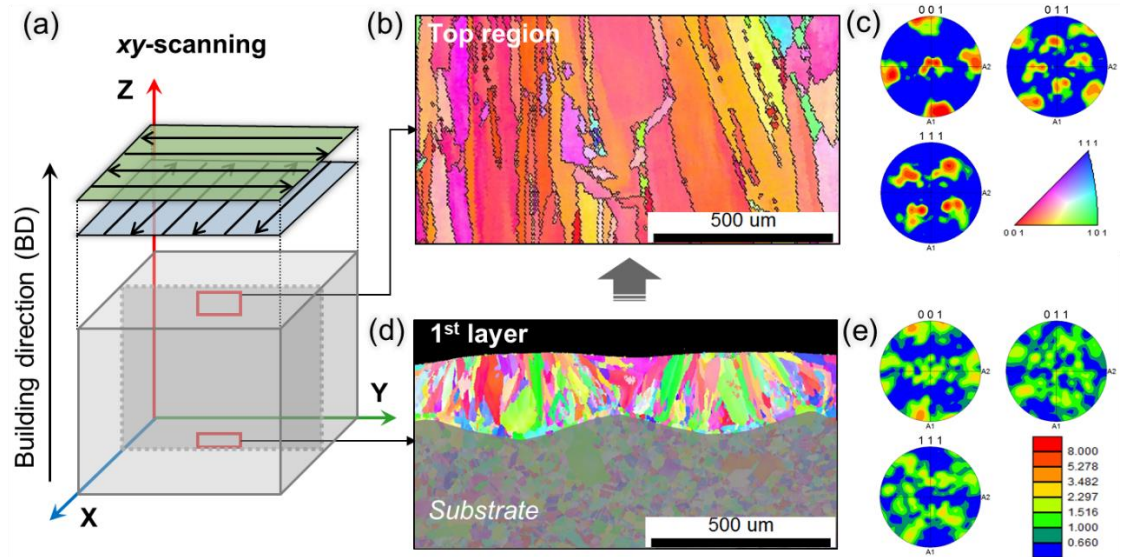
Fig. 5.2. (a) CCM alloy block fabricated using *xy*-scanning strategy. (b)(c) EBSD IPF map and pole figures of the top part of the building block: grains become coarse and align mainly with the building direction, and a near-cubic texture presents. (d)(e) EBSD IPF map and pole figures of one-layer melting were obtained to refer to the grain structure of the first layer: grains with arbitrary orientations grow almost perpendicularly to the molten pool boundary.
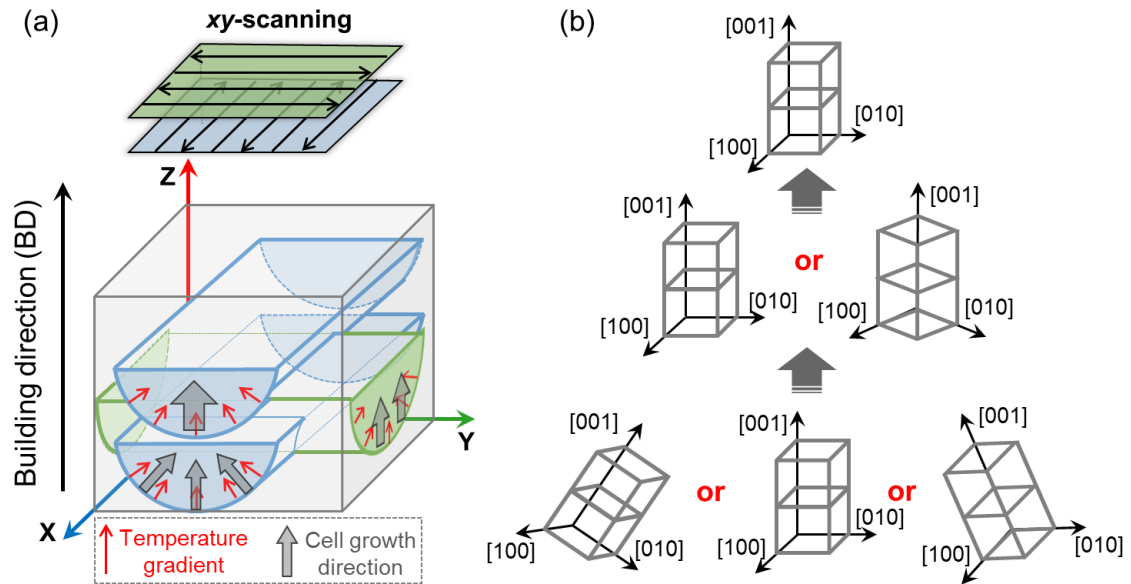
Fig. 5.3. Schematic diagram of the crystal development under the xy-scanning strategy: (a) The single-track melt region is assumed to be a semi-circular cylinder; the directions of the temperature gradient and cell growth are indicated by the red and gray arrows. (b) With the competitive growth in the layer-by-layer process, the preferred <001> orientation tends to be limited in the yz- and xz-planes because of the x- and y-scans, respectively, due to the conditional temperature gradient. Consequently, xy-scanning leads to relatively coarse columnar grains typically with near-cubic texture.
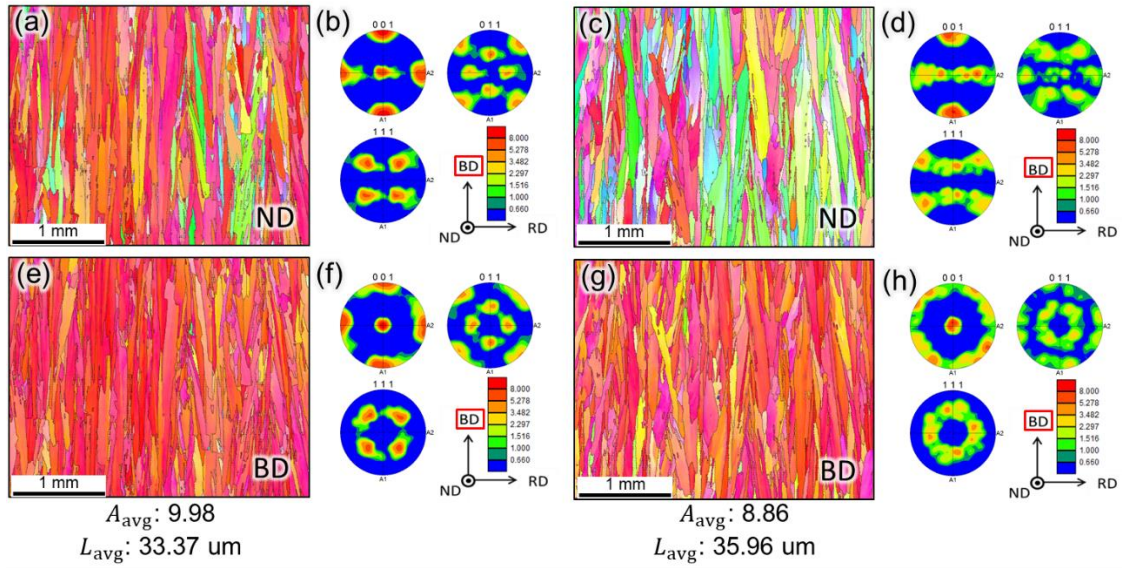
Fig. 5.4. EBSD IPF maps and pole figures of the samples with (a)(b)(e)(f) typical single-crystal-like texture and (c)(d) (g)(h) fiber texture. The crystallographic orientations are indicated along the (a)(b)(c)(d) normal direction and (e)(f)(g)(h) building direction. A_{avg} and L_{avg} are shown below the figures. The process conditions are (a)(b)(e)(f) $P=$ 200 W, $V=$ 300 mm/s, $l_{off}=$ 250 μm; (c)(d)(g)(h) $P=$ 400 W, $V=$ 300 mm/s, $l_{off}=$ 605 μm.
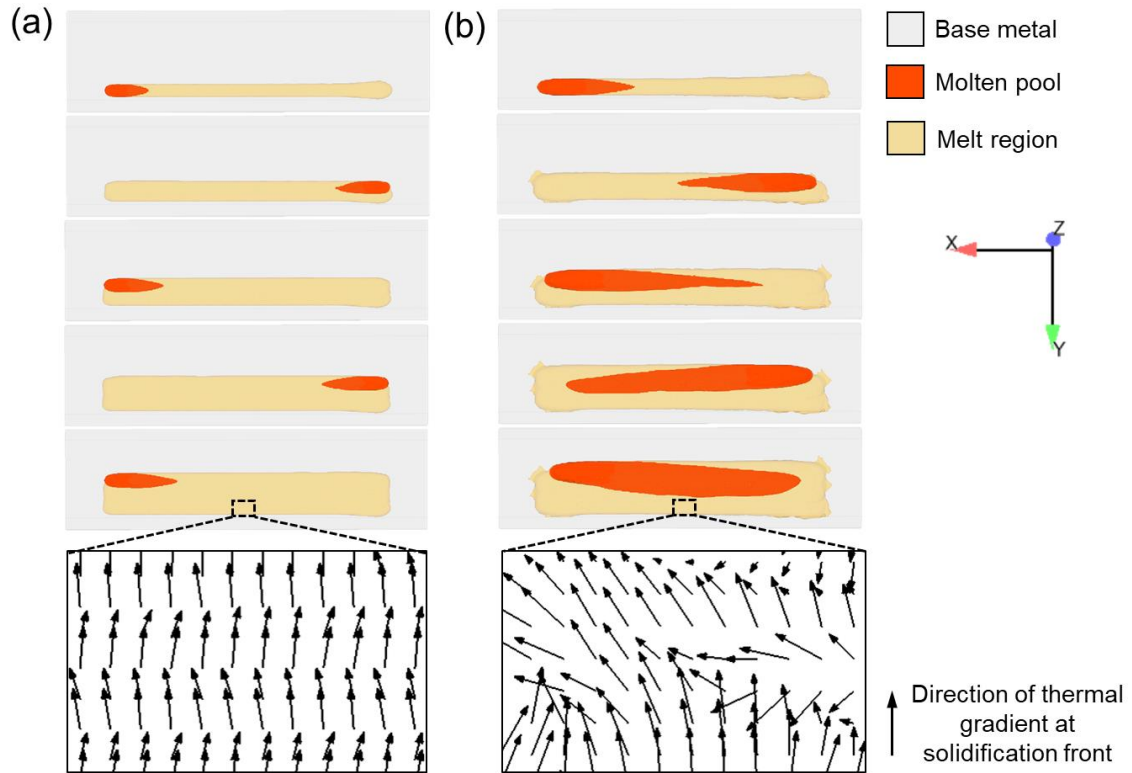
Fig. 5.5. The top view of the simulated melting process. (a) The molten pool maintains a normal teardrop shape and solidifies independently between adjacent melt tracks, resulting in the single-crystal-like texture. (b) The molten pool connection between adjacent melt tracks increases the remelting times of the local region and irregular fusion boundary. The near-random temperature gradient direction resulted in random <001> orientation around the z-axis in the xy-plane. The process conditions are (a)(c) $P= 200$ W, $V= 300$ mm/s, $l_{off}= 250$ μm; (b)(d) $P= 400$ W, $V= 300$ mm/s, $l_{off}= 605$ μm.
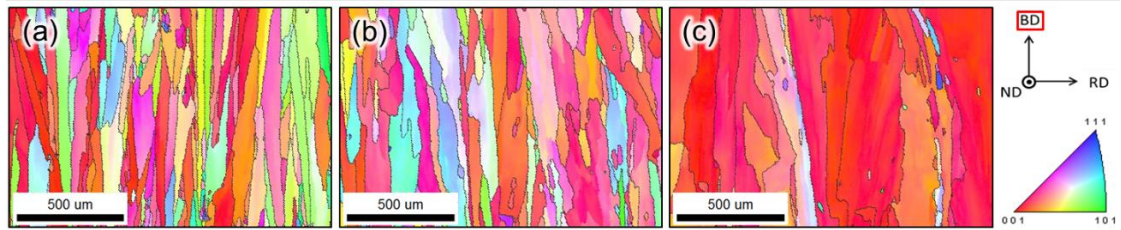
Fig. 5.6. Grain size of the samples consisting of columnar grains increases with increasing E_{line}. The E_{line} is (a) 0.33 J/mm; (b) 4 J/mm; (c) 6 J/mm.
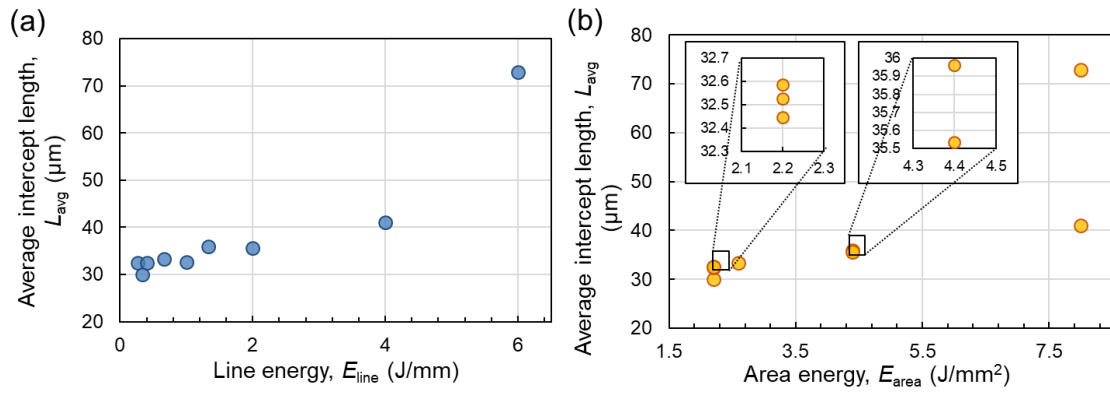
Fig. 5.7. Size of columnar grain is depicted as a function of (a) E_{line} and (b) E_{area}. The average intercept lengths of columnar grains are more closely correlated with E_{line} than with E_{area}.
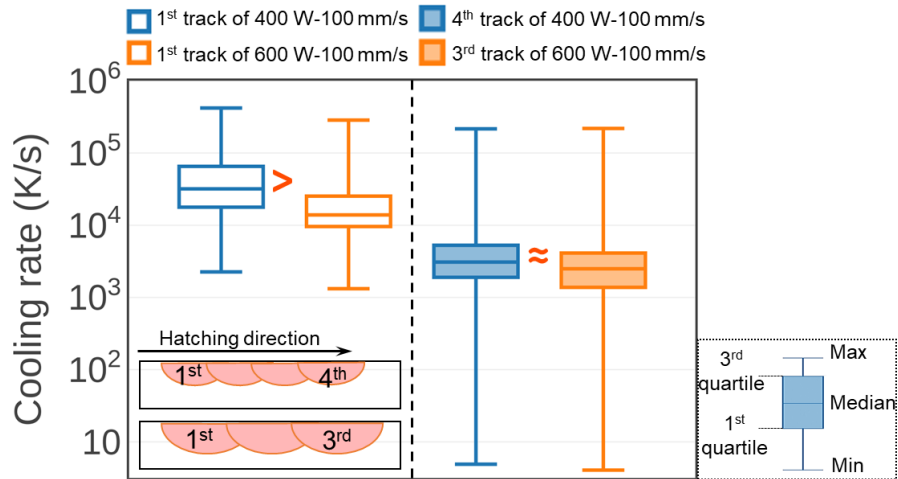
Fig. 5.8. Box plots of the cooling rate at the solidification front of the 1st melt tracks in both cases and the 4th and 3rd tracks in the fine-grained case and coarse-grained case, respectively. With the same E_{area}, the cooling rate that corresponds to melting and solidification of multiple tracks tends to be consistent.
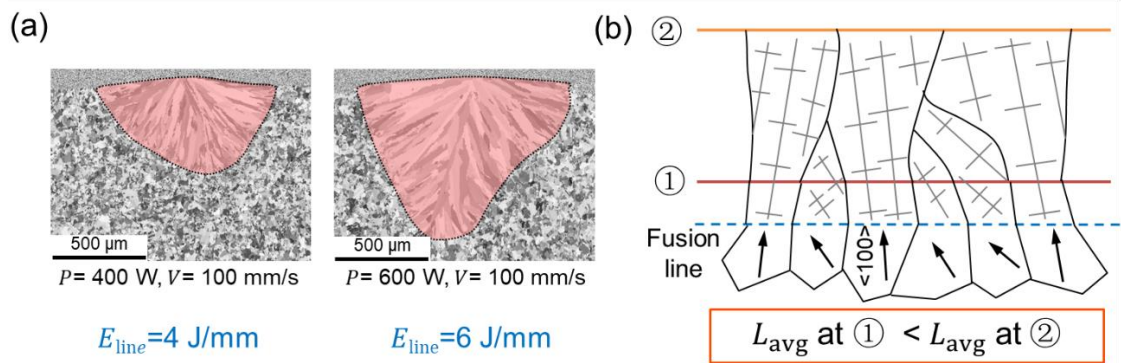
Fig. 5.9. (a) Transverse cross-sections of single-track melting on CCM base plate with single-layer powder with the two process conditions. The transient volume of the molten pool increases with the increasing line energy. (b) Schematic illustration of competitive epitaxial grain growth in the molten pool during solidification, which demonstrates that the L_{avg} of columnar grain at location ①, which has limited space for grain growth, is smaller than that at location ②, where competitive growth is highly developed.
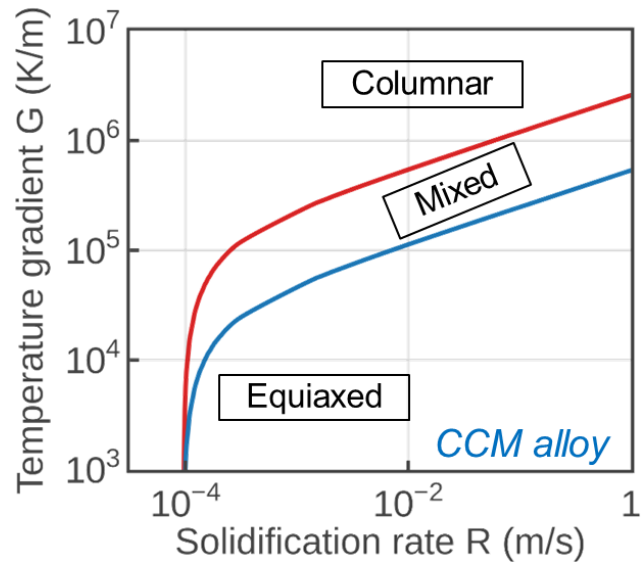
Fig. 5.10. Qualitative solidification map of CCM alloy obtained using the described analytical model.
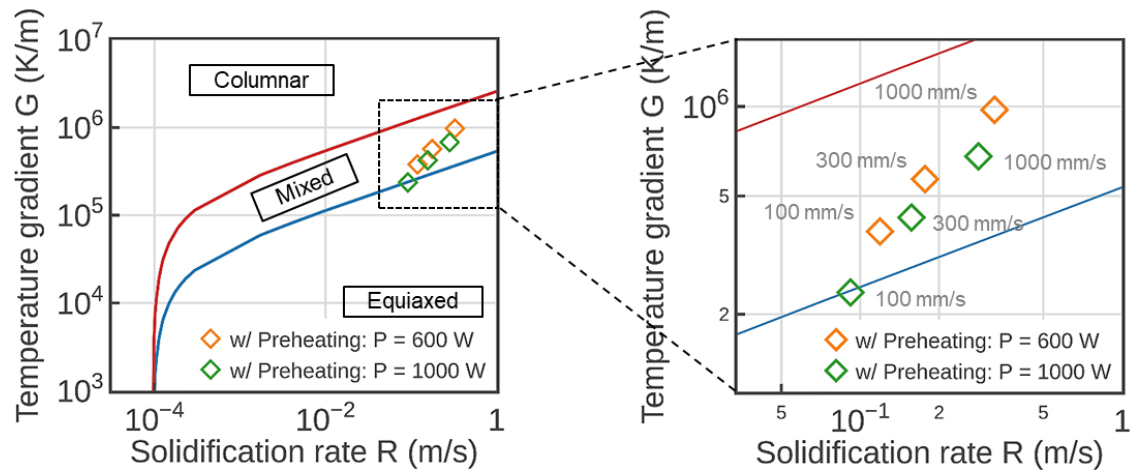
Fig. 5.11. *G-R* plot under different process conditions is superimposed on the qualitative solidification map of CCM alloy.
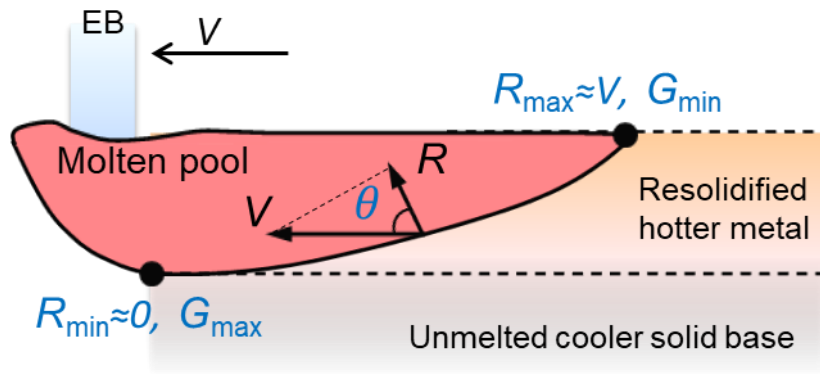
Fig. 5.12. Schematic illustration of the change in G and R as a function of location along the solidification front in common perception.
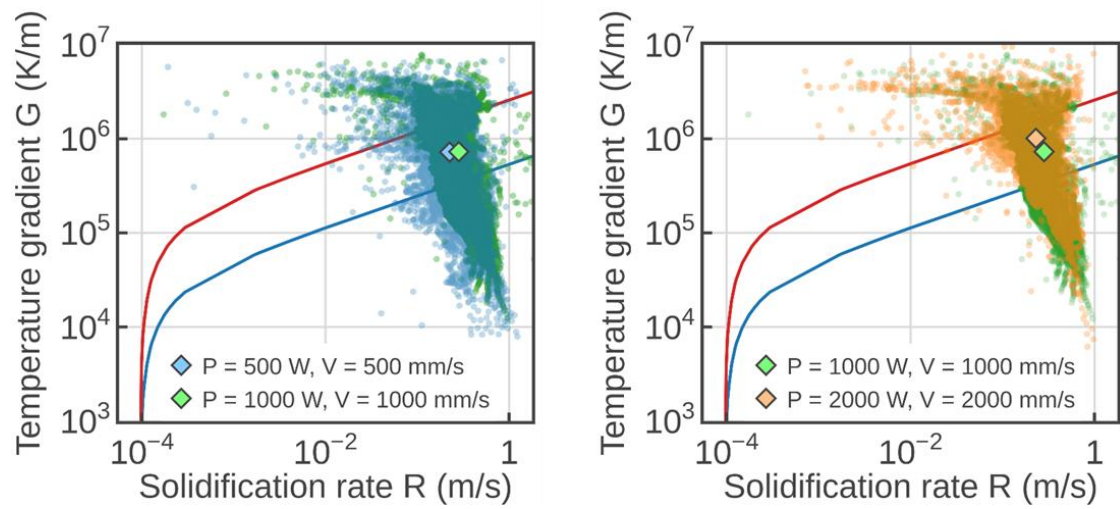
Fig. 5.13. Simulation results of *G-R* plots of CCM alloy under three sets of process parameters.
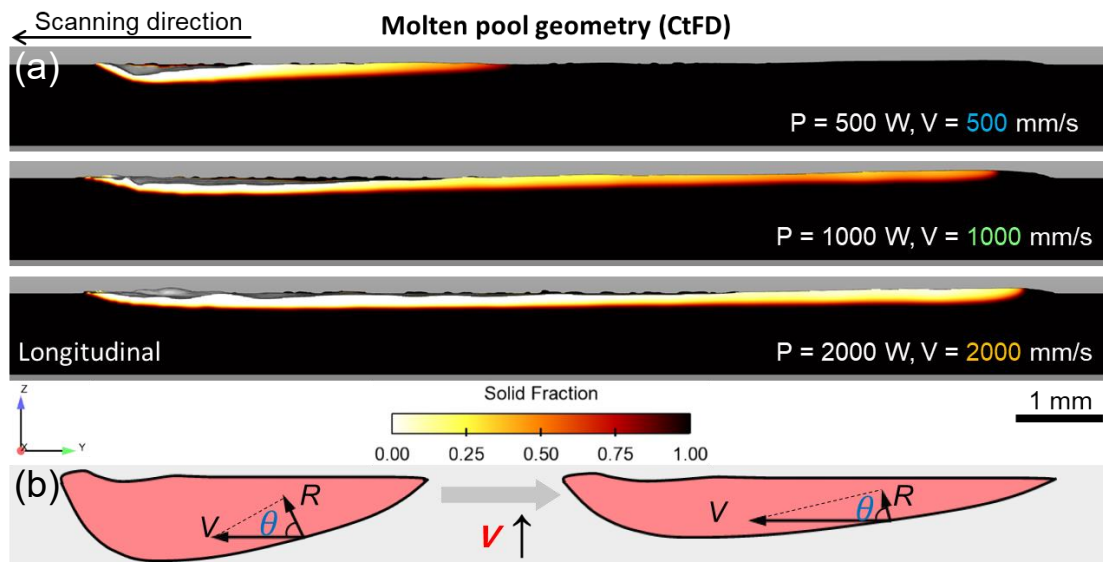
Fig. 5.14. (a) Simulation results of longitudinal cross-sections of the molten pool under the three sets of process parameters corresponding to that in Fig. 5.5. (b) Molten pool geometry was elongated, and solid/liquid interface tended to be horizontal as *V* increased, by which the angle between *V* and *R* increased.
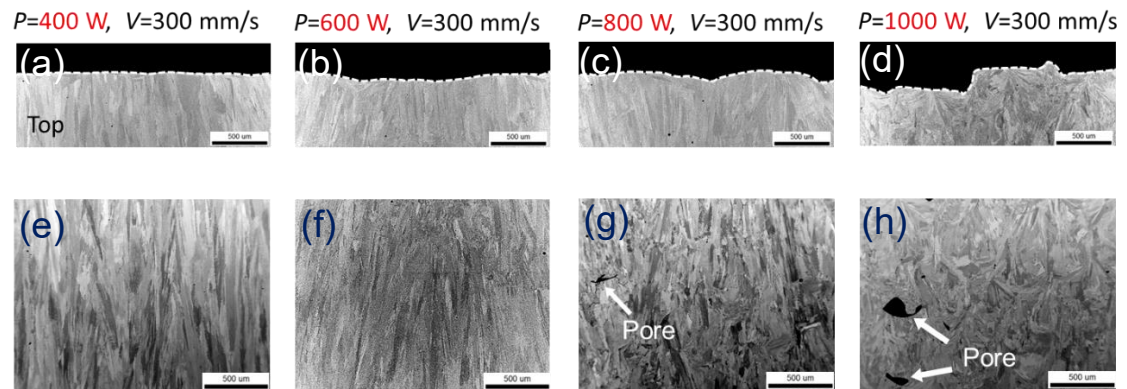
Fig. 5.15. BSE images of (a)(b)(c)(d) top surface profile and (e)(f)(g)(h) internal observation of PBF-EB-built CCM alloy block.
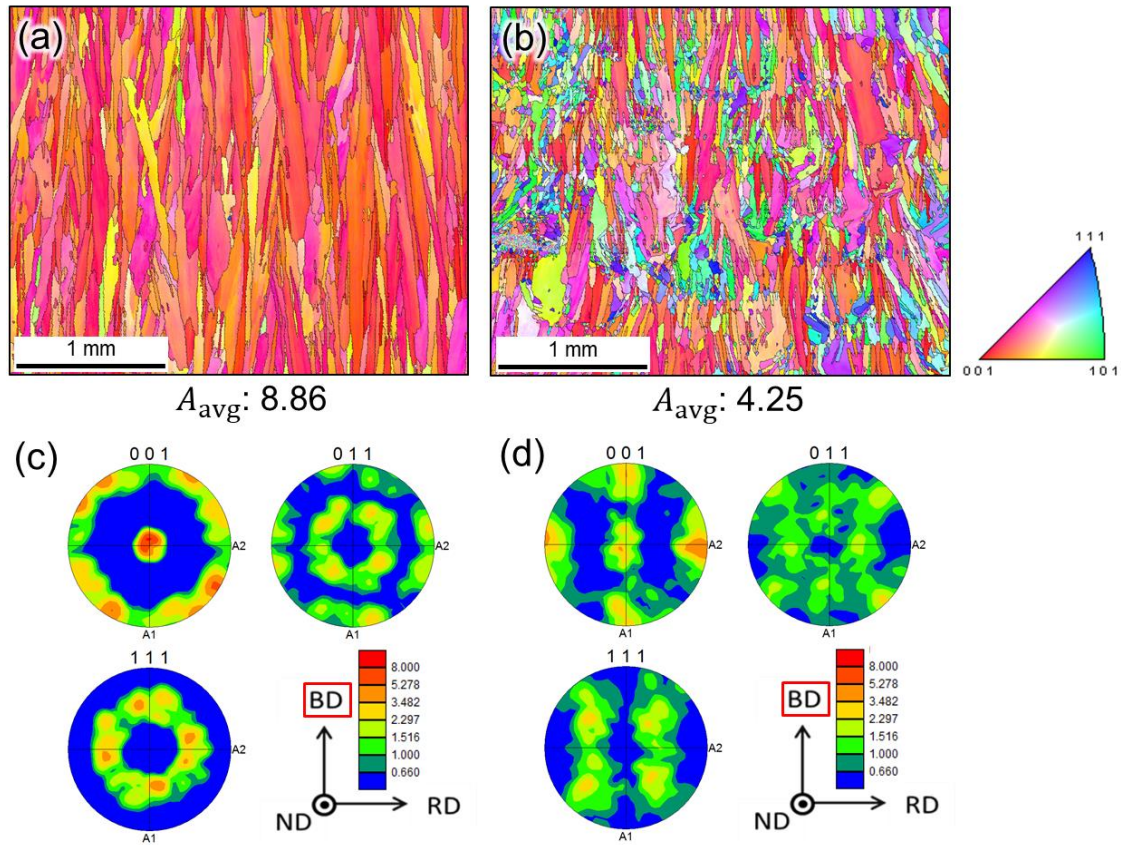
Fig. 5.16. EBSD IPF maps and pole figures of the samples fabricated with different P but the same V and E_{area}. The formation of new/stray grains is facilitated under high P, and the associated texture is weakened due to the random orientation of these new/stray grains. A_{avg} is shown below the figures. The process conditions are (a)(c) P= 400 W, V= 300 mm/s, l_{off}= 300 μm; (b)(d) P= 800 W, V= 300 mm/s, l_{off}= 605 μm.
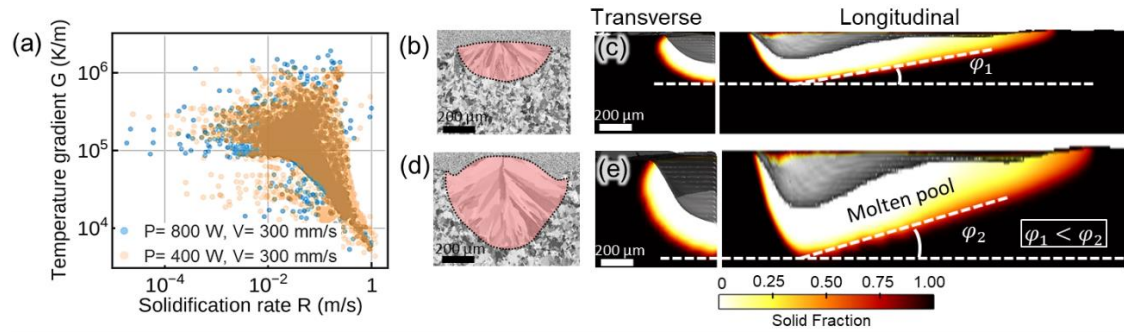
Fig. 5.17. (a) With the same V and E_{area}, G vs. R tends to be consistent after several scans under the two sets of conditions. The molten pool geometries obtained in the (b)(d) experiments and (c)(e) simulations under the two processing conditions. As the power increases, the slope of the solidification front increases, yielding a significant deviation of the thermal gradient with respect to the building direction. The process conditions are (b)(c) $P=400$ W, $V=300$ mm/s; (d)(e) $P=800$ W, $V=300$ mm/s.
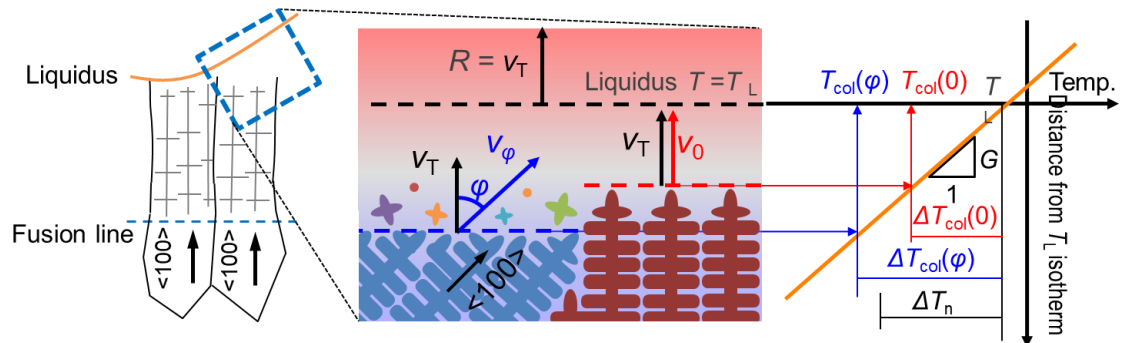
Fig. 5.18. Schematic illustration of the mechanism causing the high nucleation rate appearing ahead of the inclined cell/dendrite with respect to the thermal gradient. The cell/dendrite from the previous layer with the preferred <001> direction aligned with the building direction tilts relative to the direction of the temperature gradient of the sloping S/L interface. There would be a great undercooling ahead of the inclined dendrites, and nucleation may occur when it is larger than undercooling required for grain nucleation ΔT_n.
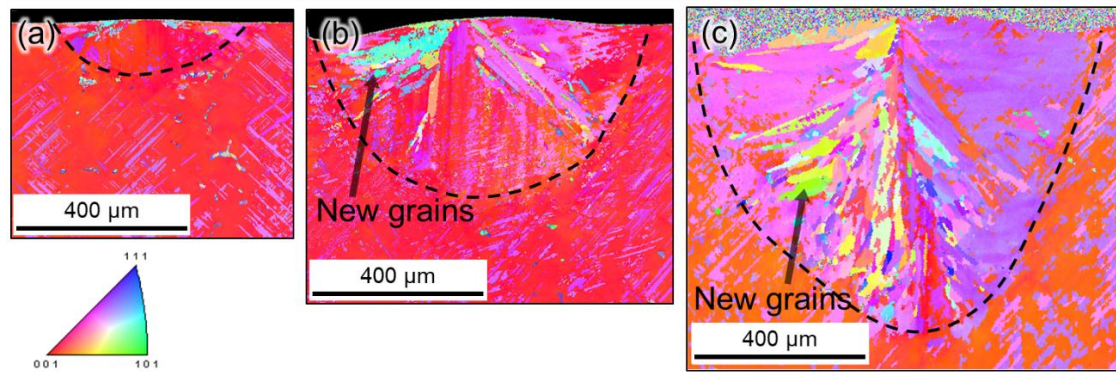
Fig. 5.19. Evidence of new grain formation under relatively high power. On the single-crystal substrate, single-track melting was conducted with increased P but the same V. The process conditions are (a) $P = 200$ W, $V = 100$ mm/s; (b) $P = 600$ W, $V = 300$ mm/s; (c) $P = 1000$ W, $V = 100$ mm/s.
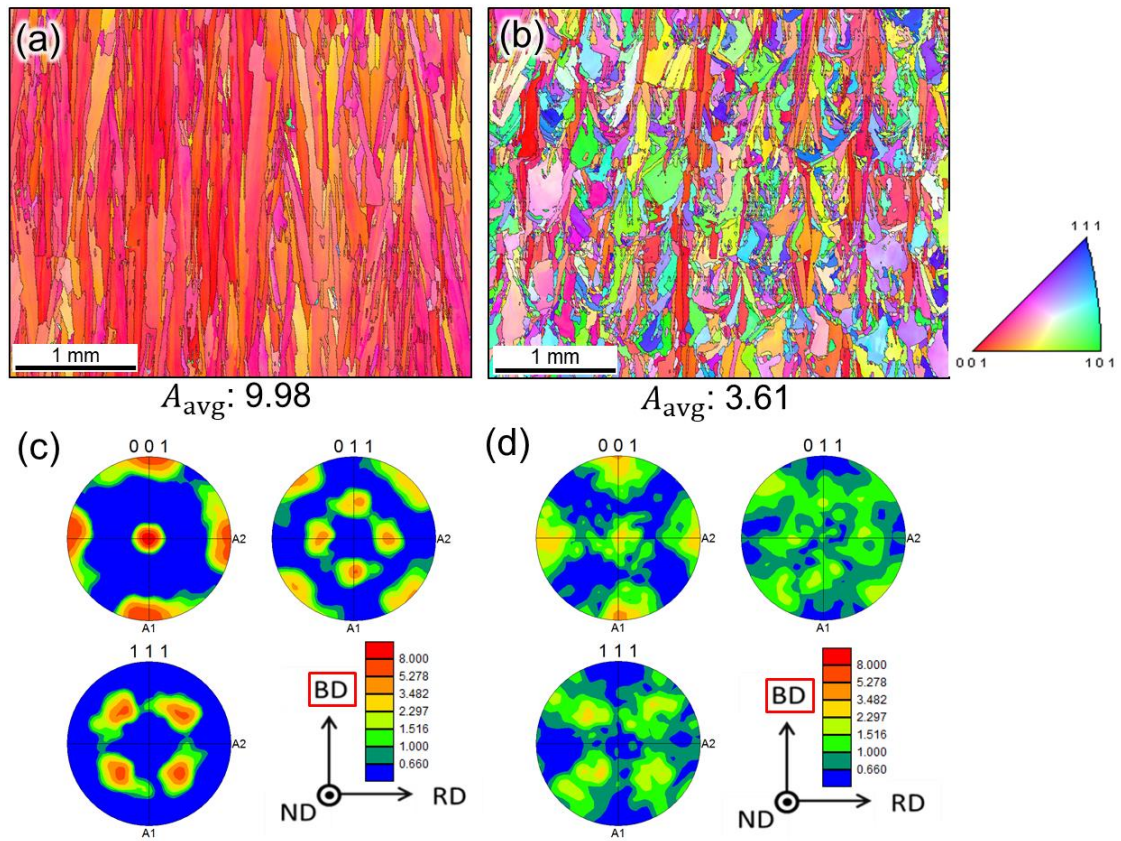
Fig. 5.20. EBSD IPF maps and pole figures of the samples (with the same E_{area} of 2.6 J/mm^2) with (a)(c) columnar grains and (b)(d) columnar-equiaxed mixture. A_{avg} is shown below the figures. The process conditions are (a)(c) P= 200 W, V= 300 mm/s, l_{off}= 250 μm; (b)(d) P= 100 W, V= 100 mm/s, l_{off}= 385μm.
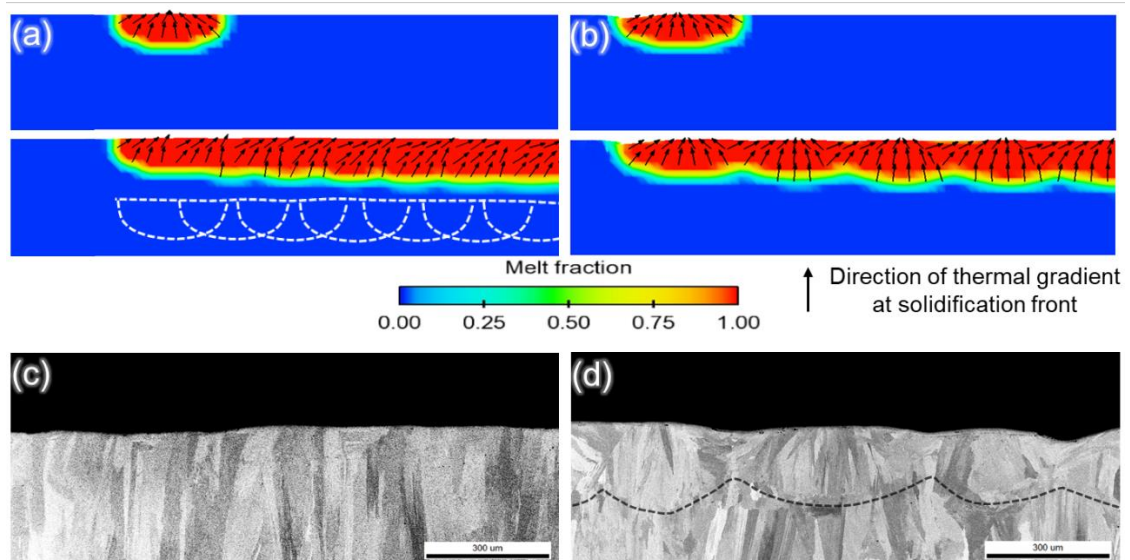
Fig. 5.21. (a)(b) Simulated melt region with thermal gradient direction (depicted as black arrows). The resulting temperature gradients are distributed radially and orientated inconsistently with a small remelting fraction of adjacent melt tracks. (c)(d) BSE images show the grain structures near the tops of the two samples. The molten pool trace of the top layer is more easily recognizable in the sample with a small remelting fraction than in the other sample. The process conditions are (a)(c) $P = 200$ W, $V = 300$ mm/s, $l_{off} = 250$ μm; (b)(d) $P = 100$ W, $V = 100$ mm/s, $l_{off} = 385$μm.
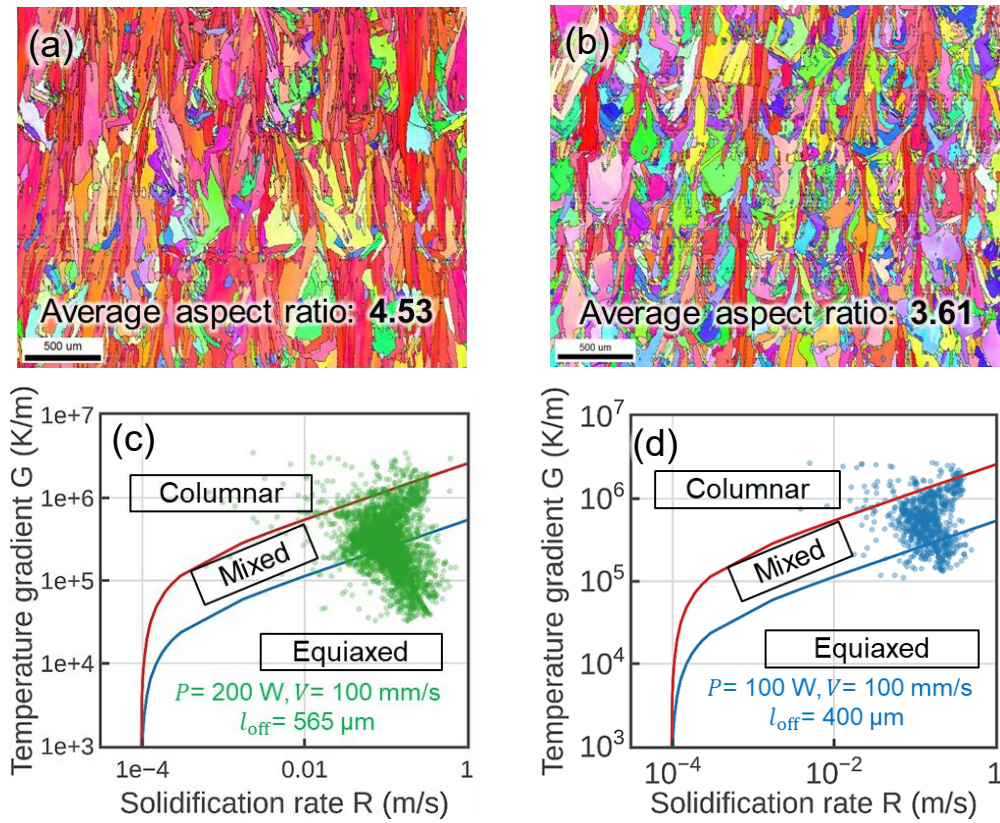
Fig. 5.22. (a)(b) EBSD IPF maps and pole figures of the samples fabricated with modified remelting faction of adjacent melt track. (c)(d) Corresponding *G-R* plots extracted from CtFD simulations. The process conditions are (a)(c) *P*= 200 W, *V*= 100 mm/s, l_{off} = 565 μm; (b)(d) *P*= 100 W, *V*= 100 mm/s, l_{off} = 385μm.
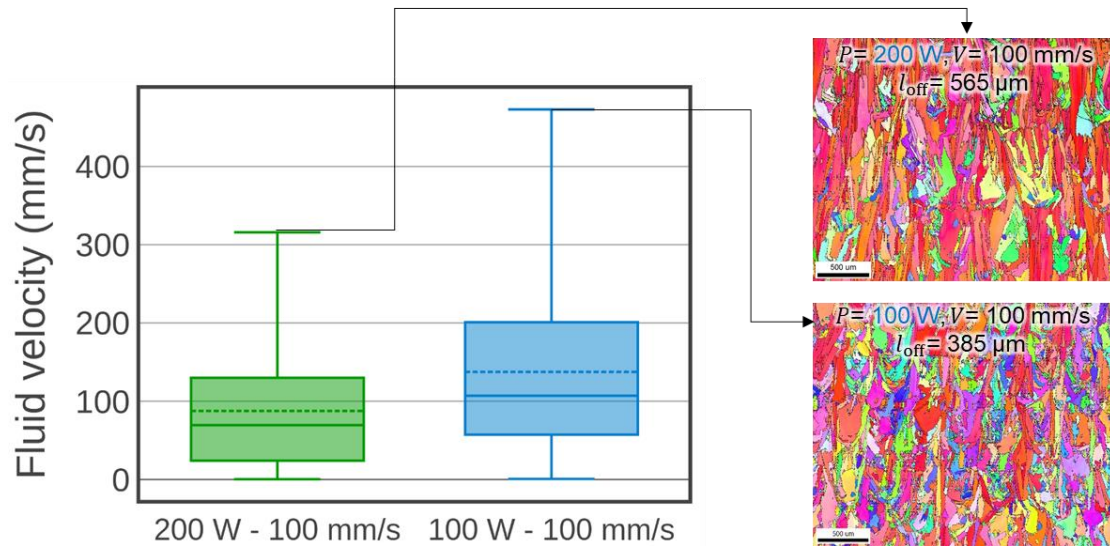
Fig. 5.23. Fluid velocity at the solidification front represented by box plot under the process conditions of the above two samples during solidification was extracted from CtFD simulation.
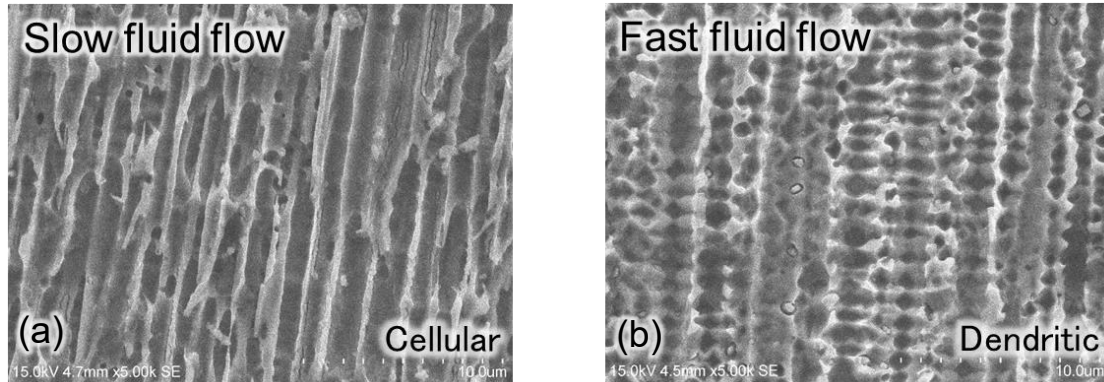
Fig. 5.24. SEM images of subgrain structures of CCM samples fabricated under different process conditions with different fluid velocity. The process conditions are (a) P= 200 W, V= 100 mm/s, l_{off} = 565 μm; (b) P= 100 W, V= 100 mm/s, l_{off} = 385μm.
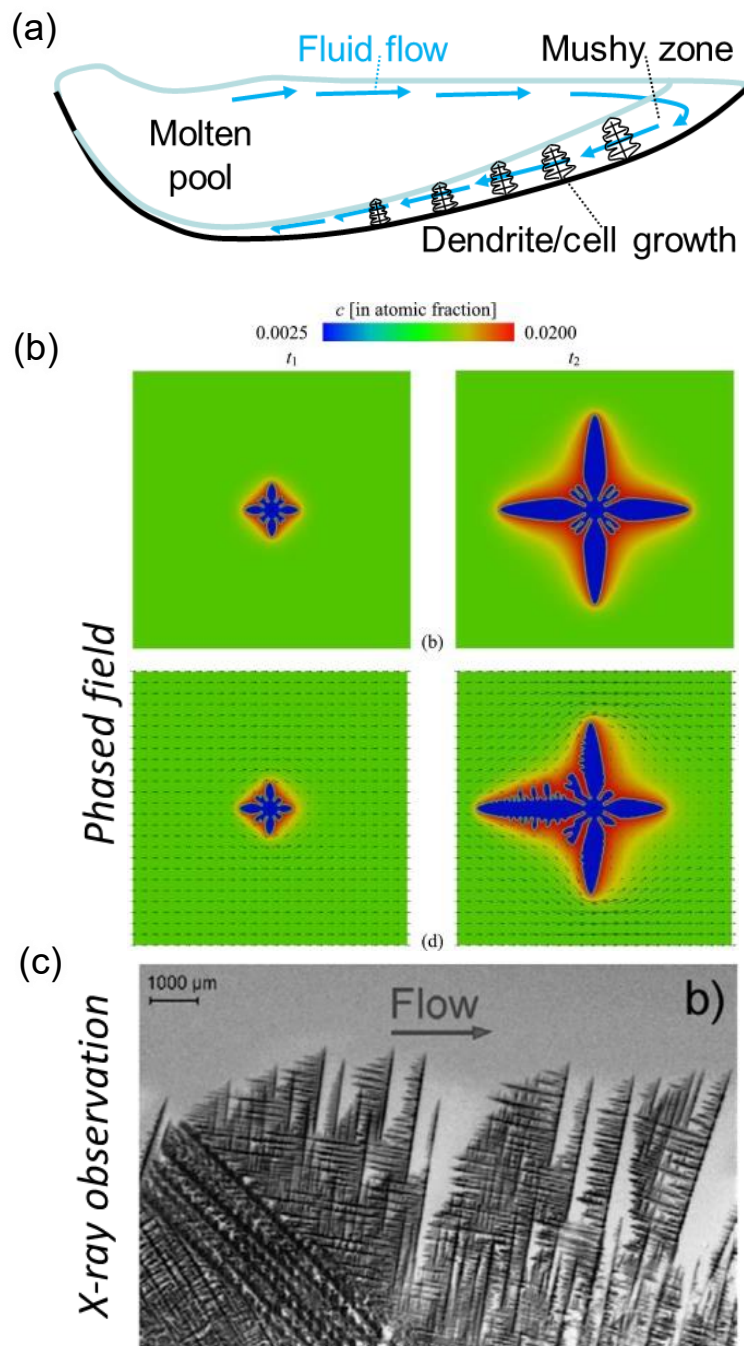
Fig. 5.25. (a) Fluid flow is indicated by streamlines and is vertical to the growing direction of dendrite/cell during solidification is shown in a schematic description. The effect of melt convection significantly influences the dendritic formation, which is shown by (b) phase-field simulation [36] and (c) experimental X-ray observation [37].
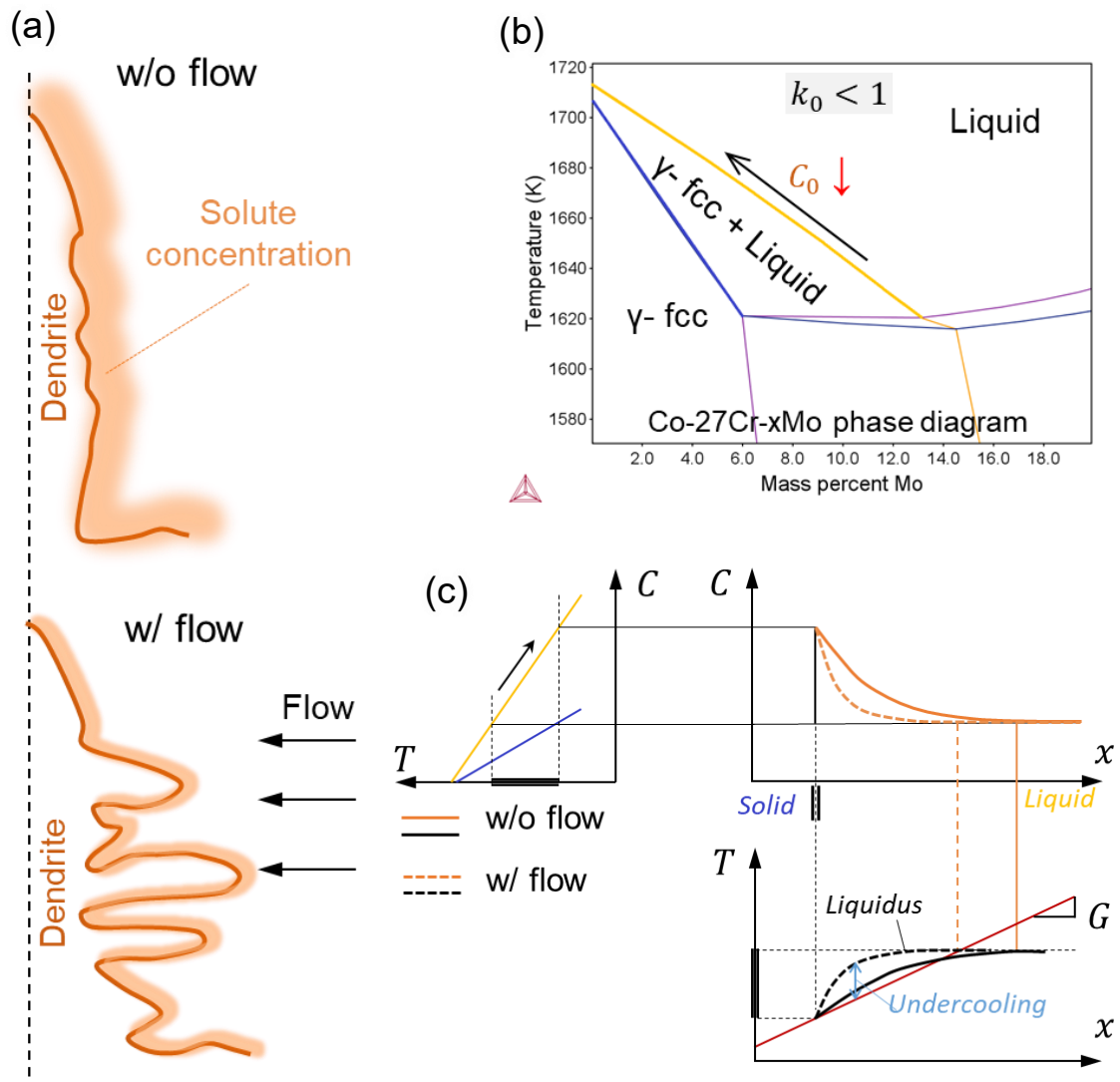
Fig. 5.26. Schematic illustrations show that (a) fluid flow can change the local gradient of solute concentration near the solid/liquid interface. (b) For alloys with $k_0 < 1$, as solute concentration decreases, liquidus increases. (c) Thus, under fast fluid flow, the local gradient of solute concentration near the solid/liquid interface increases to enlarge the undercooling ahead of solidification front.
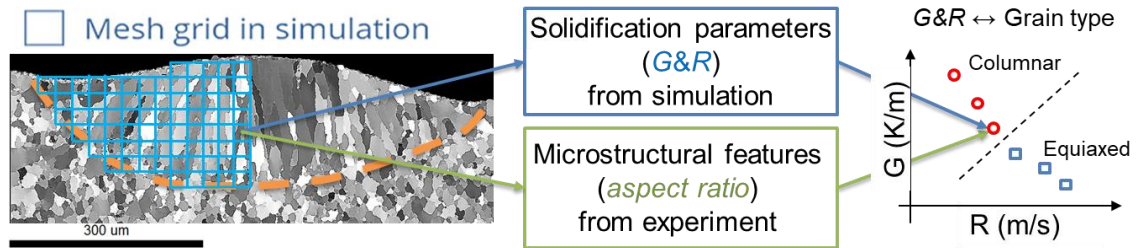
Fig. 5.27. Spatiotemporal values of *G*, *R,* and fluid velocity (*U*) were obtained from each mesh at the solidification front of the computing domain. They corresponded to the grain morphology determined experimentally.
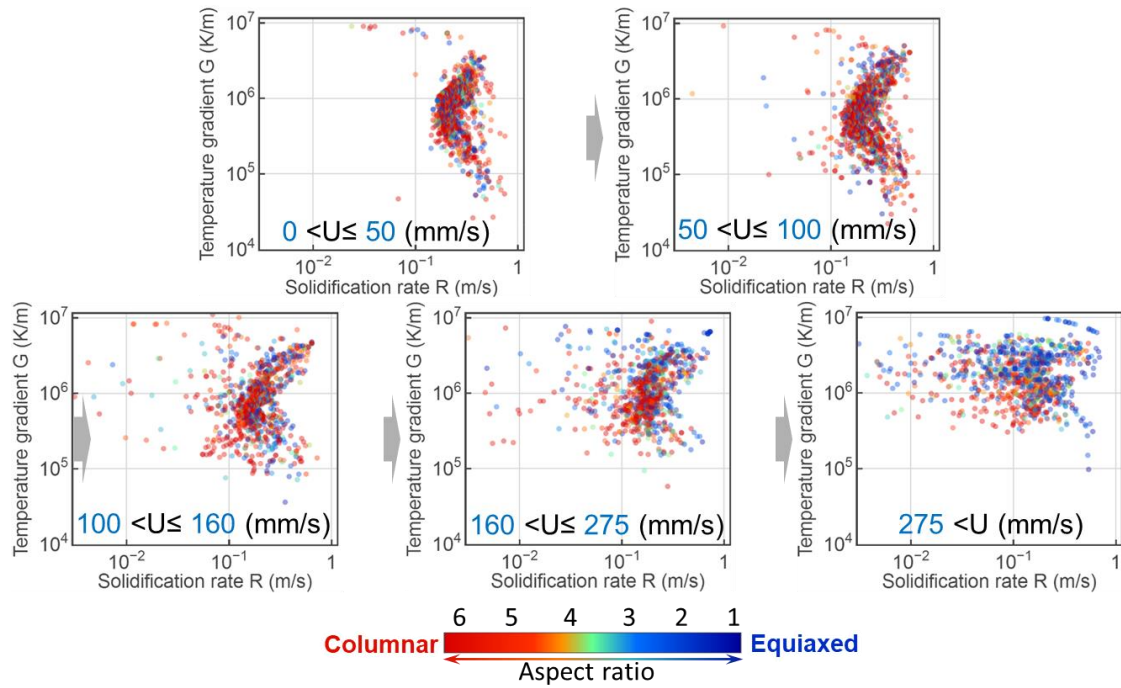
Fig. 5.28. *G–R* points colored by the aspect ratio of grains and organized to be segmentation depending on the fluid velocity (*U*) of the solidification front, the data was extracted under a series of process parameters (*P* = 200, 400, 600, 800, 1000 W and *V* = 300 mm/s).

References

[1]   A. Rai, H. Helmer, and C. Körner, "Simulation of grain structure evolution during powder bed based additive manufacturing," *Additive Manufacturing*, vol. 13, pp. 124–134, Jan. 2017.

[2]   H. Helmer, A. Bauereiß, R. F. Singer, and C. Körner, "Grain structure evolution in Inconel 718 during selective electron beam melting," *Materials Science and Engineering: A*, vol. 668, pp. 180–187, Jun. 2016.

[3]   S.-H. Sun, Y. Koizumi, S. Kurosu, Y.-P. Li, and A. Chiba, "Phase and grain size inhomogeneity and their influences on creep behavior of Co–Cr–Mo alloy additive manufactured by electron beam melting," *Acta Materialia*, vol. 86, pp. 305–318, Mar. 2015.

[4]   M. J. Bermingham, D. H. StJohn, J. Krynen, S. Tedman-Jones, and M. S. Dargusch, "Promoting the columnar to equiaxed transition and grain refinement of titanium alloys during additive manufacturing," *Acta Materialia*, vol. 168, pp. 261–274, Apr. 2019.

[5]   N. Raghavan, R. Dehoff, S. Pannala, S. Simunovic, M. Kirka, J. Turner, N. Carlson, and S. S. Babu, "Numerical modeling of heat-transfer and the influence of process parameters on tailoring the grain morphology of IN718 in electron beam additive manufacturing," *Acta Materialia*, vol. 112, pp. 303–314, Jun. 2016.

[6]   Y. Kok, X. P. Tan, P. Wang, M. L. S. Nai, N. H. Loh, E. Liu, and S. B. Tor, "Anisotropy and heterogeneity of microstructure and mechanical properties in metal additive manufacturing: A critical review," *Materials & Design*, vol. 139, pp. 565–586, Feb. 2018.

[7]   V. Manvatkar, A. De, and T. DebRoy, "Spatial variation of melt pool geometry, peak temperature and solidification parameters during laser assisted additive manufacturing process," *Materials Science and Technology*, vol. 31, no. 8, pp. 924–930, 2015.

[8]   A. Bauereiß, T. Scharowsky, and C. Körner, "Defect generation and

propagation mechanism during additive manufacturing by selective beam melting," *Journal of Materials Processing Technology*, vol. 214, no. 11, pp. 2522–2528, Nov. 2014.

[9] W. Yan, Y. Qian, W. Ge, S. Lin, W. K. Liu, F. Lin, and G. J. Wagner, "Meso-scale modeling of multiple-layer fabrication process in Selective Electron Beam Melting: Inter-layer/track voids formation," *Materials & Design*, vol. 141, pp. 210–219, Mar. 2018.

[10] C. Körner, "Additive manufacturing of metallic components by selective electron beam melting — a review," *International Materials Reviews*, vol. 61, no. 5, pp. 361–377, Jul. 2016.

[11] John D Anderson, "Governing equations of fluid dynamics," *Computational Fluid Dynamics*, pp. 15–51, 2009.

[12] FlowScience, "FLOW-3D | Highly-Accurate CFD Software | Free Surface Transient Flows," 2015. [Online]. Available: https://www.flow3d.com/products/flow-3d/. [Accessed: 17-Feb-2018].

[13] R. W. Messler, Ed., *Principles of Welding*. Weinheim, Germany: Wiley-VCH Verlag GmbH, 1999.

[14] Y. Zhao, Y. Koizumi, K. Aoyagi, D. Wei, K. Yamanaka, and A. Chiba, "Molten Pool Behavior and Effect of Fluid Flow on Solidification Conditions in Selective Electron Beam Melting (SEBM) of a Biomedical Co-Cr-Mo Alloy," *Additive Manufacturing*, Dec. 2018.

[15] L. Thijs, F. Verhaeghe, T. Craeghs, J. Van Humbeeck, and J.-P. Kruth, "A study of the microstructural evolution during selective laser melting of Ti–6Al–4V," *Acta Materialia*, vol. 58, no. 9, pp. 3303–3312, May 2010.

[16] L. Thijs, B. Vrancken, J.-P. Kruth, and J. Van Humbeeck, "The influence of process parameters and scanning strategy on the texture in Ti6Al4V part produced by selective laser melting," in *Advanced Materials, Processes and Applications for Additive Manufacturing*, 2013.

[17] H. Y. Wan, Z. J. Zhou, C. P. Li, G. F. Chen, and G. P. Zhang, "Effect of scanning strategy on grain structure and crystallographic texture of Inconel 718

processed by selective laser melting," *Journal of Materials Science & Technology*, Feb. 2018.

[18] Z. W. J. W. C. G. Junjie LI, "Recent Progresses in Competitive Grain Growth During Directional Solidification," *Acta Metallurgica Sinca*, vol. 54, no. 5, pp. 657–668, Mar. 2018.

[19] N. Sridharan, P. Wolcott, M. Dapino, and S. S. Babu, "Microstructure and texture evolution in aluminum and commercially pure titanium dissimilar welds fabricated using ultrasonic additive manufacturing," *Scripta Materialia*, vol. 117, pp. 1–5, May 2016.

[20] G. P. Dinda, A. K. Dasgupta, and J. Mazumder, "Texture control during laser deposition of nickel-based superalloy," *Scripta Materialia*, vol. 67, no. 5, pp. 503–506, Sep. 2012.

[21] F. Geiger, K. Kunze, and T. Etter, "Tailoring the texture of IN738LC processed by selective laser melting (SLM) by specific scanning strategies," *Materials Science and Engineering: A*, vol. 661, pp. 240–246, Apr. 2016.

[22] L. Thijs, K. Kempen, J.-P. Kruth, and J. Van Humbeeck, "Fine-structured aluminium products with controllable texture by selective laser melting of pre-alloyed AlSi10Mg powder," *Acta Materialia*, vol. 61, no. 5, pp. 1809–1819, Mar. 2013.

[23] F. Yan, W. Xiong, and E. Faierson, "Grain Structure Control of Additively Manufactured Metallic Materials," *Materials*, vol. 10, no. 11, p. 1260, Nov. 2017.

[24] S. Kou, *Welding metallurgy*, Second. Hoboken: John Wiley & Sons, 2003.

[25] J. C. Ion, H. R. Shercliff, and M. F. Ashby, "Diagrams for laser materials processing," *Acta Metallurgica et Materialia*, vol. 40, no. 7, pp. 1539–1551, Jul. 1992.

[26] J. C. Ion, K. E. Easterling, and M. F. Ashby, "A second report on diagrams of microstructure and hardness for heat-affected zones in welds," *Acta Metallurgica*, vol. 32, no. 11, pp. 1949–1962, Nov. 1984.

[27] J. D. Hunt, "Steady state columnar and equiaxed growth of dendrites and

eutectic," *Materials Science and Engineering*, vol. 65, no. 1, pp. 75–83, Jul. 1984.

[28]   W. Kurz, B. Giovanola, and R. Trivedi, "Theory of microstructural development during rapid solidification," *Acta Metallurgica*, vol. 34, no. 5, pp. 823–830, May 1986.

[29]   T. Lienert, T. Siewert, S. Babu, V. Acoff, and S. W. P. Specifications, "ASM Handbook, Volume 6A, Welding Fundamentals and Processes," *system*, vol. 286, p. 287, 2011.

[30]   S. A. David, S. S. Babu, and J. M. Vitek, "Welding: Solidification and microstructure," *JOM*, vol. 55, no. 6, pp. 14–20, 2003.

[31]   H. E. Helmer, C. Körner, and R. F. Singer, "Additive manufacturing of nickel-based superalloy Inconel 718 by selective electron beam melting: Processing window and microstructure," *Journal of Materials Research*, vol. 29, no. 17, pp. 1987–1996, Sep. 2014.

[32]   B. Chalmers, *Principles of solidification.* New York: Wiley, 1964.

[33]   M. R. Jonathan Dantzig, *Solidification*, Second edi. Lausanne: EPFL Press, 2016.

[34]   N. Raghavan, S. Simunovic, R. Dehoff, A. Plotkowski, J. Turner, M. Kirka, and S. Babu, "Localized melt-scan strategy for site specific control of grain size and primary dendrite arm spacing in electron beam additive manufacturing," *Acta Materialia*, vol. 140, pp. 375–387, Nov. 2017.

[35]   V. Matilainen, H. Piili, A. Salminen, T. Syvänen, and O. Nyrhilä, "Characterization of process efficiency improvement in laser additive manufacturing," in *Physics Procedia*, 2014, vol. 56, no. C, pp. 317–326.

[36]   R. Rojas, T. Takaki, and M. Ohno, "A phase-field-lattice Boltzmann method for modeling motion and growth of a dendrite for binary alloy solidification in the presence of melt convection," *Journal of Computational Physics*, vol. 298, pp. 29–40, Oct. 2015.

[37]   N. Shevchenko, O. Roshchupkina, and S. Eckert, "X-ray Observations Showing the Effect of Fluid Flow on Dendritic Solidification in Ga-In Alloys,"

in *Advances in the Science and Engineering of Casting Solidification*, Cham: Springer International Publishing, 2015, pp. 241–248.

[38]   A. Kumar, P. Dutta, S. Sundarraj, and M. J. Walker, "Remelting of Solid and its Effect on Macrosegregation During Solidification," *Numerical Heat Transfer, Part A: Applications*, vol. 51, no. 1, pp. 59–83, Nov. 2007.

Chapter 6

Mechanisms for phase transformation of PBF-EB-built Co-Cr-Mo alloy

6.1. Introduction

PBF-EB allows CCM implants with patient-customization to be fabricated with high quality and complex geometry. However, the variability in the properties of PBF-EB-built CCM alloy, mainly due to the lack of understanding of the mechanisms that govern microstructural inhomogeneity, brings limitations in wide application. Though prior studies [1][2][3][4][5] revealed the variability of critical microstructural features of AM-built CCM alloy, the more in-depth understanding of the physical mechanisms that govern microstructural inhomogeneity and expected flexible control still deserve much of exploration. Depending on temperature conditions, the γ-fcc → ε-hcp phase transformation in CCM alloy can take place via diffusional-massive transformation or diffusionless-martensitic transformation [6][7][8]. Alloys undergoing massive transformations whose driving force is the difference in free energy, will generally also transform in a martensitic manner when they are cooled down at sufficiently high quench rates (athermal-martensitic), or they are aged at sufficiently low aging temperatures (isothermal-martensitic) to overwhelm the nucleation of the massive ε phase [8]. In AM, each as-built sample experiences a different and complex thermal history depending upon the sample geometry, building height [9][10], and especially the process parameters [11][12][13] during the layer-by-layer process. Thus, by manipulating the process conditions of PBF-EB, the phase transformation mechanism needs to be understood deeply, and more importantly, the distributions and fractions of γ/ε phases are highly expected to be controlled.

In this study, the microstructural inhomogeneity in terms of matrix phase constitution of PBF-EB-built Co-28Cr-6Mo alloy was characterized. The present paper addressed the determination of the thermal history of the PBF-EB process and its effect

on phase transformation, aided by the analysis of the numerical simulation of heat transfer.

6.2. Methodology

6.2.1. PBF-EB processing and microstructure characterization

The samples with cube-shape and dimensions of 10 mm ×10 mm ×10 mm were produced using an Arcam®A2X machine. We applied a gas-atomized Co-28Cr-6Mo alloy powder (mean diameter: 65 μm) with a layer thickness of 70 μm. The electron beam power (P) ranged between 100 and 1000 W, and the scan speed (V) ranged between 100 and 10000 mm/s. The process parameters shown in Fig. 6.2(b) were determined depending on our prior experience of processability for CCM. For ensuring the dense formations, the pre-implemented single-track melting experiments determined the line offset (l_{off}) according to the dimensions of the melt region. Under such line offsets, the overlap between the adjacent melt tracks should be more than 1.5 times of the layer thickness. The resulting line energy ($E_{line} = P/V$) ranged between 0.1 and 10 J/mm, and the area energy ($E_{area} = P/(V \cdot l_{off})$) ranged between 2.2 and 11 J/mm2. The preheating temperature was kept at 1123 K for all of the samples to avoid powder smoke. As shown in Fig. 6.5(b), a xy-scanning strategy in which the bidirectional scanning direction was rotated by 90° in each layer was applied for the building process.

The block samples were cut along the building direction (z-axis) using a wire electric discharge machine. The sectioned samples were ground and polished by standard metallographic techniques followed by a final polishing using 0.04 μm colloidal silica suspension for one hour. Electron backscattered diffraction (EBSD) and scanning electron microscopy based on the backscattered electron (BSE) signals were then utilized to analyze the microstructure near the center of the width in each sample.

6.2.2. Numerical simulation for evaluating the thermal history

We have established a 3D heat transfer model that developed using a commercial Multiphysics-modeling program—Flow 3D$^®$ [14]. The energy efficiency of the electron beam was assumed to be 90% [15]. The heat loss of the object was induced by conduction and radiation. Given the high vacuum condition of 0.1 Pa in the PBF-EB building chamber, cooling by air convection was neglected, which also improved the calculation efficiency. Our previous study [16] described the detailed information of the setup of the numerical model, thermophysical properties of the material, parameters/coefficients applied in the simulation, and modeling validation.

To ensure reasonable calculation accuracy yet affordable time expense of simulation, we performed a 3D steady-state heat transfer simulation with some simplifications. As with rapid electron beam translation speed (~ 10000 mm/s) in this work, the moving-spot heat source was approximated as an equivalent plane heat source P_{plane}, shown in Fig. 6.1(a). In addition, since the layer thickness (70 μm) was much smaller than the height of sample (10000 μm), the layer-by-layer building was simplified as bulk increment with each increment height of 2500 μm (Fig. 6.1(b)). While building the samples, the heat source was carried out in a loop: $\Delta t_{\text{scan}} \times n_1$ ($P_{\text{plane}} = P_{\text{spot}}$) → $\Delta t_{\text{standby}}$ ($P_{\text{plane}} = 0$), repeating as n_2 times. Δt_{scan} was the time for a single-track scan, and n_1 was the scan numbers of one layer in a sample. $\Delta t_{\text{standby}}$ was the time for the building of all the other samples in one-layer except the targeted sample, and n_2 was the effective layer number of a bulk increment.

6.3. Isothermal and athermal γ → ε phase transformation during PBF-EB

During PBF-EB, the earlier built part is kept at high temperatures during the subsequently repeated melting process that is similar to an isothermal-aging treatment. Thus, the γ → ε phase transformation can occur at the lower part of a PBF-EB-built

CCM alloy with considerable height.

Figure 6.3 shows the EBSD phase map of vertical cross-sectional microstructure and EBSD pole figures of selected ε grain and original γ grain at the lower part of the as-PBF-EB-built sample. At the left side of Fig. 6.3(a), the ε grain grew across the grain boundary of the adjacent γ grain. There was no S-N OR between the ε grain and the adjacent γ grain (Fig. 6.3(b)), which indicated that the ε phase here formed due to isothermal aging involving a diffusional-massive transformation. On the other hand, on the right side of Fig. 6.3(a), the ε grains were embedded within the original γ grain. The corresponding EBSD pole figures (Fig. 6.3(c)) revealed that the Shoji-Nishiyama orientation relationship (S-N OR: $(111)_\gamma // (0001)_\varepsilon$; $[10\bar{1}]_\gamma//[11\bar{2}0]_\varepsilon$) was satisfied between the new ε grain and original γ grain. This indicated that the ε phase observed here originated from the isothermal $\gamma \to \varepsilon$ martensitic transformation in which the nucleation and growth of new ε grain are limited within the original γ grain. Above results suggested that the isothermal $\gamma \to \varepsilon$ phase transformation taken place via both diffusionless-martensitic and diffusion-massive manners in the as-PBF-EB-built sample. As shown in Fig. 6.4, these two different manners are thought to be competitive with each other, depending on temperature condition [20][17].

In addition, as shown in Fig. 6.5, the athermal ε martensite characterized by the parallel arrays of thin straight markings [18] was observed within γ-fcc dendrites in the upper part of the as-PBF-EB-built sample. This small amount of athermal ε martensite was considered to be induced by rapid cooling during solidification of PBF-EB.

6.4. Distributions of γ and ε phases in as-PBF-EB-built samples

Since the relative position of the sample on the base plate affects the conditions of heat accumulation and conduction [3], the samples located at axisymmetric positions with respect to the base plate were selected for observation. Moreover, the selected two samples exhibited two typical microstructural features regarding the distributions of γ and ε phases. As shown in Fig. 6.6(a), Sample A and Sample B with different process

parameters and located on both sides of the base plate, were taken as the subjects of the study. Fig. 6.6(c)(d) show the EBSD IPF maps and phase maps of cross-sectional microstructures in different parts along with the building height. The orientation shown in the IPF maps was in the normal direction (*x*-direction in Fig. 6.6(b)). γ and ε phases in the phase maps were colored as red and green, respectively. In Sample A (Fig. 6.6(c)), the fraction of the ε phase decreased from the bottom to top of the sample. Notably, being different from the results of Sample A and previous studies [1][2][3][4][5], in Sample B (Fig. 6.6(d)), there was no ε phase in the top and bottom but ε phase only appeared in a short range of the lower part away from the bottom. As with the similar conditions of heat accumulation and conduction, the difference in ε phase distribution between Sample A and Sample B was considered to originate from the variation of thermal history determined by process parameters.

6.5. Effect of thermal history on phase transformation

Figure 6.7 shows the experimental thermal history during PBF-EB process at the bottom center of the base plate measured by a thermocouple equipped in the building chamber. The variation in temperature corresponded to the process stages consisting of (i) preheating process in which the base plate is heated to the pre-set temperature (1123 K) by using a de-focused beam at a considerably high scan speed of 14600 mm/s; (ii) heating & building process in which preheating repeats following the building of each layer to slightly sinter the newly raked powder and keep the temperature of the base plate to be almost constant; and (iii) cooling after completion of the total build objects.

The simulation of the temperature field of the base plate is shown in Fig. 6.8. The base plate was heated by an equivalent plane heat source with a power of 2280 W (standard parameter of heating) till the temperature in the bottom center reached 1098 K (the average temperature during the heating & building process (Fig. 6.7)). Then the temperature field of the base plate acted as the thermal boundary condition for simulating the thermal history of each sample. Figure 6.9 shows the simulated temperature evolutions of Sample A and Sample B. Note that, as build height increased

(from increment ① to ④), the temperature of the center position in each increment increased because the building region was becoming far from the base plate accompanied with reduced thermal conduction but increased thermal accumulation, which was a result of the long distance for the heat transfer through the earlier-built part. Besides, as with more considerable energy input ($E_{area} = 4.4$ J/mm^2) of Sample B than that ($E_{area} = 2.6$ J/mm^2) of Sample A, the individual increment in Sample B possessed a higher temperature than the corresponding increment in Sample A.

The isothermal martensitic transformation occurs at 973 K or below, while the massive transformation is dominant at a higher temperature range [20]. The diffusional-massive transformation occurs via a short-range diffusion process and associated interface migration, involving a kinetic process [19][20]. The solid-state transformation usually involves nucleation and growth and are generally described by the Johnson–Mehl–Avrami–Kolmogorov (JMAK) model in which nucleation and growth rates are time-dependent under isothermal condition [21]. The phase transition rate (X) is a function of holding time (t):

$$X = 1 - \exp(-kt^n), \tag{6-1}$$

where k is the coefficient of the temperature-dependent reaction rate, and n is a constant dependent on the nature of growth mechanisms involved in the transformation (Avrami). Then,

$$X(\gamma \to \varepsilon) \approx 1 - \exp\{-(4\pi/3)n_0 r_\varepsilon^3 t^3\}, \tag{6-2}$$

where n_0 is the nuclei density (m^{-3}). The growth rate of the ε phase r_ε is expressed as

$$r_\varepsilon = \left(D_{Co}^{\gamma/\varepsilon}/\delta RT\right) \cdot \Delta G_{\gamma \to \varepsilon}, \tag{6-3}$$

where $D_{Co}^{\gamma/\varepsilon}$ is the diffusion coefficient of cobalt (m^2·s^{-1}) obtained in [22], $\Delta G_{\gamma \to \varepsilon}$ is the difference in free energy between γ and ε phases (J·mol^{-1}) calculated by Thermo-Calc [23], and δ is the γ/ε interface width of three atomic sites (4.5×10^{-10} m) [24]. From the above calculation, the isothermal TTT curve of the $\gamma \to \varepsilon$ diffusional-massive transformation was obtained and shown in Fig. 6.10. This diagram showed a good agreement with the experimental data in [20]. The temperature region for martensitic

transformation should locate below this TTT curve.

From the simulated temperature fields of each part shown in Section 3.3 (Fig. 6.8), the temperature ranges that Sample A and Sample B underwent during PBF-EB are annotated on the right side of Fig. 6.10. Accordingly, the middle and lower parts of Sample A were roughly at the temperature range of martensitic transformation. On the other hand, as with more considerable energy input (E_{area} = 4.4 J/mm^2) of Sample B than that (E_{area} = 2.6 J/mm^2) of Sample A, Sample B was generally kept at a higher temperature range of massive transformation. EBSD data can help to clarify which mechanism the γ → ε phase transformation is taking place. Figure. 6.11 shows the pole figures taken from the γ and ε phases in the middle and lower parts of Sample A and Sample B. S-N OR: $(111)_\gamma$ // $(0001)_\varepsilon$; $[10\bar{1}]_\gamma$//$[11\bar{2}0]_\varepsilon$ between γ and ε phases was observed in Sample A, while no clear orientation correlation between γ and ε phases was observed in Sample B. In addition, the histograms of the misorientation angle between adjacent ε phase in Sample A and Sample B are shown in Fig. 6.12. In the case of martensitic transformation, the four martensite variants corresponding to the $(0001)_\varepsilon$ plane transformed from the four $\{111\}_\gamma$ planes, would present the expected misorientation angle of 70.5° [25]. Hence, in Sample A (Fig. 6.12(a)), there was a peak near 70.5° in the histogram of misorientation angle, which clearly showed that the martensitic transformation with S-N OR was dominant. In sample B (Fig. 6.12(b)), no apparent peak near 70.5° was recognized, indicating that the ε phase with near-random orientation formed here via diffusional-massive transformation. Above results showed a good agreement between the simulated temperature fields and phase transformation mechanism clarified by experiments. We can conclude that the process parameters substantially influence the thermal history, and subsequently, the γ → ε phase transformation mechanism in CCM alloy during PBF-EB.

As with the similar conditions of heat accumulation and conduction correlated to the relative positions on the base plate, the difference in γ/ε phase distributions between Sample A and Sample B should be closely related to the thermal history.

The building period of PBF-EB based on experimental temperature history beneath

the center of the base plate (Fig. 6.7), is additionally annotated in Fig. 6.10. In Sample A, the temperatures of the middle and lower parts were estimated in the range of martensitic transformation, as discussed in the above section. The kinetics of isothermal martensitic transformation is difficult to evaluate without a specific experiment because the rate controlling mechanisms are sophisticated and do not yield general rules [26][27][28]. Nevertheless, the displacive-martensitic transformation is coordinated action rather than a diffusional movement. Thus, the propagation of ε-martensite is assumed not to show significant time dependency as massive transformation possesses, when there has already been some martensite in the matrix [29] (athermal ε-martensite (Fig. 6.5) in the case of this study). As the building height increased far and far from the base plate, the holding time for isothermal $\gamma \rightarrow \varepsilon$ martensitic transformation decreased. Though the top of Sample A was held at temperature range for massive transformation, the holding time was too short for the transformation taking place (Fig. 6.10). Accordingly, the ε phase fraction decreased with increasing distance from the bottom of Sample A (Fig. 6.6(c)) in which isothermal $\gamma \rightarrow \varepsilon$ martensitic transformation was dominant during PBF-EB.

Sample B experienced a temperature history in the range of massive $\gamma \rightarrow \varepsilon$ transformation or higher, as with more considerable energy input ($E_{area} = 4.4$ J/mm^2) of Sample B than that ($E_{area} = 2.6$ J/mm^2) of Sample A. We can see from Fig. 6.10, in the upper part, the temperature achieved was almost higher than that of the $\gamma \rightarrow \varepsilon$ transition range, and thus, single γ phase was inferred to remain without phase transformation after the completion of PBF-EB building process. The lower part was mainly kept at the range for massive transformation. Notably, as the position was getting closer to the bottom (from increment ② to ① of Sample B in Fig. 6.10), the time period required for activation of massive $\gamma \rightarrow \varepsilon$ transformation increased and even became longer than the total period of the heating & building during PBF-EB. Thus, no ε phase appeared in the lowest part of Sample B even though the part underwent the longest holding time. This can explain why ε phase only presented in a short range of the lower part away from the bottom of Sample B (Fig. 6.6(d)) where time period

required for massive $\gamma \rightarrow \varepsilon$ transformation is relatively short (Fig. 6.10). The results also indicated that the martensitic transformation carried out more easily and quickly than massive transformation during the isothermal aging process of post-melting in PBF-EB.

The above discussion suggests that the difference in γ/ε phase distribution is a result of the thermal history determining the mechanism by which the $\gamma \rightarrow \varepsilon$ phase transformation is taking place, depending on PBF-EB process parameters. Accordingly, the phase transformation can be controlled by manipulating the process parameters. For example, in Fig. 6.13, the sample almost without the ε phase was fabricated with a considerably large energy input ($E_{\text{area}} = 11.1$ J/mm^2), because the overall sample was assumed to hold at a higher temperature that exceeds the temperature range for $\gamma \rightarrow \varepsilon$ transformation. To make a better use of the mechanisms identified in the presented study, a feasible control of phase constitution and distribution of γ/ε phases needs to be developed in PBF-EB of CCM alloy in the future, in which broader process conditions need to be considered such as preheating temperature, scan strategy, selective melting area, size and shape of built object and the position within the object.

Conclusions

Through the experimental characterization of the microstructure and analysis of the simulation results, the mechanisms of microstructural inhomogeneity regarding matrix phase constitution of PBF-EB-built Co-28Cr-6Mo alloy were analyzed and summarized as follows:

1) The isothermal and athermal $\gamma \rightarrow \varepsilon$ phase transformations took place in CCM alloy during PBF-EB. Isothermal $\gamma \rightarrow \varepsilon$ transformation occurred through both manners: diffusionless-martensitic and diffusion-massive transformation.

2) The difference in γ/ε phase distribution was a result of the thermal history. Depending on PBF-EB process conditions, thermal history determined the mechanism by which the $\gamma \rightarrow \varepsilon$ phase transformation was taking place.

3) In the sample with a lower energy input ($E_{area} = 2.6$ J/mm^2), $\gamma \rightarrow \varepsilon$ martensitic transformation with S-N OR was dominant. With the building height increasing away from the base plate, ε phase fraction decreased, because the holding time for martensitic transformation decreased.

4) In the sample with a higher energy input ($E_{area} = 4.4$ J/mm^2), the ε phase with near-random orientation formed via diffusional-massive transformation. ε phase only presented in a short range of the lower part away from the bottom where the time period required for massive $\gamma \rightarrow \varepsilon$ transformation was relatively short.

Fig. 6.1. Schematic diagram of the modeling simplification for numerical simulation of thermal history: (a) the moving-spot heat source was approximated as an equivalent plane heat source; (b) the layer-by-layer building was simplified as bulk-increment.
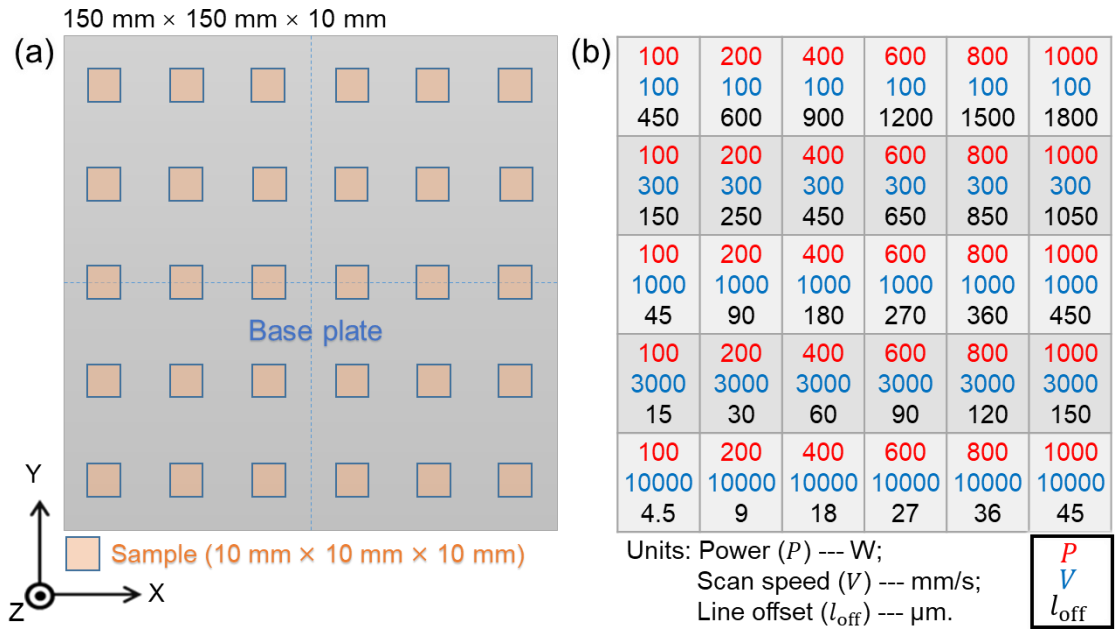
Fig. 6.2. (a) Samples with cube-shape and dimensions of 10 mm ×10 mm ×10 mm were built on a base plate with the size of 150 mm × 150 mm × 10 mm and (b) process parameters of each sample is shown in the corresponding position.
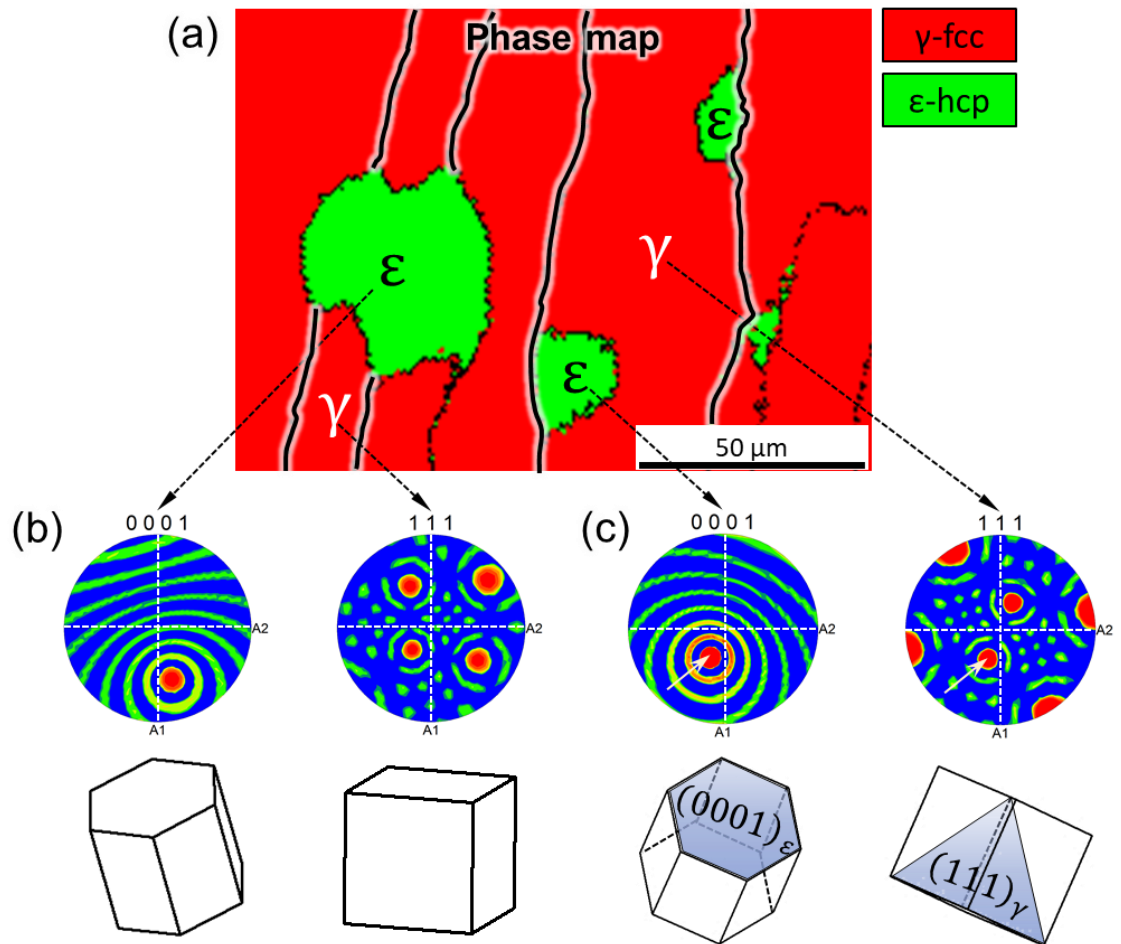
Fig. 6.3. (a) EBSD phase map of vertical cross-sectional microstructure and (b)(c) EBSD pole figures of selected ε grain and original γ grain at the lower part of the as-PBF-EB-built sample. The process parameter is $P=600$ W, $V=300$ mm/s, $l_{off}=455$ μm.
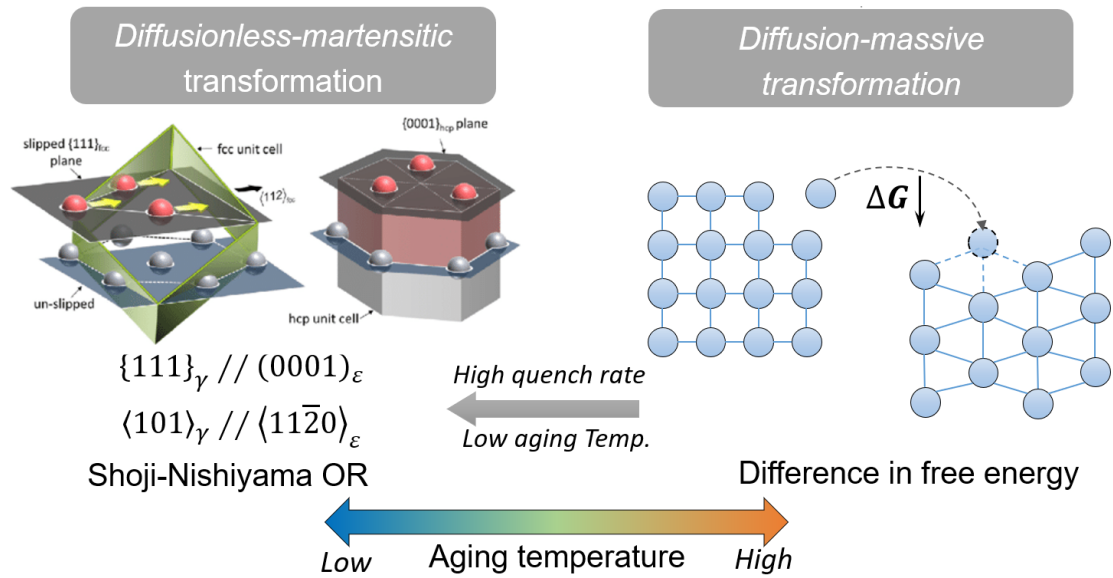
Fig. 6.4. Isothermal γ → ε phase transformation taken place via both diffusionless-martensitic and diffusion-massive manners in the as-PBF-EB-built sample. These two different manners are thought to be competitive with each other, depending on temperature condition.
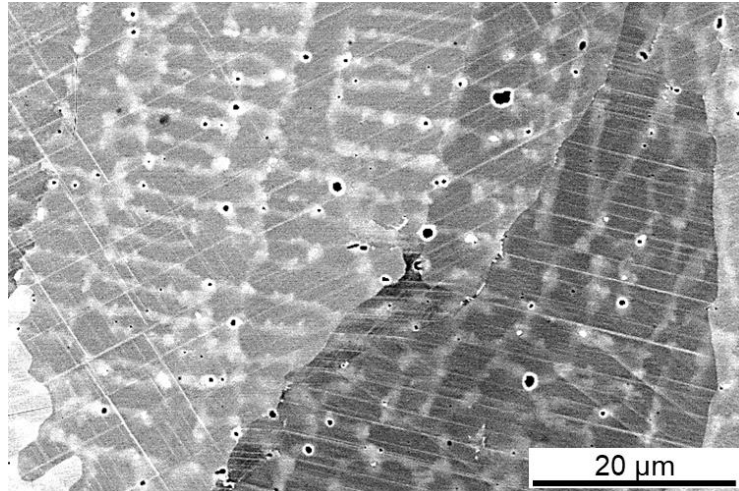
Fig. 6.5. Athermal ε martensite characterized by the parallel arrays of thin markings was observed within γ-fcc dendrites at the upper part of the as-PBF-EB-built sample. The process condition is $P = 600$ W, $V = 300$ mm/s, $l_{off} = 455$ μm.
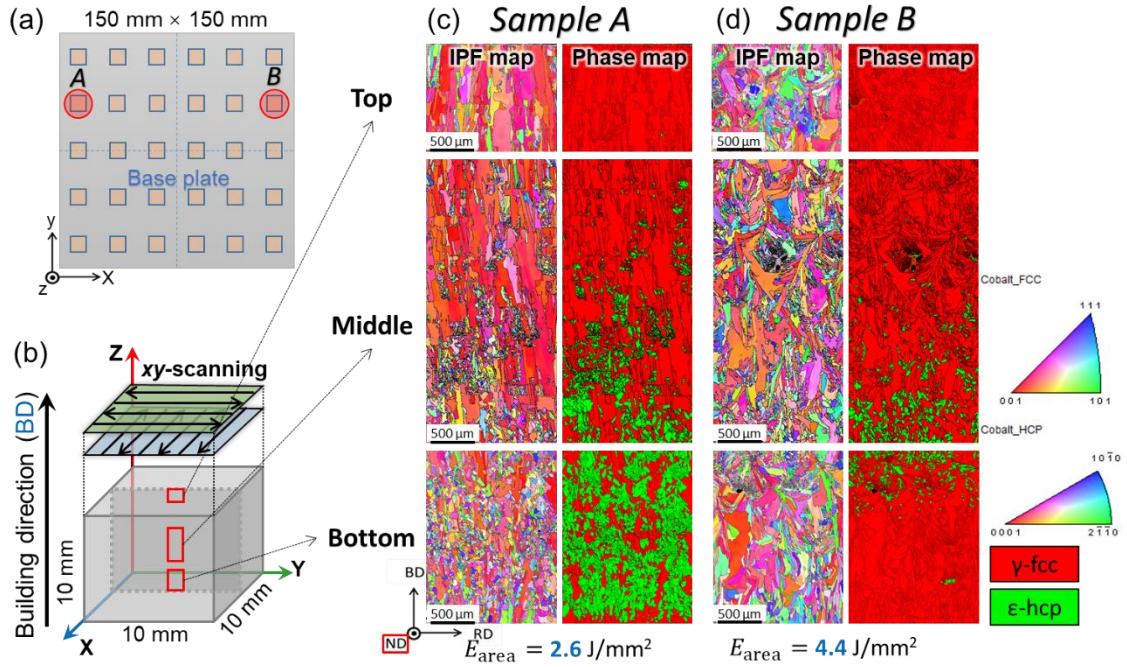
Fig. 6.6. Selected samples that exhibited typical microstructure locates at (a) axisymmetric positions with respect to the base plate. The field-of-view is depicted in (b). (c)(d) EBSD IPF maps and phase maps of vertical cross-sectional microstructure in different parts along with the building height. The process parameters are: $P= 100$ W, $V= 300$ mm/s, $l_{off}= 125$ μm (Sample A); $P= 1000$ W, $V= 300$ mm/s, $l_{off}= 750$ μm (Sample B).
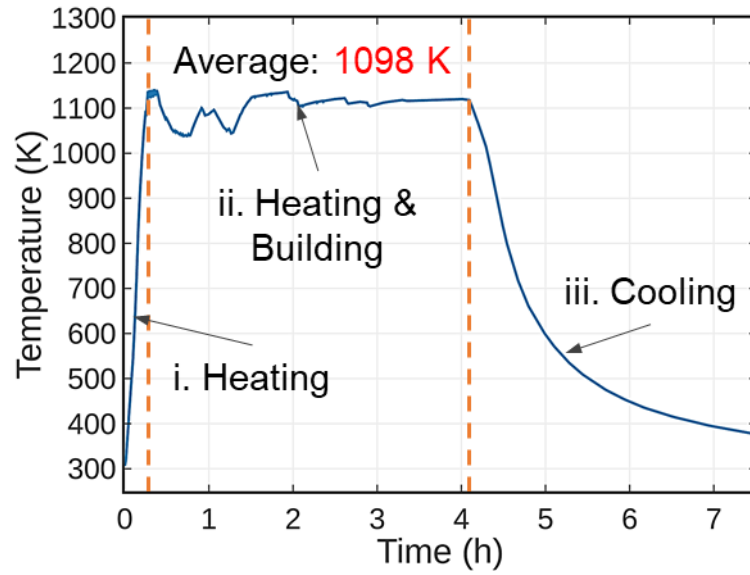
Fig. 6.7. Experimental thermal history during PBF-EB process at the bottom center of the base plate measured by a thermocouple equipped in the building chamber.
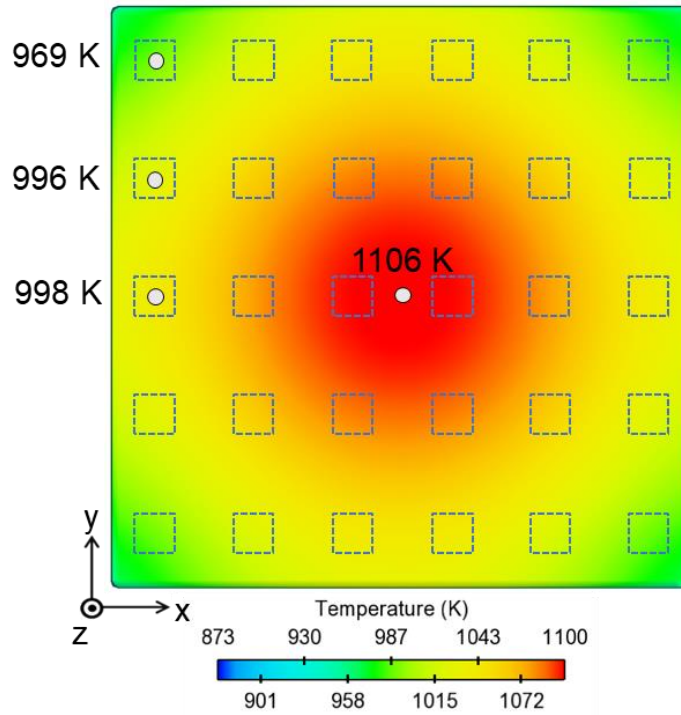
Fig. 6.8. Top view of the simulated temperature field of the base plate. The base plate was heated by an equivalent plane heat source till the temperature in the bottom center reached 1098 K.
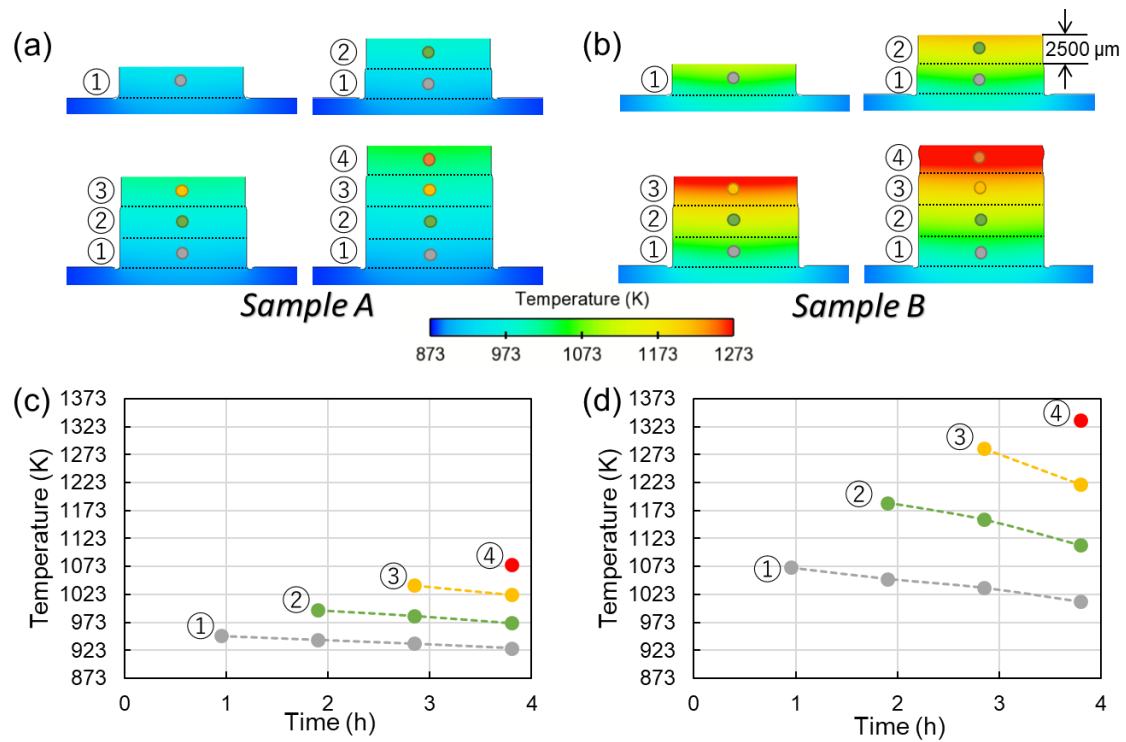
Fig. 6.9. Simulated temperature fields of (a) Sample A and (b) Sample B during the building process. (c)(d) The evolution of temperature at the center position in each increment of (c) Sample A and (d) Sample B.
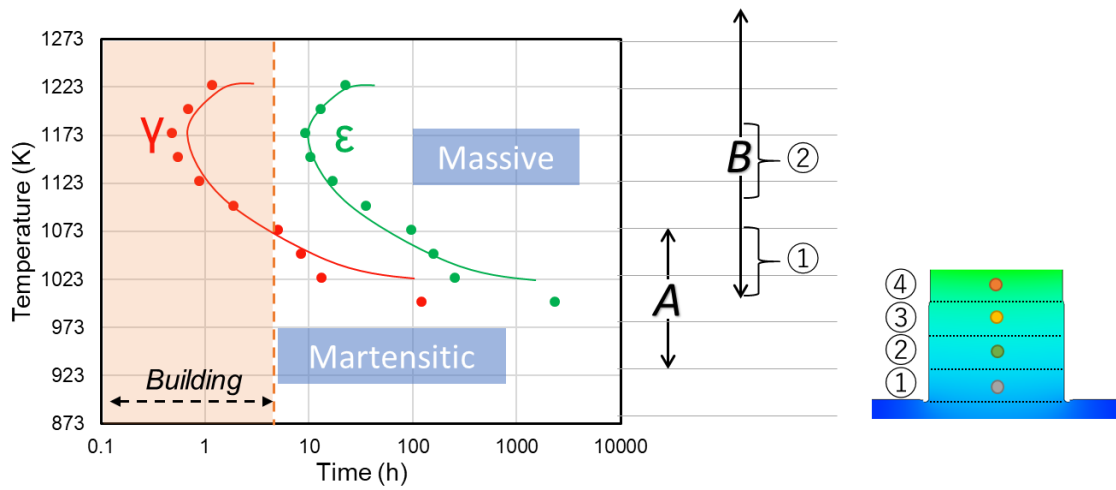
Fig. 6.10. Isothermal TTT curve of the γ → ε diffusional-massive transformation. The red and green curves present the start and end of transformation, respectively. The building period of PBF-EB was additionally annotated. The temperature ranges that Sample A and Sample B underwent during PBF-EB are annotated on the right side.
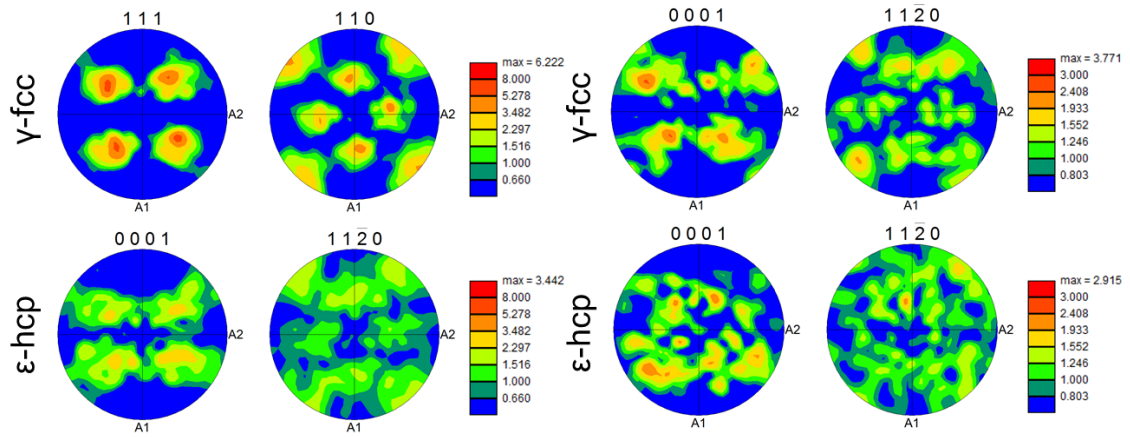
Fig. 6.11. EBSD pole figures were taken from the γ and ε phases in the middle and lower parts of (a) Sample A and (b) Sample B.
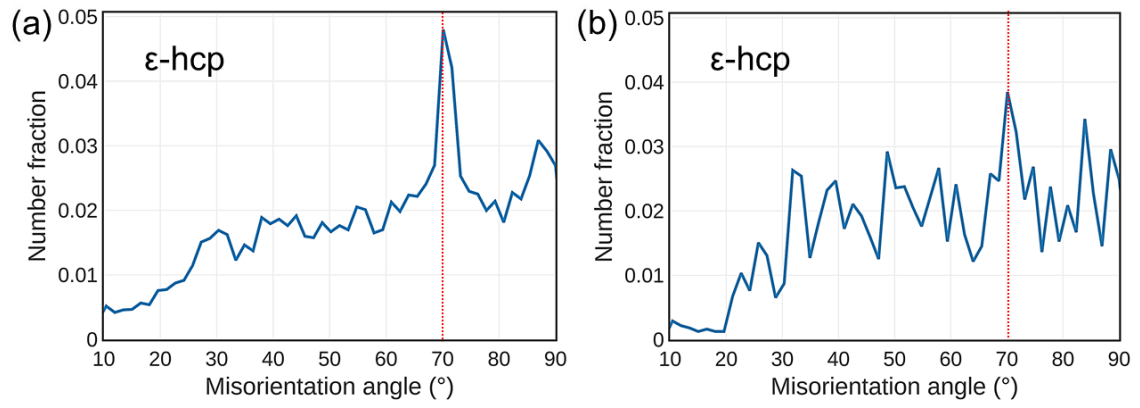
Fig. 6.12. Histograms of misorientation angle between adjacent ε phase in (a) Sample A and (b) Sample B.
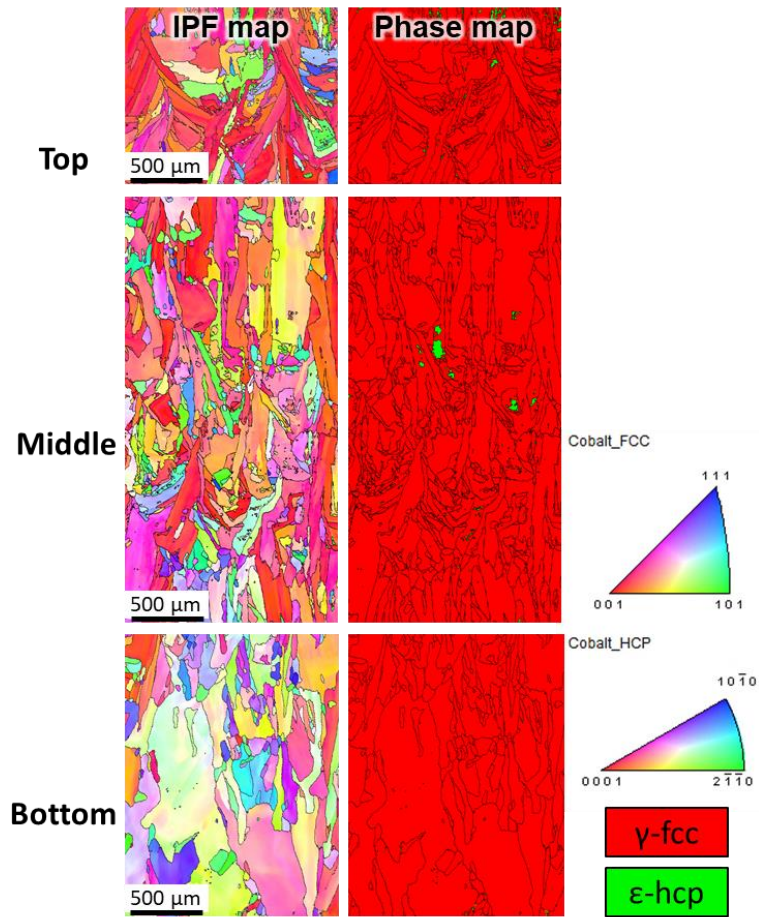
Fig. 6.13. EBSD IPF maps and phase maps of vertical cross-sectional microstructure in the sample almost without the ε phase. The process parameter is P= 1000 W, V= 100 mm/s, l_{off}= 900 μm.

References

[1] S.-H. Sun, Y. Koizumi, S. Kurosu, Y.-P. Li, and A. Chiba, "Phase and grain size inhomogeneity and their influences on creep behavior of Co–Cr–Mo alloy additive manufactured by electron beam melting," *Acta Materialia*, vol. 86, pp. 305–318, Mar. 2015.

[2] D. Wei, Y. Koizumi, A. Chiba, K. Ueki, K. Ueda, T. Narushima, Y. Tsutsumi, and T. Hanawa, "Heterogeneous microstructures and corrosion resistance of biomedical Co-Cr-Mo alloy fabricated by electron beam melting (EBM)," *Additive Manufacturing*, vol. 24, pp. 103–114, Dec. 2018.

[3] T. Takashima, Y. Koizumi, Y. Li, K. Yamanaka, T. Saito, and A. Chiba, "Effect of Building Position on Phase Distribution in Co-Cr-Mo Alloy Additive Manufactured by Electron-Beam Melting," *MATERIALS TRANSACTIONS*, vol. 57, no. 12, pp. 2041–2047, Dec. 2016.

[4] G. Barucca, E. Santecchia, G. Majni, E. Girardin, E. Bassoli, L. Denti, A. Gatto, L. Iuliano, T. Moskalewicz, and P. Mengucci, "Structural characterization of biomedical Co–Cr–Mo components produced by direct metal laser sintering," *Materials Science and Engineering: C*, vol. 48, pp. 263–269, Mar. 2015.

[5] Y. Kajima, A. Takaichi, N. Kittikundecha, T. Nakamoto, T. Kimura, N. Nomura, A. Kawasaki, T. Hanawa, H. Takahashi, and N. Wakabayashi, "Effect of heat-treatment temperature on microstructures and mechanical properties of Co–Cr–Mo alloys fabricated by selective laser melting," *Materials Science and Engineering: A*, vol. 726, pp. 21–31, May 2018.

[6] H. F. López and A. J. Saldivar-Garcia, "Martensitic Transformation in a Cast Co-Cr-Mo-C Alloy," *Metallurgical and Materials Transactions A*, vol. 39, no. 1, pp. 8–18, Jan. 2008.

[7] A. L. Ramirez-Ledesma, E. Lopez-Molina, H. F. Lopez, and J. A. Juarez-Islas, "Athermal ε-martensite transformation in a Co–20Cr alloy: Effect of rapid solidification on plate nucleation," *Acta Materialia*, vol. 111, pp. 138–147, Jun.

2016.

[8]   S. Kurosu, H. Matsumoto, and A. Chiba, "Isothermal Phase Transformation in
        Biomedical Co-29Cr-6Mo Alloy without Addition of Carbon or Nitrogen,"
        Metallurgical and Materials Transactions A, vol. 41, no. 10, pp. 2613–2625,
        Oct. 2010.

[9]   H. Zhao, A. Ho, A. Davis, A. Antonysamy, and P. Prangnell, "Automated
        image mapping and quantification of microstructure heterogeneity in additive
        manufactured Ti6Al4V," *Materials Characterization*, vol. 147, pp. 131–145,
        Jan. 2019.

[10]   B. E. Carroll, T. A. Palmer, and A. M. Beese, "Anisotropic tensile behavior of
        Ti–6Al–4V components fabricated with directed energy deposition additive
        manufacturing," *Acta Materialia*, vol. 87, pp. 309–320, Apr. 2015.

[11]   B. Bax, R. Rajput, R. Kellet, and M. Reisacher, "Systematic evaluation of
        process parameter maps for laser cladding and directed energy deposition,"
        Additive Manufacturing, vol. 21, pp. 487–494, May 2018.

[12]   J. J. S. Dilip, S. Zhang, C. Teng, K. Zeng, C. Robinson, D. Pal, and B. Stucker,
        "Influence of processing parameters on the evolution of melt pool, porosity,
        and microstructures in Ti-6Al-4V alloy parts fabricated by selective laser
        melting," *Progress in Additive Manufacturing*, vol. 2, no. 3, pp. 157–167, Sep.
        2017.

[13]   E. J. Schwalbach, S. P. Donegan, M. G. Chapman, K. J. Chaput, and M. A.
        Groeber, "A discrete source model of powder bed fusion additive
        manufacturing thermal history," *Additive Manufacturing*, vol. 25, pp. 485–498,
        Jan. 2019.

[14]   FlowScience, "FLOW-3D | Highly-Accurate CFD Software | Free Surface
        Transient Flows," 2015. [Online]. Available:
        https://www.flow3d.com/products/flow-3d/. [Accessed: 17-Feb-2018].

[15]   R. W. Messler, Ed., *Principles of Welding*. Weinheim, Germany: Wiley-VCH
        Verlag GmbH, 1999.

[16]   Y. Zhao, Y. Koizumi, K. Aoyagi, D. Wei, K. Yamanaka, and A. Chiba,

"Molten Pool Behavior and Effect of Fluid Flow on Solidification Conditions in Selective Electron Beam Melting (SEBM) of a Biomedical Co-Cr-Mo Alloy," *Additive Manufacturing*, Dec. 2018.

[17] S. Loewy, B. Rheingans, S. R. Meka, and E. J. Mittemeijer, "Unusual martensite-formation kinetics in steels: Observation of discontinuous transformation rates," *Acta Materialia*, vol. 64, pp. 93–99, Feb. 2014.

[18] C. Song, H. Park, H. Seong, H. F. Lo´pez, and L. Lo´pez, "Development of Athermal and Isothermal e-Martensite in Atomized Co-Cr-Mo-C Implant Alloy Powders," 1050.

[19] S. Cao and J.-C. Zhao, "Application of dual-anneal diffusion multiples to the effective study of phase diagrams and phase transformations in the Fe–Cr–Ni system," *Acta Materialia*, vol. 88, pp. 196–206, Apr. 2015.

[20] S. Mayer, M. Petersmann, F. D. Fischer, H. Clemens, T. Waitz, and T. Antretter, "Experimental and theoretical evidence of displacive martensite in an intermetallic Mo-containing γ-TiAl based alloy," *Acta Materialia*, vol. 115, pp. 242–249, Aug. 2016.

[21] J. W. Christian, *The Theory of Transformations in Metals and Alloys : Part I + II.* Elsevier, 2002.

[22] S. S. Naghavi, V. I. Hegde, and C. Wolverton, "Diffusion coefficients of transition metals in fcc cobalt," *Acta Materialia*, vol. 132, pp. 467–478, Jun. 2017.

[23] Thermo-Calc Software AB, "Thermo-Calc Software - Computational Materials Engineering." .

[24] The Japan Institute of Metals and Materials, *Thermal Dynamics of Microstructure*. Tokyo: Maruzen, 2005.

[25] Z. Nishiyama, *Martensitic Transformation.* Elsevier Science, 1978.

[26] L. Kaufman and M. Cohen, "Thermodynamics and kinetics of martensitic transformations," *Progress in Metal Physics*, vol. 7, pp. 165–246, Jan. 1958.

[27] G. B. Olson and M. Cohen, "A general mechanism of martensitic nucleation: Part I. General concepts and the FCC → HCP transformation," *Metallurgical*

Transactions A, vol. 7, no. 12, pp. 1897–1904, Dec. 1976.

[28] S. Kajiwara, "Mechanism of Isothermal Martensitic Transformation," *Materials Transactions, JIM*, vol. 33, no. 11, pp. 1027–1034, 1992.

[29] C. H. Shih, B. L. Averbach, and M. Cohen, "Some Characteristics of the Isothermal Martensitic Transformation," *JOM*, vol. 7, no. 1, pp. 183–187, Jan. 1955.

Conclusions

■ The dynamic behaviors of the powder raking process were simulated using DEM modeling to examine how the powder properties affect the quality of the powder bed during the raking process. The effects of the different physical parameters on powder bed quality, focusing on packing density, powder flowability, particle size distribution, and their interplays:

1) The practical powder packing density was influenced by corresponding layer thickness, and with an increase in nominal thickness, final steady layer thickness increased, and high powder packing density was obtained.

2) The better flowability of powder was preferable for homogeneity of powder layer with higher packing density because the higher flowability favored the greater tendency for a fine particle moving downward during powder raking.

3) The mixture of powder with large and small size could increase packing density, but it might be detrimental to the flowability and homogeneity. The excessive fraction of fine powder made the friction to be the main factor that limited the powder flowability.

■ Fundamentals of molten pool behavior in PBF-EB of the CCM alloy, focusing on the forming quality- and solidification condition-correlated fluid dynamics and the differences compared with PBF-L(laser) were investigated via CtFD simulations and experiments. The effect of fluid flow was examined by comparison between simulation cases with actual and artificially high viscosities. The following conclusions can be drawn:

1) CtFD simulation showed greater agreement with experiment than the pure-thermal model because fluid flow showed essential effects on temperature distribution and molten pool geometry.

2) The CtFD simulation results revealed the decisive influence of the Marangoni effect on fluid behavior and heat convection of the molten pool. The Marangoni effect of molten metal primarily determined the molten pool geometry and significantly affected molten pool instability and resultant formation quality in

PBF-EB of the CCM alloy.

3) The fluid behavior of PBF-EB was dominated by Marangoni effect rather than vapor recoil pressure that exerted a decisive force in PBF-L under atmospheric environment. The fluid behavior of PBF-EB was dominated by Marangoni effect rather than vapor recoil pressure that exerts a decisive force in PBF-L under atmospheric environment.

4) Fluid flow played a vital role in determining the solidification rate, R (solid-liquid interface velocity). The increasing R values was attributed to the changes in the spatial relation to the scan direction under the effect of active fluid convection.

■ The dynamic behaviors of a powder collection during the powder raking process was simulated using DEM modeling. In addition, CtFD simulations of the heat transfer and fluid flow processes were performed to elucidate the effects of physical properties of powder layer on PBF-EB fusion process. The main conclusions derived from this study can be summarized as follows:

1) Powder layer, with its stochastic nature, provided more fluid disturbance caused by non-uniform capillary actions, efficiently producing the irregularity or disconnection of melt-track with increasing scan speed.

2) Concerning the particle size, for the powder bed with small-size powder, the increased emissivity and decreased thermal conductivity of the powder bed induced the instability of the melt track.

3) The spherical and non-spherical powders possessed different surface features; thus, the amount of heat radiation was different. PREP powder with high circularity and small surface area was appropriate for PBF-EB, which was favorable for melt stability and could enlarge the process window.

■ The experimental results obtained in this study revealed the mechanisms governing the grain morphology and texture evolution of PBF-EB-built CCM alloy. Epitaxial growth with resulting columnar grains and near-cubic texture dominated the crystal growth. However, nucleation and new grain growth rather than extensive epitaxial growth could be achieved by manipulating the molten pool behaviors. Through the

experimental characterization of the microstructure and analysis of the simulation results, the microstructure evolution mechanisms could be summarized as follows:

1) The typical growth behavior of columnar grains and the resulting near-cubic texture were determined by competitive epitaxial grain growth governed by the heat flow characteristics with *xy*-scanning.

2) The molten pool connection between adjacent melt tracks produced a random orientation of <001> around the *z*-axis in the *xy*-plane, resulting in the development of a fiber-like texture. Therefore, the crystallographic texture was closely related to the transient geometry of the molten pool boundary, where the heat flow direction determined the crystallographic orientation during solidification.

3) E_{line} primarily controlled the columnar grain size. The large molten pool was conducive to the development of competitive growth, and the kinetic grain growth in the HAZ was induced by increasing E_{line}, promoting the formation of coarse columnar grains.

4) As the power increased, the slope of the S/L interface of the molten pool increased, producing a considerable mismatch between the resulting temperature gradient and the fast growth <001> orientation of the grains solidified in the preceding layer. Consequently, nucleation ahead of the solidification front was facilitated.

5) Investigation of the sub-grain structure and the *G–R*–grain morphology considering the fluid flow showed that the enlarged undercooling and probable dendrite fragmentation owing to fast fluid flow would promote the nucleation probability and new grains might form, which suggested that fluid convection was an important mechanism promoting CET during the PBF-EB process.

■ Through the experimental characterization and analysis of the simulation results, the mechanisms of microstructural inhomogeneity regarding matrix phase constitution of PBF-EB-built CCM alloy were analyzed depending on specific thermal history of PBF-EB and could be summarized as follows:

1) The isothermal and athermal $\gamma \rightarrow \varepsilon$ phase transformations took place in CCM alloy during PBF-EB. Isothermal $\gamma \rightarrow \varepsilon$ transformation occurred through both manners: diffusionless-martensitic and diffusion-massive transformation.

2) The difference in γ/ε phase distribution was a result of the thermal history. Depending on PBF-EB process conditions, thermal history determined the mechanism by which the $\gamma \rightarrow \varepsilon$ phase transformation was taking place.

3) In the sample with a lower energy input ($E_{area} = 2.6$ J/mm^2), $\gamma \rightarrow \varepsilon$ martensitic transformation with S-N OR was dominant. With the building height increasing away from the base plate, ε phase fraction decreased, because the holding time for martensitic transformation decreased.

4) In the sample with a higher energy input ($E_{area} = 4.4$ J/mm^2), the ε phase with near-random orientation formed via diffusional-massive transformation. ε phase only presented in a short range of the lower part away from the bottom where the time period required for massive $\gamma \rightarrow \varepsilon$ transformation was relatively short.

Significance and limitation of present study

Significance:

- The numerical modeling framework developed in the present thesis is effective for simulating and elucidating the underlying physics of the powder-bed AM processes (not limited to PBF-EB). The framework allows the modeling of powder, thermal, fluid flow, and solidification, covering the almost all of the key issues involved in powder-bed AM building process.

- The conclusions obtained from the present study here are not exclusive for PBF-EB-built CCM alloy. The enlightenments of building process in Chapters 2, 3, and 4 is applicable for PBF-EB, being not confined to a specific material. The strategies for microstructure control in Chapter 5 may be universal, applying not only to the CCM alloy but also to other alloy system.

Limitation:

- The numerical simulations applied in the present study are currently limited to the single layer melting with multi tracks. Though multi-layer building is possible to qualitatively simulate, the quantitative calculation would be much expensive and time consuming. Thus, current modeling framework is not suitable for precise simulation of large-scale building.

- With current technical means, the validation of the numerical simulation was conducted through the comparison with experimental results in terms of powder bed pattern, size and dimension of melt region, etc. While, the experimentally dynamic processes of particle motion, melting and molten pool formation were unable to be captured, which is important for modeling calibration with higher degree of precision. The in-situ process monitoring or sensing would cover this shortage.

Prospect

AM processes, including PBF-EB, are now increasingly used in aerospace, automotive and biomedical industries owing to the capability for fabricating value-added components that cannot be made easily by conventional techniques. For the increasing market share of commercial PBF-EB toward a more in-depth market penetration in the future, several scientific and technological issues that determine the component quality and production cost, still need to be addressed furthermore. These issues are including the prevalence of defects in components such as porosity, void caused by a lack of fusion, poor surface finish, dimension distortion, and residual stresses.

Mechanical properties of PBF-EB-built components are in some industrial fields have become comparable with those of components produced by conventional techniques. However, quality fluctuation easily occurs depending on process parameters and relative location in the building part. Controlled forming quality and microstructure of parts require a deep understanding of process mechanisms based on scientific theories and principles. The task is to avoid defects and to tailor the composition, structure, and properties of PBF-EB-built components, and finally to achieve repeatable production with consistent quality.

Based on the goals shown above, a high level of in-situ process monitoring or sensing, and automatic control is critical in the further development of PBF-EB. The real-time information capture and handling require the synchronous developments and possible coordination of the hardware and software equipped in PBF-EB system. Given the specificity of PBF-EB system, processing in a vacuum and transient nature of the electron beam, electronic imaging system, and combined utilization of multiple types of equipment should be under consideration. Moreover, establishing a precise and rapid closed-loop feedback and control system, the machine learning algorithm can be applied for image recognition and statistical analysis that act as foundations for control-decisions.

Acknowledgment

Publications

1. **<u>Zhao, Y.</u>**, Koizumi, Y., Aoyagi, K., Yamanaka, K., & Chiba, A. (2017). **Characterization of powder bed generation in electron beam additive manufacturing by discrete element method (DEM)**. *Materials Today: Proceedings*, 4(11), 11437-11440.

2. **<u>Zhao, Y</u>**., Koizumi, Y., Aoyagi, K., Wei, D., Yamanaka, K., & Chiba, A. (2019). **Molten pool behavior and effect of fluid flow on solidification conditions in selective electron beam melting (SEBM) of a biomedical Co-Cr-Mo alloy**. *Additive Manufacturing*, 26, 202-214.

3. **<u>Zhao, Y</u>**., Koizumi, Y., Aoyagi, K., Wei, D., Yamanaka, K., & Chiba, A. (2019). **Comprehensive study on mechanisms for grain morphology evolution and texture development in electron beam additive manufacturing of Co-Cr-Mo alloy**. *Materialia*, 6, 100346.

4. **<u>Zhao, Y</u>**., Koizumi, Y., Aoyagi, K., Yamanaka, K., & Chiba, A. **Manipulating the local heat accumulation towards controlled forming quality and solidification microstructure in powder bed fusion with electron beam**. *Materials Letters*, 254, 269-272.

5. **<u>Zhao, Y</u>**., Koizumi, Y., Aoyagi, K., Yamanaka, K., & Chiba, A. **Analysis of phase transformation mechanism of Co-28Cr-6Mo alloy during powder-bed fusion electron beam additive manufacturing**. *Journal of alloys and compounds*. (Under review)

Presentations

International conference presentations:

1. **<u>Zhao, Y.</u>**, Koizumi, Y., Aoyagi, K., Wei, D., Yamanaka, K., & Chiba, A. **"Investigation of solidification conditions in electron beam melting using computational thermal-Fluid dynamics simulation"**. *The 13th World Congress on Computational Mechanics.* New York City, US, July 22-27, 2018. [Oral]

2. **<u>Zhao, Y.</u>**, Koizumi, Y., Aoyagi, K., Wei, D., Yamanaka, K., & Chiba, A. **"Molten pool behavior and solidification microstructure of Co-Cr-Mo alloy in powder-bed electron beam additive manufacturing"**. *The 14th U.S. National Congress on Computational Mechanics*. Montreal, Canada, July 17-20, 2017. [Oral]

3. **<u>Zhao, Y.</u>**, Koizumi, Y., Aoyagi, K., Wei, D., Yamanaka, K., & Chiba, A. **"Molten pool behavior and mechanism of biomedical Co-Cr-Mo alloy in powder-bed electron beam additive manufacturing"**. *The 2nd International Symposium on Creation of Life Innovation Materials for Interdisciplinary and International Researcher Development*. Nagoya, Japan, September 29-October 1, 2017. [Poster]

4. **<u>Zhao, Y.</u>**, Koizumi, Y., Aoyagi, K., Yamanaka, K., & Chiba, A. **"Investigation on molten pool behavior in electron beam melting of Co–Cr–Mo alloy"**. *2017 Annual Meeting of Excellent Graduate Schools for Materials Integration Center and Materials Science Center in conjunction with 2017 Russia-Japan Conference*. Sendai, Japan, March 21-22, 2017. [Poster]

5. **<u>Zhao, Y.</u>**, Koizumi, & Chiba, A. **"Molten pool behavior during electron beam melting of Co-Cr-Mo alloy simulated by computational fluid dynamics"**. *TFC ELyT Off-campus Workshop for Intensive Discussions*. Miyagi, Japan, October 6-8, 2016. [Poster]

Award:

<u>Y. Zhao</u>, Yuichiro Koizumi, Akihiko Chiba, **Best Poster Award**, *TFC ELyT Off-campus Workshop for Intensive Discussions*, 2016.10.7.

Japan domestic conference presentations:

1. 趙 宇凡, 小泉 雄一郎, 青柳 健大, 山中 謙太, 千葉 晶彦, **"Effects of Powder Layer and Particle Size Distribution on Fusion Process during Powder Bed Fusion with Electron Beam"**, *日本金属学会 2019 年春期講演大会*, 東京電機大学東京千住キャンパス, 2019.3.21.

2. 趙 宇凡, 小泉 雄一郎, 青柳 健大, 千葉 晶彦, **"Grain Morphology and Texture Formation in a Co-Cr-Mo Alloy Fabricated by Electron Beam Melting"**, *日本金属学会 2019 年秋期講演大会*, 東北大学, 2018.9.19. [ポスター]

3. 趙 宇凡, 小泉 雄一郎, 青柳 健大, 山中 謙太, 千葉 晶彦, **"Solidification Conditions in Molten Pool with Dynamic Fluid Flow in Electron Beam Melting of Co-Cr-Mo Alloy"**, *日本金属学会 2018 年春期講演大会*, 千葉工業大学新習志野キャンパス, 2018.3.20.

4. 趙 宇凡, 小泉 雄一郎, 青柳 健大, 山中 謙太, 千葉 晶彦, **"Numerical Investigations on Fusion Process in Electron Beam Melting of Biomedical Co-Cr-Mo Alloy"**, *粉体粉末冶金協会平成 29 年度秋季大会*, 京都大学百周年時計台記念館, 2017.11.10.

5. 趙 宇凡, 小泉 雄一郎, 青柳 健大, 山中 謙太, 千葉 晶彦, **"Investigation on Molten Pool Behavior and Solidification Microstructure in Electron Beam Melting of Co-Cr-Mo alloy"**, *日本金属学会 2017 年春期講演大会*, 首都大学東京, 2017.3.16.

6. 趙 宇凡, 小泉 雄一郎, 青柳 健大, 山中 謙太, 千葉 晶彦, **"Numerical Assessment of Dominant Factor on Powder Bed Fusion in Electron Beam Melting of Co-Cr-Mo Alloy"**, *粉体粉末冶金協会平成 28 年度秋季大会*, 東北大学, 2016.11.9-11.

7. 趙 宇凡, 小泉 雄一郎, 青柳 健大, 山中 謙太, 千葉 晶彦, **"Numerical Simulation of Solidification and Microstructure Evolution in Co-Cr-Mo Alloy fabricated by Electron Beam Melting"**, *日本金属学会 2016 年秋期講演大会*, 大阪大学, 2016.9.21-23.

受賞:

趙 宇凡, **優秀講演発表賞**, *粉体粉末冶金協会平成 28 年度秋季大会*, 2016.11.11.